THE UNIVERSITY OF CHICAGO

ELECTROWEAK SYMMETRY IN THE EARLY UNIVERSE

A DISSERTATION SUBMITTED TO
THE FACULTY OF THE DIVISION OF THE PHYSICAL SCIENCES
IN CANDIDACY FOR THE DEGREE OF
DOCTOR OF PHILOSOPHY

DEPARTMENT OF PHYSICS

BY
YIKUN WANG

CHICAGO, ILLINOIS
AUGUST 2021

TABLE OF CONTENTS

LIST OF FIGURES

LIST OF TABLES

ACKNOWLEDGMENTS

Throughout of my Ph.D. study and research, I have received a great amount of support and assistance.

I would first like to thank my advisor, Professor Marcela Carena, without whose advisory, support and trust, I couldn't have enjoyed this fascinating journey. She teaches and inspires me with her rich knowledge, deep insights and sharp intinction in physics. It has been the most fun and valuable experience learning from and working with her during the past few years. She has also been a good friend and role model of mine beyond a mentor. As a woman scientist, her experience has and will continue to encourage me to pave through the road in academia.

I would like to thank the University of Chicago for the financial support during my Ph.D. research. I would also like to thank the theory department of Fermilab for hosting and financially supporting me for my thesis research. Discussion with scientists and colleagues in both institutes has been such a joy inspiring a lot of exciting physics ideas.

I would like to thank all my collaborators, Sebastian Baum, Stefan Hoeche, Jonathan Kozaczuk, Claudius Krause, Zhen Liu, Andrew Long, Nausheen Shah, Jessica Turner and Carlos Wagner, for their contribution, inspiration and advisory through completing my thesis research. I would like to specially thank the faculty, Stefan Hoeche, Zhen Liu, Nausheen Shah, Jessica Turner and Carlos Wagner, for their help with my job search.

I would like to thank my thesis committee, Professors Dan Hooper, Mark Oreglia and Carlos Wagner, for their evaluation of my thesis and defense.

I would like to thank my friends, Claudius Krause, Yin Lin, Shuoguang Liu, Jessica Turner, Shuyi Zhang, Xining Zhang, for their chatting and hanging out with me in the good or bad days.

Last but not least, I would like to thank my family – my parents, Kai Qiao and Li Wang, and my husband, Haiming Deng, without whom I couldn't have gone through some of the

difficult times. They gave me endless support, consultation and encouragement with their kind understanding and sympathetic ears. I would also like to thank my cat, Bubble, whose arrival was like a gift and whose companionship has supported me emotionally.

ABSTRACT

The thermal history of the Higgs boson and its connection with electroweak symmetry breaking play an important role in the production of cosmological relics. In this thesis, I study different patterns of the electroweak symmetry at finite temperatures to build a bridge connecting particle cosmology, Higgs phenomenology and physics beyond the Standard Model, that may provide answers to some of the open questions in particle physics. I carefully scrutinize the experimental probes, e.g. measurements of the properties of the Higgs boson and gravitational wave detection, that can directly or indirectly provide information on the validity of the theories I investigate and their early universe electroweak symmetry behavior.

The existence of a strong first order electroweak phase transition in the early universe is a necessary building block of the electroweak baryogenesis mechanism, that can explain the matter-antimatter asymmetry of the universe. I investigate representative extensions of the Standard Model Higgs sector, which allow for a strong first order electroweak phase transition and open opportunities for new Higgs decay channels at colliders. I study the electroweak phase transition dynamics, and the relevance of nucleation in models with an additional singlet, both in theories with SM gauge symmetries and in the case of supersymmetry. I also propose a novel scenario, where the electroweak symmetry remains broken up to very high temperatures, thereby allowing to evade strong experimental bounds from CP violation that otherwise plays important limitations on electroweak baryogenesis scenarios.

Dynamics of Higgs field bubbles can directly affect the power spectrum of the gravitational wave signals generated during a strong first order phase transition. I perform a first study of the speed of the Higgs bubble wall, and show that it can be significantly slowed down by friction from particles in the hot plasma with resumed soft and collinear radiations.

CHAPTER 1

INTRODUCTION

The discovery of the Higgs boson [1,2], as the last missing piece of the Standard Model [3–14], is a great triumph of particle physics. The spontaneous electroweak symmetry breaking, that is induced by the non-zero expectation value of the Higgs boson, is a cornerstone of the Standard Model and is responsible for the masses of most massive elementary particles that we have detected, with the possible exception of neutrinos.

After the Higgs boson discovery, the next step has become understanding the Higgs boson properties and its possible departures from the Standard Model predictions. Numerous ongoing and proposed high-energy explorations are targeted to this. Although the Standard Model has been successfully predicting most of the experimental observations, there exist evidence and unsolved questions in particle physics indicating new physics beyond the Standard Model. As perhaps the least understood and the only fundamental scalar particle, looking for deviations from the Standard Model in the Higgs sector is at the frontier of new physics searches. In addition, the thermal history of the Higgs field plays an important role in cosmology, determining the dynamics of the electroweak symmetry breaking in the early universe. Most relevantly, it has the potential of affecting the production of various cosmological relics, including the matter-antimatter asymmetry [15], topological defects [16], primordial magnetic fields [17], and a stochastic background of gravitational wave radiation [18]. Thus, studying the Higgs thermal history serves as a bridge connecting particle cosmology with Higgs phenomenology, and may provide answers to some of the open questions in particle physics.

In this chapter, we give an introduction and overview to establish the relevant role played by the electroweak symmetry in the hot early universe, determined by the Higgs thermal history, as well as its connections to the ongoing efforts in understanding the Higgs boson properties. We introduce one of the major motivations, i.e. the generation of matter-antimatter

asymmetry, for exploring alternative behaviors of the electroweak symmetry in the early universe beyond what is expected in the Standard Model. A particularly interesting early universe phenomenon associated with the electroweak phase transition, will be introduced, along with its potential role in the production of the cosmological relics mentioned above.

1.1 The thermal Higgs and electroweak symmetry in the early universe

As the first part of this section, we will give a brief introduction to the Higgs field, its role in the Standard Model (SM) of particle physics, and its behavior in today's universe. The SM is constructed based on the $\mathrm{SU}(3)_C \times \mathrm{SU}(2)_L \times \mathrm{U}(1)_Y$ gauge group, which predicts force mediators to be massless. However, people first noticed that the weak interaction, which is unified with the electromagnetism and together described by the $\mathrm{SU}(2)_L \times \mathrm{U}(1)_Y$ **electroweak** (EW) gauge group, is short range, indicating massive mediators. Indeed, experiments have confirmed that the $W^{\pm}$ and Z bosons, the force mediators of the weak interaction, have finite masses [19], since when, how the weak interaction is screened at long distances has been a theoretical difficulty. A solution was eventually proposed independently by Brout, Englert and Higgs [20–23], which is known as the Higgs mechanism, by introducing a scalar degree of freedom (the only option without breaking the Lorentz invariance) acquiring a non-zero vacuum expectation value (VEV), which spontaneously breaks the EW gauge symmetry. Formally, in the SM, the scalar degree of freedom is embedded in a complex doublet [7],

$$\phi = \frac{1}{\sqrt{2}} \begin{pmatrix} \chi_1 + i\chi_2 \\ h + i\chi_3 \end{pmatrix}, \tag{1.1}$$

that is charged under the EW gauge group. The potential for such a doublet, that is gauge invariant and renormalizable, reads

$$V(\phi) = -\mu^2 \phi^\dagger \phi + \lambda (\phi^\dagger \phi)^2. \tag{1.2}$$

In the case where the squared mass parameter μ^2 is positive, i.e. $\mu^2 > 0$, the global minimum of such a potential is at $|\phi|^2 = \frac{\mu^2}{2\lambda}$. As an illustration, one could visualize such a potential in the 'zero T' panel in Figure 1.1, assuming a complex singlet, which exhibits a 'sombrero' shape. In this two dimensional field space along the real and imaginary direction of the singlet, there are infinite number of degenerate minima with the same value in the radial direction, namely a Higgs mode, and arbitrary values (averaged to be zero) in the tangent direction, namely a massless Nambu-Goldstone mode. Generalizing to the case of a complex doublet, there are, in total, four scalar degrees of freedom, with one Higgs mode acquiring a non-zero VEV and three massless Nambu-Goldstone modes with zero VEV. Choosing which one of the four degrees of freedom in the Higgs doublet parametrization shown in Equation (1.1) to be the Higgs direction is arbitrary, and conventionally, one chooses $h(x)$ to be the Higgs field with

$$v \equiv \langle h \rangle = \sqrt{\frac{\mu^2}{\lambda}}. \tag{1.3}$$

The perturbation theory should be expanded around such a vacuum, at which the EW symmetry is spontaneous broken. Non-zero masses for gauge bosons thus are generated through the Higgs kinematic term

$$\mathcal{L}_{\text{Higgs}} \supset D_\mu \phi^\dagger(x) D^\mu \phi(x), \tag{1.4}$$

where the covariant derivative for the EW gauge group reads

$$D_\mu = \partial_\mu - igT^a W_\mu^a - ig' Y B_\mu \tag{1.5}$$

by expanding the $h(x)$ component of the doublet $\phi(x)$ around its VEV,

$$h(x) = v + H(x). \tag{1.6}$$

The perturbative degree of freedom $H(x)$ is the Higgs boson, which was eventually discovered by Large Hadron Collider (LHC) in 2012 after decades' hunt, confirming this proposed Higgs mechanism. Notice that the non-zero VEV of the Higgs field also generates finite masses for leptons and quarks in the SM through Yukawa coupling interactions.

In summary, in today's universe, the existence of the Higgs boson and the signature of the Higgs potential, induce the spontaneous breaking of the EW symmetry, which is the cornerstone to the SM's success. Moreover, if one traces back to early times in the universe, the Higgs potential and the EW symmetry behavior at finite temperatures, could be a bridge to new physics, that is in need to answer open questions the SM fails to explain, which will be the subject of this thesis.

As opposed to today's universe where most elementary particles have decoupled and are confined into hadrons, at early times in the universe, particle degrees of freedom were unbounded and kept in thermal equilibrium by rapidly interacting with each other (given the interaction rates much larger than the universe's expansion rate), which can be characterized by finite densities and temperatures. The relation between the time and temperature in the early universe can be estimated as

$$T \propto g_{*S}^{-1/3} a(t)^{-1}, \tag{1.7}$$

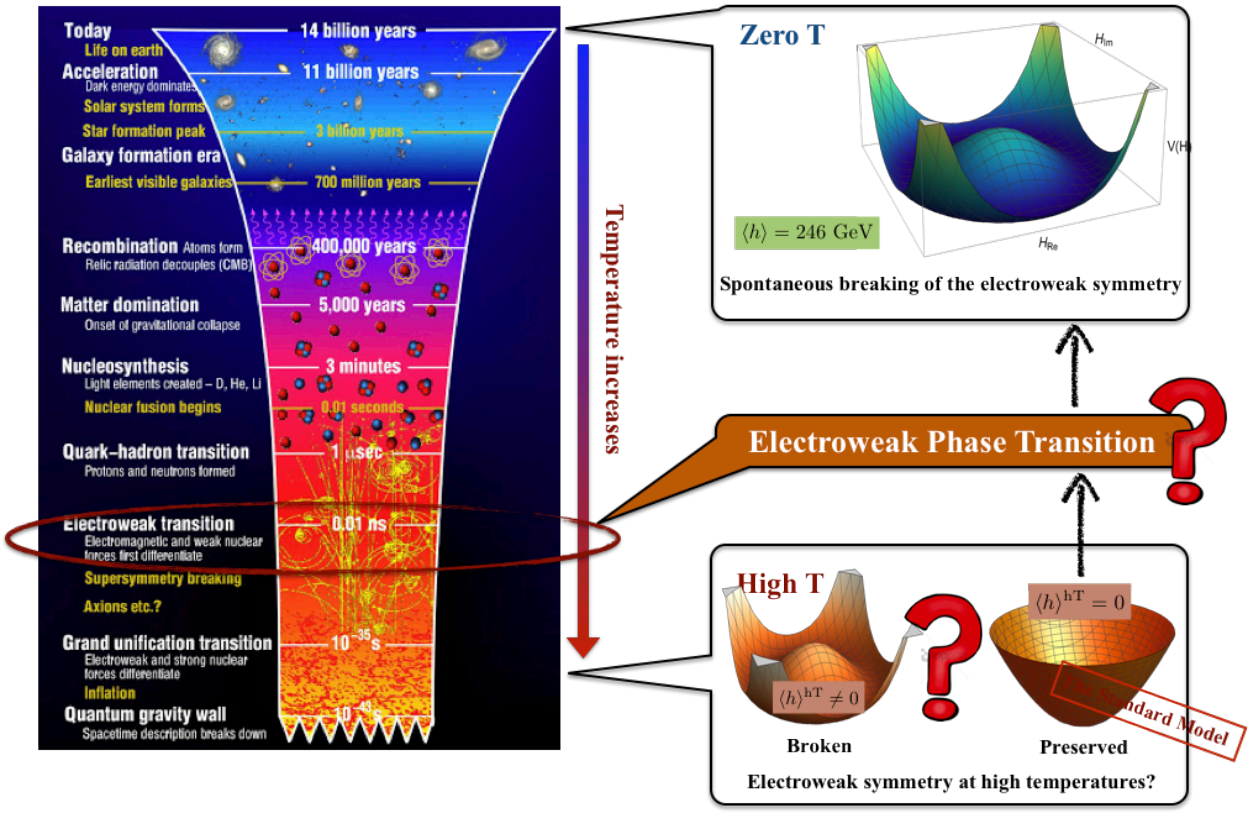

Figure 1.1: History of the universe with the Higgs potential and electroweak symmetry at early times of the universe.

where g_{*S} is the effective number of relativistic degrees of freedom for entropy and $a(t)$ is the scale factor at time t. At finite temperatures, the Higgs potential receives radiative thermal corrections from degrees of freedom interacting with the Higgs doublet, resulting in a different vacuum location and potentially a different EW symmetry behavior. As has been discussed above, the Higgs potential has a 'sombrero' shape today, where the vacuum is at a non-zero field value of the Higgs and the EW symmetry is broken. However, as is shown in Figure 1.1, with thermal corrections, the (effective) Higgs potential at finite temperatures may have a different signature where the vacuum is at the origin and the EW symmetry was preserved/restored, provided with a negative thermal corrected square mass parameter in Equation (1.2), $\mu^2 \to \mu^2_{\rm thermal} \leq 0$. Based on theoretical calculations, this is

indeed the case in the SM [24–27], given the SM particle content interacting with the Higgs and sizes of the corresponding coupling constants as have been measured by experiments. Alternatively, the Higgs potential could have maintained its zero temperature signature with EW symmetry broken given BSM degrees of freedom interacting with the SM Higgs and/or EW gauge bosons. As the subject of chapter 4, we will discuss such a possibility with a well-defined SM Higgs sector extension.

If the EW symmetry was restored in the early universe, as is in the SM, there would be a time/temperature when the universe converted from the EW preserving phase to the EW broken phase, which is called the **Electroweak Phase Transition** (EWPT). The nature of the EWPT has important impacts on the production of various thermal relics, and may provide solutions to one of the open questions in particle physics, the generation of the matter-antimatter asymmetry, through an electroweak baryogenesis mechanism, which will be the topic for the next two sections.

1.2 Matter-antimatter asymmetry and electroweak baryogenesis

In today's universe, there is more matter than antimatter. This is both a fact that one may observe in daily life, and a property that has been confirmed and precisely measured by scientific experiments. Formally, the asymmetry between matter and antimatter, namely the baryon asymmetry of the universe (BAU), is characterized by the ratio

$$\eta = \frac{n_B - n_{\bar{B}}}{n_\gamma}, \tag{1.8}$$

where n_B ($n_{\bar{B}}$) is the number density of (anti)baryons and n_γ is the number density of photons. Notice that such a quantity is a good measure as it stays almost constant during late times of the universe's expansion. In early times, instead, one may choose to use the quantity defined in case of the entropy s for convenience, $\frac{n_B - n_{\bar{B}}}{s}$, which has a conversion

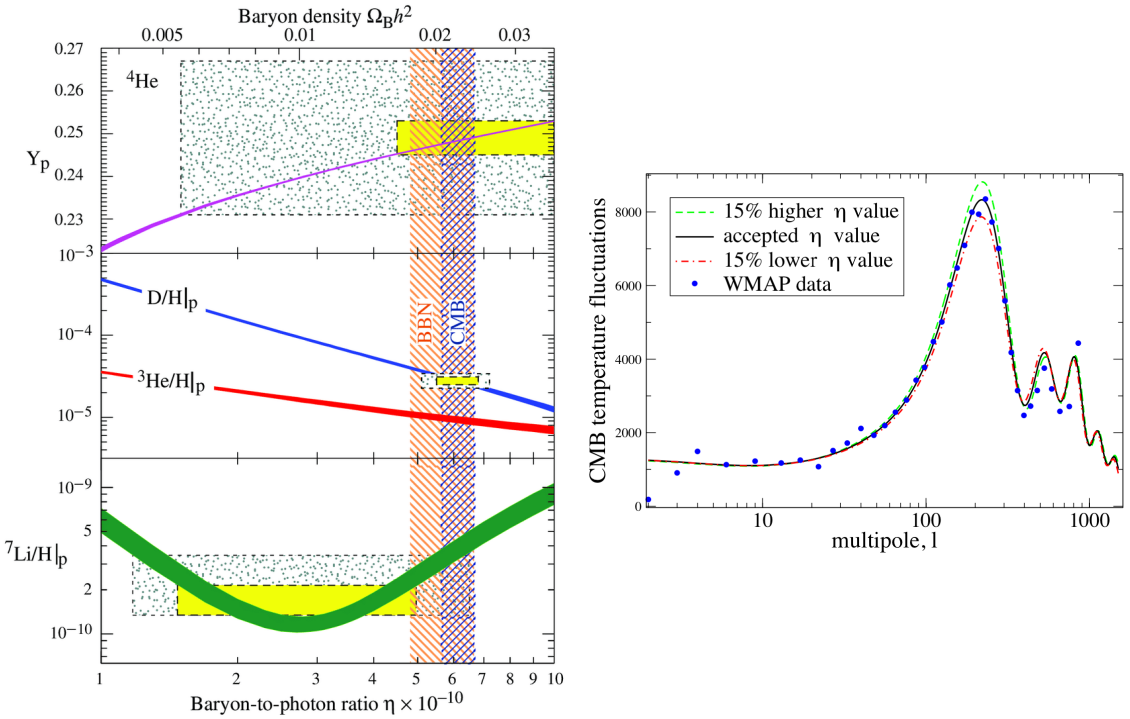

Figure 1.2: Determination of the baryon asymmetry of the universe η. Left panel: abundances of light elements as a function of η from BBN [28]; Right panel: CMB temperature power spectrum with different values of η in comparison with the WMAP data [29].

factor of $\sim 1/7$ to η.

Currently, we have a good knowledge of the value of the BAU η from theoretical prediction and experimental observations. The BAU was first determined by the big bang nucleosynthesis (BBN), where the value of η should give the correct abundances of ^{3}He, ^{4}He, D, ^{6}Li and ^{7}Li, which can be measured by experiments. The left panel in Figure 1.2 shows abundances of these light elements as a function of η, as predicted by the SM of BBN, and boxes indicate observed values of the abundance. Accordingly, the value of η is constrained to be [28]

$$\text{BBN}: \quad 4.7 \times 10^{-10} \leq \ \eta \ \leq 6.5 \times 10^{-10} \quad (95\%\ \text{CL}), \tag{1.9}$$

as one may read out from the orange shaded bin in the figure. In comparison, the blue shaded

bin on the left panel in Figure 1.2 shows the value of η determined by Cosmic Microwave Background (CMB) measurements, which is an independent and more precise measurement of η developed later [30]. The CMB provides information on the shape and content of the universe, where η will affect the relative sizes of the Doppler peaks in the CMB temperature anisotropies, as shown in the right panel of Figure 1.2. Based on the Wilkinson Microwave Anisotropy Probe 7-year (WMAP) data, CMB constrains η to be [31]

$$\text{CMB}: \quad \eta = (6.16 \pm 0.15) \times 10^{-10}. \tag{1.10}$$

One can see that these two independent determinations have very good agreement.

Despite the confident observation of the BAU, there exits no explanation of such a number either within the SM or within the standard cosmology. If there was no baryon asymmetry in the beginning of the universe, the BAU that we could observe today, due to the fact that baryons and antibaryons won't annihilate perfectly after freezing out, is of the order of 10^{-20} [32], which is far below the observed BAU shown above. If instead, the BAU is assumed to be an initial condition before the big bang, it would be diluted during the inflation because of the entropy. Thus, a dynamical generation of the baryon asymmetry prior to the BBN is the only option to explain the BAU, named as **baryogenesis**, which was first realized in 1967 by A. Sakharov [33]. Perhaps more importantly, also proved in this ground-breaking paper are the three necessary conditions for baryogenesis, known as the Sakharov conditions:

- baryon (B) violation;
- charge conjugate (C) and charge conjugate and parity (CP) violation;
- departure from thermal equilibrium.

It is natural to see the need for B violation. Interestingly, B violation processes actually exist in the SM, e.g. sphaleron process in the EW sector that is associated with the structure

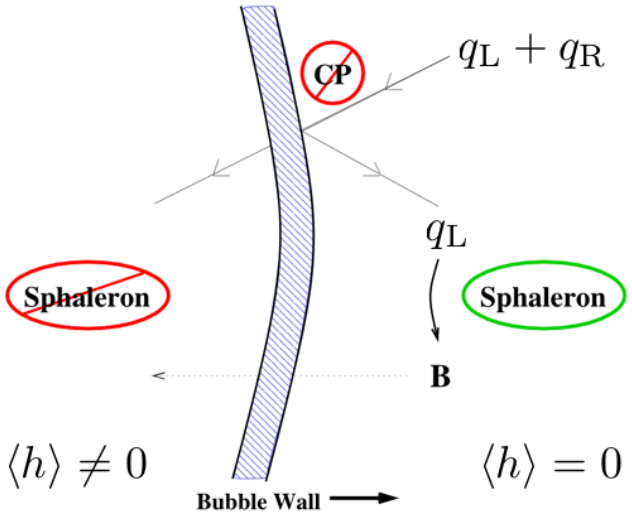

Figure 1.3: Electroweak baryogenesis in the vicinity of the Higgs bubble wall [34].

and anomaly of the gauge group. We will discuss the sphaleron process with more details in the next section. For the second condition, the C violation is needed in the sense that, in the case where C is a symmetry, any B violation process and its C conjugate process will have the same rate, and would result in zero net B creation, as the net B creation rate is proportional to their difference. Similar argument applies to the need for CP violation, where CP conjugate process would remove any asymmetries in the quark sector. Last but not least, departure from thermal equilibrium is necessary, otherwise any net B created through a B violation process would be destroyed by its inverse process, which has the same rate in thermal equilibrium.

As has been mentioned above, one can find B violation source in the SM that can be rapid at high temperatures. There also exit C and CP violation in the SM, e.g. in the CKM matrix in the SM quark sector. Of course, either the small CP violation phase in the CKM matrix is enough to create the amount of asymmetry that we observed today needs more careful investigation based on the specifics of the asymmetry generation. It is, however, tricker to realize departure from thermal equilibrium. Naively, ways of creating out of equilibrium

environment mainly fall into two categories [35]

- through a first order phase transition (PT);
- during the decay of heavy particles.

Interestingly, as has been introduced in the last section, an EWPT would take place in the early universe based on the SM prediction, and if it is strong first order, the universe would depart from thermal equilibrium. Thus, it is natural to propose an **Electroweak Baryogenesis** mechanism [15,36,37], that happes during the epoch of EWPT, provided with all necessary ingredients readily existing within the SM. Figure 1.3 provides an illustration of such a mechanism. A first order EWPT, with more details to be presented in the next section, proceeds through the nucleation, growth, and percolation of bubbles. Outside of the bubbles, the expectation value of the Higgs field vanishes, i.e. $\langle h \rangle = 0$, and EW symmetry is restored. Inside of the bubbles, the average Higgs field has a nonzero value, i.e. $\langle h \rangle \neq 0$, giving mass to the quarks, charged leptons, and weak gauge bosons. A differential vacuum pressure across the phase boundary drives the bubbles to expand and collide, on time scales typically much less than one Hubble time, filling all of spacetime with the broken-symmetry phase. The EWBG, as shown in Figure 1.3, took place in the vicinity of the phase boundaries, i.e. the bubble wall. In the first step of EWBG, C and CP violation interactions between quarks and the Higgs will bias the scattering of quarks off the bubble wall, resulted in more left handed quarks and right handed antiquarks in the broken phase, and more right handed quarks and left handed antiquarks in the symmetric phase, i.e. C and CP asymmetries in particle number density are generated. In the second step, the EW sphaleron process, which violates the B and is only active in the symmetric phase, converts the CP asymmetry to be the B asymmetry. Lastly, the B asymmetry in the symmetric phase diffuses into the broken phase as the bubble expands, where it will be preserved until today because of the inactive sphalerons associated with the strong first order nature of the EWPT, that will be further defined and quantified in the next section. On top of the Sakharov conditions, a successful

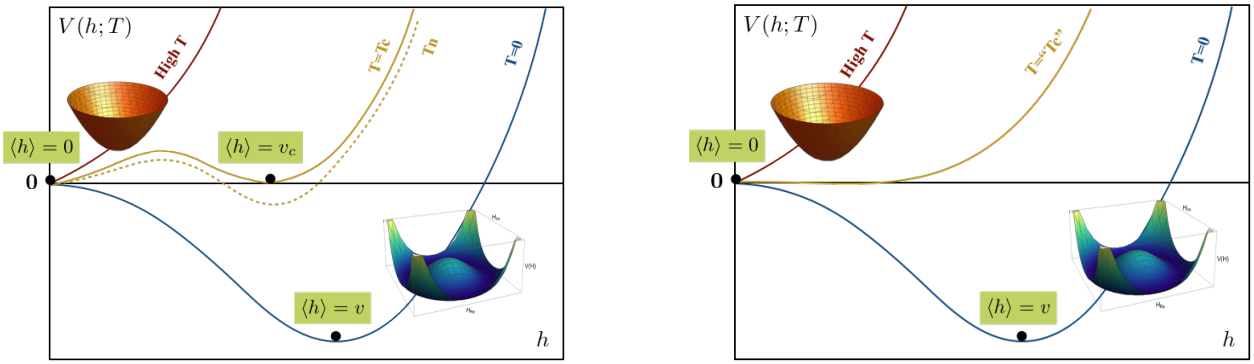

Figure 1.4: The Higgs potential at different temperatures. Left panel: the electroweak phase transition proceeded in a first order nature; Right panel: the electroweak phase transition proceeded in a cross over/second order nature.

EWBG further requires: 1. sufficient amount of CP violation; 2. the EWPT being strong first order. In reality, neither of these two requirements can be satisfied in the SM, that is why although all ingredients exist in the SM, it doesn't give rise to a successful explanation of the BAU. Accordingly, BSM physics compatible with EWBG needs to introduce additional CP violation source and renders a **strong first order electroweak phase transition** (SFOEWPT). Notice that sectors responsible for these two inputs are typically separated, where the former typically originates from fermionic sectors while the latter is determined by the nature of the scalar sector. Thus, one is entitled to discuss these two aspects separately. As the focus of this thesis, we will concentrate on discussing the phenomenon of SFOEWPT while leaving the CP violation discussion for other interesting works.

1.3 Electroweak phase transition

We have introduced the concept of EWPT and its role in EWBG from a schematic point of view. In this section, we will take a closer look to its dynamics and investigate some of its properties quantitively, that will be relevant to determine if the EWBG can be successful.

The nature of the EWPT is determined by the Higgs potential at finite temperatures,

which is illustrated in Figure 1.4 corresponding to different natures of the EWPT projected into the Higgs direction of the Higgs doublet. A characteristic temperature is when the symmetry vacuum is degenerate with the broken vacuum,

$$V(h = 0, T_c) = V(h = v_c, T_c), \tag{1.11}$$

that is called the critical temperature T_c, and the VEV of the Higgs field at the critical temperature is noted as v_c. Above such a temperature, the global minimum of the potential is the symmetric phase, while below such a temperature, the broken phase becomes deeper and the global minimum. Either the value of v_c is zero or not serves as an important criterial categorizing the nature of the transition:

- $v_c = 0$: the phase transition is second order or a cross over ;
- $v_c \neq 0$: the phase transition is first order.

A first order PT exhibits discontinuity in the first order derivative of the system's free energy, namely the order parameter, which, in the case of EWPT reads

$$\xi = \frac{v_c}{T_c}. \tag{1.12}$$

One may trivially read out that $v_c \neq 0$ corresponds to a discontinuity in the order parameter, and the Higgs potential for such a case can be found on the left panel in Figure 1.4, where the two vacua are separated in the field space by a barrier in between. On the contrary, the order parameter of a second order PT or a cross over is continuous, and a discontinuity appears only in the second order derivative of the free energy for the former, while the free energy is continuous in any orders of its derivative for the latter. Nevertheless, for either a second order EWPT or a cross over, $v_c = 0$, and the Higgs potential is illustrated on the right panel in Figure 1.4, where the vacuum smoothly rolls down from the symmetric phase

to the broken phase. Because there is latent heat released during the process, the universe will remain adiabatically and not depart from thermal equilibrium. This is one of the reasons the successful EWBG requires a first order EWPT, during which there will be a tunneling from the false vacuum to the true vacuum, that actually took place at a lower temperature compared to T_c, namely the nucleation temperature T_n, when the tunneling probability is roughly one per Hubble volume and Hubble time. We will give a more detailed discussion on such a temperature in section 3.3. Because of the latent heat released during the tunneling, the universe will depart from thermal equilibrium.

In addition, the created B asymmetry should be preserved against the sphaleron process, which will wash out any asymmetry in the B+L direction, where L is the net lepton number. Sphalerons refer to static and saddle point solutions to the field equations of the Higgs and EW gauge fields, that is the top points of barriers separating equivalent EW vacua in the Chern-Simons number space of the gauge group. The sphaleron process is a non-perturbative finite temperature process of hopping over the barriers provided with enough thermal energy. Based on a semi-classical evaluation of path integral, the rate for such a process for the EW gauge theory reads [38, 39]

$$\frac{\Gamma}{V} = 4\pi\omega_{-}\mathcal{N}_{tr}\mathcal{N}_{rot}T^3\left(\frac{v_{\rm EW}(T)}{T}\right)^6 \kappa \exp\left[-E_{sph}(T)/T\right], \tag{1.13}$$

where parameters involved in the equation will be discussed with more details in section 4.2. Here, we would emphasis the most relevant quantity to the EWPT in the sphaleron rate equation, the sphaleron energy $E_{sph}(T)$ at finite temperatures, which is linear on the VEV of the Higgs field, that gives

$$E_{sph}(T) = E_{sph}(T=0)\frac{v(T)}{v(T=0)} = \frac{4\pi}{g}B\,v(T), \tag{1.14}$$

where B is a constant and again we will discuss it in section 4.2. Manifestly one can see that

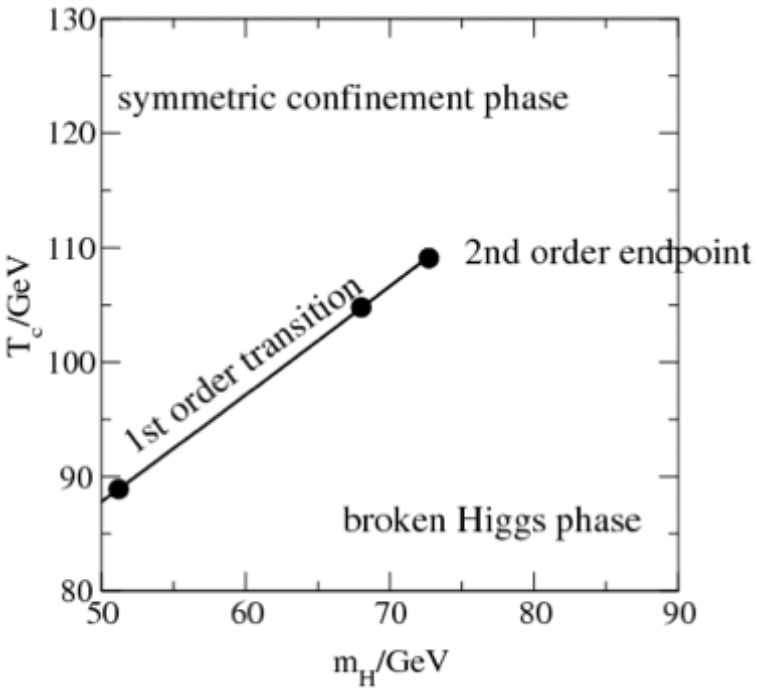

Figure 1.5: Phase diagram of electroweak phase transition in the Standard Model (SM) based on lattice simulation [40].

a large ratio between $v(T)$ and the temperature T in the broken phase would suppress the sphaleron rate such that the generated B asymmetry can be preserved. Based on the SM Higgs structure, $v(T)/T$ in the broken phase has its largest value at the time of the phase transition. Accordingly, a requirement on the order parameter of the phase transition,

$$\xi = \frac{v_c}{T_c} \gtrsim 0.8 - 1.3, \tag{1.15}$$

should be imposed to guarantee suppressed sphaleron rate to be much slower than the universe's expansion rate, which is the commonly implemented criterial for a SFOEWPT in the literature.

However, in the SM, the EWPT has been predicted to be a cross over, given the measured Higgs mass of 125 GeV. Figure 1.5 shows the phase diagram of the EWPT based on lattice simulation [41–43], where the order parameter is shown as a function of the SM Higgs mass.

One can read easily from the diagram that the possibility of a first order EWPT is ruled out with a Higgs mass above ~ 72 GeV, and the mass of the Higgs is pushed down to ~ 10 GeV for the possibility of a SFOEWPT. The existence of a light Higgs was quickly excluded and with the final Higgs discovery in 2012, showing a Higgs mass of 125 GeV, the possibility of a succesful EWBG within the SM was ruled out.

Nevertheless, EWBG still remains to be an appealing candidate explaining the mystery of BAU going beyond the SM, as it is the only baryogenesis mechanism where all the ingredients readily exist in the SM [44] along with other features. Given the lack of strong experimental deviations from the SM, it is likely that the new physics solution lies near the SM regime. Thus it is an interesting subject to explore the possibility of a SFOEWPT provided with BSM inputs, those are compatible with experimental probes, especially on the Higgs properties. At the same time, understanding the electroweak history of the universe, and if there was a SFOEWPT, also remains a relevant question. In the following chapters of this thesis, we will dedicate to these questions and present our investigations.

CHAPTER 2

FINITE TEMPERATURE EFFECTIVE POTENTIAL

In this chapter, I review the perturbative method, i.e. the effective potential approach with appropriate improvements, to study the Higgs field thermal history and the dynamics of the electroweak phase transition, that will be used for the rest of this thesis.

The effective potential includes radiative corrections to the scalar potential from zero temperature loop effects, as well as from thermal effects, where the latter are calculated based on the finite temperature field theory [45–58]. Both types of contributions are derived from the background field method [59], and are functionals of field-dependent masses of particles in the plasma, those interacting with the scalar fields (e.g. the SM Higgs, BSM singlets, multiplets etc). In section 2.1, following [39], we review the basic method and show the resulting general formulas for the zero and finite temperature effective potential at one loop order. We will also discuss features of the formulas that are relevant for analytical and numerical analysis for the thermal history and the electroweak phase transition.

In some regions of the field and temperature space, the perturbative convergence of the fixed-order calculation becomes compromised, for both the zero and finite temperature effective potential. In section 2.2, we introduce the thermal resummation methods to systematically include higher loop thermal contributions which are the most divergent in the infrared region, and discuss the associated theoretical uncertainties. In section 2.3, we introduce the renormalization group improvements of the effective potential to systematically resum higher order logarithms beyond the leading order logarithm included in the one loop zero temperature effective potential, those become relevant in certain regions in the field and temperature space.

2.1 The effective potential at zero and finite temperatures

The effective potential (EP) method has been introduced to study the spontaneous symmetry breaking associated with scalar fields acquiring none-zero VEV that is determined by the potential shape including radiative corrections [48, 60, 61].

For a translationally invariant theory, the EP as a function of a constant scalar field $\hat{\phi} = \bar{\phi}(x)$ can be calculated order by order as

$$V_{\text{eff}}(\hat{\phi}) = \sum_{n=0}^{\infty} V_n(\hat{\phi}) \quad \text{with} \quad V_n(\hat{\phi}) = -\frac{1}{n!}\hat{\phi}^n \Gamma^{(n)}(p_i = 0), \tag{2.1}$$

where $\Gamma^n(p_i)$ is the $n-$th order contribution to the effective action expanded in powers of $\hat{\phi}$ in the momentum space. The effective action is the Legendre transform of connected generating functional (vacuum-to-vacuum amplitude) given a Lagrangian density for the scalar field, that can be written in a Green function representation expanding in powers of the source. The zeroth order contribution to the EP, V_0, is the tree level potential. At loop order, the zero temperature contribution is computed based on the regular Green functions as ordered product of the field operators, while at finite temperatures, the Green functions should be taken as the grand canonical average of the ordered product, the so-called thermal Green function.

At zero temperature, the one loop contribution V_1 was first computed by Coleman and Weinberg thus commonly known as Coleman-Weinberg (CW) potential [49]. Considering a scalar sector composed by N_s complex scalar fields ϕ_a, the contribution to V_1 from the scalars with the Lagrangian

$$\mathcal{L} = \partial^\mu \phi^a \partial_\mu \phi_a^\dagger - V_0(\phi^a, \phi_a^\dagger) \tag{2.2}$$

reads

$$V_1^{\text{scalars}} = \frac{1}{2}\text{Tr}\int \frac{d^4p}{(2\pi)^4}\log\left[p^2 + M_s^2(\hat{\phi}^a, \hat{\phi}_b^\dagger)\right], \tag{2.3}$$

where

$$\left(M_s^2\right)_b^a \equiv \frac{\partial^2 V}{\partial\phi_a^\dagger \partial\phi_b}, \tag{2.4}$$

as a function of constant values of the scalar fields is called the field-dependent mass (matrix) of the scalar fields. Similarly, the contribution to V_1 from fermions ψ_a with the Lagrangian

$$\mathcal{L} = i\bar{\psi}_a\gamma_\mu\partial^\mu\psi^a - \bar{\psi}_a(M_f)_b^a\psi^b, \tag{2.5}$$

where $(M_f)_b^a$ as a function of constant values of the scalar fields is the field-dependent mass (matrix) of the fermions, reads

$$V_1^{\text{fermions}} = -2\lambda\frac{1}{2}\text{Tr}\int \frac{d^4p}{(2\pi)^4}\log\left[p^2 + M_f^2(\hat{\phi}^a, \hat{\phi}_b^\dagger)\right], \tag{2.6}$$

where $\lambda = 1(2)$ for Weyl (Dirac) fermions. Lastly, the contribution to V_1 from gauge bosons with the Lagrangian

$$\mathcal{L} = -\frac{1}{4}\text{Tr}(F_{\mu\nu}F^{\mu\nu}) + \frac{1}{2}\text{Tr}(D_\mu\phi_a)^\dagger D^\mu\phi^a + \cdots, \tag{2.7}$$

which contains the interacting/mass term $\frac{1}{2}\left(M_{gb}^2\right)_{\alpha\beta}A_\mu^\alpha A^{\mu\beta}$, reads

$$V_1^{\text{gb}} = (\text{Tr}\Delta)\frac{1}{2}\text{Tr}\int \frac{d^4p}{(2\pi)^4}\log\left[p^2 + M_{gb}^2(\hat{\phi}^a, \hat{\phi}_b^\dagger)\right], \tag{2.8}$$

where $\text{Tr}\Delta$ is the number of degrees of freedom of massive gauge bosons. Notice that here

we work in the Landau gauge, in which case there are no ghosts. We will stop here at one loop order, higher loop corrections can be found, e.g. in [51, 62].

The above expressions are ultraviolet divergent. Formalism of the EP after the renormalization depends on the renormalization scheme one chooses. However, any physical results, for example, the location of the vacuum determined by the EP, should be independent of the renormalization scheme, which needs more detail investigation and treatments. The scheme dependence would introduce uncertainty, although typically small and negligible, to the relevant calculation. The two commonly used renormalization schemes for the EP are the $\overline{\text{MS}}$ scheme and the on-shell scheme. Under the $\overline{\text{MS}}$ scheme, after the renormalization, the CW potential reads

$$V_{\text{CW}}^{\overline{\text{MS}}} = \frac{1}{64\pi^2} \sum_{i=B,F} n_i m_i^4(\hat{\phi}^a, \hat{\phi}_b^\dagger) \left[\log \frac{m_i^2(\hat{\phi}^a, \hat{\phi}_b^\dagger)}{\mu_R^2} - C_i \right], \tag{2.9}$$

where i runs over all mass eigenstates in the boson and fermion sector, n_i is the number of degrees of freedom for each eigenstate, $C_i = \frac{5}{6}\left(\frac{3}{2}\right)$ for gauge boson (scalars and fermions) and μ_R is the renormalization scale. As one can see, the EP, and potential physical quantities derived from the EP, depend on the choice of the renormalization scale, which can be treated by renormalization group (RG) improvement. If physical scales of the problem are close, choosing a μ_R close to the physical scale will minimize the dependence and introduce only small and negligible uncertainties. However, if there is large scale separation, the RG improvement would become essential, which will be discussed in detail in a later section 2.3. Another scheme that is commonly used in the literature is the on-shell scheme, which has the benefit of not shifting the vacuum from the tree level location. Under the on-shell scheme,

the CW potential reads

$$V_{\rm CW}^{\rm OS}=\frac{1}{64\pi^2}\sum_{i=B,F}n_i\left\{m_i^4(\hat{\phi}^a,\hat{\phi}_b^\dagger)\left[\log\frac{m_i^2(\hat{\phi}^a,\hat{\phi}_b^\dagger)}{m_i^2\left(\langle\hat{\phi}^a\rangle,\langle\hat{\phi}_b^\dagger\rangle\right)}-\frac{3}{2}\right]+2m_i^2(\hat{\phi}^a,\hat{\phi}_b^\dagger)m_i^2\left(\langle\hat{\phi}^a\rangle,\langle\hat{\phi}_b^\dagger\rangle\right)\right\},\tag{2.10}$$

where related notations have been introduce above, and $\langle\hat{\phi}^a\rangle$ denotes the vacuum expectation value of the scalar fields. Notice the feature of the EP under such a scheme is that $\partial V_1^{\rm OS}/\partial\hat{\phi}^a|_{\rm vacuum}=0$ at the vacuum location, thus it doesn't contribute to the extreme condition determining the location of the vacuum. However, such a scheme is ill-defined when there are massless particles in the theory, where the logarithm dependent on the physical masses $m_i^2\left(\langle\hat{\phi}^a\rangle,\langle\hat{\phi}_b^\dagger\rangle\right)$ diverges at any location in the field space. In comparison, the CW potential under the $\overline{\rm MS}$ scheme in Equation (2.9) is safe from the massless degrees of freedom in the sense that it is well defined away from the vacuum, and in the vacuum, the divergence only appears in the second order derivatives of the EP, which can be treated by introducing a small infrared regulator [63, 64].

At finite temperatures, the thermal Green function is defined as the grand canonical average, where the product of the field operators should be ordered along a path on the analytically continued complex plane of time. The path can be parametrized along the imaginary time axis, which is called the imaginary time formalism, or along the real time axis, i.e. the real time formalism. The two formalisms give rise to the same results for the finite temperature EP. Here we list the Feynman rules at finite temperatures based on the imaginary time formalism

- boson propagator: $\frac{i}{p^2-m^2};\ p^\mu=[2ni\pi\beta^{-1},\vec{p}]$
- fermion propagator: $\frac{i}{\gamma_\mu p^\mu-m};\ p^\mu=[(2n+1)i\pi\beta^{-1},\vec{p}]$
- loop integral: $\frac{i}{\beta}\sum_{n=-\infty}^{\infty}\int\frac{d^3p}{(2\pi)^3}$

- vertex function: $\quad -i\beta(2\pi)^3\delta_{\sum_i \omega_i}\delta^{(3)}(\sum_i \vec{p}_i)$,

based on which, one loop contribution to the finite temperature EP from a scalar reads

$$V_1^{\beta,\text{scalar}} = \frac{1}{2\beta}\sum_{n=-\infty}^{\infty}\int\frac{d^3p}{(2\pi)^3}\log(\omega_n^2+\omega^2), \tag{2.11}$$

where $\beta = 1/T$, ω_n is the bosonic Matsubara frequency and $\omega^2 = \vec{p}^2 + m^2(\hat{\phi})$ with $m(\hat{\phi})$ is the field-dependent mass of the scalar. The one loop EP from a scalar in Equation (2.11) contains a temperature independent part, which is the same piece that's been derived in Equation (2.3), and a temperature dependent part, which reads

$$V_1^{\text{T,scalar}} = \frac{1}{2\pi^2\beta^4}J_B\left(m^2(\hat{\phi})\beta^2\right), \tag{2.12}$$

where the thermal bosonic function J_B is defined as

$$J_B(m^2\beta^2) = \int_0^\infty y^2\ln\left[1-e^{-\sqrt{y^2+m^2\beta^2}}\right]dy. \tag{2.13}$$

The temperature dependent contribution to the one loop EP from gauge bosons can be derived in the same way, and the formalism reads the same as in Equation (2.11) where the field-dependent masses should be replaced by the masses of gauge bosons, as well as a multiplier given by the corresponding number of degrees freedom:

$$V_1^{\text{T,gb}} = (\text{Tr}\Delta)\frac{1}{2\pi^2\beta^4}J_B\left(m_{gb}^2(\hat{\phi})\beta^2\right). \tag{2.14}$$

For fermions,

$$V_1^{\beta,\text{fermion}} = -\frac{2\lambda}{2\beta}\sum_{n=-\infty}^{\infty}\int\frac{d^3p}{(2\pi)^3}\log(\omega_n^2+\omega^2), \tag{2.15}$$

where ω_n is the fermionic Matsubara frequency and $\omega^2 = \vec{p}^2 + m_f^2(\hat{\phi})$, and after summing over n, the temperature dependent part reads

$$V_1^{\mathrm{T,fermion}} = -2\lambda \frac{1}{2\pi^2\beta^4} J_F\left(m_f^2(\hat{\phi})\beta^2\right), \tag{2.16}$$

with the thermal fermionic function J_F defined as

$$J_F(m^2\beta^2) = \int_0^\infty y^2 \ln\left[1 + e^{-\sqrt{y^2+m^2\beta^2}}\right] dy. \tag{2.17}$$

Summarizing contributions from scalars, gauge bosons and fermions, the temperature dependent one loop EP reads

$$V_1^{\mathrm{T}} = \frac{T^4}{2\pi^2}\left[\sum_{i=B} n_i J_B\left(\frac{m_i^2(\hat{\phi})}{T^2}\right) + \sum_{i=F} n_i J_F\left(\frac{m_i^2(\hat{\phi})}{T^2}\right)\right]. \tag{2.18}$$

The $J_{B/F}$ functions can be evaluated numerically. In the mean time, to gain analytical understanding of the thermal history, a high-temperature expansion can be used to obtain an analytical expression for the thermal potential:

$$\begin{aligned} J_B^{\mathrm{high}-T}(y) &= -\frac{\pi^4}{45} + \frac{\pi^2}{12}y - \frac{\pi}{6}y^{\frac{3}{2}} - \frac{1}{32}y^2 \log\left(\frac{y}{a_b}\right) + \cdots, \\ J_F^{\mathrm{high}-T}(y) &= \frac{7\pi^4}{360} - \frac{\pi^2}{24}y - \frac{1}{32}y^2 \log\left(\frac{y}{a_f}\right) + \cdots, \end{aligned} \tag{2.19}$$

where $a_b = 16\pi^2 \exp(3/2 - 2\gamma_E)$, $a_f = \pi^2 \exp(3/2 - 2\gamma_E)$ and γ_E is the Euler constant. The high-temperature expansion in Equation (2.19) guarantees a good convergence for values of the argument of the $J_{B/F}$ functions up to $2-5$, while values are constrained to be below/about 1 without inclusion of the logarithmic terms. As the field-dependent squared masses $m_i^2(\hat{\phi})$ can go negative at some field values, where the J functions have unphysical complex values, the functions should be regulated by taking their real parts [65], which are

oscillating functions. A common practice in the literature, is taking the central value of the oscillating function (asymptotically becomes zero with large function arguments), which would result in a stable function, as well as make good prediction as at the physical vacuum, the field-dependent squared masses shouldn't have large negative tree level values when their loop corrected values should be positive definite. In some numerical packages instead, e.g. `CosmoTransitions` [66], the treatment is assigning constant values after a certain large cut-off value of the function argument.

Evaluation of the $J_{B/F}$ functions beyond the high temperature expansion needs to be performed numerically. Moreover, common numerical packages in the market, e.g. CosmoTransitions, BubbleProfiler [67] etc, also contain algorithms tracing phases given the EP of a model, finding degeneracy conditions (the critical behavior) between phases, as well as calculating the bounce action to find tunneling path and predict bubble nucleation, for a EWPT. Numerical simulations of the thermal history in works included in this thesis are performed using `CosmoTransitions`. Notice that even with numerical tools, exact evaluation of the $J_{B/F}$ functions is highly time consuming. Therefore, `CosmoTransitions` uses spline interpolation of $J_{B/F}$ functions based on pre-computed look-up tables for numerical evaluation, which we have checked to have good agreement with the exact evaluation results using benchmark points of our model, which will be introduced in the next chapter.

2.2 Thermal resummation

As it is well understood in the literature, at finite temperatures, the self energy of a particle receives higher loop corrections from daisy diagrams, e.g. see [68, Fig. 3a]. Such corrections at $\mathcal{N}$-loop order contain powers of a field- and temperature-dependent parameter α (up to

a normalization factor) [26, 68–71],

$$\alpha^{\mathcal{N}} = \lambda_i^{\mathcal{N}} \frac{T^{2\mathcal{N}}}{m_i^{2\mathcal{N}}(\hat{\phi})}, \tag{2.20}$$

where λ_i is the coupling corresponding to $m_i(\hat{\phi})$ in the theory. At large temperatures, such contributions exhibit severe IR divergence for some field values such that $m_i(\hat{\phi}) \ll T$, for example around the origin, where higher loop contributions dominate and convergence of the fixed-order calculation becomes problematic. Various treatments have been proposed to resum higher loop thermal contributions and solve the associated IR problem [26, 68–74]. A full dressing daisy resummation involves adding thermal corrections to the tree level effective masses in the EP. For the one loop EP it follows,

$$\begin{aligned} &V_{\rm CW}(\{m_i^2(\hat{\phi})\};\mu_R^2) + V_1^T(\{m_i^2(\hat{\phi})\};T) \rightarrow \\ &V_{\rm CW}\left(\{m_i^2(\hat{\phi}) + \Pi_i^2\};\mu_R^2\right) + V_1^T\left(\{m_i^2(\hat{\phi}) + \Pi_i^2\};T\right), \end{aligned} \tag{2.21}$$

where Π_i^2 is the squared thermal mass for the specie "i". Such a procedure effectively resums higher order corrections from daisy diagrams. There are several relevant discussions in the literature, e.g. [73–75], pointing out different types of finite temperature contributions due to the different implementation of thermal mass effects, including full vs partial daisy resummation, as well as higher order loop corrections from finite temperature resummations such as those coming from superdaisy, lollipop and sunset diagrams.

The squared thermal masses Π_i^2 are in general field- and temperature-dependent and can be solved by gap equations. At one-loop level the gap equations read

$$\Pi_{i,\rm gap}^2 = \frac{\partial^2}{\partial \hat{\phi}_i^2} \sum_k V_{1-\rm loop}^T\left(\{m_k^2(\hat{\phi}) + \Pi_{k,\rm gap}^2\};T\right), \tag{2.22}$$

where the degree of freedom i appears as a background field in the EP. A truncated treatment

involves doing an expansion of the right hand side of the gap equation with respect to Π_k^2 and truncate to a given order. To the leading order, the truncated squared thermal mass reads

$$\Pi^2_{i,\text{trunc}} = \frac{\partial^2}{\partial \hat{\phi}_i^2} \sum_k V^T_{1-\text{loop}} \left(\{ m_k^2(\hat{\phi}) \}; T \right). \tag{2.23}$$

If the thermal potential is evaluated to leading order in high-temperature expansion, one obtains the well known field-independent form of the squared thermal masses

$$\Pi^2_{i,\text{hT}} = c_i T^2. \tag{2.24}$$

The c_i are constant coefficients dependent on couplings determined by the theory.

2.3 Renormalization group improvements

The fixed-order EP at finite temperature, including both the zero temperature and thermal contributions, depends on the scale μ_R at which the theory is renormalized. For example, at one loop order, using the high-temperature expansion in eq. (2.19), the potential has a logarithmic dependence on the renormalization scale as

$$\log \left(\frac{T^2}{\mu_R^2} \right), \tag{2.25}$$

where the $\log(m_i^2(\hat{\phi}) + \Pi_i^2)$ piece is cancelled between the CW and logarithmic term in the high-temperature expansion of the thermal potential contribution. By implementing RG improvement, where the parameters, fields and vacuum energy of the potential are evaluated at the scale μ_R, one would cancel the scale dependence to the order of the calculation [76–81]. As we only calculate the EP and the RG improvement at one-loop order, the scale μ_R needs to be chosen wisely to avoid un-resummed large logarithms from higher-order loop effects.

Formally, at $T = 0$ with a convenient choice of the renormalization scale, the L-loop EP with an RG improvement at (L + 1)-loop order, is exact up to L-th-to-leading log order [76–78]. At finite temperature, the choice of the renormalization scale, should vanish or minimize the un-resummed logarithms such as $\log^{\mathcal{N}}\left(\frac{m_i^2(\hat{\phi})+\Pi_i^2}{\mu_R^2}\right)$ for $\mathcal{N} \geq 2$ [73, 75]. For models with multiple degrees of freedoms, therefore, there is no single choice of the scale to make all the logarithms negligible [77,78,82–86]. One may make a convenient choice close to one physical scale as long as there is no large separation between scales of the particles' masses, including the thermal mass contribution, as well as between the particle masses and the temperature. The CW potential further includes polynomial contributions of the radiative corrections. It also partially accounts for multi-scale particle threshold effects beyond the one single scale threshold taken into account through the RG improvement. [1]

1. Notice that here the RG improvement does not involve temperature flow as has been proposed, for example in [87–89], where they treat temperature as an independent scale that participates in the RG flow and thermal diagrams, like daisy and super-daisy, would have been resumed as a result.

CHAPTER 3

ELECTROWEAK PHASE TRANSITION IN NEW PHYSICS MODELS

In order to generate the observed baryon asymmetry, for a successful electroweak baryogenesis, out-of-equilibrium processes and sources of CP violation beyond those found in the SM must be realized in nature. One interesting possibility to achieve the latter is via a strong first order electroweak phase transition, as well as to assure that the baryonic asymmetry generated during the bubble nucleation would not be erased by the sphaleron process. In this chapter, we discuss how beyond the Standard Model physics could enhance the electroweak phase transition offering new possibilities for electroweak baryogenesis, and investigate two representative extensions to the SM which allow for a strong first order electroweak phase transition as well as their theoretical and experimental signatures.

In section 3.1, we start by discussing the electroweak phase transition in the SM, and give an analytical understanding of its strength, based on which, from an effective theory point of view, we provide general perspectives on the impact from new physics degrees of freedom.

In section 3.2, we investigate a simple, representative extension of the SM with a new real singlet degree of freedom, the sector of which undergoes a spontaneous Z_2 breaking. We perform analytical and numerical calculations that systematically include one-loop thermal effects, CW corrections, and daisy resummation, as well as the evaluation of bubble nucleation. We study the rich thermal history and identify the conditions for a strong first order electroweak phase transition with nearly degenerate extrema at zero temperature. This requires a light scalar with mass below 50 GeV. Exotic Higgs decays, as well as Higgs coupling precision measurements at the LHC and future collider facilities, will test this model. Additional information may be obtained from future collider constraints on the Higgs self-coupling. Gravitational-wave signals could potentially be probed by future gravitational

wave experiments. The work of this section was performed in collaboration with Marcela Carena and Zhen Liu. It has been published in Journal of High Energy Physics [90].

In section 3.3, we study the Next-to-Minimal Supersymmetric Standard Model (NMSSM), whose scalar sector contains two SU(2) doublets and one gauge singlet. Importantly, we compare the phase transition patterns suggested by the vacuum structure at the critical temperatures, at which local minima are degenerate, with those obtained from computing the probability for nucleation via tunneling through the barrier separating local minima. Heuristically, nucleation becomes difficult if the barrier between the local minima is too high, or if the distance (in field space) between the minima is too large, where the NMSSM is an example of a model exhibiting such behavior. We find that the calculation of the nucleation probabilities prefers different regions of parameter space for a strong first order electroweak phase transition than the calculation based solely on the critical temperatures. Our results demonstrate that analyzing only the vacuum structure via the critical temperatures can provide a misleading picture of the phase transition patterns, and, in turn, of the parameter space suitable for electroweak baryogenesis. The work of this section was performed in collaboration with Sebastian Baum, Marcela Carena, Nausheen Shah and Carlos Wagner. It has been published in Journal of High Energy Physics [91].

3.1 Electroweak phase transition: from the SM to beyond

In this section, we start by analyzing the strength of the EWPT in the SM using a leading order perturbative approach under a high temperature expansion to the finite temperature effective Higgs potential, leading to the discussion of general perspectives on enhancing the strength of the EWPT introducing BSM degrees of freedom.

The finite temperature EP of the SM Higgs receives contributions from particle degrees of freedom in the hot plasma which couple to the SM Higgs. In the SM, particles which couple to the Higgs as well as the size of their couplings are known. Thus, one could

calculate the finite temperature EP using perturbative method, or simulate the dynamics of the phase transition using lattice gauge theory. We have discussed the phase diagram of the EWPT based on lattice simulation in section 1.3, which shows that with a Higgs mass of 125 GeV, the EWPT is rather a cross over. In order to gain an analytical understanding of the properties of EWPT, importantly of their dependence on the model particle content and parameters, which would provide information on how BSM degrees of freedom would affect the strength of the EWPT, one could use the perturbative EP method under high temperature approximation to arrive at analytical expressions of the PT properties.

Using the one loop thermal potential in Equation (2.18) and keeping up to the logarithmic order of the high temperature expansions in Equation (2.19), whose validity has been discussed in section 2.1, along with the tree level potential , the effective SM Higgs potential at finite temperatures up to one-loop order reads

$$V_{\rm SM}(h;T;\mu_R) \approx -\frac{1}{2}\left[\mu_h^2(\mu_R) - c_h^{\rm SM}T^2\right]h^2 - E^{\rm SM}Th^3 + \frac{1}{4}\lambda_h(T;\mu_R)h^4, \tag{3.1}$$

where μ_R is the renormalization scale for the CW potential, $\mu_h^2(\mu_R)$ is the squared mass parameter for the SM Higgs with **effective** zero temperature loop correction from CW potential, whose tree level value is $\mu_{h,\rm tree}^2 = (125\ \text{GeV})^2/2$, and $\lambda_h(T;\mu_R)$ is the SM Higgs quartic with effective radiative corrections from both thermal and CW potential, whose tree level value is $\lambda_{h,\rm tree} = 125^2/(2\times 246^2)$. The coefficients $c_h^{\rm SM}$ and $E^{\rm SM}$ in Equation (3.1) are temperature induced, which read

$$\begin{aligned} c_h^{\rm SM} &= \frac{1}{48}\left(9g^2 + 3g'^2 + 12h_t^2 + 24\lambda_h\right), \\ E^{\rm SM} &= \frac{1}{32\pi}\left(2g^3 + \sqrt{g^2+g'^2}^3\right), \end{aligned} \tag{3.2}$$

where h_t is the SM top Yukawa coupling, g and g' are the SM gauge couplings, and we have only included the top contribution in the SM fermion sector because of the relative small

size of other Yukawa couplings. Based on the potential in Equation (3.1), one can solve for the order parameter of the EWPT, that has been introduced in section 1.3,

$$\left.\frac{v_c}{T_c}\right|_{\mathrm{SM}} \approx \frac{2E^{\mathrm{SM}}}{\lambda_h(T_c;\mu)}. \tag{3.3}$$

Such a value in the SM is of the order of 0.2 which renders a weakly first order phase transition. Although lattice simulation further improves the result and predict a cross over, one can read from this expression why the EWPT in the SM is not strong first order. Firstly, a SFOEWPT relies on a large barrier in between the false and the true vacuum, which is characterized by a large value of the coefficient E^{SM} of the thermal trilinear (in case of the Higgs field) term. However, in the SM, such a coefficient only receives contribution from massive gauge bosons (and a small negligible contribution from the Higgs and Goldstone bosons), such that its value is only of the order of 10^{-2}. Secondly, the denominator $\lambda_h(T_c;\mu_R)$ in Equation (3.3), whose tree level value is associated with the Higgs mass, has a relative large value in the SM. The lighter the SM Higgs, the smaller the value of $\lambda_h(T_c;\mu_R)$, the stronger the EWPT, which is consistent with the prediction from the EWPT phase diagram Figure 1.5 from lattice simulation.

Now going beyond the SM by introducing new degrees of freedom coupling to the SM Higgs, taking an effective theory point of view by integrating out these particles, Equation (3.3) could already give information on how the EWPT can be enhanced with different classes of effects, which are [92]

- Tree level effect

  New scalar degrees of freedom which couple to the SM Higgs could introduce new terms to the tree level Higgs potential. These new terms can lead to an explicit tree level barrier between the true and the false vacuum. For example, a new scalar S with a none-zero vacuum expectation value couples to the SM Higgs through a

trilinear term $\lambda_3\langle S\rangle h^3$ would induce a tree level barrier whose size is characterized by the dimensionful coefficient $\lambda_3\langle S\rangle$ effectively added to the numerator in Equation (3.3), which being large enough would onset a SFOEWPT. These terms could also change the location and depth of the physical vacuum at zero temperature, leading to a different critical temperature compared to the SM case, resulted in a stronger EWPT. As an example, we will show next in section 3.2 that how this is realized through a real singlet extension of the SM, where at zero temperature, the singlet acquires a non-zero VEV spontaneously thus the physical vacuum is shifted and lifted from its SM location. Both of these effects rely on non-zero VEVs of the BSM scalar fields developing when the EWPT happened.

- Loop effects (zero temperature)

  At zero temperature, radiative corrections could modify values of the Higgs potential parameters, as well as terms of the form $h^4 \log h^2$, which effectively change the size of the denominator in Equation (3.3). A well-known example is the CW mechanism for spontaneous symmetry breaking [49].

- Thermal effects

  Thermal loop effects could introduce new contributions to the thermal trilinear coefficient E compared to its SM value. For example, a new scalar S couples to the SM Higgs with a quartic term $\lambda_m h^2 S^2$ introduces a contribution to E of the size of $\sim \lambda_m^{3/2}$, thus a sizable mixing coupling could induce a SFOEWPT. Notice that such a contribution relies on a zero/tiny mass parameter for the scalar, which can be resulted from the interplay between the zero temperature mass parameter and the thermal correction. An example for such an effect is in the minimal supersymmetric model, where the thermal mass and tree level mass parameter of the stop cancels and a contribution of the size of $h_t^{3/2}$ is added to the thermal trilinear coefficient. New gauge bosons couple

to the SM Higgs would also add contribution of the size of $g_D^{3/2}$ to E, where g_D is the gauge coupling of the new gauge group. Notice that the thermal trilinear term doesn't have contributions from fermions, thus thermal effects from fermions would enter in a more subtle way.

Lastly, one can also perform the study using non-renormalizable operators [65,93–99], which is beyond the scope of this thesis, thus is included in the discussion here. Now we have some qualitative perspectives on the ways the EWPT can be enhanced with new BSM degrees of freedom. However different contributions have different quantitive contribution, and importantly, the new degrees of freedom would also change the Higgs properties at zero temperature, which have been the hunting target of high energy experiments since the discovery of the Higgs. Thus how the requirement of a SFOEWPT can be compatible with current and future constraints on the Higgs phenomenology needs explicit investigation given the nature of the new particles as well as the way they couple to the SM Higgs, which will be the subject for the remainder of this chapter.

3.2 Electroweak phase transition with spontaneous Z_2 breaking

Singlet extensions of the SM provide a unique opportunity to generate a SFOEWPT [100–121], and are the subject of exploration in this section. These extensions, however, are relatively difficult to test, in comparison with other SM particle extensions with particles charged under the SM gauge groups. On the other hand, dark sector model building, involving a hidden sector with dark matter, often invokes spontaneously broken dark gauge symmetries. The simplest scalar sector charged under the dark symmetries would be a complex scalar, which is a singlet under the SM gauge groups. The effects from the dark Higgs, which obtains a VEV, on the EWPT can be approximated by a singlet extension of the SM with spontaneous Z_2 breaking, after rescaling the parameters by the corresponding degrees of freedoms. Given the above picture, in this section, we consider a comparative study of

a real singlet extension of the SM and its impact on the strength of the EWPT, in the presence of spontaneous Z_2 breaking, through a detailed inclusion of various thermal and zero temperature quantum corrections to the tree-level potential.

Before moving on to details of this study, it is useful to review our current understanding of the EWPT in singlet extensions of the SM. The strictly Z_2-preserving version of this model has been studied to great detail in Ref. [100–106], presented as the so-called 'nightmare scenario' for its challenges in testing it at future colliders. These scenarios generally enhance the EWPT through loop effects of the singlet via the large quartic couplings (O(few)) between the singlet and Higgs pairs. This, however, occurs in the regime where perturbative unitarity is in question, where the one-loop corrections are large, and further studies are needed. A special mechanism, where the EWPT is enhanced by tree-level effects through a two-step phase transition, can also be realized in these scenarios [102–106]. However, once the requirement of a non-relativistic bubble wall motion is imposed, solutions under this category only exist in a narrow region of parameter space. For general Z_2-explicit breaking models, the large number of free parameters often requires numerical studies which can provide benchmark point solutions [102–104, 107–113]. The solutions in these scenarios often invoke additional tree-level barriers from the explicit Z_2 breaking terms.

For the well-motivated scenario we are considering, where the Z_2 is spontaneously broken, it is a priori not clear if a sufficiently strong first-order EWPT can be in place. First, a large mixing quartic coupling between the singlet pairs and the Higgs pairs is generically disfavored by Higgs precision tests, as this term will generate a sizable singlet-Higgs mixing when the singlet acquires a non-zero VEV. A small mixing quartic, instead, precludes a possible large loop effect from the singlet, which is one of the main mechanisms to enhance the EWPT. Second, one might expect that the spontaneous Z_2 breaking singlet VEV could add additional trilinear terms and generate the $|H^\dagger H|^n$ or higher-order operators that could modify the Higgs potential directly via these tree-level couplings. Due to the relations among couplings

in the spontaneous Z_2 breaking theory, it turns out that these operators are only generated at loop-level as if the Z_2 symmetry were not broken [122]. Hence this property prevents tree-level modifications to the Higgs potential that would be sizable enough to enhance the first-order EWPT strength.

The above considerations imply that it is far from trivial to anticipate the behavior of the EWPT in singlet SM extensions with spontaneously discrete symmetry breaking. Understanding the situation and the possible region of allowed parameter space for a strong first order EWPT demands a detailed study, which is the purpose of this work.[1] As we shall show, we obtain a particular type of solutions that enhances the EWPT via engineering nearly degenerate zero temperature vacua in a very predictive manner. The section is organized as follows: In subsection 3.2.1 we introduce the SM extension and write down the expressions for the full one-loop potential and the daisy resummation. In subsection 3.2.2 we classify the possible thermal histories, utilizing semi-analytic solutions that guide the understanding of our results. We also show the allowed region of parameter space for a strong first order EWPT, and further check the robustness of our results against a nucleation calculation. An unavoidable, distinctive feature of our study is the prediction of a light singlet-like scalar. We present the phenomenological consequences of this model studying the implications for the Higgs exotic decays, Higgs precision measurements, double Higgs production, and gravitational wave signatures in subsection 3.2.3. Finally, we reserve subsection 3.2.4 to conclude and Appendices A-D to show some specific details of our analysis.

1. It is well known that domain wall problems are associated with the existence of multiple vacua in theories with spontaneous Z_2 breaking. However, domain wall problems can be alleviated by allowing for highly suppressed higher-dimensional operators that will minimally break the Z_2 symmetry explicitly. Such highly suppressed contributions will not affect the discussion about phase transitions and their related phenomenology. We will not consider this issue any further in this work.

3.2.1 Singlet extension of the SM with spontaneous Z_2 breaking

Tree-level potential

We start with the tree-level Higgs boson potential with an additional real singlet s:

$$V_0 = -\mu_h^2 H^\dagger H + \lambda_h (H^\dagger H)^2 + \frac{1}{2}\mu_s^2 s^2 + \frac{1}{4}\lambda_s s^4 + \frac{1}{2}\lambda_m s^2 (H^\dagger H) + V_{\rm SM}. \tag{3.4}$$

There is an important discrete Z_2 symmetry in the singlet sector, under which $s \to -s$ and the rest of the fields remain unchanged. The singlet scalar field s can spontaneously break this symmetry.

The SM Higgs doublet H is written as

$$H = \frac{1}{\sqrt{2}} \begin{pmatrix} \chi_1 + i\chi_2 \\ h + i\chi_3 \end{pmatrix}, \tag{3.5}$$

where χ_1, χ_2, χ_3 are three Goldstone bosons, and h is the Higgs boson. The tree-level potential of h and s in the unitary gauge reads

$$V_0(h,s) = -\frac{1}{2}\mu_h^2 h^2 + \frac{1}{4}\lambda_h h^4 + \frac{1}{2}\mu_s^2 s^2 + \frac{1}{4}\lambda_s s^4 + \frac{1}{4}\lambda_m s^2 h^2. \tag{3.6}$$

At zero temperature, there are four non-degenerate extrema, with the possibility of the scalars having zero or non-zero VEVs. Amongst these four extrema, only two of them are consistent with the Higgs doublet obtaining a non-zero VEV. In this section, we are in particular interested in the case where the singlet also acquires a VEV. The VEVs of the Higgs doublet and the real singlet in terms of the bare parameters of the potential can be

written as

$$v|_{T=0} = v_{\rm EW} = \sqrt{\frac{2(2\lambda_s\mu_h^2 + \lambda_m\mu_s^2)}{4\lambda_h\lambda_s - \lambda_m^2}}, \quad w|_{T=0} = w_{\rm EW} = \sqrt{\frac{2(-2\lambda_h\mu_s^2 - \lambda_m\mu_h^2)}{4\lambda_h\lambda_s - \lambda_m^2}}. \tag{3.7}$$

The physical scalar masses are obtained by diagonalizing the squared mass matrix evaluated at the physical VEV,

$$\begin{aligned} M^2 &= \begin{pmatrix} \frac{\partial^2 V}{\partial h^2} & \frac{\partial^2 V}{\partial h \partial s} \\ \frac{\partial^2 V}{\partial h \partial s} & \frac{\partial^2 V}{\partial s^2} \end{pmatrix} \Big|_{(v_{\rm EW}, w_{\rm EW})} \\ &= \begin{pmatrix} 3h^2\lambda_h - \mu_h^2 + \frac{1}{2}\lambda_m s^2 & \lambda_m h s \\ \lambda_m h s & \frac{1}{2}\lambda_m h^2 + \mu_s^2 + 3\lambda_s s^2 \end{pmatrix} \Big|_{(v_{\rm EW}, w_{\rm EW})}. \end{aligned} \tag{3.8}$$

Electroweak Symmetry Breaking (EWSB) requires that the physical VEV $(v_{\rm EW}, w_{\rm EW})$ is the deepest minimum of the potential. For $(v_{\rm EW}, w_{\rm EW})$ to be a minimum,

$$\mathrm{Det}M^2 = v_{\rm EW}^2 w_{\rm EW}^2 \left(4\lambda_h\lambda_s - \lambda_m^2\right) \geq 0, \tag{3.9}$$

rendering $4\lambda_h\lambda_s - \lambda_m^2 \geq 0$ a necessary condition for EWSB at tree level.

There are five bare parameters $\{\mu_h^2, \mu_s^2, \lambda_h, \lambda_s, \lambda_m\}$ in the tree-level potential. They can be traded by five physical parameters, two of which, the Higgs VEV and the Higgs mass m_H, are fixed by boundary conditions

$$v_{\rm EW} = 246 \text{ GeV}, \quad m_H = 125 \text{ GeV}. \tag{3.10}$$

The remaining three physical parameters are related to the singlet VEV, the singlet mass and the mixing angle of the mass eigenstates, and we defined $\tan\beta = w_{\rm EW}/v_{\rm EW}$. Detailed discussion of the parametrization can be found in subsection 3.A.1.

One-loop effective potential at finite temperature

As has been introduced in chapter 2, the one-loop effective potential at finite temperatures is calculated in the background of the Higgs and singlet fields. Effective masses of all degrees of freedom in the plasma dependent on the background fields are:

$$\begin{aligned}
&m_W^2(h,s) = \frac{g^2}{4}h^2, \quad m_Z^2(h,s) = \frac{g'^2+g^2}{4}h^2, \quad m_t^2(h,s) = \frac{1}{2}h_t^2h^2,\\
&m_{\chi_{1,2,3}}^2(h,s) = -\mu_h^2 + \lambda_h h^2 + \frac{1}{2}\lambda_m s^2,\\
&m_h^2(h,s) = -\mu_h^2 + 3\lambda_h h^2 + \frac{1}{2}\lambda_m s^2,\\
&m_s^2(h,s) = \mu_s^2 + \frac{1}{2}\lambda_m h^2 + 3\lambda_s s^2,\\
&m_{sh}^2(h,s) = \lambda_m hs,
\end{aligned} \tag{3.11}$$

where $\chi_{1,2,3}$ are the Goldstone bosons and the particle degrees of freedom are:

$$n_W = 6,\ n_Z = 3,\ n_t = -12,\ n_h = 1,\ n_{\chi_{1,2,3}} = 1,\ n_s = 1. \tag{3.12}$$

For the Higgs and singlet degrees of freedom, mass eigenvalues entering the effective potential are

$$\begin{aligned}
m_{\varphi_1,\varphi_2}^2(h,s) = \frac{1}{2}\Big\{&(3\lambda_h + \lambda_m/2)h^2 + (3\lambda_s + \lambda_m/2)s^2 - \mu_h^2 + \mu_s^2\\
&\pm \sqrt{\left[(3\lambda_h - \lambda_m/2)h^2 + (-3\lambda_s + \lambda_m/2)s^2 - \mu_h^2 - \mu_s^2\right]^2 + 4\lambda_m^2 s^2 h^2}\Big\},
\end{aligned} \tag{3.13}$$

where φ_1, φ_2 are the Higgs and singlet mass eigenstates with particle degrees of freedom $n_{\varphi_1,\varphi_2} = 1$.

In this study we work in the Landau gauge and the Goldstone modes contribute separately in addition to the massive bosons. There has been ample discussion in the literature on the issue of gauge dependence in perturbative calculations of the effective potential, both at

zero and finite temperature [51, 52, 80, 81, 123–128]. In that sense, we understand that our treatment is not manifestly gauge invariant. We expect, however, that our analysis provides a realistic estimate of the EWPT strength.[2]

In this section, the numerical study is performed using a modified version of `CosmoTransitions` [66], where spline interpolation is implemented. For better analytical control, we use high-temperature expansion for analytical analyses in the next section, based on which (up to leading order in T), without the CW potential and daisy resummation contributions to be introduced below, the field-dependent part of the one-loop EP at finite temperature reads

$$\begin{aligned} V(h,s,T) &= V_0(h,s) + V^T_{1-\text{loop}}(h,s,T) \\ &\approx -\frac{1}{2}(\mu_h^2 - c_h T^2)h^2 - E^{\text{SM}} T h^3 + \frac{1}{4}\lambda_h h^4 \\ &\quad + \frac{1}{2}(\mu_s^2 + c_s T^2)s^2 + \frac{1}{4}\lambda_s s^4 + \frac{1}{4}\lambda_m s^2 h^2 - E(h,s)T, \end{aligned} \tag{3.14}$$

where

$$\begin{aligned} c_h &\equiv \frac{1}{48}[9g^2 + 3g'^2 + 2(6h_t^2 + 12\lambda_h + \lambda_m)], \\ E^{\text{SM}} &\equiv \frac{1}{32\pi}\Big[2g^3 + \sqrt{g^2 + g'^2}^3\Big], \\ c_s &\equiv \frac{1}{12}(2\lambda_m + 3\lambda_s), \\ E(h,s) &\equiv \frac{1}{12\pi}\Big[\big(m^2_{\varphi_1}(h,s)\big)^{3/2} + \big(m^2_{\varphi_2}(h,s)\big)^{3/2} + 3\big(-\mu_h^2 + \lambda_h h^2 + \frac{1}{2}\lambda_m s^2\big)^{3/2}\Big], \end{aligned} \tag{3.15}$$

and $m^2_{\varphi_{1,2}}$ is given in Eq. (3.13).

The temperature-independent part of the EP at one-loop order is included in the CW potential as has been discussed in chapter 2, where in this section we used the $\overline{\text{MS}}$ renormal-

2. The reason for this is that gauge dependence appears at loop level in perturbation theory, while, as will be discussed later in the section, in our model the important enhancement of the EWPT strength, $v_c/T_c > 1$, is due to tree level effects in the potential that come into play once the finite temperature barrier turns on. Indeed, as we will discuss in Section subsection 3.2.2, the thermal contributions are subdominant. We however intend to study the effects of gauge dependence further in a future work.

ization scheme with the renormalization scale chosen to be $Q = 1000$ GeV. In our numerical studies, we perform a 5-dimensional scan of the bare model parameters, selecting those consistent with the SM Higgs VEV $v_{\rm EW} \simeq 246$ GeV and the Higgs-like particle mass $m_{\varphi_i} \simeq 125$ GeV, with $i = 1$ or 2 depending on the mass hierarchy between mass eigenstates, where we allow for an uncertainty of ± 2 GeV in the VEV and the mass value, respectively. Observe that adding the CW contributions is required to perform a consistent one-loop calculation, but significantly decreases the efficiency of the numerical scanning in comparison to the only one-loop thermal potential approximation, for which the number of scanning parameters is reduced to three.

Lastly, corrections from daisy resummation of ring diagrams are included in the full one-loop potential using the truncated full dressing implementation to ensure validity of the perturbative expansion, where the leading order resummation results give thermal corrections of $\Pi_i = d_i T^2$ to effective masses with [105]

$$\begin{aligned} &d^L_{W^{\pm},3} = \frac{11}{6} g^2, \quad d^T_{W^{\pm},3} = 0, \quad d^L_B = \frac{11}{6} g'^2, \quad d^T_b = 0, \\ &d_\chi = \frac{3}{16} g^2 + \frac{1}{16} g'^2 + \frac{1}{2} \lambda_h + \frac{1}{4} y_t^2 + \frac{1}{24} \lambda_m, \\ &d_{hh} = \frac{3}{16} g^2 + \frac{1}{16} g'^2 + \frac{1}{2} \lambda_h + \frac{1}{4} y_t^2 + \frac{1}{24} \lambda_m, \quad d_{ss} = \frac{1}{4} \lambda_s + \frac{1}{6} \lambda_m, \quad d_{sh} \approx 0. \end{aligned} \tag{3.16}$$

3.2.2 Enhancing the Electroweak phase transition

In this section, we analyze all possible electroweak phase transition patterns appearing in our real singlet scalar extension of the SM. The thermal history could be very rich, as depicted in Figure 3.1. We highlight the cases for which a strong first order electroweak phase transition that is consistent with current SM EW and Higgs precision data is feasible.

Before proceeding with a more detailed analysis, we shall briefly described the possible thermal histories for the scalar potential defined in the previous section. The spontaneous Z_2 breaking singlet extension of the SM differs from the Z_2-preserving case significantly

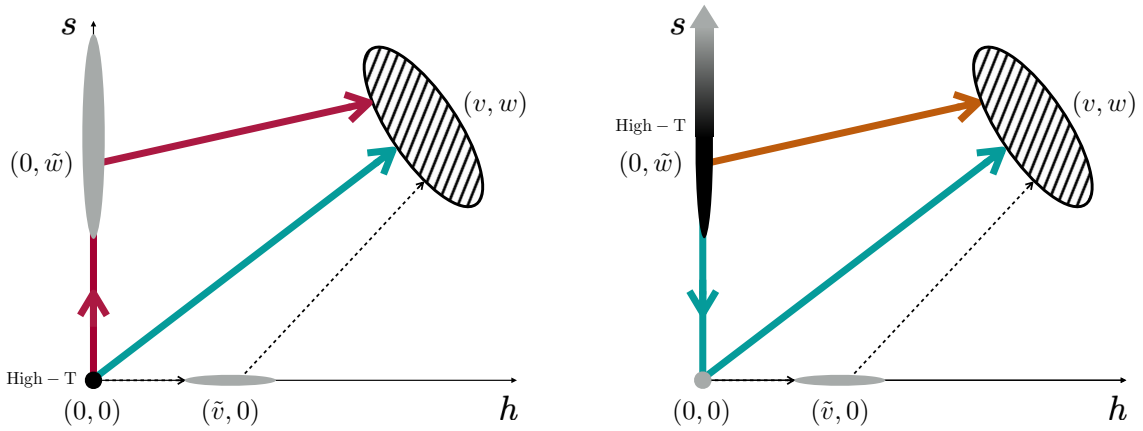

Figure 3.1: Schematic picture of the thermal histories with different phase transition patterns. Left: restoration scenarios, where the thermal history starts from the symmetric phase at $(0, 0)$. Right: non-restoration scenarios, where the thermal history starts from the Z_2 non-restored phase at $(0, \tilde{w})$. Phases are represented by bubble areas: the high temperature phase by a black bubble, the zero temperature phase by a hatched bubble, and the intermedia phases by gray bubbles. Phase transition steps are represented by arrow lines with a color code depicting the different scenarios: magenta for scenario A, orange for scenario A-NR, teal for scenario B/B-NR, respectively. The dashed arrow line scenario is discussed in subsection 3.A.2.

through the allowed size of the mixing quartic coupling λ_m. Large λ_m certainly helps with enhancing the EWPT by enhancing the thermal barrier term ETh^3 since the singlet is a new bosonic degree of freedom. However, in the spontaneous Z_2 breaking case, λ_m is not an independent free parameter, but rather proportional to the Singlet-Higgs mixing angle $\sin\theta$, which in turn is constrained by LHC Higgs precision data to be smaller than 0.4. Hence, in the spontaneous Z_2 breaking case, the smaller size of λ_m implies that a sufficiently strong first-order EWPT is only achievable via more subtle effects in the potential.

For scenarios of our interests, both the electroweak symmetry and the Z_2 symmetry are broken at zero temperature. At high temperatures, instead, the electroweak symmetry is preserved (high-temperature restoration of the EW symmetry), and the Z_2 symmetry can be either broken or restored. As a result, we will show how the path to the zero temperature electroweak physical vacuum can involve a one- or two-step phase transition.

In the following, we shall focus on the following four relevant scenarios:

- Scenario A: Two-step phase transition

$$(0,0)\rightarrow(0,\tilde{w})\rightarrow(v,w)$$

- Scenario B: One-step phase transition

$$(0,0)\rightarrow(v,w)$$

and their corresponding counterparts with Z_2 non-restoration (NR) at high temperatures:

- Scenario A-NR: One-step phase transition

$$(0,\tilde{w})\rightarrow(v,w)$$

- Scenario B-NR: Two-step phase transition

$$(0,\tilde{w})\rightarrow(0,0)\rightarrow(v,w)$$

The correspondence between the restoration and non-restoration scenarios is defined by them sharing the same final path towards the electroweak physical vacuum. All the minima defined above are temperature dependent, and different VEVs are associated with different paths in the thermal history.

There exist other possible scenarios, in which although the final step towards the true EW vacuum can involve a strong first order phase transition, it occurs when the sphalerons are already inactive. In such cases, the temperature at which the sphalerons are still active is associated with a previous step in which the EW symmetry breaking yields a false EW breaking vacuum and does not involve a sufficiently strong first order phase transition. These scenarios are:

$$(0,0)\rightarrow(\tilde{v},0)\rightarrow(v,w)$$

$$(0,\tilde{w})\rightarrow(0,0)\rightarrow(\tilde{v},0)\rightarrow(v,w)$$

For completeness, they are briefly discussed in subsection 3.A.2, however, they are not of interests to our study.

Scenario A: (0,0)→(0,$\tilde{w}$)→(v,w)

We shall show that the electroweak phase transition can be strong first order if the transition occurs from a Z_2 breaking/EW preserving vacuum, $(0, \tilde{w})$, to the true EW physical vacuum with Z_2 breaking, (v, w). This behavior can develop in two different ways: the one discussed in this subsection, scenario A, that involves a two-step transition in which at high temperatures the system is in a symmetric vacuum $(0, 0)$, and then evolves to a spontaneous Z_2 breaking/EW preserving vacuum at lower temperatures, to final transition to the true EW physical vacuum with Z_2 breaking. A different, one step phase transition path, that we call scenario A-NR, in which the system starts directly at a Z_2 breaking/EW preserving vacuum at high temperatures and then transitions to the true EW physical vacuum with Z_2 breaking, will be discussed in detail in section 3.2.2.

First, we start considering a high-temperature expansion to show analytically the behavior. Under the high-temperature expansion, the finite temperature potential (without CW potential and daisy resummation) is given in Equation (3.14). The complicated field-dependent term $-E(h, s)T$ can enhance the trilinear coefficient E beyond the SM value used in Equation (3.17) below, due to the effect of the additional quartic couplings. For simplicity, however, we shall neglect such subdominant effects in the following analytical considerations. Without such a term, the effective potential reads

$$V(h, s, T) \approx \frac{1}{2}(-\mu_h^2 + c_h T^2)h^2 - E^{\rm SM} T h^3 + \frac{1}{4}\lambda_h h^4 + \frac{1}{2}(\mu_s^2 + c_s T^2)s^2 + \frac{1}{4}\lambda_s s^4 + \frac{1}{4}\lambda_m s^2 h^2, \tag{3.17}$$

where relevant coefficients are given in the Equation (3.15).

For scenario A, the electroweak symmetry breaking proceeds through the second step from a Z_2 breaking/EW preserving vacuum, $(0, \tilde{w})$, to the true EW physical vacuum with

Z_2 breaking, (v, w), at a critical temperature T_c given by

$$T_c^2 = \frac{2\lambda_s\mu_h^2 + \lambda_m\mu_s^2}{2c_h\lambda_s - c_s\lambda_m - 16\frac{(E^{\rm SM})^2\lambda_s^2}{4\lambda_h\lambda_s - \lambda_m^2}}, \tag{3.18}$$

where both vacua coexist and are degenerate. In the Z_2 breaking/EW preserving vacuum, the singlet has a temperature dependent VEV that at T_c reads

$$\tilde{w}(T_c) = \sqrt{\frac{-\mu_s^2 - c_s T_c^2}{\lambda_s}}, \tag{3.19}$$

while in the true EW physical vacuum with Z_2 breaking, both the Higgs and the singlet fields have non-zero temperature dependent VEVs which at T_c respectively read

$$v_c \equiv v(T_c) = \frac{8E^{\rm SM}\lambda_s}{4\lambda_h\lambda_s - \lambda_m^2}T_c, \qquad w(T_c) = \sqrt{\frac{-\mu_s^2}{\lambda_s} - T_c^2\big[\frac{c_s}{\lambda_s} + 32\frac{(E^{\rm SM})^2\lambda_s\lambda_m}{4\lambda_h\lambda_s - \lambda_m^2}\big]}. \tag{3.20}$$

The phase transition strength is determined by the ratio

$$\frac{v_c}{T_c} = \frac{2E^{\rm SM}}{\lambda_h - \lambda_m^2/(4\lambda_s)} = \frac{2E^{\rm SM}}{\lambda_h^{\rm SM}}\Big[1 + \sin^2\theta\frac{m_H^2 - m_S^2}{m_S^2}\Big], \tag{3.21}$$

where a sufficiently strong first-order phase transition requires $\frac{v_c}{T_c} \gtrsim 1$. Accordingly, the EWPT strength can be enhanced by having smaller singlet scalar mass m_S compared to the Higgs boson mass m_H. The lighter the singlet scalar and the larger the Higgs-singlet mixing parameter, $\sin\theta$, the stronger the phase transition. In terms of the bare parameters, we observe that the strength of the phase transition is governed by the magnitude of the effective quartic coupling defined as

$$\tilde{\lambda}_h \equiv \lambda_h - \lambda_m^2/(4\lambda_s). \tag{3.22}$$

Notice that the EWSB condition shown in Equation (3.9) requires $\tilde{\lambda}_h \leq 0$, which ensures $\frac{v_c}{T_c}$ being positive definite, without constraining its absolute value. $\tilde{\lambda}_h \gtrsim 0$ is the near criticality condition for EWSB, which at the same time yields maximal enhancement of the strength of the EWPT.

In the following we discuss the behavior of the potential at zero temperature, that will provide information of the potential energy difference between the true EW physical vacuum and the Z_2 breaking/EW preserving extremum at zero temperature, which in turn has information on the magnitude of the critical temperature, and hence on the strength of the EWPT. Moreover, to better understand the EWPT behavior, we shall further discuss the dependence of the relevant quantities at the critical temperature in terms of the model parameter $\tilde{\lambda}_h$ that governs them.

At zero temperature, the tree-level potential difference between the true vacuum, $(v_{\rm EW}, w_{\rm EW})$, and the Z_2 breaking/EW preserving extremum, $(0, \tilde{w}|_{T=0})$ is given by,

$$\Delta V_{\rm A} \equiv V(0, \tilde{w}|_{T=0}, T=0) - V(v_{\rm EW}, w_{\rm EW}, T=0) = \frac{v^4}{4}\left(\lambda_h - \frac{\lambda_m^2}{4\lambda_s}\right) = \frac{v^4}{4}\tilde{\lambda}_h. \qquad (3.23)$$

This zero temperature potential energy difference reduces to the SM value, $\Delta V^{\rm SM} = V^{\rm SM}(0) - V^{\rm SM}(v_{\rm EW}) = \frac{v_{\rm EW}^4}{4}\lambda_h^{\rm SM}$, in the limit in which the singlet decouples. Equation (3.23) depicts the proportionality between $\Delta V_{\rm A}$ and $\tilde{\lambda}_h$, and implies that near criticality, for which $\tilde{\lambda}_h$ is small, $\Delta V_{\rm A}$ is small as well. Given Equation (3.21), we see that a small value of $\Delta V_{\rm A}$ is naturally associated to a large value of $\frac{v_c}{T_c}$.

When the Z_2 breaking/EW preserving extremum and the true vacuum have less potential energy difference at zero temperature, the critical temperature is lower. We consider now the specific dependence of the critical temperature on the model parameter $\tilde{\lambda}_h$. The thermal evolution of the two zero temperature extrema is controlled by temperature dependent coefficients in the thermal potential. More specifically, we rewrite the critical temperature

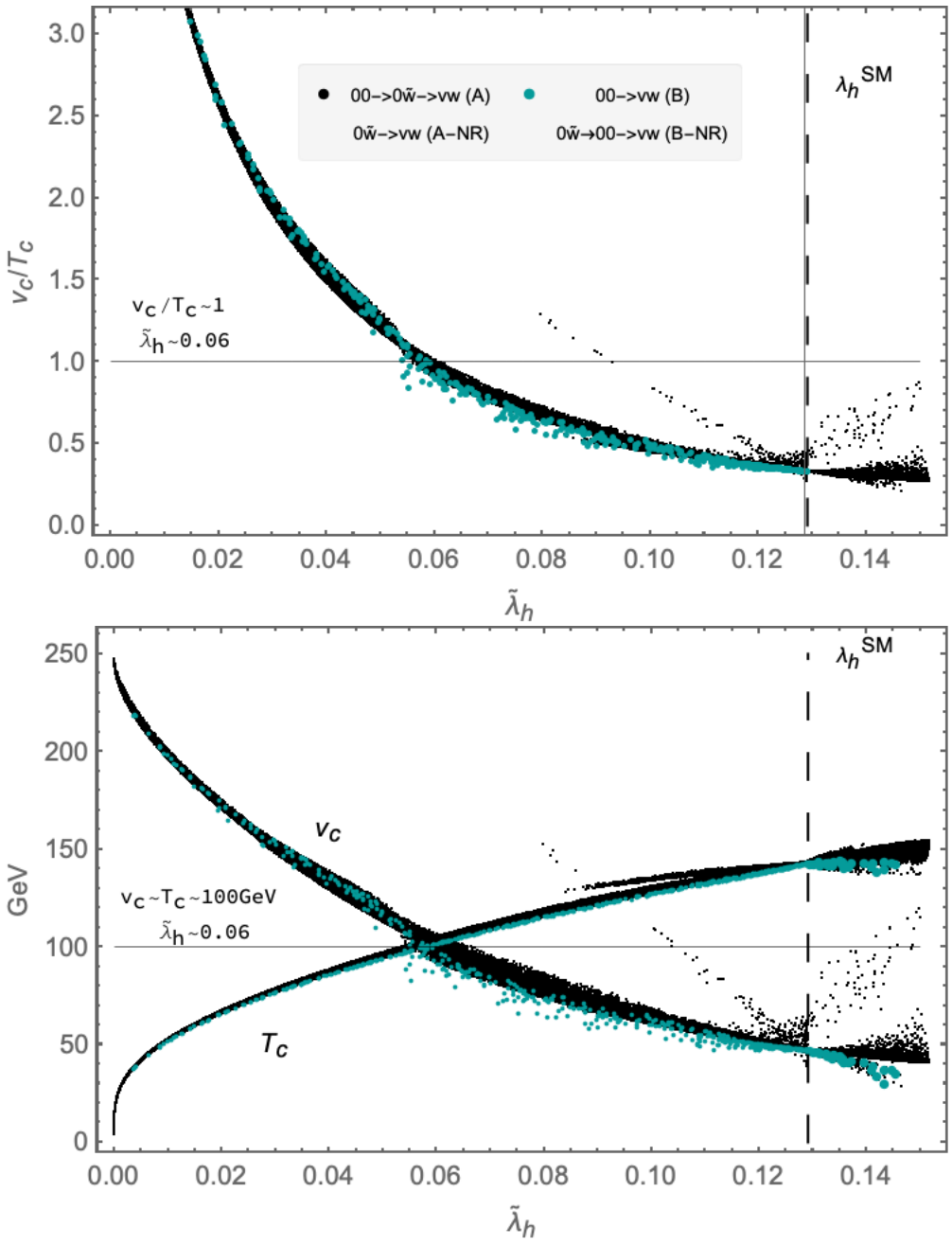

Figure 3.2: Results for the electroweak phase transition in a spontaneous Z_2 breaking singlet extension of the SM, with full numerical study of the one-loop thermal potential. EWPT information of scenario A and A-NR are shown in black dots and scenario B and B-NR are shown in green dots. Upper panel: v_c/T_c versus the effective quartic coupling $\tilde{\lambda}_h$. Lower panel: v_c and T_c versus $\tilde{\lambda}_h$.

in Equation (4.2.29) as

$$T_c^2 = v^2 \frac{\tilde{\lambda}_h^2}{\left(c_h - \frac{\lambda_m}{2\lambda_s} c_s\right) \tilde{\lambda}_h - 2(E^{\mathrm{SM}})^2}, \tag{3.24}$$

where $(E^{\mathrm{SM}})^2 \sim 10^{-4}$ and $c_h - \frac{\lambda_m}{2\lambda_s} c_s \approx 0.33 + \frac{1}{2}\lambda_h - \frac{\lambda_m}{12}\left(1 + \frac{\lambda_m}{\lambda_s}\right)$. Numerically, the $(E^{\mathrm{SM}})^2$ term is negligible and we shall drop it. This corresponds to the fact that the temperature dependent quadratic terms dominate the thermal evolution. The critical temperature then reads

$$T_c \simeq \frac{v}{\sqrt{c_h - \frac{\lambda_m}{2\lambda_s} c_s}} \tilde{\lambda}_h^{\frac{1}{2}}. \tag{3.25}$$

We observe that near criticality, the critical temperature is very close to zero. Meanwhile, the Higgs VEV at the critical temperature is larger and closer to the zero temperature VEV of 246 GeV. More specifically,

$$v_c = \frac{2E^{\mathrm{SM}}}{\lambda_h - \frac{\lambda_m^2}{4\lambda_s}} T_c \simeq 2E^{\mathrm{SM}} \frac{v}{\sqrt{c_h - \frac{\lambda_m}{2\lambda_s} c_s}} \tilde{\lambda}_h^{-\frac{1}{2}}. \tag{3.26}$$

Notice that the E^{SM} factor here, or else the trilinear term in the thermal potential, is required to give a non-zero value of v_c. E^{SM} is not essential to render a low critical temperature, but does ensure that the phase transition is first-order instead of second-order.

In summary, we have determined all relevant quantities to the phase transition strength at the critical temperature in terms of the effective quartic coupling $\tilde{\lambda}_h$, that controls our model behavior, as

$$\Delta V_{\mathrm{A}} \propto \tilde{\lambda}_h, \quad T_c \propto \tilde{\lambda}_h^{\frac{1}{2}}, \quad v_c \propto \tilde{\lambda}_h^{-\frac{1}{2}}, \quad \frac{v_c}{T_c} \propto \tilde{\lambda}_h^{-1}. \tag{3.27}$$

Within the mean field analysis considered, the effective quartic coupling $\tilde{\lambda}_h$ is bounded from

above by the Higgs quartic coupling λ_h , and from below at 0 by EWSB requirements. The near criticality condition, which corresponds to small values of $\tilde{\lambda}_h$, yields low values of the critical temperature and, therefore, a strong first order phase transition (SFOEWPT).

Figure 3.2 shows numerical results obtained with `CosmoTransitions` with full consideration of the one-loop thermal potential, as shown by the scattered black points. The dependence of v_c, T_c, and the transition strength v_c/T_c on the effective quartic coupling $\tilde{\lambda}_h$, shows excellent agreement with our analytical results [3] derived within a high-temperature expansion of the one-loop thermal potential, as shown in Equation (3.27). Figure 3.2 also includes results for other scenarios that will be discussed below.

The enhancement of the phase transition strength due to the reduction of the potential depth at zero temperature has been discussed in the literature in other contexts triggered by loop effects [101,105,106,129]. However, when such a sizable reduction of the potential depth is due to loop effects, it requires sizable couplings, which in turn may break perturbativity, or it needs multiple singlets. In our scenarios, the potential depth reduction at zero temperature arises at tree level, similar to some other SM extensions [129–131], and relies on the spontaneous breaking of the Z_2 symmetry. These effects could be sizable even for sufficiently small coupling constants, which open a window to interesting Higgs phenomenology.

In Figure 3.3, we show the same data set from the numerical scan as in Figure 3.2, but depicted in the $c_s - \mu_s^2$ plane of model parameters, where $c_s \equiv \frac{1}{12}(2\lambda_m + 3\lambda_s)$ is a parameter controlling the boundary between high temperature Z_2 restoration and non-restoration behaviors, as will be discussed in detail in section 3.2.2. Scenario A is shown in burgundy, and regions rendering SFOEWPT are shown with a burgundy darker shade. In this figure, we also show the approximated boundaries for SFOEWPT, in burgundy solid and dashed lines, that are obtained from the mean field analysis with $\tilde{\lambda}_h \sim 0.06$, that is the value of $\tilde{\lambda}_h$

3. The agreement is excellent in the low $\tilde{\lambda}_h$ region, while for larger values of $\tilde{\lambda}_h$ other effects, for example those from thermal trilinear terms, start to contribute and dominate over the tree-level effect associated with small $\tilde{\lambda}_h$. Such effects could possibly enhance the EWPT; however, we did not find a relevant enhancement. Thus we do not further discuss them in the remaining of this section

at which $v_c/T_c \approx 1$, as obtained from numerical estimation (see Figure 3.2). The contours agree well with the dark region of SFOEWPT from the numerical scanning. Points inside the burgundy solid and dashed lines are for values of $\tilde{\lambda}_h \lesssim 0.06$ as required for SFOEWPT. We shall discuss this figure in further detail when considering the other scenarios, including those with non-restoration of the Z_2 symmetry.

Scenario B: (0,0)→(v,w)

A direct one-step phase transition from a fully symmetric phase to the physical vacuum could be realized in restricted regions of parameter space, while allowing for a strong first-order EWPT. As we shall discuss in the following, such a one-step transition requires a comparable critical temperature for the $(0,0) \to (\tilde{v},0)$ and $(0,0) \to (0,\tilde{w})$.

In Figure 3.3, we show in green a scan of points for scenario B (and its non-restoration counterpart, scenario B-NR to be discussed later on), whereas regions rendering SFOEWPT are shown in a darker green shade. As we observe in Figure 3.3, the scenario B lies within a narrow restricted region where $\sqrt{\frac{-\mu_s^2}{c_s}} \sim 140$ GeV (shown as a black line in the figure). This can be understood in the sense that $\sqrt{\frac{-\mu_s^2}{c_s}}$ features the temperature of Z_2 breaking, while 140 GeV features the temperature of the electroweak breaking in the limit of decoupling the singlet. When these two temperatures are comparable, the Z_2 symmetry and the electroweak symmetry may break simultaneously, which is realized in scenario B through the phase transition step $(0,0) \to (v,w)$. Observe that, given our knowledge of EWPT in the SM, we would need the actual temperature of simultaneous Z_2/EW breaking to be below $\sqrt{\frac{-\mu_s^2}{c_s}} \sim$ 140 GeV, if we expect this scenario to allow for a sufficiently strong first-order EWPT. We shall study this in the following. Using the high temperature expansion of the effective potential, Equation (3.17), we can compute analytically, for scenario B (and similarly for

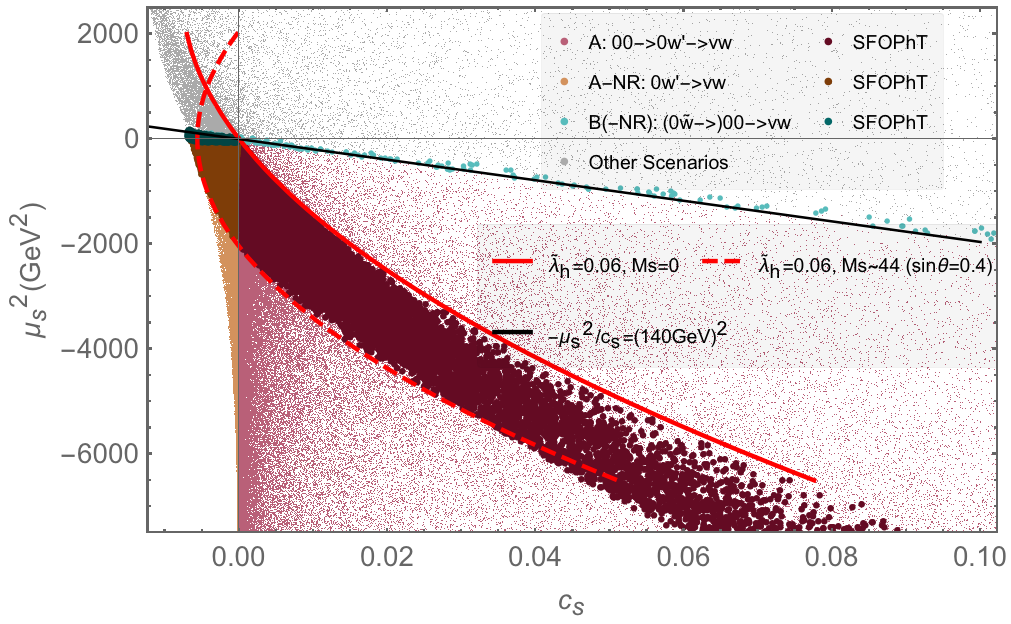

Figure 3.3: Parameter space on the c_s-μ_s^2 plane with different phase transition scenarios. Color scheme of the scattered points for different scenarios: magenta for scenario A: two step phase transition with $c_s \geq 0$; orange for scenario A-NR: one step phase transition with $c_s < 0$; teal for scenario B/B-NR: one/two step phase transition with positive/negative c_s. Darker regions correspond to regions rendering strong first-order electroweak phase transitions for specific scenarios. Rough boundaries of $\tilde{\lambda}_h \sim 0.06$ for strong first-order EWPT are shown. The solid red boundary is a boundary under the limit of $m_S \to 0$ when $\tilde{\lambda}_h \sim 0.06$. The dashed red boundary is a boundary at $\sin\theta = 0.4$ (corresponds to $m_S \approx 44$ GeV provided $\tilde{\lambda}_h \sim 0.06$). Points inside the burgundy solid and dashed lines are for values of $\tilde{\lambda}_h \lesssim 0.06$ as required for SFOEWPT (corresponding to nearly degenerate minima at zero temperature). The fine tuned region for scenario B is featured by the condition $\frac{-\mu_s^2}{c_s} \sim (140\text{ GeV})^2$ (shown in black line).

scenario B-NR), the strength of the phase transition by solving for the ratio,

$$\frac{v_c}{T_c} = \frac{2E^{\rm SM}}{\tilde{\lambda}_h + \frac{(\mu_s^2/T_c^2+c_s)^2}{\lambda_s\left[\frac{v(T_c)}{T_c}\right]^4}}. \tag{3.28}$$

In the above, $\tilde{\lambda}_h$ is defined as in Equation (3.23) and T_c is the critical temperature at which the Z_2/EW symmetric vacuum, $(0,0)$, is degenerate with the physical vacuum, (v,w). Since both terms in the denominator are positive definite (without one-loop CW correction), they must be sufficiently small for the transition to be strong first order. Indeed, the second term in the denominator, $(\mu_s^2/T_c^2 + c_s)^2/(\lambda_s\left[\frac{v(T_c)}{T_c}\right]^4)$, is numerically small for scenario B, and one can then approximate the v_c/T_c ratio by

$$\frac{v_c}{T_c} \simeq \frac{2E^{\rm SM}}{\tilde{\lambda}_h}, \tag{3.29}$$

showing identical behavior, mainly controlled by the parameter $\tilde{\lambda}_h$ as in scenario A above. Observe that the difference between the v_c/T_c expression in scenarios A and B, Equation (3.21) and (Equation (3.28), is correlated with the difference between $\Delta V_{\rm A}$ defined in Equation (3.23), and the corresponding quantity for scenario B,

$$\Delta V_{\rm B} \equiv V(0,0,T=0) - V(v_{\rm EW}, w_{\rm EW}, T=0) = \frac{v^4}{4}\tilde{\lambda}_h + \frac{(\mu_s^2)^2}{4\lambda_s}. \tag{3.30}$$

Equation (3.29) is a reflection that $\Delta V_{\rm A}$ and $\Delta V_{\rm B}$ only differ by the term $\frac{(\mu_s^2)^2}{4\lambda_s}$, which again is small for Scenario B with SFOEWPT.

The numerical results shown in Figure 3.2, highlight scattered points for scenario B (and scenario B-NR) in green. According to our discussion above, the quantity v_c/T_c (upper panel) follows closely the expected behavior as a function of $\tilde{\lambda}_h$, in a very good agreement with Equation (3.29). We observed that the data are scattered more downward compared

with scenario A, and this is due to the small correction from the additional second term in the denominator of Equation (3.28).

Z_2 Non-restoration scenarios

In scenarios A and B discussed above, the phase transition, either one-step or two-steps, starts from the trivial phase $(0,0)$ at high temperatures. Interestingly, it is also possible to consider that the Z_2 symmetry is not restored at high temperatures.

Using the same high temperature approximation as in Equation (3.17), when the coefficient c_h is negative, h will acquire a non-zero VEV at high temperatures, which has been recently discussed in [132, 133]. For c_h to be negative, a relevant negative contribution to it from λ_m is required (see Equation (3.15)), and this can be in general achieved in models with multiple singlets. However, since, in our case, we only have one singlet, such large negative contributions will require a large value of λ_m. Thus, the electroweak symmetry is always restored at high temperatures $\langle h \rangle^{\rm hT} = 0$ in our one-singlet extension of the SM.

With $\langle h \rangle = 0$ at high temperatures, the singlet phase reads

$$\tilde{w}(T) \equiv \langle s(T) \rangle^{h=0} = \left(\frac{-\mu_s^2 - c_s T^2}{\lambda_s} \right)^{1/2} . \tag{3.31}$$

For $c_s \geq 0$, with $\mu_s^2 \geq 0$, the phase $(0, \tilde{w})$ does not exist throughout the thermal history; while with $\mu_s^2 < 0$, the finite temperature phase $(0, \tilde{w})$ can undergo Z_2 symmetry restoration into the trivial phase $(0,0)$ at a higher temperature

$$T_r^{Z_2} = \left(\frac{-\mu_s^2}{c_s} \right)^{1/2} . \tag{3.32}$$

The case $c_s \geq 0$ and $\mu_s^2 < 0$ is what drives Scenario A. Observe that for Scenario B we also consider $c_s \geq 0$ (see Equation (3.31)), and because the transition is from $(0,0)$ to (v,w), it also requires a positive defined $T_r^{Z_2}$ which in turn needs to be of same order of the

$T_r^{EW} \approx 140$GeV. Hence scenario B also requires $\mu_s^2 < 0$ as clearly shown in Figure 3.3.

For $c_s < 0$, which can be achieved with negative λ_m, Eq. (3.31) shows that the Z_2 symmetry remains non-restored at very high temperatures. This allows for thermal histories that start from a $(0, \tilde{w})$ phase and can lead to extending scenarios A and B to their Z_2 non-restoration corresponding cases. For both signs of μ_s^2, depending on its magnitude and the one of c_s, one obtains the one-step phase transition that leads to scenario A-NR. If, however, $\mu_s^2 \geq 0$, the Z_2 symmetry is temporarily restored at the temperature $T_r^{Z_2}$, given in Equation (3.32), and it is broken again to a different vacuum state, (v, w), during a later phase transition at a yet lower temperature. This is the path for scenario B-NR.

In summary, the novel condition of a SFOEWPT with Z_2-NR explored in this section demands a negative value of c_s, while different thermal histories are possible depending on the value of μ_s^2, as specify in Equation (3.33) below and more clearly shown in Figure 3.3,

$$\begin{aligned} &\mathrm{Z}_2 - \mathrm{R}: \ c_s \geq 0 && && \mathrm{Z}_2 - \mathrm{NR}: c_s < 0. \\ &\mathrm{A}: (0,0) \to (0,\tilde{w}) \to (v,w) && \implies && \mathrm{A} - \mathrm{NR}: (0,\tilde{w}) \to (v,w) \\ &\mathrm{B}: (0,0) \to (v,w) && \implies && \mathrm{B} - \mathrm{NR}: (0,\tilde{w}) \to (0,0) \to (v,w). \end{aligned} \tag{3.33}$$

The correspondence between the restoration and non-restoration scenarios is defined by them sharing the same final path towards the electroweak physical vacuum. Thus, the enhancement effects on the transition strength from the singlet contribution can be described in the same manner. This implies that the ratio of v_c/T_c for scenario A-NR is described by the same Equation (3.21) as in the scenario A. Analogously, v_c/T_c for scenario B-NR is described by Equation (3.28), that after simplification becomes Equation (3.29) as in scenario B, and therefore the same result as for scenario A. This also agrees with the fact that $\Delta V_{\mathrm{A}} \approx \Delta V_{\mathrm{B}}$ for the points with SFOEWPT, as discussed before, and it is clearly apparent from Figure 3.2 where there is a significant overlap of data points in the v_c/T_c -

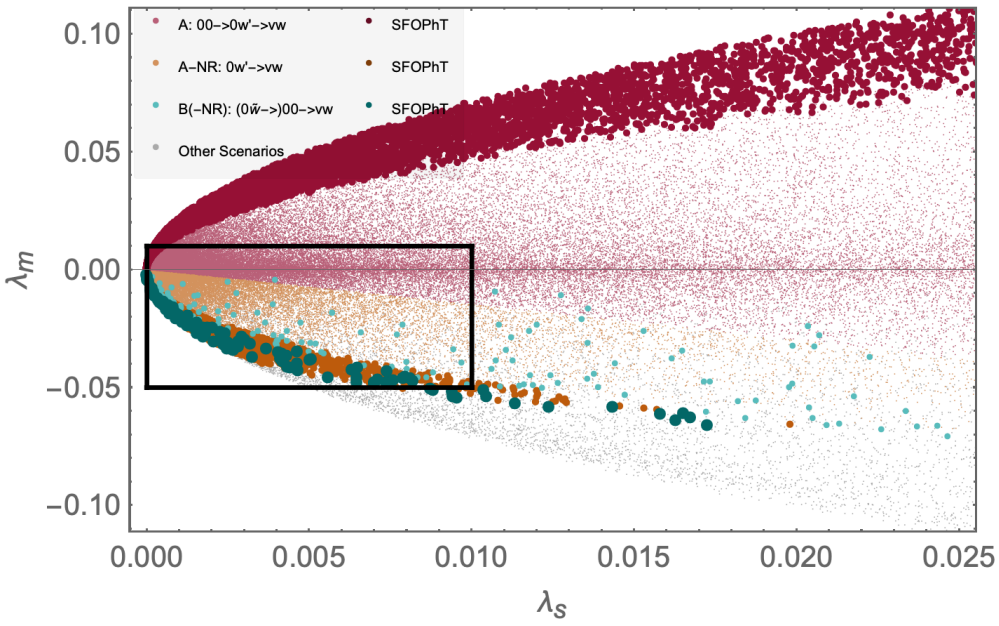

Figure 3.4: Parameter space on the λ_s-λ_m plane with different phase transition scenarios, zoomed into the small λ_s region. Color scheme for different scenarios is the same as in Figure 3.3.

$\tilde{\lambda}_h$ plane, both for scenarios A and B as well as for the Z_2 restoration and non-restoration cases.

The separation between the Z_2 restoration and non-restoration cases is clear in Figure 3.3, corresponding to the positive and negative c_s regions, respectively. We have already described the restrictive region of scenario B. For scenario B-NR, $\sqrt{\frac{-\mu_s^2}{c_s}}$ is the temperature scale where Z_2 is temporarily restored from the high temperature Z_2 non-restoration phase, provided $\mu_s^2 > 0$. For a strong electroweak phase transition to happen in the step of $(0,0) \to (v,w)$ in scenario B-NR, this temperature needs to be below the 140 GeV scale, i.e. $\sqrt{\frac{-\mu_s^2}{c_s}} < 140$ GeV, otherwise after Z_2 symmetry restoration to the trivial phase, the transition to an electroweak breaking vacuum $(\tilde{v},0)$ will develop at a temperature around 140 GeV, which will imply a small perturbation to the SM situation that we already know does not produce a SFOEWPT. In addition, we expect this will result in scenario B-NR transitioning from $(0,0) \to (v,w)$ at a temperature significantly below 140 GeV, rendering a SFOEWPT. In Figure 3.3, this can be seen in the dark green shade points with negative c_s.

Also observe from Figure 3.3 that there is no SFOEWPT points for the Z_2 restored scenario B.

In Figure 3.4, we show the same data set as in Figure 3.2 and Figure 3.3 for all the scenarios, now projected in the λ_s-λ_m plane of the quartic couplings, zoomed into the small λ_s region. As the Higgs quartic λ_h varies within a small numerical range, the EWSB condition $\tilde{\lambda}_h \geq 0$ corresponds to the outer parabolic boundary of the dark region, and the SFOEWPT condition $\tilde{\lambda}_h \lesssim 0.06$ corresponds to the inner parabolic boundary of the dark region. Different scenarios are coded by color in the same way as in Figure 3.3 with dark shaded points corresponding to a SFOEWPT. The points inside the rectangle are compatible with current bounds on the Higgs exotic decays, as will be discussed in section 3.2.3.

Full one-Loop study and nucleation

In this section, we shall show the results of the numerical scanning after implementing the CW and daisy resummation corrections introduced in section 3.2.1. All scanning results satisfy the Higgs mass and Higgs VEV boundary conditions. Other bounds will be introduced and shown in the following discussions.

Figure 3.5 shows the parameter space rendering SFOEWPT after implementation of the full one-loop effective potential, including the one-loop thermal and CW potential, and the daisy resummation, projected on the physical parameter space of the singlet mass m_S and the mixing angle $\sin\theta$. Observe that the sign of $\sin\theta$ is opposite of the sign of λ_m for values of $m_S < m_H$, as those of relevance in this study, see Equation (3.A.96). In addition, positive (negative) values of λ_m are correlated to restoration (non-restoration) scenarios with SFOEWPT (e.g. see Figure 3.4). As a result, it follows that all the solutions with SFOEWPT and $\sin\theta < 0$ in Figure 3.5 correspond to the thermal history of scenario A (with Z_2 restoration), while solutions for $\sin\theta > 0$ in Figure 3.5 correspond to the thermal histories of scenarios A-NR (black) and B-NR (green), respectively. Our study shows that

the valid parameter region rendering SFOEWPT has been reduced after including the full one-loop results and features smaller singlet mass values. Importantly, including the full one-loop effective potential with daisy resummation still allows for all types of solutions that existed in the thermal only analysis.

The CW correction to the scalar potential effectively accounts for the one-loop running of the tree-level potential parameters [76, 79–81, 134, 135]. The top quark Yukawa coupling yields the most relevant contribution in the running of the quartic couplings, with the possibility of rendering them negative at large scales. Furthermore, as we have discussed in detail in section 3.2.2, the effective quartic $\tilde{\lambda}_h(v_{\rm EW})$, which is directly related to the phase transition strength, is required to be small to yield a SFOEWPT. Hence the stronger the first-order phase transition, the smaller the effective quartic $\tilde{\lambda}_h(v_{\rm EW})$ and the most likely it is to be rendered negative at large scales, through the effects of the top Yukawa coupling in its running. This implies that after including the CW potential in the analysis, the points with stronger first-order phase transition strength in the thermal only analysis will be more likely to become unstable (acquire a negative effective quartic coupling) and will be discarded from the accepted solutions. If instead, one would implement a RG improvement of the CW potential, this will include the effects of running of the top quark Yukawa coupling itself, diminishing its value at large scales and, hence, also its impact in rendering the effective quartic coupling unstable. As a result, the inclusion of the one-loop CW without the RG improvement has the effect of reducing the parameter space of SFOEWPT as shown in Figure 3.5, beyond what would be the case with a more comprehensive analysis. In this sense the results presented in Figure 3.5 are conservative. We shall postpone a full study of the RG-improved effective one-loop scalar potential, as well as exploration of gauge dependence effects, for future work.

It is crucial to check that our results are robust against the nucleation calculation. Figure 3.6 shows the nucleation calculation results including the full one-loop effective potential

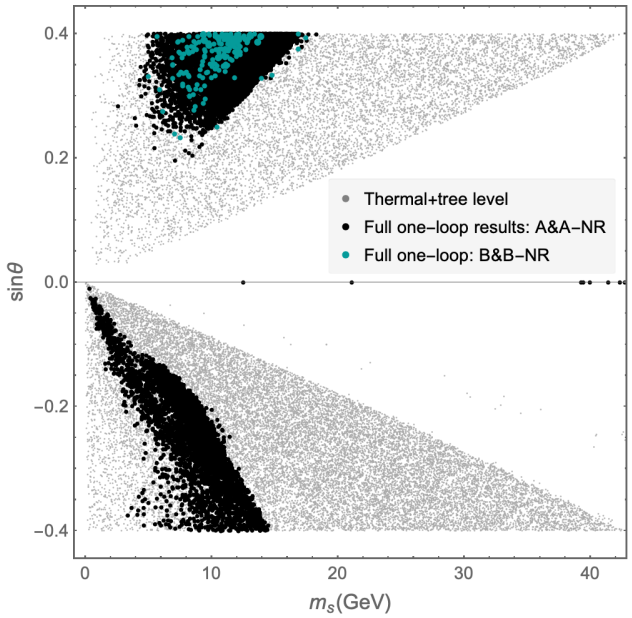

Figure 3.5: Parameter space for SFOEWPT in the m_S - $\sin\theta$ plane, after including the full potential up to one loop order (tree-level potential, one-loop thermal potential and one-loop zero temperature CW potential) plus finite temperature daisy resummation (darker shaded points in green and black for the B-NR and A/A-NR cases, respectively). Also shown are the points with SFOEWPT when only the tree-level with one-loop thermal potential is considered (gray scattered points).

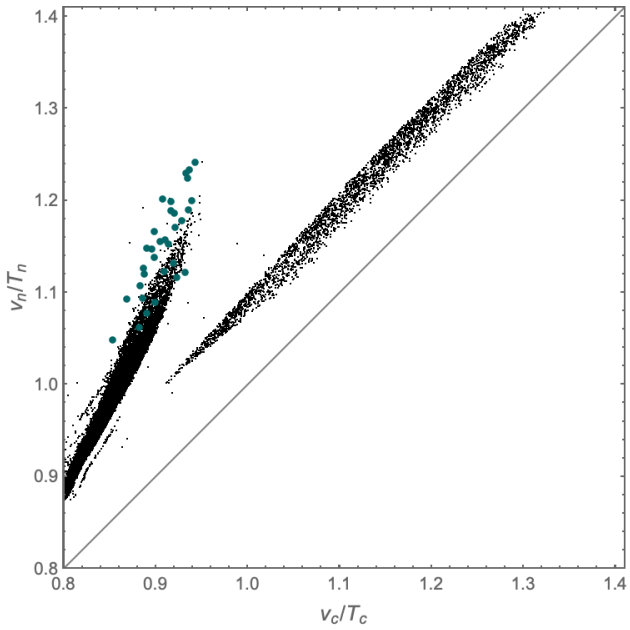

Figure 3.6: Nucleation calculation results at a full one loop level with daisy resummation corrections. Black: scenario A and A-NR. Green: scenario B and B-NR.

and the daisy resummation correction, we observe that the actual transition strength at nucleation temperatures is stronger than the strength evaluated at the critical temperatusres. For computational efficiency, all the previous calculations have been done at the critical temperature that gives a good indication of the actual transition strength at the nucleation temperature. Therefore, Figure 3.6 indicates that it is sufficient to require $v_c/T_c \gtrsim 0.8$ as criteria for a SFOEWPT.

3.2.3 Phenomenology

The analysis of the thermal history of the spontaneous Z_2 breaking singlet extension of the SM leads to a firm prediction of a light singlet-like scalar mass eigenstate. The viable parameter space can be tested through various phenomenological probes. First of all, the spontaneous Z_2 breaking will result in mixing between the singlet scalar and the doublet Higgs boson. The Higgs precision measurements and electroweak precision measurements

constrain the mixing angle $\sin\theta$ to be smaller than 0.4 for light singlets.[4] This constraint has been applied directly to our numerical scans. Furthermore, the precision Higgs program will improve with the full HL-LHC dataset [136, 137], and even more with data from future colliders [138–145].

In this section, we discuss three leading observational aspects of the model in regions of parameter space compatible with a SFOEWPT. First of all, the 125 GeV Higgs-like boson can decay to a pair of singlet-like scalars that can be directly searched for at the HL-LHC and/or at a future collider Higgs factory. Second, the Higgs trilinear coupling is modified when compared with the SM one. Third, the strong first order phase transition can be potentially probed by the next generation of gravitational wave detectors. In the following discussions we do not attempt to disentangle between the different possible thermal histories of the spontaneous Z_2 breaking singlet extension of the SM. For the collider phenomenology one would need to identify the signal dependence on the sign of the mixing angle $\sin\theta$. This would require to perform a more involved phenomenological study beyond the scope of this work. Such a study will be relevant in case high precision LHC data points towards a Higgs exotic decay signal and an anomalous Higgs trilinear coupling.

Higgs exotic decays

Since the singlet consistent with SFOEWPT should have a mass well below half of the SM-like Higgs boson one, the Higgs boson will decay into a pair of the new singlet scalars, $H \to SS$. The singlet-like scalar S will then decay back to SM particles, dominantly into a $b\bar{b}$ final state, if m_S is greater than 10 GeV, and into other fermions and hadrons for lower singlet-like scalar masses [147]. The partial width of the SM Higgs decaying to the light singlet-like scalar S is

$$\Gamma(H \to SS) = \frac{\Lambda_{HSS}^2}{32\pi m_H}\beta_S, \tag{3.34}$$

4. The constrain improves to 0.2 for heavy singlets. For more details, see the appendix of Ref. [122].

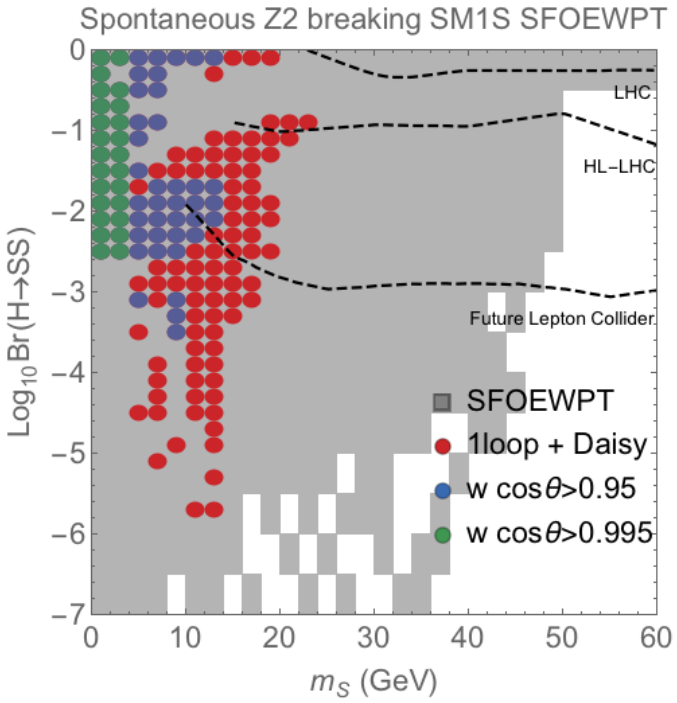

Figure 3.7: The Higgs decay branching fractions to S pairs for points consistent with SFOEWPT, where $v_c/T_c \gtrsim 0.8$. The gray region includes one-loop thermal potential only. The red region in addition, include the one-loop CW potential and daisy resummation. The blue and green regions are compatible with $\cos\theta > 0.95$, while the green region additionally requires $\cos\theta > 0.995$, which are the HL-LHC and the future lepton-collider Higgs factory expected precision sensitivities on the Higgs-singlet mixing angle θ [145]. The upper and middle dashed lines define the lower value of the current and HL-LHC projected sensitivities to $H \to SS \to 4j$ searches. The lower dashed line corresponds to constraints from direct exotic Higgs decay searches at future lepton colliders [146].

where Λ_{HSS} is the dimensionful coupling of the term HSS in the mass basis. Λ_{HSS} can be expressed as (without CW corrections),

$$\Lambda_{HSS} = \frac{(m_H^2 + 2m_S^2)(-\cos\theta + \tan\beta \sin\theta)\sin 2\theta}{4\tan\beta\ v}. \tag{3.35}$$

and $\beta_S = \sqrt{1 - 4m_S^2/m_H^2}$.

The current LHC Higgs exotic decay searches constrain the BR($H \to SS$) to be smaller than around 25% from a global fit [148–151] and 30-50% from direct searches [152,153]. This translates into a constraint on the HSS coupling Λ_{HSS} to be smaller than about 3 GeV. Given that for a large part of the parameter space, the size of this coupling reaches values up to $O(100)$ GeV, the Higgs exotic decay bounds provide an important constraint on this model.

Figure 3.7 shows the allowed values in the $\log_{10} BR(H \to SS) - m_S$ parameter space for different calculations of the SFOEWPT, with $v_c/T_c \gtrsim 0.8$. The gray region includes only the tree-level and one-loop thermal contributions to the scalar potential. The full one-loop results, including the CW corrections as well as the daisy resummation, are shown as the red, blue, and green regions for different requirements on the value of the Higgs-singlet mixing angle θ. The HL-LHC Higgs precision measurements will be able to probe deviations of the Higgs boson couplings at the 5% level, and this is shown by the blue and green regions. A future Higgs precision program at a prospective Higgs factory will measure the Higgs couplings at the 0.5% level, which would limit the Higgs-singlet mixing angle $\cos\theta$ to be greater than 0.995, and is shown by the green region.[5] Above the dashed lines in Figure 3.7 are regions constrained by direct searches of the Higgs decaying to a singlet scalar pair: from top to bottom, the dashed lines represent the current LHC coverage, the corresponding HL-

5. Note that the colored regions show allowed solutions without implying any assumptions on the density of such solutions, since this would be correlated to the density of scanned points, implying a highly prior dependent result. The same consideration is valid for Figure 3.8.

LHC coverage, and projections for a future electron-positron collider [146], respectively. As shown in Figure 3.7, imposing the future Higgs precision bounds implies a strong preference towards low singlet masses, however, we expect that a more intense numerical scan targeted to specific mass regions may expand the mass values allowed.[6] The boundary is also affected by the renormalization scale choice of the CW potential . We argue that the HL-LHC will be able to actively probe a significant region of the SFOEWPT parameter space in a spontaneous Z_2 breaking singlet extension of the SM and that a future Higgs factory could compellingly test this model.

Higgs pair production

The Higgs pair production process provides a unique handle in exploring the vacuum structure of the Higgs potential [122,154,155]. The HL-LHC program can probe the Higgs trilinear coupling through double Higgs boson production with an accuracy of 50% [136], whereas it could be measured at the 40% level at a low energy lepton collider [156], and at the 5-7% level at the FCC-hh [144] as well as at CLIC [138].

The Higgs pair production receives three contributions: the triangle diagram of an s-channel off-shell singlet S through a SHH vertex, the triangle diagram of an s-channel off-shell H through a HHH vertex, and a top-quark box diagram with double top Yukawa insertions. The first contribution from the s-channel off-shell scalar S is additional to the other SM ones, while the SM diagrams in turn are modified by mixing effects. The couplings governing the Higgs pair production are

$$\begin{aligned} \Lambda_{HHH} &= \frac{m_H^2\left(-\sin^3\theta + \tan\beta\cos^3\theta\right)}{2\tan\beta\ v} \\ \Lambda_{SHH} &= \frac{(2m_H^2 + m_S^2)(\sin\theta + \tan\beta\cos\theta)\sin 2\theta}{4\tan\beta\ v}. \end{aligned} \tag{3.36}$$

6. Note that for these results on a five-dimensional parameter space, we performed scans with approximately 10^5 CPU hours. We have a total of 10^7 points, of which 10^5 are compatible with SFOEWPT, and 10^4 satisfy the current Higgs precision and exotic decay constraints.

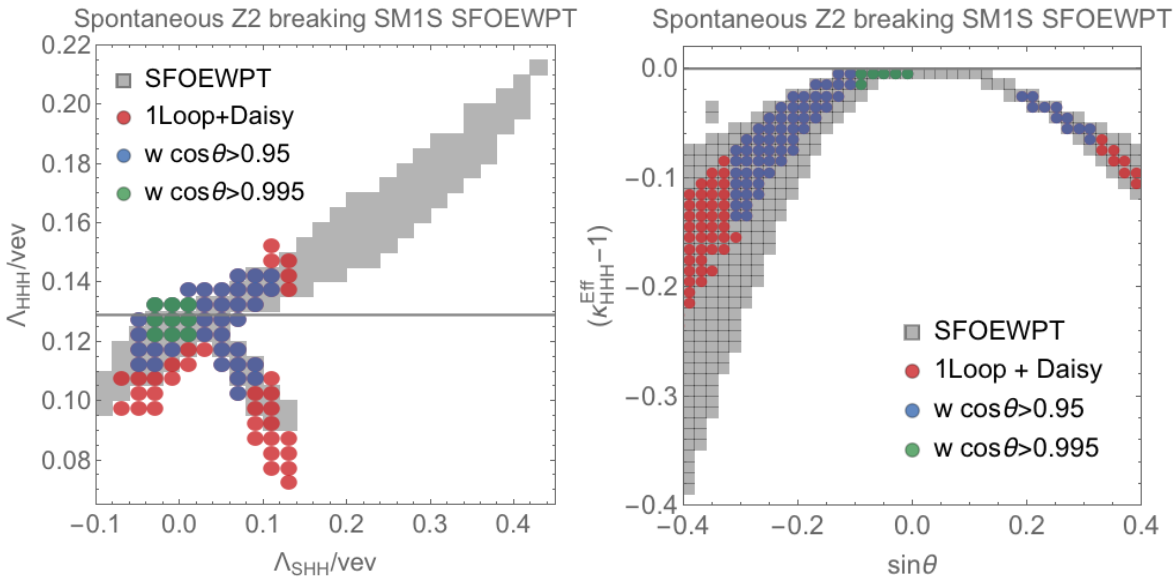

Figure 3.8: Left: Plane of the trilinear Higgs boson coupling and the singlet scalar-di-Higgs coupling, normalized to the SM Higgs boson VEV. Right: Departure of the effective trilinear coupling $\Lambda^{\text{Eff}}_{HHH}$ from its SM value as a function of the mixing angle $\sin\theta$. For both figures the color coding is as follows: The gray region corresponds to results including the tree-level and one-loop thermal potential only. The red, blue and green disks, include the one-loop CW potential and daisy resummation. The blue and green disks further require $\cos\theta > 0.95$, while the green disks additionally require $\cos\theta > 0.995$. The horizontal gray line indicates the SM value of the y-axis parameter.

A further simplification can be made due to the fact that m_S is much smaller than twice the Higgs mass. For the double Higgs production at hadron colliders such as the LHC and FCC-hh, within a good approximation, one can define an effective trilinear coupling that combines the two triangle diagrams via

$$\Lambda_{HHH}^{\text{Eff}} = \frac{2}{3}\sin\theta\frac{\hat{s}^2}{(\hat{s}-m_S^2)^2+i\Gamma_S m_S}\Lambda_{SHH}+\cos\theta\frac{\hat{s}^2}{(\hat{s}-m_H^2)^2+i\Gamma_H m_H}\Lambda_{HHH} \quad (3.37)$$

$$\simeq \frac{2}{3}\sin\theta\Lambda_{SHH}+\cos\theta\Lambda_{HHH}. \quad (3.38)$$

The determination and measurement of the trilinear Higgs coupling uses the differential information of the process as a result of the different diagrams and the interferences between the SM di-Higgs box diagram and the effective triangle diagram. Indeed, given the smallness of the singlet mass, the double Higgs production is far off-shell and can be absorbed into the above effective Higgs trilinear redefinition, which is valid at the differential cross-section level.

We show the contributing trilinear couplings, Λ_{HHH} and Λ_{SHH}, in the mass basis in the left panel of Figure 3.8. The modified Higgs trilinear coupling Λ_{HHH} varies broadly between 0.08 to 0.20. There is, in general, a positive correlation between Λ_{HHH} and the singlet scalar-di-Higgs trilinear coupling Λ_{SHH}. Such a positive correlation follows from Equation (3.36) for a subdominant contribution of the negative $\sin^3\theta$ term in Λ_{HHH}, which corresponds to the mixing quartic coupling contribution. The case of negative correlation, instead, follows from the dominance of the negative $\sin^3\theta$ term over the positive second term in Λ_{HHH}. The shading and color choices are the same as in Figure 3.7. We can see that as we restrict the Higgs-singlet mixing parameter $\sin\theta$ to be smaller, the Higgs trilinear coupling is also reduced to be closer to the SM value (which is shown as a gray reference line). The right panel of Figure 3.8 shows the departure of the effective trilinear coupling $\Lambda_{HHH}^{\text{Eff}}$ from its SM value as a function of the mixing parameter $\sin\theta$. We have defined the

ratio

$$\kappa_{HHH}^{Eff} \equiv \frac{\Lambda_{HHH}^{Eff}}{\Lambda_{HHH}^{SM}},$$

with Λ_{HHH}^{Eff} defined in Equation (3.38) and, again, the color code is the same as in Figure 3.7. We observe that for negative values of the mixing parameter $\sin\theta$, the effective Higgs trilinear coupling can be suppressed as much as 30%, while for positive values, the suppression is at most of the order 10%. These changes in the Higgs trilinear coupling are beyond the current reach of colliders and set a compelling challenge for the di-Higgs boson search program and related precision measurements at future colliders.

A SFOEWPT can general Gravitational Wave (GW) signals those can potentially be probed in current and future experiments, as an example, where we will leave the discussion of the GW signatures of this extension to chapter 5.

3.2.4 Summary and outlook of the section

In this section, we show a systematic study of a SFOEWPT driven by a real singlet degree of freedom coupled to the SM Higgs considering the unique scenario of spontaneous Z_2 breaking, including one-loop thermal effects with daisy resummation and the CW potential corrections. We identify several very distinctive features of the spontaneous Z_2 breaking model:

- A variety of thermal histories can be generically achieved. We classify them according to the number of steps to achieve the EWPT. We define scenario A (section 3.2.2) for $(0,0) \to (0,\tilde{w}) \to (v,w)$ (two steps) and scenario B (section 3.2.2) for $(0,0) \to (v,w)$ (one step). We also consider the possibility that at high temperatures there is non-restoration of the Z_2 symmetry and define scenario A-NR for $(0,\tilde{w}) \to (v,w)$ (one step), and scenario B-NR for $(0,\tilde{w}) \to (0,0) \to (v,w)$ (two steps) (section 3.2.2). The relation between the restoration and non-restoration scenarios is defined by them

sharing the same final path towards the electroweak physical vacuum;

- Our study shows that scenario A, A-NR and B-NR lead to solutions with strong first-order EWPT;

- We derive simple analytical relations for such scenarios and perform detailed numerical simulations. Our study has the potential to be generalized to other scalar extensions of the SM with novel phenomenology, e.g., in the limit of EW symmetry non-restoration;

- We find that in the spontaneous Z_2 breaking singlet extension of the SM, due to an upper bound on the singlet Higgs mixing quartic λ_m, the enhanced EWPT can only be achieved via a particular scenario of nearly degenerate extrema. As shown in detail in this section, having an extremum close in vacuum energy to the global minimum at zero temperature yields a low critical temperature and a large critical EW VEV, enabling strong first-order EWPT. Furthermore, we check our results performing a nucleation calculation and found v_n/T_n larger than v_c/T_c for these solutions, further validating our results;

- The realization of a strong first-order EWPT in this model predicts a light singlet-like scalar with a mass smaller than 50 GeV, which allows for a rich phenomenology. Special properties of the model can be tested through Higgs exotic decays and via Higgs coupling precision measurements at current and future collider facilities. The trilinear Higgs boson coupling is modified and can be enhanced or suppressed with respect to its SM value. Future constraints on the Higgs boson self-coupling could shed light on the physics of the EWPT. In addition, the strong first order EWPT transition can generate gravitational-wave signals, which are a challenging target for future gravitational wave experiments such as LISA and BBO.

The above points summarize distinctive aspects of the spontaneous Z_2-breaking, singlet extension of the SM. The existence of a light scalar with accessible collider signatures are

common features that can also be present in more general models connecting the SM to a plausible dark sector via a Higgs portal.

3.3 Nucleation is more than critical: a case study of the NMSSM

To study the phase transition patterns of models with extended Higgs sectors, most previous works solely rely on analyses of the temperature-dependent vacuum structure via the computation of the *critical temperature*, T_c, at which two (distinct) local minima of the effective potential become degenerate. While the critical temperature is indicative of the thermal history since it is the temperature at which the role of the global minimum passes from one vacuum phase to another, this calculation does not account for the probability of the associated phase transition actually taking place. First order phase transitions proceed via bubble nucleation, and the probability of the system transitioning from the false vacuum to the (new) true vacuum is computed via the *bounce action*, the Euclidean space-time integral over the effective Lagrangian, see, e.g., ref. [157] for a review.

Heuristically, bubble nucleation becomes difficult if the barrier separating two local minima becomes too high, or if the distance (in field space) separating the minima is too large. These conditions occur most readily if multiple scalar fields participate in the phase transition. For the EWPT, the possibility of a SM gauge singlet field participating in the phase transition is particularly interesting. While electroweak precision data tightly constrains the couplings and VEVs of any fields charged under the electroweak symmetry, such constraints do not apply to gauge singlets. Since its couplings are free parameters, a gauge singlet field can radically alter the shape of the effective potential, enabling a SFOEWPT. On the other hand, a gauge singlet may induce large barriers separating local minima and acquire a large VEV during the EWPT, increasing the distance between the local minima and reducing the nucleation probability. Therefore, a careful analysis of these effects is necessary in order to determine the region of parameter space leading to a successful SFOEWPT.

The Next-to-Minimal Supersymmetric extension of the Standard Model (NMSSM) [158, 159] is a well-motivated example of physics beyond the SM that may solve the hierarchy problem of the electroweak scale [160–164] and provide a dark matter candidate [165–175]. Its scalar sector contains a (complex) gauge singlet and two $SU(2)$ doublets, thus, it is well-suited for a case study of the comparison of the phase transition patterns suggested by the critical temperature calculation and those obtained from calculating the nucleation probabilities. Moreover, the NMSSM provides a range of possibilities for C and CP violation beyond what is found in the SM. For example, CP violation can occur in the Higgs sector, or between the superpartners of the SM particles. Assuming the latter, CP violation in the Higgs sector is induced only via (small) quantum corrections, and one can study the EWPT in the CP-conserving limit of the scalar potential.

The EWPT in the NMSSM has been studied previously in the literature. To the best of our knowledge, Pietroni [176] was the first to consider electroweak baryogenesis in the NMSSM, noting that the dimensionful coupling of the singlet to the Higgs doublets, A_λ, allows for shapes of the scalar potential suitable for a SFOEWPT at tree level. This is to be contrasted with the situation in the MSSM, where a barrier between the trivial and the physical minimum necessary for a SFOEWPT arises only from thermal effects. Subsequent work on the EWPT in the NMSSM includes refs. [130, 177–189], and work on closely related models can be found in refs. [190, 191]. Many of these papers focused on numerical scans of the NMSSM parameter space, aiming at identifying regions of parameter space suitable for realizing a SFOEWPT. Analytic studies have been carried out in refs. [130, 176, 179–181, 183]. A common idea in these works was to use parameters shaping the potential in the singlet-only direction to characterize the EWPT.

In the NMSSM, in general, there are ten degrees of freedom in the Higgs sector. In practice it suffices to consider the three-dimensional subspace spanned by the CP-even neutral scalar degrees of freedom. Nevertheless, computing the bounce action in this three-

dimensional field space is still numerically expensive, and, until now, results for the phase transition based on the nucleation calculation have only been presented for a few benchmark points in parameter space, see, e.g., refs. [178, 181, 184, 187, 189]. These studies mainly reported small-to-moderate *supercooling*, i.e. nucleation temperatures not much smaller than the corresponding critical temperatures for their benchmark points. More importantly, the thermal histories indicated by the critical temperatures agree with the ones obtained by the nucleation calculation. The notable exception is the recent work of Athron *et al.* [189], where results for the nucleation temperatures of four benchmark points were presented: For two of those four points, the authors reported small-to-moderate supercooling, while for the two remaining points the authors found that the nucleation condition could not be satisfied and, hence, the transition pattern indicated by the calculation of the critical temperatures was not a good indicator of the thermal history.

In this section, we present results for the EWPT in the NMSSM based on the nucleation calculation for a broad scan of the parameter space. We use `CosmoTransitions` [66] for the calculation of the bounce action, and support our results with analytic studies.[7] We focus on the region of parameter space where *alignment-without-decoupling* is realized in the Higgs sector, and on small-to-moderate values of $\tan\beta$, the ratio of the VEVs of the scalar $SU(2)$ doublets. This is motivated by the phenomenology of the 125 GeV Higgs boson observed at the Large Hadron Collider (LHC). In the NMSSM, a mass of 125 GeV of the SM-like Higgs boson can be achieved in the low-to-moderate $\tan\beta \lesssim 5$ regime without the need for large radiative corrections. The couplings of this state to SM particles are SM-like if it is (approximately) *aligned* with the interaction eigenstate that couples like the SM Higgs boson

7. In this work, we use the nucleation temperature, defined as the temperature at which the tunneling probability from the false to the true vacuum is one per Hubble volume and Hubble time, as a proxy for successful nucleation of a phase transition. We do not compute the *percolation temperature*, defined as the temperature at which a given fraction (often taken to be $1/e \sim 37\,\%$) of the Universe's volume has transitioned to the true vacuum. Sizable differences between the nucleation and percolation temperature can appear in the case of very large supercooling, however, a calculation of the percolation temperatures is beyond the scope of this work.

to other SM particles. In the NMSSM, there are two ways to achieve such alignment: i) the *decoupling* limit, that requires the non-SM-like interaction eigenstates to have masses much larger than the SM-like interaction state, and ii) the *alignment-without-decoupling* limit, where the parameters of the theory conspire to suppress the mixing of the SM-like interaction state with the non-SM-like interaction states [192]. The latter is of particular interest for realizing a SFOEWPT in the NMSSM: in the alignment-without-decoupling limit the non-SM-like states can have masses comparable to that of the SM-like Higgs boson, and hence, they can easily alter the shape of the scalar potential in ways relevant for the EWPT.

The null-results from searches for superpartners at the LHC suggests that the squarks and gluinos are heavy and decoupled from the EWPT. We use an effective field theory approach, integrating out all superpartners except for the neutralinos and charginos. This leaves the full SM particle content, an augmented scalar sector consisting of two $SU(2)$ doublets and a complex singlet, and the electroweakinos (composed of the superpartners of the photon, the Z- and W-bosons, the two Higgs doublets, and the scalar singlet) as dynamical degrees of freedom; similar approaches have been taken in refs. [184, 189, 191]. In order to maintain the location of the physical minimum in field space, the mass of the SM-like Higgs boson, and the alignment of the singlet-like and SM-like interaction eigenstates after including the radiative corrections to the effective potential from these remaining dynamical degrees of freedom, we add a set of (finite) counterterms, see refs. [185–187] for similar schemes.

The outline of our work is as follows: We begin by discussing the scalar sector of the NMSSM in subsection 3.3.1. In section 3.3.1 we discuss the radiative corrections to the scalar sector of the NMSSM, and the thermal corrections. After analyzing the zero-temperature vacuum structure of the NMSSM in subsection 3.3.2, we discuss the phase transition behavior of the NMSSM in subsection 3.3.3, in particular, we identify the relevant characteristics of the transition patterns for a SFOEWPT, and develop some analytical intuition for the regions of parameter space where phase transitions can successfully nucleate. In subsection 3.3.4, we

present our numerical results. In section 3.3.4 we study the region of parameters in which the proper physical minimum is obtained. We compare the results for the phase transitions obtained from the nucleation calculation with the transition patterns suggested by the critical temperature analysis in section 3.3.4. In section 3.3.4 we comment on the collider and dark matter phenomenology in the region of parameter space where we find SFOEWPTs. We summarize and present our conclusions in subsection 3.3.5. Explicit formulae for the field-dependent masses, the finite temperature corrections to the masses, and the equations we use to fix the counterterms are listed in appendices 3.B.1, 3.B.2, and 3.B.3, respectively. Additional discussion on model benchmark points can be found in the original paper.

The code used to perform our calculations is available at `https://github.com/sbaum90/NMSSM_CosmoTrans.git`.

3.3.1 The Next-to-Minimal Supersymmetric Standard Model and the effective potential

The Next-to-Minimal Supersymmetric Standard Model augments the particle content of the MSSM by a SM gauge-singlet chiral superfield $\widehat{S}$, see refs. [158, 159] for reviews. The best-studied version of the NMSSM is the $\mathbb{Z}_3$-NMSSM. In this model, an additional discrete symmetry is imposed, under which all left-handed chiral superfields transform as $\widehat{\Phi} \to e^{2\pi i/3}\widehat{\Phi}$ and all gauge superfields transform trivially. An interesting consequence of the $\mathbb{Z}_3$ symmetry is that it renders the superpotential of the NMSSM scale invariant; in particular the Higgsino mass parameter μ arises from the VEV of the scalar component of the singlet superfield, S. Thus, the NMSSM alleviates the MSSM's μ-problem.

Of greater phenomenological interest is that the NMSSM can accommodate a 125 GeV SM-like Higgs boson without the need for large radiative corrections to its mass. Furthermore, the presence of the scalar gauge singlet makes a SFOEWPT easily achievable in the NMSSM [130, 176–189, 191, 193]. This should be contrasted with the situation in the MSSM,

where, in the presence of a 125 GeV SM-like Higgs, the scalar potential is constrained such that a SFOEWPT is only possible if the stops are very light [194–200]. Such stops have been virtually ruled out by the LHC, not only via direct searches but also by the fact that such light stops would lead to a variation of the Higgs production cross section and decay branching ratios that are in conflict with current Higgs precision measurement data [201–207]. This places severe pressure on the possibility of electroweak baryogenesis in the MSSM. In the NMSSM, the presence of the singlet S, the bosonic component of $\widehat{S}$, allows for radically different shapes of the scalar potential, which make a SFOEWPT possible in the NMSSM without the need for light stops.

The superpotential of the $\mathbb{Z}_3$-NMSSM is given by

$$W = \lambda \widehat{S} \widehat{H}_u \cdot \widehat{H}_d + \frac{\kappa}{3} \widehat{S}^3 + W_{\text{Yuk}} \,, \tag{3.39}$$

where λ and κ are dimensionless parameters that can be chosen manifestly real in the CP-conserving case. The superfields $\widehat{H}_d = \left(\widehat{H}_d^0, \widehat{H}_d^-\right)^T$ and $\widehat{H}_u = \left(\widehat{H}_u^+, \widehat{H}_u^0\right)^T$ are the usual $SU(2)$-doublet Higgs superfields, we use a dot-notation for $SU(2)$ products

$$\widehat{H}_u \cdot \widehat{H}_d = \widehat{H}_u^+ \widehat{H}_d^- - \widehat{H}_u^0 \widehat{H}_d^0 \,, \tag{3.40}$$

and W_{Yuk} indicates the Yukawa terms which are identical to those in the MSSM [208].

Including F-, D- and soft SUSY-breaking terms, the scalar potential reads

$$\begin{aligned} V_0 = {} & m_{H_d}^2 |H_d|^2 + m_{H_u}^2 |H_u|^2 + m_S^2 |S|^2 + \lambda^2 |S|^2 \left(|H_d|^2 + |H_u|^2\right) + \left|\lambda H_u \cdot H_d + \kappa S^2\right|^2 \\ & + \left(\lambda A_\lambda S H_u \cdot H_d + \frac{\kappa}{3} A_\kappa S^3 + \text{h.c.}\right) + \frac{g_1^2 + g_2^2}{8} \left(|H_d|^2 - |H_u|^2\right)^2 + \frac{g_2^2}{2} \left|H_d^\dagger H_u\right|^2 \,, \end{aligned} \tag{3.41}$$

where m_i^2 and A_i are soft SUSY-breaking parameters of dimension mass-squared and mass,

respectively, and g_1 and g_2 are the $U(1)_Y$ and $SU(2)_L$ gauge couplings.

The Higgs fields have large couplings amongst themselves, to the electroweak gauge bosons, and to third generation (s)fermions. These couplings lead to sizable radiative corrections to V_0, to which we return in section 3.3.1. However, many of the properties of the scalar potential can already be seen from the tree level potential, Equation (3.41).

In order to be compatible with phenomenology, the NMSSM must preserve charge. While in the MSSM the scalar potential is sufficiently constrained to make charge-breaking minima very rare (see, e.g., ref. [209]), the additional freedom of the NMSSM's scalar potential makes such minima a much larger problem. However, ref. [210] demonstrated numerically that, while charge-breaking minima may be present in the NMSSM, they are virtually always accompanied by additional charge-conserving minima, and the tunneling rate from the metastable physical minimum to these charge-conserving minima is larger than to the charge-breaking minima. Hence, we can neglect such charge-breaking minima; in the following we will assume that for all phenomenologically relevant vacua the VEVs can be rotated to have the form

$$\langle H_d \rangle = \begin{pmatrix} v_d \\ 0 \end{pmatrix} , \qquad \langle H_u \rangle = \begin{pmatrix} 0 \\ v_u \end{pmatrix} , \qquad \langle S \rangle = v_S , \tag{3.42}$$

breaking $SU(2)_L \times U(1)_Y \to U(1)_{\text{em}}$. Without loss of generality, one can furthermore take all VEVs to be real-valued: While the $\mathbb{Z}_3$-NMSSM does allow for stationary points in the scalar potential which spontaneously break CP, at tree level such points are either saddle points or local maxima [211]. In summary, it suffices to allow the neutral real components of H_d, H_u, and S to take non-trivial VEVs[8] when studying the vacuum structure of the NMSSM. This reduction from a ten-dimensional to a three-dimensional field space makes the task considerably more tractable.

8. Observe that in general the sfermions can get non-trivial VEVs as well, potentially giving rise to charge and/or color breaking vacua. We will not entertain this possibility further in this work.

In order to ensure that the scalar potential has a stationary point at the physical minimum, we use the minimization conditions

$$\left.\frac{\partial V}{\partial H_d}\right|_{\substack{H_d=v_d\\H_u=v_u\\S=v_S}} = \left.\frac{\partial V}{\partial H_u}\right|_{\substack{H_d=v_d\\H_u=v_u\\S=v_S}} = \left.\frac{\partial V}{\partial S}\right|_{\substack{H_d=v_d\\H_u=v_u\\S=v_S}} = 0 \,, \tag{3.43}$$

replacing the squared mass parameters $m_{H_d}^2$, $m_{H_u}^2$, and m_S^2 with the VEVs v_d, v_u, and v_S in Equation (3.41). In practice, it is convenient to re-parameterize the VEVs,

$$v \equiv \sqrt{v_d^2 + v_u^2} \,, \qquad \tan\beta \equiv v_u/v_d \,, \qquad \mu \equiv \lambda v_S \,. \tag{3.44}$$

The observed mass of the electroweak gauge bosons is reproduced by fixing $v = 174\,\text{GeV}$, removing one of the NMSSM's free parameters.

In order to account for the constraints on the NMSSM imposed by the SM-like couplings of the observed 125 GeV Higgs boson, it is useful to write the Higgs fields in the *extended Higgs basis* [192, 212–218][9]

$$H_d = \begin{pmatrix} \frac{1}{\sqrt{2}}\left(c_\beta H^{\text{SM}} - s_\beta H^{\text{NSM}}\right) + \frac{i}{\sqrt{2}}\left(-c_\beta G^0 + s_\beta A^{\text{NSM}}\right) \\ -c_\beta G^- + s_\beta H^- \end{pmatrix} \,, \tag{3.45}$$

$$H_u = \begin{pmatrix} s_\beta G^+ + c_\beta H^+ \\ \frac{1}{\sqrt{2}}\left(s_\beta H^{\text{SM}} + c_\beta H^{\text{NSM}}\right) + \frac{i}{\sqrt{2}}\left(s_\beta G^0 + c_\beta A^{\text{NSM}}\right) \end{pmatrix} \,, \tag{3.46}$$

$$S = \frac{1}{\sqrt{2}}\left(H^{\text{S}} + iA^{\text{S}}\right) \,. \tag{3.47}$$

H^{SM}, H^{NSM}, and H^{S} are the three neutral CP-even interaction states of the Higgs basis, A^{NSM} and A^{S} are the CP-odd states, and $H^\pm$ is the charged Higgs. The neutral and charged

9. Note, that there are different conventions in the literature for the Higgs basis differing by an overall sign of H^{NSM} and A^{NSM}.

Goldstone modes are denoted by G^0 and $G^\pm$, respectively, and we used a shorthand notation

$$s_\beta \equiv \sin\beta\,, \qquad c_\beta \equiv \cos\beta\,. \tag{3.48}$$

In this basis, the couplings to pairs of SM particles take a particularly simple form. Focusing on the CP-even states, the couplings to pairs of down-type and up-type fermions and pairs of vector bosons (VV) are

$$H^{\mathrm{SM}}(\text{down},\,\text{up}\,,\text{VV}) = (g_{\mathrm{SM}},\ g_{\mathrm{SM}},\ g_{\mathrm{SM}})\ , \tag{3.49}$$

$$H^{\mathrm{NSM}}(\text{down},\,\text{up}\,,\text{VV}) = (-g_{\mathrm{SM}}\tan\beta,\ g_{\mathrm{SM}}/\tan\beta,\ 0)\ , \tag{3.50}$$

$$H^{\mathrm{S}}(\text{down},\,\text{up}\,,\text{VV}) = (0,\ 0,\ 0)\ , \tag{3.51}$$

where g_{SM} is the corresponding coupling of the SM Higgs boson to pairs of such particles. Thus, H^{SM} has the same couplings to pairs of SM particles as the SM Higgs boson. Furthermore, H^{SM} is the only Higgs boson which couples to pairs of vector bosons. H^{NSM} has $\tan\beta$ enhanced (suppressed) couplings to pairs of down-type (up-type) SM fermions, and H^{S} does not couple to pairs of SM particles. Note that at the physical minimum, only $\langle H^{\mathrm{SM}}\rangle = \sqrt{2}v$ and $\langle H^{\mathrm{S}}\rangle = \sqrt{2}v_S$ take non-trivial VEVs, while $\langle H^{\mathrm{NSM}}\rangle = 0$.

The interaction states mix into mass eigenstates. We denote the CP-even mass eigenstates as $\{h_{125}, H, h_S\}$, where h_{125} is identified with the 125 GeV state observed at the LHC, H is the non-SM-like state with the largest H^{NSM} component, and h_S the state with the largest H^{S} component. Similarly, the CP-odd interaction states A^{NSM} and A^{S} mix into two mass eigenstates, which we denote as A and a_S.

In order to ensure compatibility with the observed Higgs boson phenomenology, the h_{125} state must be dominantly composed of H^{SM}. Denoting the squared mass matrix for the CP even states as $\mathcal{M}_S^2$ in the basis $\left\{H^{\mathrm{SM}}, H^{\mathrm{NSM}}, H^{\mathrm{S}}\right\}$, the tree-level mass of the SM-like state

is given by

$$m_{h_{125}}^2 \simeq \mathcal{M}_{S,11}^2 = m_Z^2 \cos^2(2\beta) + \lambda^2 v^2 \sin^2(2\beta) \,, \tag{3.52}$$

where $m_Z^2 = v^2 \left(g_1^2 + g_2^2\right)/2$ is the Z-boson mass. While $m_{h_{125}}$ receives sizable radiative corrections via the stops, see section 3.3.1, it is interesting to note that the term proportional to $\lambda^2 v^2$ allows one to obtain $m_{h_{125}} = 125\,\text{GeV}$ already at tree level for small values of $\tan\beta \lesssim 3$ if λ takes values $0.7 \lesssim \lambda \lesssim 1$. Thus, there is no need for large radiative corrections to the mass of the SM-like Higgs, i.e. no need for heavy stops, in the NMSSM. Including moderate corrections from the stops, the required value for the mass of the SM-like Higgs boson is obtained for $0.6 \lesssim \lambda \lesssim 0.8$ in the small-to-moderate $\tan\beta \lesssim 5$ regime.

In order to ensure that the mass eigenstate h_{125} is dominantly composed of H^{SM}, the mixing angles of H^{NSM} and H^{S} with H^{SM} must be suppressed. The mixing of H^{SM} with H^{NSM} is suppressed if

$$\left|\mathcal{M}_{S,12}^2\right| \ll \left|\mathcal{M}_{S,22}^2 - \mathcal{M}_{S,11}^2\right| \,, \tag{3.53}$$

and similarly, the mixing of H^{SM} with H^{S} is suppressed if

$$\left|\mathcal{M}_{S,13}^2\right| \ll \left|\mathcal{M}_{S,33}^2 - \mathcal{M}_{S,11}^2\right| \,. \tag{3.54}$$

Here, the $\mathcal{M}_{S,ij}^2$ again are the entries of the squared mass matrix for the CP-even states in the basis $\left\{H^{\text{SM}}, H^{\text{NSM}}, H^{\text{S}}\right\}$. There are two possibilities to achieve such (approximate) *alignment* of h_{125} with H^{SM}: either, the entries of the squared mass matrix corresponding to such mixing are small, or, the right hand sides of Equation (3.53) and Equation (3.54) become large. The latter option is the so-called *decoupling limit*. Realizing alignment in this way implies $\left\{m_H, m_{h_S}\right\} \gg m_{h_{125}}$. As we will see below, a relatively light singlet-like state gives the scalar potential a favorable shape for SFOEWPT. Thus, the former option, the so-called *alignment without decoupling* limit, is more interesting for electroweak baryogenesis.

At tree-level, alignment between the two states originating from the Higgs doublets,

Equation (3.53), is achieved for

$$\mathcal{M}^2_{S,12} = -\left(m_Z^2 - \lambda^2 v^2\right)\sin(2\beta)\cos(2\beta) \to 0\ . \tag{3.55}$$

It is convenient to instead rewrite this condition as

$$\mathcal{M}^2_{S,12} = \frac{1}{\tan\beta}\left[\mathcal{M}^2_{S,11} - m_Z^2\cos(2\beta) - 2\lambda^2 v^2 \sin^2\beta\right] \to 0\ , \tag{3.56}$$

because this form is robust against radiative corrections [192]. Identifying $\mathcal{M}^2_{S,11} = m^2_{h_{125}}$, one obtains the alignment condition

$$\lambda^2 = \frac{m^2_{h_{125}} - m_Z^2\cos(2\beta)}{2v^2\sin^2\beta}\ . \tag{3.57}$$

For small to moderate values of $\tan\beta$, this condition yields $0.6 \lesssim \lambda \lesssim 0.7$. It is interesting to note that, for moderate values of $\tan\beta \lesssim 5$, this range of λ coincides with the range for which one obtains $m_{h_{125}} = 125\,\text{GeV}$ without the need for large radiative corrections.

Suppressing the mixing of H^{SM} with H^{S}, Equation (3.54), yields a second alignment condition from demanding $\mathcal{M}^2_{S,13} \to 0$, namely

$$M_A^2 = \frac{4\mu^2}{\sin^2(2\beta)}\left(1 - \frac{\kappa}{2\lambda}\sin 2\beta\right)\ , \tag{3.58}$$

where we introduced the parameter

$$M_A^2 = \frac{2\mu}{\sin 2\beta}\left(A_\lambda + \frac{\kappa\mu}{\lambda}\right)\ . \tag{3.59}$$

M_A^2 is the (squared) mass parameter of A^{NSM} and controls the mass scale of the mostly doublet-like CP-even and CP-odd mass eigenstates as well as the mass scale of the charged Higgs boson. The alignment condition Equation (3.58) gives rise to a mass spectrum where,

provided $\kappa < \lambda$, the doublet-like mass eigenstates have approximate masses $m_H, m_A, m_{H^\pm} \sim 2\mu/\sin 2\beta$ [219, 220].

In the remainder of this section, we will consider the NMSSM in the alignment limit, choosing parameters to satisfy Equation (3.57) and Equation (3.58). While current data [150, 221] allow for some deviation from perfect alignment, the phenomenological impact of such departures on the EWPT in the NMSSM is small. Note also that in refs. [219, 220] it was demonstrated that, in random parameter scans where the alignment conditions are not *a priori* enforced, requiring compatibility with the phenomenology of the observed 125 GeV Higgs boson selects the region of parameter space where Equation (3.57) and Equation (3.58) are (approximately) satisfied.

The NMSSM parameter space is constrained by a number of additional arguments. Let us briefly discuss two of them here, while we derive constraints arising from the stability of the electroweak vacuum in subsection 3.3.2. It is well known, that large values of the dimensionless parameters λ and κ lead to Landau poles. Avoiding the appearance of Landau poles below the GUT scale [$Q_{\rm GUT} \sim \mathcal{O}(10^{16})\,\text{GeV}$] entails constraining the values of the NMSSM's couplings, at the electroweak scale, to [159]

$$\sqrt{\lambda^2 + \kappa^2} \lesssim 0.7 \,. \tag{3.60}$$

As discussed above, both the SM-like nature of the observed Higgs boson and its mass value lead to a preference of sizable values of $0.6 \lesssim \lambda \lesssim 0.7$ in the NMSSM. Hence, avoiding Landau poles below $Q_{\rm GUT}$ limits the value of $|\kappa| \lesssim 0.3$ in the alignment limit. Note that the NMSSM with larger couplings (and Landau poles between the TeV and the GUT scale) is known as λ-SUSY, see, for example, refs. [222–224].

The parameter space is also constrained by avoiding tachyonic masses. The most relevant constraint arises from the singlet-like CP-odd mass eigenstate a_S. Taking into account first-

order mixing effects, its mass is approximately [192]

$$m_{a_S}^2 \simeq 3\kappa v^2 \left[\frac{3\lambda}{2} \sin(2\beta) - \left(\frac{\mu A_\kappa}{\lambda v^2} + \frac{3\kappa \mu^2}{M_A^2} \right) \right] . \tag{3.61}$$

Recalling that alignment requires $M_A^2 \simeq 4\mu^2 / \sin^2(2\beta)$, we can deduce the condition the NMSSM parameters must satisfy to keep a_S from becoming tachyonic:

$$\frac{\kappa \mu A_\kappa}{v^2} \lesssim \frac{3\kappa \lambda^2 \sin(2\beta)}{2} \left[1 - \frac{\kappa \sin(2\beta)}{2\lambda} \right] . \tag{3.62}$$

For small-to-moderate values of $\tan\beta$ and in the alignment limit, where $0.6 \lesssim \lambda \lesssim 0.7$, the right-hand side of Equation (3.62) is approximately $\kappa \times \mathcal{O}(1)$. Hence, equation Equation (3.62) implies $\mu A_\kappa \lesssim v^2$ for $\kappa > 0$, while for $\kappa < 0$ the condition becomes $\mu A_\kappa \gtrsim v^2$; in particular, disfavoring $\mathrm{sgn}(\mu A_\kappa) = -1$ for $\kappa < 0$.

Radiative and thermal corrections

The scalar potential receives sizable radiative corrections from the large couplings between the Higgs bosons themselves as well as from their large couplings to the electroweak gauge bosons and the (s)fermions, in particular the (s)tops, see, for example, refs. [159, 225–227]. Since the precise interplay between the higher-order corrections to the Higgs mass and the mass values of the SM particles and their superpartners does not play a relevant role in our study of the EWPT, we shall take only the dominant one loop corrections into account in this work. The null-results from SUSY searches at the LHC suggest that all squarks as well as the gluinos have masses $\gtrsim 1\,\mathrm{TeV}$. LHC constraints on new states neutral under QCD are less stringent. Furthermore, to yield a scalar potential sufficiently different from that of the SM to accommodate a SFOEWPT, the Higgs bosons' masses should not be much larger than the electroweak scale. These considerations motivate studying a scenario

in which all sfermions[10] and the gluinos are heavy and can be integrated out, yielding an effective theory where the remaining dynamical degrees of freedom are the SM particles, the new Higgs bosons $\left\{H, h_S, A, a_S, H^{\pm}\right\}$, the five neutralinos $\widetilde{\chi}_i^0$, and the two charginos $\widetilde{\chi}_i^{\pm}$; see refs. [184, 189, 191] for similar approaches. The parameters of this effective theory are obtained by matching onto the full theory (containing all the NMSSM's degrees of freedom) at an intermediate scale. The leading operator one obtains from this procedure is

$$\Delta\mathcal{L} = -\frac{\Delta\lambda_2}{2}\left|H_u\right|^4 \ , \tag{3.63}$$

arising from stop loops. At one loop, the coefficient $\Delta\lambda_2$ is related to the parameters of the stop sector via [228–231]

$$\Delta\lambda_2 = \frac{3}{8\pi^2}h_t^4\left[\log\left(\frac{M_S^2}{m_t^2}\right) + \frac{A_t^2}{M_S^2}\left(1 - \frac{A_t^2}{12M_S^2}\right)\right] \ , \tag{3.64}$$

where h_t is the top Yukawa coupling determined from the (running) top quark mass $m_t = h_t v \sin\beta$, M_S is the geometric mean of the stop masses, and A_t is the soft trilinear stop-Higgs coupling. We note that for small to moderate values of $\tan\beta$, the top quark superfield has a sizable coupling only to $\widehat{H}_u$ in the superpotential. After the singlet acquires a non-trivial VEV, an effective μ-term is generated and additional effective quartic couplings, which involve not only H_u but also H_d, arise via stop loops. However, these contributions are suppressed by powers of μ/M_S. We shall work in a region of parameter space where $|\mu| \ll M_S$ and, hence, the dominant contribution induced by integrating out the stop sector is given by Equation (3.63). At higher loop orders, the exact relation between $\Delta\lambda_2$ and the parameters in the stop sector is modified, but, for small values of $|\mu|$, the stop radiative corrections can still be effectively parametrized by $\Delta\lambda_2$ (see, for example, refs. [229, 231, 232]).

10. For simplicity we also take the sleptons to be heavy here. Because the couplings of sleptons to the scalar sector are much smaller than the gauge couplings and the top Yukawa coupling, lighter sleptons would not lead to large radiative corrections to the scalar sector.

The scalar potential of this effective theory is then given by

$$V_0^{\rm eff} = V_0 + \frac{\Delta\lambda_2}{2}\,|H_u|^4 \ . \tag{3.65}$$

This new contribution gives sizable corrections to the Higgs mass matrix. In particular, the mass of the SM-like Higgs state is given by

$$m_{h_{125}}^2 \simeq \mathcal{M}_{S,11}^2 = m_Z^2\cos^2(2\beta) + \lambda^2 v^2 \sin^2(2\beta) + 2\Delta\lambda_2 v^2 \sin^4\beta \ . \tag{3.66}$$

Note that the alignment conditions in Equation (3.57) and Equation (3.58) are not modified by $\Delta\lambda_2$. While the value of $\Delta\lambda_2$ is in principle controlled by the soft parameters in the stop sector, see Equation (3.64), in the remainder of this section we use Equation (3.66) to set $\Delta\lambda_2$ to reproduce the observed mass of the SM-like Higgs boson, $m_{h_{125}} = 125\,\text{GeV}$.

The radiative corrections to the effective potential from the remaining dynamical degrees of freedom are given by the CW potential We denote the field-dependent masses computed from $V_0^{\rm eff}$ by

$$\widehat{m}_i^2 = \widehat{m}_i^2(H^{\rm SM}, H^{\rm NSM}, H^{\rm S}) \ , \tag{3.67}$$

and work in the Landau gauge; explicit expressions for the $\widehat{m}_i^2$ are collected in appendix 3.B.1. The bosonic fields entering Equation (2.9) are $B = \left\{h_i, a_i, H^\pm, G^0, G^\pm, Z, W^\pm\right\}$ with $n_B = \{1,1,2,1,2,3,6\}$ degrees of freedom, respectively. Here, h_i and a_i denote the three neutral CP-even and two CP-odd Higgs bosons, $H^\pm$ the charged Higgs, G^0 and $G^\pm$ the neutral and charged Goldstone modes, and Z and $W^\pm$ the electroweak gauge bosons. The fermionic fields entering the CW potential are[11] $F = \left\{\widetilde{\chi}_i^0, \widetilde{\chi}_i^\pm, t\right\}$ with $n_F = \{2,4,12\}$, where $\widetilde{\chi}_i^0$ and $\widetilde{\chi}_i^\pm$ denote the five neutralinos and two charginos, respectively, and t is the top quark. We have chosen m_t as the renormalization scale, implying that the parameters are defined

11. We neglect the (small) radiative corrections from the SM fermions other than the top quark.

at such scale. In order to guarantee the one-loop renormalization scale independence and preserve the supersymmetric relations, the parameters at the scale m_t must be related with those at higher energies, up to the supersymmetry breaking scale, by including all particles in the effective theory in the running to higher energies.

Note that since the Goldstone modes' masses vanish at the physical minimum, their contributions to the CW potential lead to divergent contributions to physical masses and coupling coefficients computed from derivatives of the loop-corrected effective potential. This divergence is an artifact of the perturbative calculation [63,64] and can be dealt with by shifting the masses of the Goldstone modes by an infrared regulator, $\widehat{m}_G^2 \to \widehat{m}_G^2 + \mu_{\rm IR}^2$. In our numerical calculations, we use a value of $\mu_{\rm IR}^2 = 1\,{\rm GeV}^2$; note, however, that in numerical calculations numerical errors on $\widehat{m}_G^2$ typically suffice to "regulate" the logarithmically divergent contribution from $\widehat{m}_G^2 \to 0$, even before including an explicit infrared regulator.

The CW corrections alter the location of the minima as well as the physical masses. We include a set of counterterms

$$\delta\mathcal{L} = -\delta_{m_{H_d}^2}\,|H_d|^2 - \delta_{m_{H_u}^2}\,|H_u|^2 - \delta_{m_S^2}\,|S|^2 - \delta_{\lambda A_\lambda}\,(S H_u \cdot H_d + \text{h.c.}) - \frac{\delta_{\lambda_2}}{2}\,|H_u|^4 \ , \quad (3.68)$$

to keep the location of the physical minimum at $\left\{H^{\rm SM}, H^{\rm NSM}, H^{\rm S}\right\} = \sqrt{2}\,\{v, 0, \mu/\lambda\}$, ensure $\mathcal{M}^2_{S,13} \to 0$, preserving alignment, and maintain $m_{h_{125}} = 125\,{\rm GeV}$. Note that these counterterms correspond to a redefinition of the soft SUSY-breaking terms[12], see refs. [185–187] for similar approaches. We list equations for the fixing of the counterterms in appendix 3.B.2.

The input parameters for our model are thus

$$\tan\beta\ , \quad \mu\ , \quad \kappa\ , \quad A_\kappa\ . \quad (3.69)$$

12. The counterterm δ_{λ_2} corresponds to a soft SUSY-breaking term in the sense that it can be understood as a counterterm shifting the soft parameters in the stop sector and, in turn, the threshold correction $\Delta\lambda_2$ that we obtain from integrating out the stops.

All other parameters are fixed by the various conditions we impose on the model, namely, λ and M_A^2 are determined by alignment, $\Delta\lambda_2$ by setting $m_{h_{125}} = 125\,\text{GeV}$, and the counterterms are fixed by the conditions discussed in the previous paragraph.

The thermal corrections are taken into account with the one-loop finite temperature potential introduced in section 2.1, and we have included the daisy corrections re-summing hard thermal loops with

$$\widetilde{m}_i^2 \equiv \widetilde{m}_i^2(H^{\text{SM}}, H^{\text{NSM}}, H^{\text{S}}; T) = \widehat{m}_i^2(H^{\text{SM}}, H^{\text{NSM}}, H^{\text{S}}) + c_i T^2 \,. \tag{3.70}$$

where the daisy coefficients for the relevant fields in appendix 3.B.3. Including the CW and the thermal corrections, the temperature-dependent effective potential at one-loop order is given by

$$V_1(T) = V_0^{\text{eff}} + V_{1-\text{loop}}^{\text{CW}}(\widetilde{m}_i^2) + V_{1-\text{loop}}^{T\neq 0}(\widetilde{m}_i^2) \,. \tag{3.71}$$

3.3.2 Zero-temperature vacuum structure

While the NMSSM's scalar potential is subject to radiative as well as thermal corrections as discussed in section 3.3.1, one can already learn much about the possibility of a SFOEWPT from considering the effective potential, V_0^{eff}, obtained after integrating out all sfermions and the gluinos and prior to including the CW and thermal corrections. In this section, we derive the most interesting regions of NMSSM parameter space for realizing a SFOEWPT from V_0^{eff}. As we shall show later on, these regions of parameter space are only mildly affected by radiative corrections. Recall that in order to study the vacuum structure of the NMSSM, it suffices to consider the three-dimensional field space spanned by the neutral CP-even fields $\left\{H^{\text{SM}}, H^{\text{NSM}}, H^{\text{S}}\right\}$,

$$V_0^{\text{eff},3}(H^{\text{SM}}, H^{\text{NSM}}, H^{\text{S}}) \equiv V_0^{\text{eff}}\Big|_{\substack{A^{\text{NSM}}=0 \\ A^{\text{S}}=0 \\ H^{\pm}=0}} \,, \tag{3.72}$$

where V_0^{eff} is the potential given in Equation (3.65).

As discussed above, the singlet plays a special role for realizing a SFOEWPT. Its coupling to the Higgs doublets, λ, and its self-coupling, κ, are free parameters, while the quartic couplings between the Higgs doublets are governed by the gauge couplings (and $\Delta\lambda_2$). Furthermore, as a consequence of $U(1)_Y$ symmetry, $V_0^{\text{eff},3}$ is invariant under the transformation $H^{\text{SM}} \to -H^{\text{SM}}$, $H^{\text{NSM}} \to -H^{\text{NSM}}$, $H^{\text{S}} \to H^{\text{S}}$. This residual $\mathbb{Z}_2$ symmetry ensures that any extrema in the singlet-only direction, i.e. where $H^{\text{SM}} = H^{\text{NSM}} = 0$, are also extrema (or saddle points) of $V_0^{\text{eff},3}$. In the alignment limit (or, more specifically, as long as the second alignment condition, Equation (3.54), is satisfied) the scalar potential in the singlet-only direction is given by

$$V_0^{\text{eff},3}(0,0,H^{\text{S}}) \to -\kappa^2 \frac{\mu}{\lambda}\left(\frac{\mu}{\lambda}+\frac{A_\kappa}{2\kappa}\right)(H^{\text{S}})^2 + \frac{\kappa A_\kappa}{3\sqrt{2}}(H^{\text{S}})^3 + \frac{\kappa^2}{4}(H^{\text{S}})^4 \,. \tag{3.73}$$

This potential has extrema at

$$H^{\text{S}} = \left\{0\,, \quad \frac{\sqrt{2}\mu}{\lambda}\,, \quad -\sqrt{2}\left(\frac{\mu}{\lambda}+\frac{A_\kappa}{2\kappa}\right)\right\}\,. \tag{3.74}$$

The first of these field values corresponds to the trivial minimum of the scalar potential $H^{\text{SM}} = H^{\text{NSM}} = H^{\text{S}} = 0$, and the second value coincides with the VEV of H^{S} at the physical minimum $v_S = \mu/\lambda$. The third field value marks a new special location in H^{S} space, which, in the following, we refer to as

$$v_S' \equiv -\left(\frac{\mu}{\lambda}+\frac{A_\kappa}{2\kappa}\right)\,. \tag{3.75}$$

Recall that since we used the minimization conditions, Equation (3.43), to replace the m_i^2 parameters in the scalar potential with v, $\tan\beta$, and μ, the physical minimum $\left\{H^{\text{SM}}, H^{\text{NSM}}, H^{\text{S}}\right\} = \sqrt{2}\,\{v, 0, \mu/\lambda\}$ is also guaranteed to be a stationary point of the scalar potential.

Hence, in the alignment limit, all first-order derivatives of $V_0^{\text{eff},3}$ vanish at

$$\left\{H^{\text{SM}}, H^{\text{NSM}}, H^{\text{S}}\right\} = \{0,0,0\} \vee \left\{0,0,\sqrt{2}v_S'\right\} \vee \left\{0,0,\frac{\sqrt{2}\mu}{\lambda}\right\} \vee \left\{\sqrt{2}v,0,\frac{\sqrt{2}\mu}{\lambda}\right\} \ . \quad (3.76)$$

The potential $V_0^{\text{eff},3}$ may have additional stationary points; we will return to the possibility of such minima below.

In order to constrain the allowed parameter space, we consider the value of the potential at the field values given in Equation (3.76) and demand the physical minimum to be the global minimum. As we will see, the $|\mu|$ vs. v_S'/v_S plane is a useful projection of the parameter space. In the alignment limit, the potential at the physical minimum takes the value

$$V_0^{\text{eff},3}(\sqrt{2}v,0,\frac{\sqrt{2}\mu}{\lambda}) = -\frac{m_Z^2 c_{2\beta}^2 + \lambda^2 v^2 s_{2\beta}^2 + 2\Delta\lambda_2 v^2 s_\beta^4}{4} v^2 - \frac{\kappa^2\mu^3}{\lambda^3}\left(\frac{\mu}{\lambda} + \frac{A_\kappa}{3\kappa}\right) \quad (3.77)$$

$$= -\frac{1}{4}m_{h_{125}}^2 v^2 - \frac{1}{3}\frac{\kappa^2\mu^4}{\lambda^4}\left(1 - 2\frac{v_S'}{v_S}\right) \ , \quad (3.78)$$

where we used Equation (3.66) and Equation (3.75) for the second equality.

We can derive a first constraint on the parameter space by demanding the physical minimum to be deeper than the trivial minimum. The scalar potential vanishes at the trivial minimum, $V_0^{\text{eff},3}(0,0,0) = 0$. Thus, in the alignment limit, demanding $V_0^{\text{eff},3}(\sqrt{2}v,0,\sqrt{2}\mu\lambda) < V_0^{\text{eff},3}(0,0,0)$ yields the condition

$$\frac{v_S'}{v_S} < \frac{1}{2}\left(1 + \frac{3}{4}\frac{\lambda^4}{\kappa^2}\frac{m_{h_{125}}^2 v^2}{\mu^4}\right) \ . \quad (3.79)$$

At $\left\{H^{\text{SM}}, H^{\text{NSM}}, H^{\text{S}}\right\} = \left\{0,0,\sqrt{2}\mu/\lambda\right\}$ the potential takes the value

$$V_0^{\text{eff},3}(0,0,\frac{\sqrt{2}\mu}{\lambda}) = -\frac{\kappa^2\mu^3}{\lambda^3}\left(\frac{\mu}{\lambda} + \frac{A_\kappa}{3\kappa}\right) = -\frac{1}{3}\frac{\kappa^2\mu^4}{\lambda^4}\left(1 - 2\frac{v_S'}{v_S}\right) \ . \quad (3.80)$$

Comparing with Equation (3.78), we see that this stationary point of the potential is never deeper than the physical minimum; $\left\{H^{\rm SM}, H^{\rm NSM}, H^{\rm S}\right\} = \left\{0, 0, \sqrt{2}\mu/\lambda\right\}$ is a saddle point of the scalar potential in the alignment limit.

On the other hand, at $\left\{H^{\rm SM}, H^{\rm NSM}, H^{\rm S}\right\} = \left\{0, 0, \sqrt{2}v'_S\right\}$, the scalar potential (in the alignment limit) takes the value

$$V_0^{\rm eff,3}(0, 0, \sqrt{2}v'_S) = -\frac{\kappa^2}{3}\left(\frac{\mu}{\lambda} + \frac{A_\kappa}{2\kappa}\right)^3\left(\frac{3\mu}{\lambda} + \frac{A_\kappa}{2\kappa}\right) = \frac{1}{3}\frac{\kappa^2\mu^4}{\lambda^4}\left(\frac{v'_S}{v_S}\right)^3\left(2 - \frac{v'_S}{v_S}\right) \ . \quad (3.81)$$

Demanding this minimum to be shallower than the physical minimum, $V_0^{\rm eff,3}(0, 0, \sqrt{2}v'_S) > V_0^{\rm eff,3}(\sqrt{2}v, 0, \frac{\sqrt{2}\mu}{\lambda})$, yields the condition

$$\left(\frac{v'_S}{v_S} - 1\right)^3\left(\frac{v'_S}{v_S} + 1\right) < \frac{3}{4}\frac{\lambda^4}{\kappa^2}\frac{m_{h_{125}}^2 v^2}{\mu^4} \ , \quad (3.82)$$

defining a range of v'_S/v_S for which the physical minimum is deeper than the minimum at $\left\{H^{\rm SM}, H^{\rm NSM}, H^{\rm S}\right\} = \left\{0, 0, \sqrt{2}v'_S\right\}$.

As we noted above, the potential may feature additional stationary points beyond those listed in Equation (3.76). In particular, minima deeper than the physical minimum can easily appear in the NMSSM for field configurations where $H^{\rm NSM}$ and $H^{\rm SM}$ take non-zero VEVs. Such minima break the electroweak symmetry, and, unless $\langle H^{\rm NSM}\rangle = 0$ and $\langle H^{\rm SM}\rangle = \sqrt{2}v$, do not lead to electroweak physics compatible with observations. In general, $V_0^{\rm eff,3}$ does not have stationary points in the $H^{\rm NSM}$-only direction, $V_0^{\rm eff,3}(0, H^{\rm NSM}, 0)$, except for the trivial point $H^{\rm SM} = H^{\rm NSM} = H^{\rm S} = 0$. Instead, both $H^{\rm NSM}$ and $H^{\rm SM}$ (and sometimes $H^{\rm S}$) take non-vanishing values at these additional electroweak symmetry breaking minima. Such field configurations are very challenging to identify analytically, thus, we resort to numerical techniques to infer the constraints on the NMSSM parameter space arising from demanding

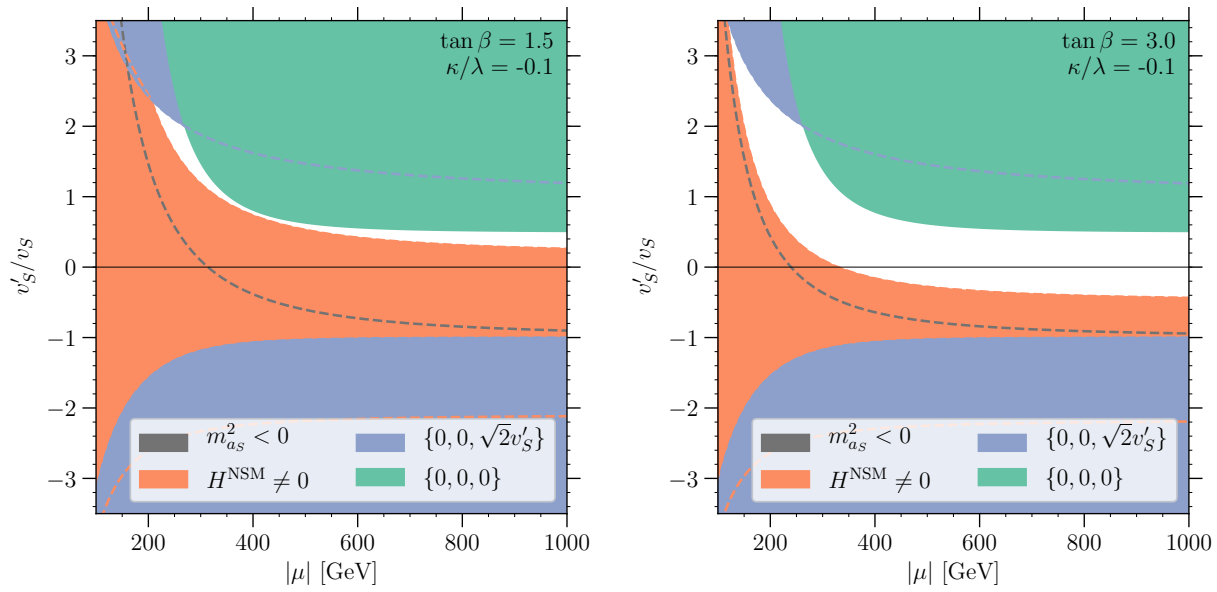

Figure 3.9: The white region indicates the region of NMSSM parameter space where (in the alignment limit) the physical minimum $\left\{H^{\rm SM}, H^{\rm NSM}, H^{\rm S}\right\} = \sqrt{2}\left\{v, 0, v'_S\right\}$ is the global minimum of the potential. In the gray region labeled as $m^2_{a_S} < 0$, the singlet-like CP-odd state becomes tachyonic, see Equation (3.83). In the orange region labeled as $H^{\rm NSM} \neq 0$, there exist minima with $H^{\rm NSM} \neq 0$ that are deeper than the physical minimum (they are only found numerically). In the blue region labeled $\left\{0, 0, \sqrt{2}v'_S\right\}$, there exists a minimum at $\left\{H^{\rm SM}, H^{\rm NSM}, H^{\rm S}\right\} = \left\{0, 0, \sqrt{2}v'_S\right\}$ deeper than the physical minimum, see Equation (3.82). Similarly, in the green region labeled $\{0, 0, 0\}$, the trivial minimum is deeper than the physical minimum, see Equation (3.79). The regions are shaded on top of each other in the order described in this caption; the dashed lines of the respective colors mark the edges of the respective regions where overlapping. In the figures, we chose $\tan\beta = 1.5$ ($\tan\beta = 3$) for the left (right) panel, and $\kappa/\lambda = -0.1$ for both panels.

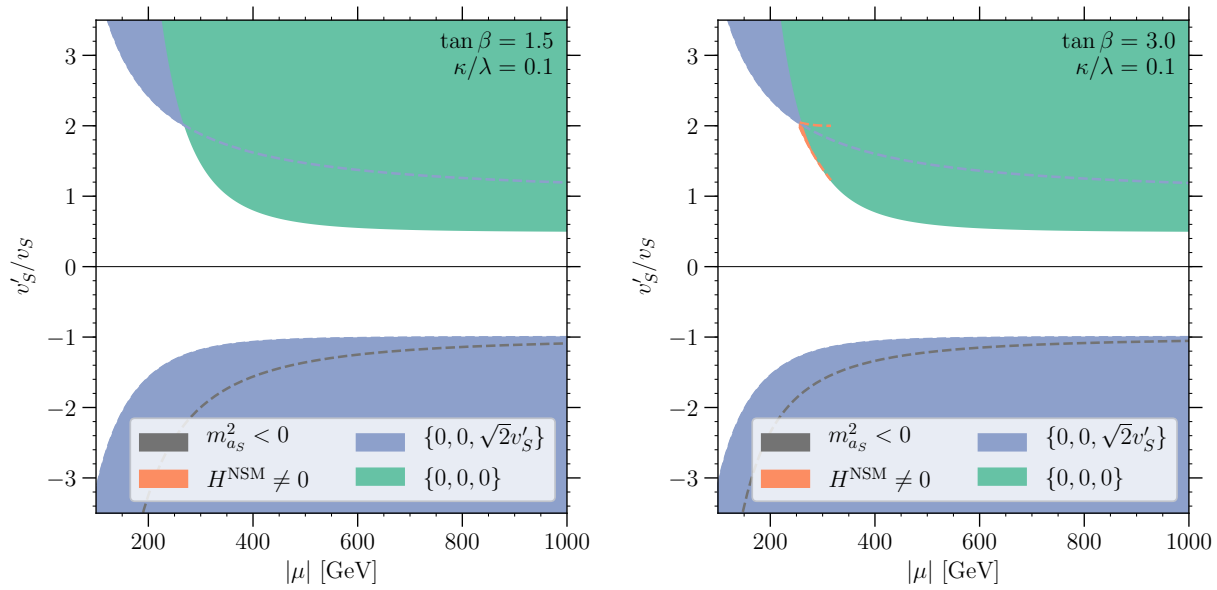

Figure 3.10: Same as Figure 3.9 but for $\kappa/\lambda = 0.1$.

the physical minimum to be deeper than any minima where $H^{\rm NSM} \neq 0$.[13]

Finally, the parameter space of the NMSSM is also constrained by avoiding tachyonic masses. As discussed in subsection 3.3.1, the most relevant constraint arises from avoiding the singlet-like neutral CP-odd state, a_S, becoming tachyonic. In terms of v'_S/v_S, the constraint arising from Equation (3.62) can be rewritten as

$$\frac{v'_S}{v_S} + 1 \gtrsim -\frac{3}{4}\frac{\lambda^2 v^2}{\mu^2}\sin(2\beta)\left[\frac{\lambda}{\kappa} - \frac{\sin(2\beta)}{2}\right] . \tag{3.83}$$

Figure 3.9–Figure 3.11 show the allowed region of parameter space in the $|\mu|$ vs. v'_S/v_S plane for values of $\tan\beta = \{1.5, 3\}$ and $\kappa/\lambda = \{-0.1, 0.1, 0.3\}$. The different shaded regions are excluded by the constraints from Equation (3.79) (green shade), Equation (3.82) (blue shade), and numerical results (orange shade). Correspondingly, these constraints come from avoiding the trivial minimum, the minimum at $\left\{H^{\rm SM}, H^{\rm NSM}, H^{\rm S}\right\} = \{0, 0, \sqrt{2}v'_S\}$, or minima with $H^{\rm NSM} \neq 0$, becoming deeper than the physical minimum. We also show

13. We use the package `HOM4PS2` [233] to solve the system of first derivatives of $V_0^{\rm eff,3}(H^{\rm SM}, H^{\rm NSM}, H^{\rm S})$ to identify the stationary points, and then check numerically if the global minimum is the physical minimum.

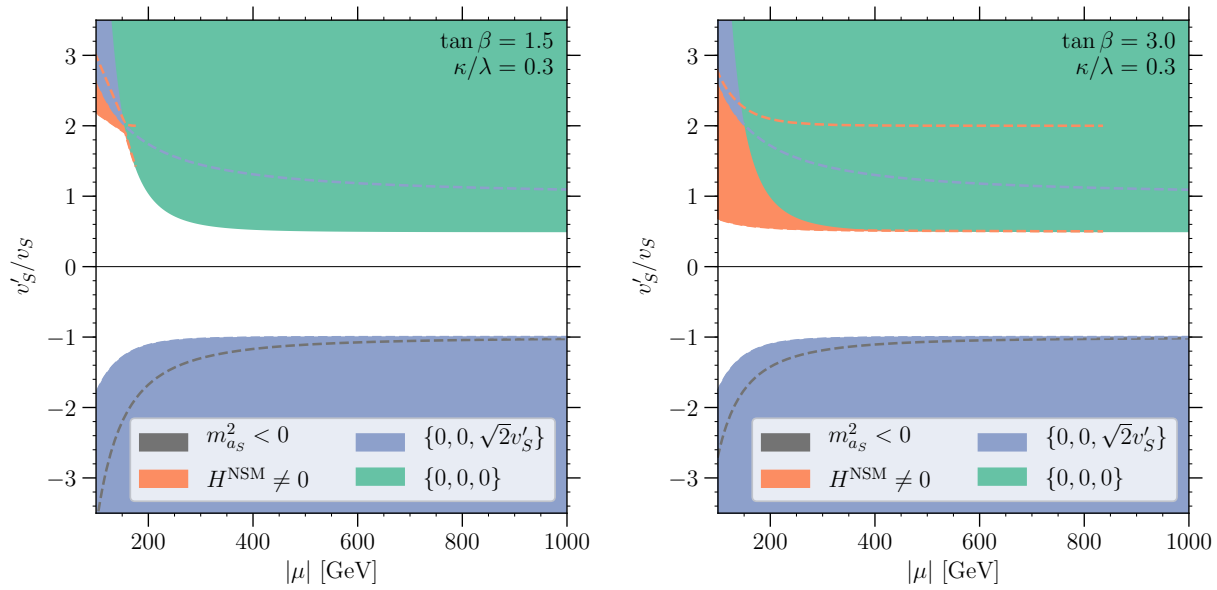

Figure 3.11: Same as Figure 3.9 but for $\kappa/\lambda = 0.3$.

the region where the singlet-like CP-odd mass eigenstate a_S becomes tachyonic, Equation (3.83), with the gray shade. Note that overlapping regions are marked by dashed lines of the corresponding colors. In all figures, we truncate the x-axis at $|\mu| = 100\,\text{GeV}$; smaller values of $|\mu|$ are disfavored by null results of chargino searches at LEP. Since we imposed alignment (without decoupling), the scalar potential is uniquely specified by v'_S/v_S (see Equation (3.75)), μ, $\tan\beta$, and κ/λ, and the potential is insensitive to the sign of μ. As we can see from Equation (3.79) and Equation (3.82) (the green and blue shaded regions, respectively), the conditions stemming from the trivial minimum and the minimum at $\left\{H^{\text{SM}}, H^{\text{NSM}}, H^{\text{S}}\right\} = \left\{0, 0, \sqrt{2}v'_S\right\}$ becoming deeper than the physical minimum do not depend on the sign of κ and are relatively insensitive to the value of $|\kappa|$.

For large values of $\left|\kappa\mu^2\right|$, Equation (3.79) implies that the physical minimum is deeper than the trivial minimum for $v'_S/v_S < 1/2$. Equation Equation (3.82) on the other hand implies, for large $\left|\kappa\mu^2\right|$, that $v'_S/v_S > -1$ to avoid the minimum at $\left\{H^{\text{SM}}, H^{\text{NSM}}, H^{\text{S}}\right\} = \left\{0, 0, \sqrt{2}v'_S\right\}$ becoming deeper than the physical minimum. These constraints relax for smaller values of $\left|\kappa\mu^2\right|$, i.e. where the term proportional to $m^2_{h_{125}}v^2$ in Equation (3.78)

becomes relevant. As can also be seen from Equation (3.79) and Equation (3.82), the range of v'_S/v_S opens up for $\left|\kappa\mu^2\right| \lesssim \lambda^2 m_{h_{125}} v$. With $\lambda \sim 0.65$ in the alignment limit, we find $\sqrt{\lambda m_{h_{125}} v} \sim 120\,\text{GeV}$. In Figure 3.9–Figure 3.11 we can observe the corresponding change in the blue and green shaded bounds for $|\mu| \lesssim 120\,\text{GeV}/\sqrt{|\kappa/\lambda|}$.

Finally, as discussed above, the region of parameter space where minima with $H^{\text{NSM}} \neq 0$ are deeper than the physical minimum can only be inferred by numerically investigating the vacuum structure. From Figure 3.9–Figure 3.11 we see that such constraints become more stringent with larger $|\kappa|$ and depend on the value of $\tan\beta$. Furthermore, the constraints arising from avoiding such minima are sensitive to the sign of κ; for $\kappa < 0$, avoiding minima with $H^{\text{NSM}} \neq 0$ effectively sets a lower limit on the value of v'_S/v_S, while for $\kappa > 0$, avoiding these minima sets an upper bound on the value of v'_S/v_S.

3.3.3 Thermal history: analytical understanding

In this section, we explore the possible phase transition patterns in the NMSSM. We first discuss the effective potential at very high temperatures, which gives guidance on the starting point of the thermal evolution. Then, we discuss the requirements a phase transition must satisfy to provide favorable conditions for electroweak baryogenesis via a SFOEWPT. We continue by discussing specific phase transition patterns which appear in the NMSSM, and fix a shorthand notation we will use to identify them. We close this section by discussing the regions in parameter space where we expect to observe different transition patterns, in particular, the regions in which we expect the nucleation probabilities of first order phase transitions to be sufficiently large for such transitions to complete.

Let us start with the vacuum structure at very high temperatures. In the limit $T^2 \gg \widehat{m}_i^2$, and neglecting the Daisy coefficients, the finite temperature potential can be written as

$$V_{1-\text{loop}}^{T\neq 0} \xrightarrow[T^2 \gg \widehat{m}_i^2]{} T^4 \left[\ldots\right] + \frac{T^2}{48}\left(2\sum_{i=B} n_i \widehat{m}_i^2 + \sum_{i=F} n_i \widehat{m}_i^2\right) + T^4 \times \mathcal{O}\left(\left|\frac{\widehat{m}_i^2}{T^2}\right|^{3/2}\right) \quad . \quad (3.84)$$

The ellipsis [...] in Equation (3.84) indicates terms which are independent of the field values. It is straightforward to see that in this limit, the field-dependent terms of the thermal potential are parameterized by the Daisy coefficients, (see Equation (3.B.34))

$$V_{1-\text{loop}}^{T\neq 0} \to \left[\frac{c_{H^{\text{SM}}H^{\text{SM}}}}{2}\left(H^{\text{SM}}\right)^2 + c_{H^{\text{SM}}H^{\text{NSM}}}H^{\text{SM}}H^{\text{NSM}} + \frac{c_{H^{\text{NSM}}H^{\text{NSM}}}}{2}\left(H^{\text{NSM}}\right)^2 + \frac{c_{H^{\text{S}}H^{\text{S}}}}{2}\left(H^{\text{S}}\right)^2\right]T^2 + \dots \tag{3.85}$$

where the ellipsis now includes both the field-independent and higher-order terms. Explicit expressions for the c_{ij} can be found in appendix 3.B.3. Note that the symmetries of the NMSSM enforce this particular form of the high-temperature potential. In particular, the $\mathbb{Z}_3$ symmetry (and gauge symmetry) ensures that terms linear in the fields (such as $\mu_i H^i T^2$, where μ_i is a coefficient of dimension mass) cancel, while gauge symmetry forbids terms mixing one doublet with one singlet state, i.e. $H^{\text{SM}}H^{\text{S}}T^2$ and $H^{\text{NSM}}H^{\text{S}}T^2$.

Since all coefficients c_{ij} are positive, and $c_{H^{\text{SM}}H^{\text{SM}}}c_{H^{\text{NSM}}H^{\text{NSM}}} > c^2_{H^{\text{SM}}H^{\text{NSM}}}$ throughout the parameter space, the trivial minimum $\left\{H^{\text{SM}}, H^{\text{NSM}}, H^{\text{S}}\right\} = \{0,0,0\}$ is guaranteed to be the global minimum of the effective potential at very high temperatures. Thus, any phase transition patterns in the NMSSM will begin in the trivial phase. In order to give rise to acceptable phenomenology, the (chain of) phase transition(s) must end in the physical minimum, $\left\{H^{\text{SM}}, H^{\text{NSM}}, H^{\text{S}}\right\} = \sqrt{2}\{v, 0, v_S\}$. If the transition pattern involves multiple steps, the most relevant property of the intermediate phase(s) for electroweak baryogenesis is if the electroweak symmetry is broken, i.e. if H^{SM} or H^{NSM} acquires a non-trivial VEV, or if, instead, $H^{\text{SM}} = H^{\text{NSM}} = 0$ and the electroweak symmetry is conserved in the intermediate phase(s).

A phase transition must satisfy certain requirements in order to give rise to favorable conditions for electroweak baryogenesis: In order for a baryon asymmetry to be produced in the transition, and such asymmetry not to be subsequently washed out in the low tem-

perature phase, electroweak sphalerons must be active in the high-temperature phase and suppressed in the low temperature phase. Estimating the rate of the sphaleron suppression is a notorious problem in the perturbative approach to the phase transition calculation, see, for example, refs. [34, 127, 128], and even more so if the electroweak symmetry is broken in multiple steps, see, for example, ref. [234].

We shall demand

$$\left(\frac{\sqrt{\left\langle H_{lT}^{\mathrm{SM}}\right\rangle^2+\left\langle H_{lT}^{\mathrm{NSM}}\right\rangle^2}}{T}>1\right) \quad \wedge \quad \left(\frac{\sqrt{\left\langle H_{hT}^{\mathrm{SM}}\right\rangle^2+\left\langle H_{hT}^{\mathrm{NSM}}\right\rangle^2}}{T}<0.5\right), \tag{3.86}$$

as conditions for a SFOEWPT. Here, $\langle\Phi_{hT}\rangle$ ($\langle\Phi_{lT}\rangle$) is the value of Φ in the high (low) temperature phase at the temperature T where the phase transition occurs. The first condition ensures that electroweak sphalerons are inactive in the low-temperature phase, while the second condition requires the sphalerons to not be unduly suppressed in the high temperature phase. We stress that while the numerical thresholds for the order parameters we chose in Equation (3.86) are indicative for the possibility of generating the baryon asymmetry through a SFOEWPT [127], obtaining the exact conditions would require a gauge-invariant evaluation of the sphaleron profile through the bubble wall which is beyond the scope of this work.

In the remainder of this section, we use a shorthand notation to classify the phase transition patterns we observe in the NMSSM:

- We use an integer $(1, 2, \ldots)$ to denote the number of steps in the transition patterns.
- For 2-step transitions (we don't observe transition patterns with more than 2 steps in our data) we use a roman number to classify the intermediate phase:
  - "(I)" denotes an intermediate phase in the singlet-only direction, i.e. where $\left\langle H^{\mathrm{SM}}\right\rangle = \left\langle H^{\mathrm{NSM}}\right\rangle = 0$ and electroweak symmetry is conserved,

  - "(II)" denotes an intermediate phase in which electroweak symmetry is broken, i.e. where at least one of the fields H^{NSM} or H^{SM} acquires non-trivial VEV.

- We use a lower case letter to denote the strength of any transitions in which electroweak symmetry is broken in the low-temperature phase,
  - "a" denotes a SFOEWPT,
  - "b" denotes a first order phase transition that is not a SFOEWPT, i.e does not satisfy one (or both) of the conditions in Equation (3.86),
  - "c" denotes a second order phase transition.

Thus, for example, "1-a" denotes a direct one-step SFOEWPT from the trivial phase to the electroweak phase. "2(I)-b" denotes a two-step transition pattern, where the first step is from the trivial phase to a singlet-only phase (since electroweak symmetry is not broken in this intermediate phase, we do not differentiate the pattern with respect to the strength of this first transition), and the second step is a first order (but not SFOEWPT) transition from the singlet-only to the electroweak phase. "2(II)-ca" on the other hand denotes a two-step phase transition pattern, where the first transition is a second order phase transition into a phase in which electroweak symmetry is broken (but which is distinct from the electroweak phase), and the second transition is a SFOEWPT from this intermediate phase to the electroweak phase.

We can get some intuition about the different regions of parameter space suitable for the respective phase transition patterns from the shape of the effective potential. While thermal effects alter the shape of the potential at finite temperatures, the zero-temperature vacuum structure still indicates the relative importance of the different possible local minima for the thermal history. Thus, we expect the results from subsection 3.3.2 to be indicative for the transition patterns suggested by the critical temperature calculation. For example, we can expect direct one-step transition patterns to most prominently be realized in the parameter

region close to where the trivial minimum becomes the global minimum at zero temperature (green shade in Figure 3.9–Figure 3.11). Similarly, we can expect "2(I)" transition patterns to appear in the parameter regions adjacent to where $\left\{H^{\mathrm{SM}}, H^{\mathrm{NSM}}, H^{\mathrm{S}}\right\} = \left\{0, 0, \sqrt{2}v'_S\right\}$ becomes the global minimum at zero temperature (blue shade), and "2(II)" transitions are expected to appear in regions close to those where the global minimum has non-trivial VEV of $H^{\mathrm{NSM}} \neq 0$ (orange shade).

The vacuum structure gives however little information about the tunneling probability from one local minimum to another, i.e. if a first order phase transition suggested by the critical temperature calculation can actually nucleate. The tunneling rate is controlled by the height of the barrier and the distance (in field space) between the respective local minima. The higher the barrier, and the larger the distance between the minima, the lower the nucleation probability. Although the shape of the potential is modified by thermal effects, we can learn some lessons from the zero-temperature potential. As discussed above, the trivial minimum is the global minimum of the effective potential at very high temperatures. Thus, any phase transition pattern starts at $H^{\mathrm{SM}} = H^{\mathrm{NSM}} = H^{\mathrm{S}} = 0$. The distance between the trivial and the physical minimum (at zero temperature) is given by $\sqrt{2v^2 + 2\mu^2/\lambda^2}$. Since the values of $v = 174\,\mathrm{GeV}$ and $\lambda \sim 0.65$ are fixed by electroweak precision data and the alignment conditions, respectively, the distance between the trivial and the physical minimum is controlled by $|\mu|$. The distance increases with the value of $|\mu|$, hence, nucleation proceeds more easily for small $|\mu|$.

The height of the barrier around the trivial minimum can be inferred from the squared mass parameters of the fields H^{SM}, H^{NSM}, and H^{S} around the trivial point, i.e. the field-dependent masses given in appendix 3.B.1 at $H^{\mathrm{SM}} = H^{\mathrm{NSM}} = H^{\mathrm{S}} = 0$. In order for a phase transition to occur, the smallest of the eigenvalues of the squared mass matrix should be approximately zero, implying a flat direction around the trivial point at zero temperature. If the smallest eigenvalue is too large, the barrier around the trivial minimum is large, and

hence the tunneling rate will be too small to allow for successful nucleation. If the smallest squared mass eigenvalue is negative, the trivial minimum is a saddle point of the potential (at zero temperature). Finite temperature effects can still give rise to a barrier between the trivial and the physical minimum required for a SFOEWPT in this situation, but only if the absolute value of the smallest squared mass parameter is not too large, such that thermal effects can overcome the zero-temperature shape of the potential.

At the trivial point $H^{\mathrm{SM}} = H^{\mathrm{NSM}} = H^{\mathrm{S}} = 0$, the matrix of the squared mass parameters is diagonal in the basis $\{H_d, H_u, S\}$, see Equation (3.41). Thus, we can directly infer the presence and height of the barrier around the trivial point from the parameters $m^2_{H_d}$, $m^2_{H_u}$, and m^2_S. In the alignment limit, $m^2_{H_u} - m^2_{H_d} = M_A^2 \cos(2\beta)$. Note that $\cos(2\beta) < 0$ for $\tan\beta > 1$ and hence, $m^2_{H_u}$ is the smaller of the doublet-like eigenvalues. In the alignment limit,

$$m^2_{H_u} = M_A^2 \cos^2\beta - \mu^2 - \frac{m^2_{h_{125}}}{2} \approx \frac{\mu^2}{\tan^2\beta}\left(1 - \frac{\kappa}{\lambda}\tan\beta\right) - \frac{m^2_{h_{125}}}{2} \,. \tag{3.87}$$

This equation yields a critical value of $|\mu|$, for which $m^2_{H_u} \approx 0$. This critical value of $|\mu|$ is increasing with larger values of $\tan\beta$ and of κ/λ. For example, for $\tan\beta = 1.5$ and $\kappa/\lambda = -0.1$, the critical value is $|\mu| \approx 125\,\mathrm{GeV}$, while for the larger value $\kappa/\lambda = 0.3$ Equation (3.87) implies $m^2_{H_u} \approx 0$ for $|\mu| \approx 180\,\mathrm{GeV}$. Instead, for a larger value of $\tan\beta = 3$ and $\kappa/\lambda = -0.1$, the critical value is $|\mu| \approx 235\,\mathrm{GeV}$. For values of $|\mu|$ larger than the critical value, we expect large barriers around the trivial minimum in the H_u direction, while for smaller values of $|\mu|$, $m^2_{H_u}$ becomes negative and the trivial point becomes a saddle point at zero temperature.

A flat direction can also arise in the H^{S} direction. The squared mass parameter of H^{S} at $H^{\mathrm{SM}} = H^{\mathrm{NSM}} = H^{\mathrm{S}} = 0$, see Equation (3.73), is

$$m^2_S = 2\frac{\kappa^2}{\lambda^2}\mu^2\frac{v'_S}{v_S} \,. \tag{3.88}$$

The alignment conditions enforce sizable values of $\lambda \sim 0.65$, thus, the value of m_S^2 is controlled by $\kappa^2\mu^2(v'_S/v_S)$. Since the temperature corrections to m_S^2, eq. (3.B.39), are of order $0.2\,T^2$, one would expect that at the characteristic temperature of the EWPT of order 100 GeV, the tunneling rate could only be large enough for successful nucleation if the squared mass parameter controlling the barrier $m_S^2 \ll (100\,\text{GeV})^2$. This condition can be achieved in two ways: either, $|v'_S/v_S| \ll 1$, or $|\kappa\mu| \ll 100\,\text{GeV}$.

Note that the conditions $m_{H_u}^2 \approx 0$ or $m_S^2 \approx 0$ are indicative for the possibility of a first order phase transition to successfully nucleate at finite temperature since they imply the presence of an approximately flat direction around the trivial minimum at zero temperature. However, this analysis does not predict the transition pattern, which is determined by the shape of the potential away from the trivial minimum (at the transition temperature). The bounce solution of the fields (the trajectory in field space connecting the local minima) is, in general, not a straight line in field space; in particular, $m_S^2 \approx 0$ does not necessarily lead to "2(I)" transition patters, and $m_{H_u}^2 \approx 0$ does not directly imply "2(II)" patterns.

3.3.4 Numerical results

In order to explore the EWPT in the NMSSM, and, in particular, find which regions of parameter space give rise to phase transition patterns suitable for electroweak baryogenesis, we perform an extensive numerical study using `CosmoTransitions_v2.0.5` [66]. As discussed in subsection 3.3.1, in the alignment limit, the Higgs sector of the NMSSM can be described by the four parameters $\left\{\tan\beta, \kappa/\lambda, \mu, v'_S/v_S\right\}$, and we perform random scans in this parameter space. We show the results of our numerical scans in Figure 3.12–Figure 3.18. In this section, we started with discussing the regions of the parameter space where points satisfy the boundary conditions we implement in our `CosmoTransitions` calculation, followed by discussing the phase transition patterns suggested by the critical temperature calculation and we compare these results with the thermal histories obtained by calculating the nucleation

rate. As we shall see, the phase transition patterns obtained from the nucleation calculation differ substantially from those indicated by the critical temperature calculation, and thus, computing only the critical temperatures provides a misleading picture of the regions of parameter space favorable for electroweak baryogenesis. Lastly in this section, we comment on the collider and dark matter phenomenology in the region of parameter space promising for baryogenesis via a SFOEWPT.

We focus our study on the region of parameter space where alignment without decoupling is realized, i.e. the region of parameter space for which the NMSSM features a Higgs mass eigenstate which (at tree-level) couples to SM particles like the SM Higgs boson. As discussed in subsection 3.3.1, the alignment conditions fix the values of λ and M_A^2 (or, equivalently, A_λ), leaving $\{\tan\beta, \mu, \kappa, A_\kappa\}$ as the four free parameters which control the effective potential. We fix the mass and mixing parameters of the stop sector (parameterized by the threshold correction $\Delta\lambda_2$ in V_0^{eff}, see section 3.3.1) to obtain $m_{h_{125}} \simeq 125\,\text{GeV}$ for the mass of the SM-like Higgs boson. As discussed in subsection 3.3.2, we use v_S'/v_S to re-parameterize A_κ. Here, $v_S = \mu/\lambda$ is the VEV of the CP-even singlet interaction state at the physical minimum, $\left\langle H^{\text{S}} \right\rangle = \sqrt{2}\mu/\lambda$, and $v_S' = -(\mu/\lambda + A_\kappa/2\kappa)$ is the location of an extremum of V_0^{eff} in the singlet-only direction, $\left\{H^{\text{SM}}, H^{\text{NSM}}, H^{\text{S}}\right\} = \left\{0, 0, \sqrt{2}v_S'\right\}$. In summary, we use

$$\tan\beta\,, \quad \mu\,, \quad \frac{\kappa}{\lambda}\,, \quad \frac{v_S'}{v_S}\,, \tag{3.89}$$

as input parameters for our numerical evaluation. Note that throughout our calculations, we fix the bino and wino mass parameters, which enter the radiative corrections from the charginos and neutralinos (see Equation (3.B.23) and Equation (3.B.24)), to $M_1 = M_2 = 1\,\text{TeV}$.

The $|\mu|$ vs. v_S'/v_S plane lends itself particularly well to characterizing the vacuum structure of the NMSSM as discussed in subsection 3.3.2. We perform two-dimensional scans over slices of the parameter spaces for fixed values of $\tan\beta$ and κ/λ, varying the values of μ

and v'_S/v_S by means of (linear-)flat distributions. While we have included counterterms to maintain the location of the physical minimum after including the CW potential (including $\left\langle H^{\rm S}\right\rangle = \sqrt{2}v_S = \sqrt{2}\mu/\lambda$), we have not included a counterterm which would similarly keep the location of the tree-level extremum at $\left\{H^{\rm SM}, H^{\rm NSM}, H^{\rm S}\right\} = \left\{0, 0, \sqrt{2}v'_S\right\}$ fixed. As a result, the location of the corresponding minimum of the effective potential after including $V^{\rm CW}_{1-{\rm loop}}$ is no longer $\left\{H^{\rm SM}, H^{\rm NSM}, H^{\rm S}\right\} = \left\{0, 0, \sqrt{2}v'_S\right\}$, but changes to a new location we denote by $\left\{H^{\rm SM}, H^{\rm NSM}, H^{\rm S}\right\} = \left\{0, 0, \sqrt{2}v'_{S,{\rm CW}}\right\}$. We find the value of $v'_{S,{\rm CW}}$ by numerically solving

$$\left.\frac{\partial V_1(T=0)}{\partial H^{\rm S}}\right|_{\substack{H^{\rm SM}=0\\ H^{\rm NSM}=0}} = 0\,. \tag{3.90}$$

This equation yields three solutions: $H^{\rm S} = 0$ and two non-trivial solutions. Of these two non-trivial solutions, we identify the one further away (in $H^{\rm S}$ space) from $v_S = \mu/\lambda$ as $v'_{S,{\rm CW}}$. We plot our numerical results in the $|\mu|$ vs. $v'_{S,{\rm CW}}/v_S$ plane.

For each randomly drawn parameter point, we first demand a number of *boundary conditions*:

- We check compatibility with the phenomenology of the observed SM-like 125 GeV Higgs boson by checking that (after including the radiative corrections and the counterterms discussed in section 3.3.1) the parameter point features a CP-even Higgs mass eigenstate with mass $122 < m_{h_{125}}/{\rm GeV} < 128$, and admixtures of the non-SM-like interactions states less than $\left|C^{\rm NSM}_{h_{125}}\right| \tan\beta < 0.05$ and $\left|C^{\rm S}_{h_{125}}\right| < 0.1$,[14] where the C^j_i denote the mixing angles in the extended Higgs basis,

$$h_{125} = C^{\rm SM}_{h_{125}} H^{\rm SM} + C^{\rm NSM}_{h_{125}} H^{\rm NSM} + C^{\rm S}_{h_{125}} H^{\rm S}\,. \tag{3.91}$$

14. Admixtures of $H^{\rm NSM}$ and $H^{\rm S}$ of this size modify the production cross sections and branching ratios of h_{125} by $\lesssim 10\,\%$ compared to the SM prediction. The currently best-measured production cross section of the observed Higgs boson is via the gluon-fusion mode with a 1σ uncertainty of $\sim 15\,\%$ [150, 221]. Similarly, the largest branching ratios of the observed Higgs bosons are measured with $\sim 15\,\%$ uncertainty [150, 221].

Note that since we fix λ and M_A^2 via the alignment conditions, Equation (3.57) and Equation (3.58), and include a counterterm to preserve the H^{SM}–H^{S} alignment after including the CW corrections, see Equation (3.68), most of our parameter points have admixtures of H^{NSM} and H^{S} to h_{125} much smaller than these thresholds. The exception are points where the mass parameters of the interaction eigenstates H^{SM} and H^{S} are approximately degenerate; in this case, relatively small off-diagonal entries in the CP-even squared mass matrix can still lead to sizable mixing of H^{SM} and H^{S}.

- In order to ensure compatibility with the null-results from chargino searches at the Large Electron Positron collider (LEP) (see, for example, refs. [235, 236]) we exclude the parameter region $|\mu| < 100\,\mathrm{GeV}$. Recall that the alignment conditions lead to a mass scale of the doublet-like Higgs bosons of $|M_A| \sim 2\,|\mu| \,/\, \sin(2\beta)$. Thus, such values of $|\mu|$ allow for doublet-like Higgs bosons as light as $|M_A| \sim 200\,\mathrm{GeV}$ if $\tan\beta \simeq 1$, which potentially are in conflict with null results from direct searches for non-SM-like Higgs bosons at the LHC. We will return to this issue in section 3.3.4. Note that searches for neutralinos and charginos at the LHC do not constrain the parameter space for $|\mu| \gtrsim 100\,\mathrm{GeV}$ in a relevant way, see, for example, ref. [237].

- We check that, at zero temperature, the physical minimum is the global minimum of the effective potential.[15]

For each point satisfying all boundary conditions, we compute the phase transition pattern with `CosmoTransitions` as discussed above.

Figure 3.12–Figure 3.17, to be discussed in detail in section 3.3.4 and section 3.3.4, show the results from our parameter scans for $\tan\beta = \{1.5, 3\}$ and $\kappa/\lambda = \{-0.1, 0.1, 0.3\}$ in the $|\mu|$ vs. $v'_{S,\mathrm{CW}}/v_S$ plane; these are the same slices of parameter space for which we have

15. Thus, in this study we exclude the region of parameter space where the physical minimum is a metastable vacuum (with sufficiently long lifetimes to allow for feasible cosmology). While interesting in its own right, considering this scenario is beyond the scope of this work.

shown constraints from the zero-temperature vacuum structure of the effective tree-level potential, V_0^{eff}, in Figure 3.9–Figure 3.11. In order to compare the results of the respective calculations, we color-code the points according to the transition patterns indicated by the critical temperature calculations in the left panels of Figure 3.12–Figure 3.17, while in the right panels, points are color-coded according to the thermal history obtained from the full nucleation calculation; see subsection 3.3.3 for our shorthand notation of the phase transition patterns. Points violating the boundary conditions described above are labeled "failed BC" in Figure 3.12–Figure 3.17. Points which satisfy all boundary conditions, but for which `CosmoTransitions` fails to return a phase transition pattern starting from the trivial minima at high temperature and ending in the physical minimum at zero temperature are labeled "no transitions". Note that the left and right panels show the same set of points in parameter space, the only difference is the color-coding of the points.

Boundary conditions

Let us begin the discussion of the results of our parameter scans with the regions of parameter space where points fail to satisfy the boundary conditions. The boundary conditions are independent of the thermal calculation, hence, the same points are labeled "failed BC" in the left and right panels of Figure 3.12–Figure 3.17.

We observe that, for large values of $|\mu|$, the range of $v'_{S,\text{CW}}/v_S$ where points satisfy the boundary conditions is $-1 \lesssim v'_{S,\text{CW}}/v_S \lesssim 0.5$. This range is only weakly dependent on the values of $\tan\beta$ and κ/λ; only in the case of $\kappa/\lambda = -0.1$, shown in Figure 3.12 and Figure 3.13, we observe a different lower bound on $v'_{S,\text{CW}}/v_S$ at large $|\mu|$, being $v'_{S,\text{CW}}/v_S \gtrsim -0.5$ for $\tan\beta = 1.5$ and $v'_{S,\text{CW}}/v_S \gtrsim -0.8$ for $\tan\beta = 3$. The range of $v'_{S,\text{CW}}/v_S$ where points satisfy the boundary conditions widens at small values of $|\mu|$, and here, the behavior depends more strongly on the values of κ/λ and $\tan\beta$, as we can see by comparing the different slices of parameter space shown in Figure 3.12–Figure 3.17. We note that the boundary conditions

widen for values of $|\mu| \lesssim 120\,\text{GeV}/\sqrt{|\kappa/\lambda|}$. Furthermore, we observe that for $\kappa/\lambda = -0.1$ and $\tan\beta = 1.5$ (Figure 3.12), points fail the boundary conditions for $|\mu| \lesssim 150\,\text{GeV}$ regardless of the value of $v'_{S,\text{CW}}/v_S$, while we do not observe such a lower bound on the value of $|\mu|$ for the other slices of parameter space.

This behavior can largely be understood from the discussion of the zero-temperature vacuum structure in subsection 3.3.2, see also Figure 3.9–Figure 3.11. The analysis of the vacuum structure in subsection 3.3.2 was based on V_0^{eff}, the potential of our effective model after integrating out all sfermions and the gluinos, but prior to including the CW corrections. We indicate the region of parameter space for which, per the analysis in subsection 3.3.2, the physical minimum is the global minimum of V_0^{eff} at zero temperature with the thin black contours in Figure 3.12–Figure 3.17. Since these contours are derived from V_0^{eff}, the y-axis for these contours is v'_S/v_S, where $v'_S = -(\mu/\lambda + A_\kappa/2\kappa)$ is the tree-level value. We see that, although these contours are derived from V_0^{eff}, they describe well many of the features of the boundary conditions seen in our parameter scan, which incorporates radiative corrections. The largest deviations appear for $\kappa/\lambda = -0.1$, see Figure 3.12 and Figure 3.13. While the contours here allow only a narrow range of v'_S/v_S values, we see that the points from our parameter scan satisfy the boundary conditions for a much wider range of values of $v'_{S,\text{CW}}/v_S$ than what the contours suggest. Comparing with Figure 3.9, we see that this discrepancy occurs in regions of parameter space where the analysis of V_0^{eff} suggested that a minimum with $\langle H^{\text{NSM}}\rangle \neq 0$ was the global minimum of the potential (indicated by the orange shade in Figure 3.9). This constraint was derived numerically in subsection 3.3.2, and hence is challenging to understand quantitatively. However, it is not surprising that the region of parameter space disfavored by vacua with $\langle H^{\text{NSM}}\rangle \neq 0$ becoming the global minimum of the potential changes considerably after including the CW corrections: the potential is subject to larger radiative corrections in the doublet-like directions of the effective potential than in the singlet-like direction, and furthermore, the H^{NSM} direction is affected

by the counterterms we have included to maintain the location of the physical minimum, $\left\{H^{\mathrm{SM}}, H^{\mathrm{NSM}}, H^{\mathrm{S}}\right\} = \sqrt{2}\,\{v, 0, \mu/\lambda\}$.

Before moving to the discussion of the phase transition patterns we observe for points satisfying the boundary conditions in section 3.3.4, let us briefly mention a few features visible in Figure 3.12–Figure 3.17. First, we can see a gap in the points around $v'_{S,\mathrm{CW}}/v_S \approx 1$, which widens for small values of $|\mu|$. This gap is due to numerical difficulties in our algorithm to find $v'_{S,\mathrm{CW}}$ if $v'_{S,\mathrm{CW}} \approx v_S$. Identifying the value of $v'_{S,\mathrm{CW}}$ is particularly challenging for small $|\mu|$, because $|\mu|$ controls the size of $v_S = \mu/\lambda$.

Second, an arc of points failing the boundary conditions crosses the region of parameter space consistent with the physical vacuum being the global minimum at zero temperature, starting at small values of $|\mu|$ and negative $v'_{S,\mathrm{CW}}/v_S$ and ending at larger values of $|\mu|$ and positive $v'_{S,\mathrm{CW}}/v_S$. This feature is particularly pronounced for $\tan\beta = 1.5$, and is due to the mass parameters of the interaction states H^{SM} and H^{S} becoming approximately degenerate for those points. As discussed below Equation (3.91), in this situation, even small deviations from the alignment conditions lead to a sizable H^{S} component of h_{125}, and thus, these points are forbidden by our requirement $\left|C^{\mathrm{S}}_{h_{125}}\right| < 0.1$.

Neither of these issues is related to the thermal history of a given parameter point, and these issues do not occur in regions of parameter space which are of special interest for the phase transition calculation. Hence, we ignore them in the following.

We also note that in the left panels of Figure 3.12–Figure 3.17, where we show the results of the critical temperature calculation, points labeled "no transition" appear. As discussed in subsection 3.3.3, the trivial minimum is guaranteed to be the global minimum of the potential at high temperatures, and for any point passing the boundary conditions, the physical minimum is the global minimum at zero temperature. For points labeled "no transition", `CosmoTransitions` failed to return a transition pattern starting in the trivial minimum at high temperatures and ending in the physical minimum at zero temperatures. This is due

to numerical errors arising in the second step of the numerical calculation described above, i.e. the step in which `CosmoTransitions` attempts to trace the local minima of the effective potential with changing temperatures. We have investigated these numerical issues, and have not found any indication that they bias our results towards particular regions of parameter space. Thus, we expect that our scanning over a large number of points throughout the parameter space gives an accurate picture of the regions of parameter space suitable for electroweak baryogenesis.

Comparison of critical temperature and nucleation results

In this section, we compare the phase transition patterns obtained from the nucleation calculation with the ones suggested by the analysis of the temperature-dependent vacuum structure at the critical temperatures. In Figure 3.12–Figure 3.17, the color-coding of the points in the left panels shows the phase transition patterns suggested by the critical temperature calculation. In the right panels of Figure 3.12–Figure 3.17, we color-code the points according to the thermal histories obtained from the nucleation calculation. Comparing the left and right panels, we see that the thermal histories obtained from the nucleation calculation differ significantly from those the critical temperature analysis suggests, leading to a marked shift in the regions of parameter space which allows for a SFOEWPT.

Let us begin by discussing the results for $\tan\beta = 1.5$ and $\kappa/\lambda = -0.1$, shown in Figure 3.12. For the critical temperature results, shown in the left panel, we observe that one-step SFOEWPT patterns ("1-a", dark green points) occur at the upper range of the values of $v'_{S,\mathrm{CW}}/v_S$ allowed by the boundary conditions, and that the range of $v'_{S,\mathrm{CW}}/v_S$ for which we find such "1-a" transition patterns becomes wider for smaller values of $|\mu|$. For smaller values of $v'_{S,\mathrm{CW}}/v_S$ and larger values of $|\mu|$, we find two-step transition patterns where the intermediate phase is in the singlet-only direction ("2(I)", blue points). However, except for a few "2(I)-a" points at values of $\mu \simeq 250$–$300\,\mathrm{GeV}$ and small values of

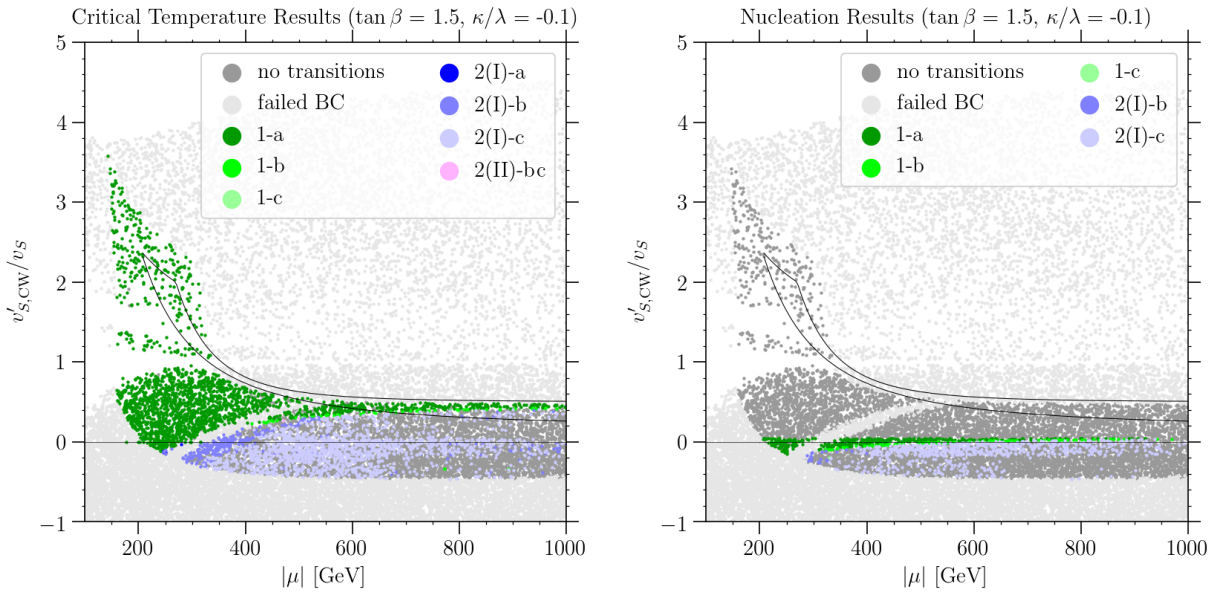

Figure 3.12: Results from our parameter scans in the $|\mu|$ vs. $v'_{S,\mathrm{CW}}/v_S$ plane for the same slice of parameter space as shown in the left panel of Figure 3.9: $\tan\beta = 1.5$ and $\kappa/\lambda = -0.1$. The left panel shows points categorized according to the phase transition patterns suggested by the critical temperature calculation. In the right panel, points are instead categorized by the thermal histories obtained from the nucleation calculation. For points labeled "no transition", `CosmoTransitions` did not return a transition chain starting in the trivial minimum at high temperatures and ending in the physical minimum at zero temperature, and points labeled "failed BC" do not satisfy our boundary conditions defined in the text. The solid lines enclose the region of parameter space for which we find feasible zero-temperature vacuum structure in subsection 3.3.2. These bounds are obtained from tree-level relations, hence, for these bounds, the y-axis is v'_S/v_S, where $v'_S = -(\mu/\lambda + A_\kappa/2\kappa)$ is the location of an extremum of V_0^{eff} in the singlet-only direction.

$\left|v'_{S,\mathrm{CW}}/v_S\right|$, the EWPT for these points is weakly first order ("2(I)-b") or a second order transition ("2(I)-c") as indicated by the lighter blue shades of the points.

Qualitatively, the patterns suggested by the critical temperature calculation can mostly be understood from the discussion of the zero-temperature vacuum structure in subsection 3.3.2. The left panel of Figure 3.9 shows the different constraints on the zero-temperature vacuum structure (at tree level) for the same slice of parameter space as Figure 3.12. At large values of v'_S/v_S, the trivial minimum is deeper than the physical minimum, indicated by the green shade in Figure 3.9. Thus, towards large $v'_{S,\mathrm{CW}}/v_S$, we expect the trivial

minimum to play a large role in the thermal history, and accordingly, we find one-step transitions from the trivial to the physical minimum in this region of parameter space in the left panel of Figure 3.12. Similarly, for small values of v'_S/v_S, the minimum in the singlet-only direction is deeper than the physical minimum (blue shaded region in Figure 3.9), hence, the singlet-only phase plays a larger role in the thermal history, explaining the appearance of "2(I)" transition patterns for smaller values of $v'_{S,\mathrm{CW}}/v_S$.

Focusing now on the results of the nucleation calculation, we should recall that electroweak baryogenesis requires a SFOEWPT, i.e. one of the phase transition patterns labeled with an "a" in our shorthand notation. The only such patterns we observe for $\tan\beta = 1.5$ and $\kappa/\lambda = -0.1$ in the right panel of Figure 3.12 are direct one-step transitions ("1-a", dark green points), that occur for a narrow range of values $v'_{S,\mathrm{CW}}/v_S \sim 0$. At small values of $|\mu|$, the range of values of $v'_{S,\mathrm{CW}}/v_S$ for which we find SFOEWPTs widens slightly, before being truncated by the boundary conditions. For values of $v'_{S,\mathrm{CW}}/v_S$ just below the "1-a" patterns, we find one-step transitions from the trivial to the physical minimum which are not strong first order ("1-b" and "1-c", lighter green colors). For even smaller values of $v'_{S,\mathrm{CW}}/v_S$, we find two-step transitions where the intermediate phase is in the singlet-only direction and where the second transition step, in which electroweak symmetry is broken, is weakly first order or second order ("2(I)-b" or "2(I)-c", light blue points). Note that outside of these bands in $v'_{S,\mathrm{CW}}/v_S$, we do not find points for which the nucleation calculation indicates thermal histories ending in the physical minimum. This should be contrasted with the phase transition patterns suggested by the critical temperature calculation, where we observe "1-a" patterns at much larger values of $v'_{S,\mathrm{CW}}/v_S$. The nucleation calculation points to a very different region of parameter space for SFOEWPTs than the critical temperature calculation, except for a small overlap of the "1-a"-regions at $\left|v'_{S,\mathrm{CW}}/v_S\right| \ll 1$ and the smallest values of $|\mu|$ allowed by the boundary conditions.

The reason for the mismatch between the critical temperature and nucleation results

was discussed in subsection 3.3.3: While the behavior of the critical temperatures can be understood from the zero-temperature vacuum structure, the nucleation probability is controlled by the height of the barrier separating the local minima, and the distance in field space between the local minima. For all parameter points, the thermal evolution starts in the trivial minimum at high temperatures. For large values of v'_S/v_S, the barriers around the trivial minimum are large, making the tunneling probability prohibitively small. Hence, for larger values of v'_S/v_S, the fields are "stuck" at $H^{\mathrm{SM}} = H^{\mathrm{NSM}} = H^{\mathrm{S}} = 0$, even if at zero temperature the trivial minimum is no longer the global minimum of the potential as required by the boundary conditions. For $v'_S/v_S \to 0$, the zero-temperature effective potential becomes flat in the singlet direction around the trivial point, and for $v'_S/v_S < 0$ the trivial point turns into a saddle point of the potential, see Equation (3.88). For small values of $\left|v'_S/v_S\right|$, thermal effects can still give rise to a barrier around the trivial minimum at finite temperatures, while for large negative values of v'_S/v_S, thermal effects can no longer overcome the zero-temperature shape of the potential to give rise to the barrier required for a SFOEWPT. This behavior of the barrier explains why the nucleation calculation singles out the region around $v'_{S,\mathrm{CW}}/v_S = 0$ for a SFOEWPT in the right panel of Figure 3.12.

For $\tan\beta = 3$, shown in Figure 3.13, we find similar results as for $\tan\beta = 1.5$. Beginning with the critical temperature results (left panel), the main difference is that for the larger values of $\tan\beta$, we observe that two-step transition patterns ("2(II)", orange and magenta points) appear at small values of $|\mu|$. This is somewhat difficult to understand from the analysis in subsection 3.3.2. The constraints coming from local minima in the doublet-like directions (orange shade in Figure 3.9) are the only vacuum structure constraints depending on the value of $\tan\beta$. However, as mentioned in section 3.3.4, the doublet-like directions are subject to large radiative corrections, explaining the mismatch between the region where "2(II)" patterns appear in our numerical results and the orange shaded region of the tree-level vacuum structure analysis in Figure 3.9. The appearance of the "2(II)" patterns can however

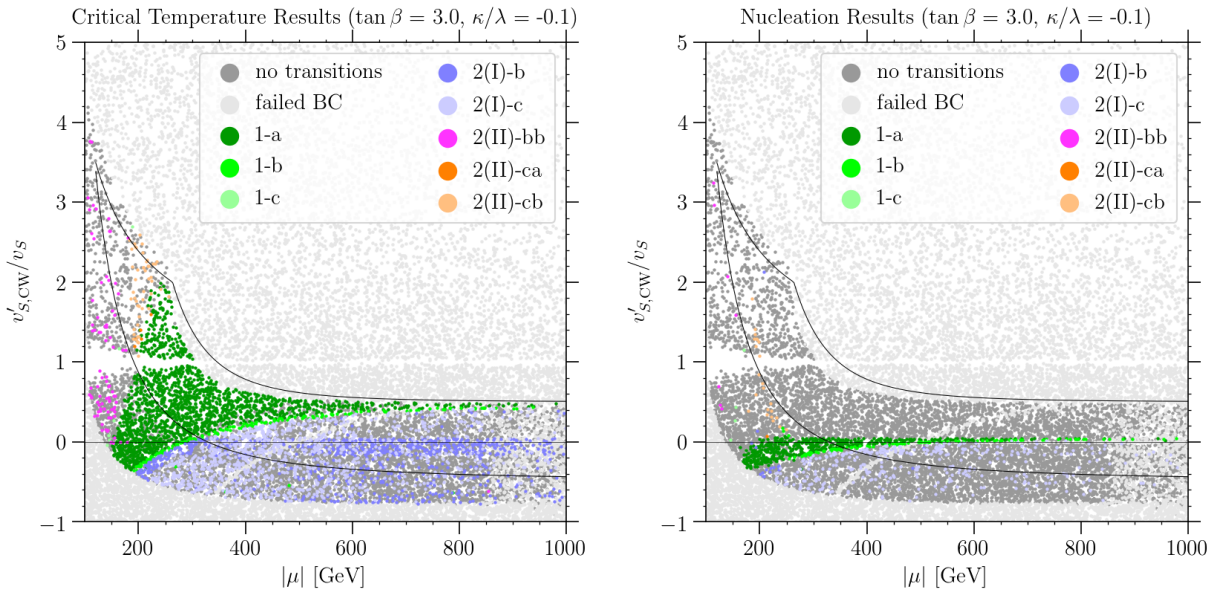

Figure 3.13: Same as Figure 3.12, but for $\tan\beta = 3$ and $\kappa/\lambda = -0.1$

be understood from the region of parameter space for which $m^2_{H_u} < 0$, Equation (3.87). In subsection 3.3.3, this condition was discussed in the context of the zero-temperature barrier in the H_u-direction disappearing for $m^2_{H_u} \lesssim 0$, leading to large tunneling rates at finite temperature. To understand the critical temperature results, it is more relevant to note that for $m^2_{H_u} < 0$, the trivial point $H^{\mathrm{SM}} = H^{\mathrm{NSM}} = H^{\mathrm{S}} = 0$ becomes a saddle point in the H_u-direction, suggesting that a local minimum should appear in the doublet-like direction. For $\tan\beta = 3$ and $\kappa/\lambda = -0.1$, at tree-level, $m^2_{H_u} \lesssim 0$ for $|\mu| \lesssim 230\,\mathrm{GeV}$, explaining the appearance of "2(II)" patterns in the small-$|\mu|$ region of the left panel of Figure 3.13. For $\tan\beta = 1.5$ and $\kappa/\lambda = -0.1$, shown in Figure 3.12, instead, $m^2_{H_u} \lesssim 0$ for $|\mu| \lesssim 125\,\mathrm{GeV}$. Such small values of $|\mu|$ are forbidden by the boundary conditions, and thus, we do not see "2(II)" patterns appear in Figure 3.12.

Comparing the nucleation calculation results for $\kappa/\lambda = -0.1$ and $\tan\beta = 1.5$ with those for $\tan\beta = 3$, shown in the right panel of Figure 3.12 and Figure 3.13, respectively, we see that the preferred region of parameter space for a SFOEWPT is almost independent of the value of $\tan\beta$. The main difference is that for $\tan\beta = 3$, points with smaller values

of $|\mu|$ satisfy the boundary conditions, leading to the band of points around $v'_{S,\mathrm{CW}}/v_S = 0$ for which we find SFOEWPTs ("1-a", dark green points) extending to lower values of $|\mu|$ than for $\tan\beta = 1.5$. For $\tan\beta = 3$, we also see the emergence of two-step transition patterns, where electroweak symmetry is broken in the intermediate phase, ("2(II)", orange and magenta points) for positive values of $v'_{S,\mathrm{CW}}/v_S$ and small values of $|\mu|$. As discussed around Equation (3.87), for small values of $|\mu|$, the barrier around the trivial point in the H_u direction disappears. Note however that these points (except for one parameter point at $v'_{S,\mathrm{CW}}/v_S \sim 0$) do not feature a SFOEWPT step, but both steps are weakly first order or second order.

Let us now discuss the results for $\kappa/\lambda = 0.1$, shown in Figure 3.14 and Figure 3.15 for $\tan\beta = 1.5$ and $\tan\beta = 3$, respectively. Comparing the $\kappa/\lambda = -0.1$ critical temperature results (left panels) with those for $\kappa/\lambda = 0.1$, we find that many of the features remain the same. The two main differences are that the boundary conditions relax for small values of $|\mu|$, allowing a larger range of values for $v'_{S,\mathrm{CW}}/v_S$, and that for $\tan\beta = 3$, "2(II)" patterns appear even more prominently in the low $|\mu|$ region. The behavior of the boundary conditions is discussed in section 3.3.4, hence, we focus on the latter difference here. As for the $\kappa/\lambda = -0.1$ case, the appearance of "2(II)" patterns can be understood from the region of parameter space where $m^2_{H_u} < 0$. From Equation (3.87), we find that, for $\tan\beta = 3$ and $\kappa/\lambda = -0.1$, the mass parameter for H_u becomes tachyonic for $|\mu| \lesssim 230\,\mathrm{GeV}$, while for $\kappa/\lambda = 0.1$, this critical value increases to $|\mu| \lesssim 320\,\mathrm{GeV}$. Accordingly, we see that "2(II)" patterns appear for larger values of $|\mu|$ for $\tan\beta = 3$ and $\kappa/\lambda = 0.1$ (left panel of Figure 3.15) than for $\kappa/\lambda = -0.1$ (left panel of Figure 3.13).

Let us now concentrate on the nucleation results for $\kappa/\lambda = 0.1$. For $\tan\beta = 1.5$, see the right panel of Figure 3.14, we find SFOEWPTs in the same regions of parameter space as for $\kappa/\lambda = -0.1$ (Figure 3.12), with the exception of the $|\mu| \lesssim 150\,\mathrm{GeV}$ region, in which points failed the boundary conditions for $\kappa/\lambda = -0.1$. For $\kappa/\lambda = 0.1$, the boundary conditions

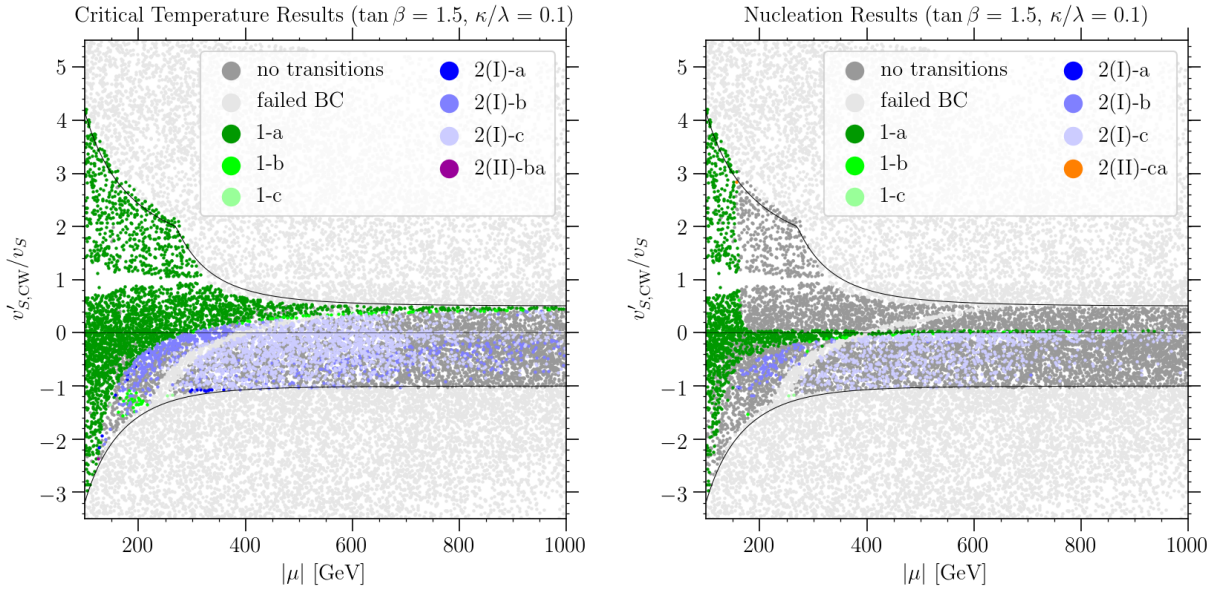

Figure 3.14: Same as Figure 3.12, but for $\tan\beta = 1.5$ and $\kappa/\lambda = 0.1$.

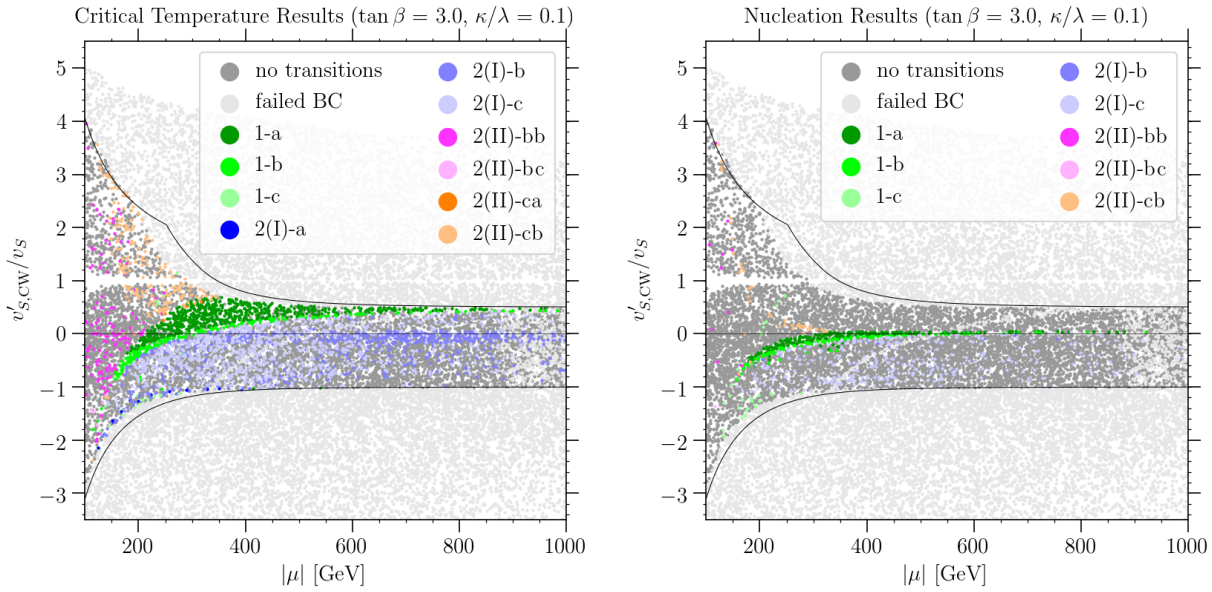

Figure 3.15: Same as Figure 3.12, but for $\tan\beta = 3.0$ and $\kappa/\lambda = 0.1$.

are satisfied in this region of parameter space, and we see that for these small values of $|\mu|$, one-step SFOEWPT patterns ("1-a", dark green points) appear for virtually the entire range of $v'_{S,\mathrm{CW}}/v_S$ allowed by the boundary conditions. As discussed above, for small values of $|\mu|$, the barrier in the H_u direction can become small. More important for the small $|\mu|$ region in this slice of the parameter space, the barrier in the singlet direction also becomes small for $|\kappa\mu| \ll 100\,\mathrm{GeV}$, since $m_S^2 \propto \kappa^2\mu^2(v'_S/v_S)$, see Equation (3.88), allowing for a SFOEWPT even if $v'_{S,\mathrm{CW}}/v_S$ takes values far from zero.

For $\tan\beta = 3$, we likewise find similar behavior for $\kappa/\lambda = 0.1$ (right panel of Figure 3.15) and for $\kappa/\lambda = -0.1$ (right panel of Figure 3.13). Here, the main difference is that for $\kappa/\lambda = 0.1$, two-step transition patterns where electroweak symmetry is broken in the intermediate phase ("2-II") play a larger role than for $\kappa/\lambda = -0.1$, restricting the values for which we find SFOEWPTs to a narrower band of values of $v'_{S,\mathrm{CW}}/v_S$. This can again be understood from the range of values for which H_u becomes tachyonic around the trivial point. Note that the presence of this tachyonic direction in the effective potential (at zero temperature) makes it more difficult to achieve transition patterns favorable for baryogenesis, which we see reflected in the absence of "1-a" transition patterns for $|\mu| \lesssim 200\,\mathrm{GeV}$ in the right panel of Figure 3.15.

Considering finally the critical temperature results for $\kappa/\lambda = 0.3$ (left panels of Figure 3.16 and Figure 3.17), we find that compared to the results for smaller values of κ/λ, two-step transition patterns play a much larger role. Comparing Equation (3.78) with Equation (3.81), we see that the depth of the singlet-like minimum is much more sensitive to the value of κ/λ than the depth of the physical minimum, and thus, the minimum in the singlet-only direction plays a larger role in the thermal history for larger values of κ/λ, leading to "2(I)" patterns (blue points) appearing more prominently for $\kappa/\lambda = 0.3$ than for $\kappa/\lambda = -0.1$ and 0.1. Likewise, we see "2(II)" patterns (orange and magenta points) appearing more prominently in the region of parameter space not ruled out by the boundary

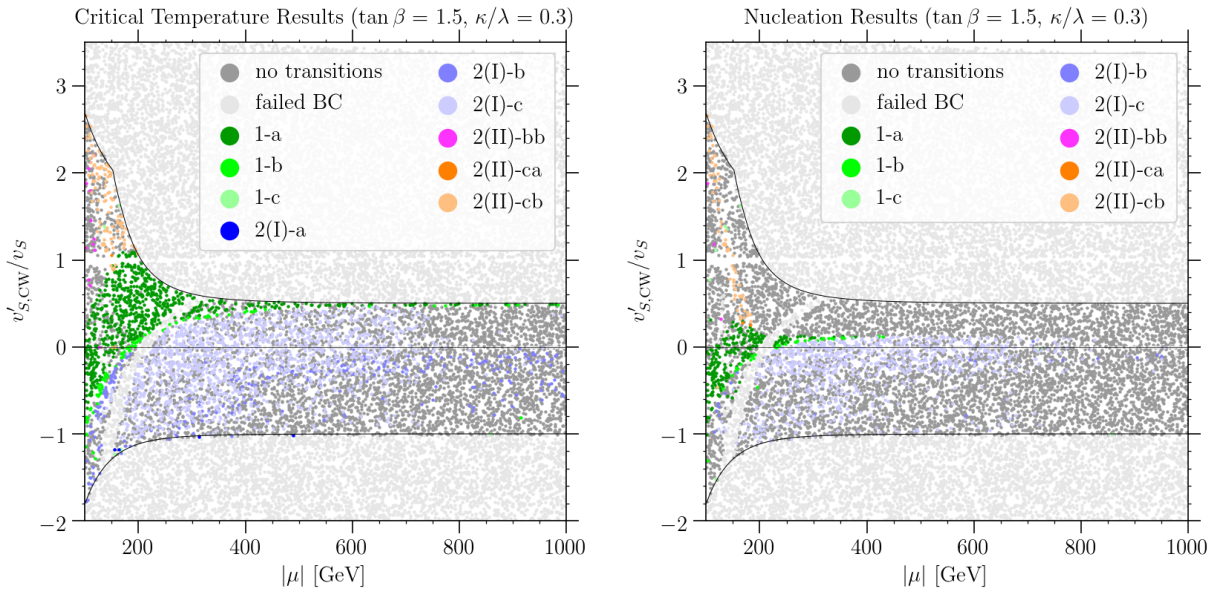

Figure 3.16: Same as Figure 3.12, but for $\tan\beta = 1.5$ and $\kappa/\lambda = 0.3$.

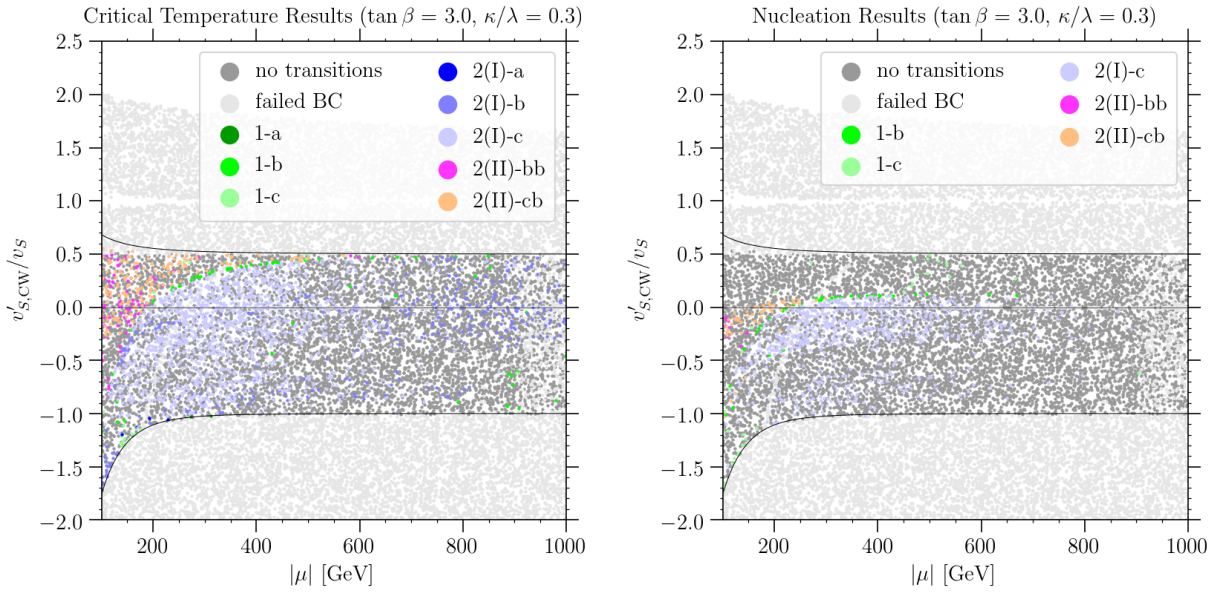

Figure 3.17: Same as Figure 3.12, but for $\tan\beta = 3.0$ and $\kappa/\lambda = 0.3$.

conditions. For $\tan\beta = 1.5$ and $\kappa/\lambda = 0.3$, we find from Equation (3.87) that $m_{H_u}^2 < 0$ (at zero temperature) for $|\mu| \lesssim 180\,\text{GeV}$, while for $\kappa/\lambda = 0.3$, the critical value is $|\mu| \lesssim 840\,\text{GeV}$.

Regarding the nucleation results, for $\tan\beta = 1.5$ and $\kappa/\lambda = 0.3$, shown in the right panel of Figure 3.16, we find SFOEWPTs for small values of $|\mu|$ and $\left|v'_{S,\text{CW}}/v_S\right|$. The scaling of the depths of the respective local minima with v'_S/v_S becomes faster the larger the value of $|\kappa/\lambda|$, making the change in phase transition behavior with the value of $v'_{S,\text{CW}}/v_S$ more rapid for this larger value of κ/λ than what we have observed for lower values of κ/λ. Thus, the range of $v'_{S,\text{CW}}/v_S$ leading to (one-step) SFOEWPTs is smaller for all values of $|\mu|$ than what we found for $\kappa/\lambda = \pm 0.1$. Furthermore, we observe that "2(II)" transition patterns appear for small values of $|\mu|$ due to the disappearance of the barrier in the H_u direction. This behavior is even more pronounced for $\tan\beta = 3$ and $\kappa/\lambda = 0.3$, see the right panel of Figure 3.17. In this slice of parameter space, $m_{H_u}^2 < 0$ (at zero temperature) for $|\mu| \lesssim 840\,\text{GeV}$, and we do not find any parameter points with a SFOEWPT.

We stress that for all slices of parameter space shown in Figure 3.12– Figure 3.17, the region providing favorable conditions for electroweak baryogenesis via a SFOEWPT differs markedly when the thermal history is inferred from the nucleation calculation instead of the simpler calculation of studying only the vacuum structure at the critical temperatures. While the critical temperature results can be explained from the zero-temperature vacuum structure, the regions of parameter space where SFOEWPTs actually nucleate can only be understood when considering the barriers of the effective potential. We find that SFOEWPTs can only nucleate if $\left|v'_{S,\text{CW}}/v_S\right| \ll 1$ and $|\kappa/\lambda|$ is not too large, leading to a small barrier in the singlet direction. If $|\kappa\mu|$ is significantly smaller than the weak scale, larger values of $v'_{S,\text{CW}}/v_S$ can still lead to a small barrier in the singlet direction and a successful SFOEWPT. For larger values of κ/λ and $\tan\beta$, the barrier in the H_u direction disappears in the small $|\mu|$ region, leading to multi-step phase transition patterns where electroweak symmetry is broken in the intermediate phase, and typically, no SFOEWPT is realized.

A collection of five benchmark points which exemplify the different types of phase transition behavior we observe in the different regions of the parameter space can be found in the original paper.

In Figure 3.18, we collect the results of our scans over the different slices of parameter space shown separately in Figure 3.12– Figure 3.17. As before, we classify points based on the thermal histories suggested by the critical temperature calculation in the left panels, while in the right panels, parameter points are color-coded according to the results of the nucleation calculation. In order to highlight the region of parameter space for which the respective calculations indicate a SFOEWPT, we show only the points falling in one of the transition patterns "1-a", "2(I)-a", "2(II)-aa", "2(II)-ab", "2(II)-ac", "2(II)-ba", or "2(II)-ca" in Figure 3.18. In the upper panels, we show results in the $|\mu|$ vs. $v'_{S,\mathrm{CW}}/v_S$ plane. Comparing the left and the right panels, it is evident that the critical temperature calculation gives a misleading picture of the parameter space favorable for electroweak baryogenesis. We note also that a one-step SFOEWPT ("1-a", green points) is by far the most generic possibility to realize a SFOEWPT in the NMSSM. While multi-step transitions including a SFOEWPT step can occur in the NMSSM, our results suggest that such transition patterns require very particular combinations of parameters, making them rare in a (random) parameter scan.

Collider and dark matter phenomenology

In this section we discuss the prospects for collider searches to cover the region of parameter space where we find SFOEWPTs and comment on the possibility of realizing a dark matter candidate in this parameter space.

In the lower panels of Figure 3.18, we show the points from our parameter scans for which we find a SFOEWPT in the plane of the masses of the two non-SM-like neutral CP-even Higgs bosons. Recall that we denote the state with the largest H^{S} component by h_S, and the state with the largest H^{NSM} component by H. Comparing the left and the right panels,

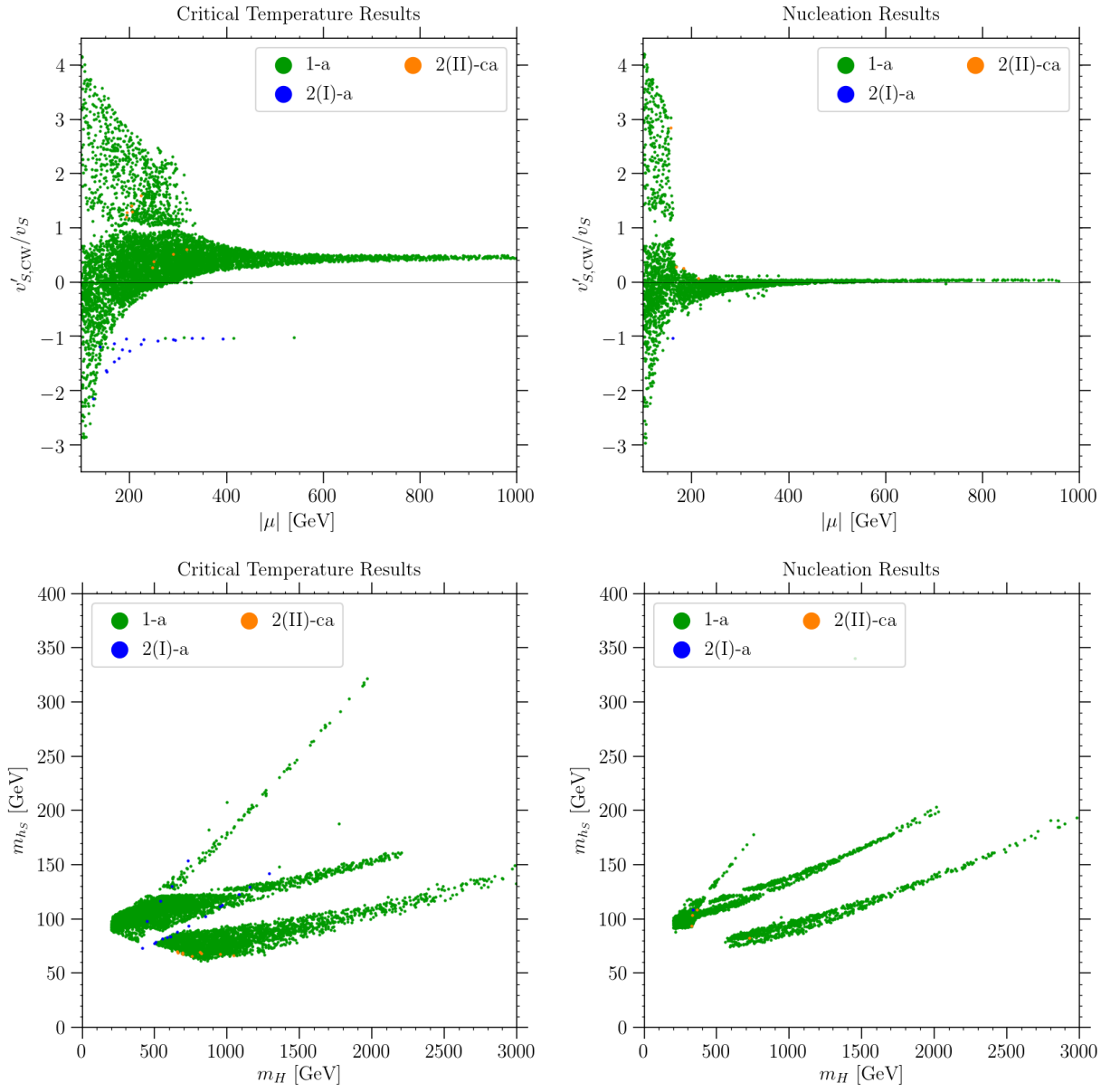

Figure 3.18: Points collected from our combined parameter scans ($\tan\beta = 1.5, 3$ and $\kappa/\lambda = -0.1, 0.1, 0.3$) for which the critical temperature calculation (left panels) or the nucleation calculation (right panels) indicates a SFOEWPT. In the upper panels, we plot the points in the same plane as in Figure 3.12–Figure 3.17, while in the lower panels we show parameter points in the plane of the masses of the non-SM-like CP-even Higgs mass eigenstates.

we observe that, similar to what we saw in the $|\mu|$ vs. $v'_{S,\mathrm{CW}}/v_S$ plane, the results based on the full nucleation calculation lead to a considerably tighter relation between m_H and m_{h_S} for points with SFOEWPTs than the results of the critical temperature calculation, as well as a significant shift of the preferred region of parameter space. As we have seen above, SFOEWPTs occur in the region of parameter space where $\left|v'_S/v_S\right| \ll 1$, or $|\kappa\mu| \ll 100\,\mathrm{GeV}$. In this limit, the mass of the singlet-like mass eigenstate (at tree-level and in the alignment limit), is approximately given by

$$m_{h_S}^2 \approx \sin^2(2\beta)\left\{\frac{\kappa^2}{\lambda^2}\frac{M_A^2}{2} + \lambda^2 v^2\left[1 - \frac{\kappa}{\lambda}\left(\frac{1+2\cos^2(2\beta)}{\sin(2\beta)}\right)\right]\right\}\,, \tag{3.92}$$

while the mass of the doublet-like mass eigenstate is approximately

$$m_H^2 \sim M_A^2 \sim 4\mu^2/\sin^2(2\beta)\,. \tag{3.93}$$

Due to the overall dependence $m_{h_S} \propto M_A \sin(2\beta)|\kappa/\lambda|$, the mass of h_S decreases with growing values of $\tan\beta$. Furthermore, m_{h_S} grows faster with m_H for larger $|\kappa/\lambda|$ values, and the dependence of m_{h_S} on the sign of κ/λ is small unless $|\kappa/\lambda|$ takes large values. These properties, together with the distribution of points in the $|\mu|$–$v'_{S,\mathrm{CW}}/v_S$ plane for the respective values of κ/λ and $\tan\beta$ shown in Figure 3.12–Figure 3.17, allow us to understand the relation between m_H and m_{h_S} visible in the lower right panel of Figure 3.18. For instance, points on the right, for which one obtains the largest values of M_H and the smallest values of m_{h_S} for a given M_H, correspond to $\tan\beta = 3$ and $\kappa/\lambda = \pm 0.1$. The points on the left, which correspond to $\tan\beta = 1.5$, separate in two branches. The branch with the lowest values of m_{h_S} corresponds to $\kappa/\lambda = \pm 0.1$, while the branch with the largest values of m_{h_S} correspond to $\kappa/\lambda = 0.3$.

While we leave a study of the collider phenomenology of the region of parameter space where we find a SFOEWPT for future work, we can make some broad statements. As we

have seen in section 3.3.4, see also Figure 3.12–Figure 3.18, SFOEWPTs can be realized in the NMSSM for small values of $|\kappa/\lambda|$ and $\tan\beta$, and not too large values of $|\mu|$, leading to relatively light non-SM-like Higgs bosons. From Equation (3.93) we find that the doublet-like state can be as light as $m_H \sim 200\,\text{GeV}$ for $\tan\beta = 1.5$ and $|\mu| \sim 100\,\text{GeV}$, as shown in the lower right panel of Figure 3.18. Similarly, the singlet-like state can be as light as $m_{h_S} \sim 70\,\text{GeV}$ for $\tan\beta = 3$, $\kappa/\lambda = 0.1$, and $|\mu| \sim 100\,\text{GeV}$. Despite the relatively small masses, this region of parameter space is challenging to probe at colliders: The direct production cross section of the singlet-like state is suppressed by its small doublet component, we find $\left|C_{h_S}^{\text{NSM}}\right| \lesssim 10\,\%$ for the points featuring a SFOEWPT. The doublet-like state H has sizable production cross sections. However, its decay patterns make it challenging to probe for the small values of $\tan\beta$ preferred by a SFOEWPT. Considering the decays into pairs of SM fermions, due to the small value of $\tan\beta$, the decay mode into top-quark pairs will dominate if kinematically accessible. Thus, for $m_H \gtrsim 350\,\text{GeV}$, the branching ratio into pairs of top quarks will be large and this final state is very challenging to probe at hadron colliders such as the LHC [238–245]. For $m_H \lesssim 350\,\text{GeV}$ on the other hand, the $H \to \tau^+\tau^-$ channel could provide some sensitivity. However, due to the preference for small values of $|\mu|$ and $|\kappa/\lambda|$, the Higgsinos and singlinos will be relatively light; their mass parameters are μ and $2\kappa\mu/\lambda$, respectively. Thus, decays of H into pairs of neutralinos will be kinematically allowed in the parameter region preferred by a SFOEWPT, and the associated branching ratios will be sizable, suppressing $H \to \tau^+\tau^-$ decays. The final states arising from decays of H into neutralinos are challenging to probe at the LHC, see, for example, refs. [237, 243, 246–249]. Out of the di-boson final states, decays of H into two SM(-like) states, e.g. $h_{125}h_{125}$, ZZ, and W^+W^- will be strongly suppressed due to alignment [192,250]. However, the branching ratios into final states containing at least one singlet-like boson, such as $h_{125}h_S$ or $a_S Z$, will be sizable if kinematically allowed [192,219,220,250–257], making these channels a promising means to explore the region of parameter space preferred for a SFOEWPT.

Considering the neutralino sector, we find that the region of parameter space where a SFOEWPT is realized features light singlinos. However, a singlino-like neutralino is only a good dark matter candidate if its spin-independent cross section is suppressed by the so-called blind-spot cancellations, see, for example, refs. [165, 167, 173]. For a singlino-like dark matter candidate, the blind-spot condition in the NMSSM is $2\kappa/\lambda \approx \sin 2\beta$, requiring larger values of κ/λ or $\tan\beta$ than those for which we find SFOEWPTs. On the other hand, the value of the bino mass parameter M_1 has practically no influence on the SFOEWPT[16]. Thus, the most promising dark matter scenario in the region of parameter space where we find SFOEWPTs is a bino-like lightest neutralino. The interaction cross sections of such a bino-like neutralino can be sufficiently small to be compatible with the null results from direct detection type experiments without requiring additional (blind-spot) cancellations [173, 258]. However, its couplings are too small to provide the correct dark matter relic density via standard thermal production. For $|M_1| \gtrsim m_t$, the correct relic density for a bino-like lightest neutralino can be achieved via co-annihilation with the singlino-like neutralino in the so-called new well-tempered scenario, where $|M_1| \sim |2\kappa\mu/\lambda|$ [173]. The bulk of the region of parameter space where we find SFOEWPTs features smaller values of $|\mu|$. There, the correct relic density for a bino-like lightest neutralino could be achieved via resonant annihilation through the singlet-like CP-even or CP-odd states, h_S or a_S, requiring the mass of the lightest neutralino χ_1 to satisfy $m_{\chi_1} \simeq m_{h_S}/2$ or $m_{\chi_1} \simeq m_{a_S}/2$, respectively. Alternatively, the NMSSM neutralinos may be unstable (on cosmological scales) and the dark matter may be provided by particles not included in the NMSSM, like axions and axinos (see, for example, ref. [259]).

16. In our calculation, M_1 enters only via the radiative corrections, see Equation (3.B.23). Any effect on the phase transition pattern of a given parameter point from changing the value of M_1 can be counteracted by, e.g., modifying the value of M_2.

3.3.5 Summary and conclusions of the section

Calculating the phase transitions in models of new physics is numerically expensive, and hence, most studies in the literature content themselves with studying the vacuum structure at the critical temperatures. At the critical temperature, the role of the global minimum of the potential passes from one local minimum to another, hence, this calculation ensures that a necessary condition for a first order phase transition is met. However, the critical temperature calculation does not ensure that the (quantum-mechanical) tunneling rate through the barrier separating the false from the true vacuum is large enough for such a first order phase transition to occur. In this section, we have investigated if a more complete calculation including the computation of the nucleation probability is necessary to understand the phase transition patterns in models of new physics. As an example model, we chose the Next-to-Minimal Supersymmetric extension of the Standard Model (NMSSM).

We focused our case study of the NMSSM on the region of parameter space where alignment-without-decoupling is realized. For the purposes of the phase transition, the remaining four-dimensional parameter space is well described by the set of parameters κ/λ, $\tan\beta$, $|\mu|$, and v_S'/v_S, where v_S' is the VEV of the singlet H^{S} at an extremum of the effective potential in the singlet-only direction, and v_S is the VEV of H^{S} at the physical minimum.[17]

Using extensive parameter scans, we have demonstrated that successful nucleation of a SFOEWPT occurs mostly in a narrow region of parameter space where $\left|v_S'/v_S\right|$ takes small values, and that the range of v_S'/v_S leading to a SFOEWPT becomes increasingly narrow for larger values of κ/λ, $\tan\beta$, and $|\mu|$. This region of parameter space differs markedly from what one would have inferred from the critical temperature calculation alone, that, in general, suggests a SFOEWPT for much larger values of v_S'/v_S. The difference between the two results can be understood from the shape of the effective potential. In the region of the

17. We will suppress the subscript "CW" which we use to differentiate between the VEV of the tree-level potential (v_S') and of the effective potential after including radiative corrections ($v_{S,\mathrm{CW}}'$) in the main text here. We refer the reader to subsection 3.3.4 for a more detailed discussion of our results.

parameter space suggested by the critical temperature calculation, the barriers around the trivial minimum, where the thermal evolution of the model begins at very high temperatures, are large, leading to prohibitively small tunneling rates. However, the barrier in the singlet direction diminishes for small values of $\left|v_S'/v_S\right|$, enabling tunneling from the trivial minimum. As we have shown, the requirement on the values for v_S'/v_S loosens for values of $|\kappa\mu|$ far below the weak scale. The dependence of the parameter region where we find a SFOEWPT on the value of $\tan\beta$ arises mainly from the disappearance of the barrier in the H_u-direction, triggering a phase transition which tends to lead to thermal histories incompatible with electroweak baryogenesis. The barrier in the H_u-direction disappears for small values of $|\mu|$, and the range of values of $|\mu|$ for which this occurs is broader for larger values of $\tan\beta$ and κ/λ.

Note that our findings are obtained in a perturbative expansion of the effective potential (to one loop, improved by relevant resummations), and, hence, may be affected by the well-known shortcomings associated with this expansion [75, 196, 260–268]. Nonetheless, our results stress the relevance of computing the nucleation probability to obtain the regions of parameter space promising for electroweak baryogenesis via a SFOEWPT. Our computations strongly rely on the accuracy of `CosmoTransitions`, thus, they would profit from corroboration with an independent calculation of the tunneling rate.

While we have focused on the phase transitions, the region of parameter space where a SFOEWPT occurs also leads to interesting collider and dark matter phenomenology. We find masses of the singlet-like state $70\,\text{GeV} \lesssim m_{h_S} \lesssim 200\,\text{GeV}$. The mass of the new doublet-like Higgs H, on the other hand, depends more strongly on $\tan\beta$. At moderate values of $\tan\beta$, we find $m_H \gtrsim 350\,\text{GeV}$, and hence, H decays prominently into pairs of top quarks. For smaller values of $\tan\beta \sim 1.5$, H can be lighter than the top pair production threshold. Although in principle this enhances the branching ratio into tau leptons, collider searches in conventional SM decay modes of these non-SM-like Higgs bosons are quite challenging due

to the presence of decays into light non-standard Higgs, neutralino, and chargino states. The most promising search channels seem to arise via the so-called Higgs cascade decays, e.g., $H \to h_{125} + h_S$. We reserve a more detailed study of the collider phenomenology for future investigation.

The preference for small values of κ/λ for a SFOEWPT implies the presence of a light singlino in the spectrum. While the spin-independent cross section of such a singlino is too large to be compatible with the null results from direct detection experiments in the region of parameter space where we find a SFOEWPT, a viable dark matter candidate could be realized via a bino-like lightest neutralino, if its annihilation cross section is enhanced through co-annihilation or resonant annihilation.

In closing, we would like to stress that arguably the most important result of this section is that the nucleation calculation yields qualitatively different results for the phase transition patterns in the NMSSM than what the simpler analysis based only on the vacuum structure at the critical temperatures suggests. While our numerical results are obtained in the NMSSM, we expect similar behavior to appear in other models where multiple scalar fields participate in the EWPT. Our results emphasize that, in order to infer the regions of parameter space where electroweak baryogenesis can be realized, it is critical to compute the thermal histories based on the nucleation probabilities.

3.A Appendices for the electroweak phase transition with spontaneous Z_2-breaking

3.A.1 Parameterization

There are five bare parameters in the tree-level potential, $\{\mu_h^2, \mu_s^2, \lambda_h, \lambda_s, \lambda_m\}$, that can be traded with five physical parameters $\{v_{\rm EW}, m_H, \tan\beta, m_S, \sin\theta\}$. The Higgs VEV $v_{\rm EW}$ and

the Higgs mass m_H are fixed by boundary conditions

$$v_{\rm EW} = 246 \text{ GeV}, \quad m_H = 125 \text{ GeV}, \tag{3.A.94}$$

whereas the remaining three parameters are the mass of the singlet-like eigenstate, the ratio of the singlet field VEV to the Higgs field VEV and the mixing between the mass eigenstates, respectively:

$$m_S, \quad \tan\beta(\equiv \frac{w_{\rm EW}}{v_{\rm EW}}), \quad \sin\theta. \tag{3.A.95}$$

The tree-level relations between these two sets of parameters are given by

$$\begin{aligned}
\mu_h^2 &= \frac{1}{4}\big(2m_H^2\cos^2\theta + 2m_S^2\sin^2\theta + (m_S^2 - m_H^2)\tan\beta\sin 2\theta\big), \\
\mu_s^2 &= -\frac{1}{4}\big(2m_H^2\sin^2\theta + 2m_S^2\cos^2\theta + (m_S^2 - m_H^2)\cot\beta\sin 2\theta\big), \\
\lambda_h &= \frac{m_H^2\cos^2\theta + m_S^2\sin^2\theta}{2v_{\rm EW}^2}, \\
\lambda_s &= \frac{m_H^2\sin^2\theta + m_S^2\cos^2\theta}{2\tan^2\beta v_{\rm EW}^2}, \\
\lambda_m &= \frac{(m_S^2 - m_H^2)\sin 2\theta}{2\tan\beta v_{\rm EW}^2}.
\end{aligned} \tag{3.A.96}$$

These tree-level relations provide a guidance for the understanding of the parametric dependence of the EWPT strength, although such relations are modified after considering the CW corrections.

3.A.2 Spontaneous Z_2-breaking: other phase transition patterns

Another type of phase transitions that could occur in the thermal history is

$$(0,0)\to(\tilde{v},0)\to(v,w)$$

$$(0,\tilde{w})\rightarrow(0,0)\rightarrow(\tilde{v},0)\rightarrow(v,w),$$

where the two scenarios differ from each other by the fact that the Z_2 symmetry is restored or non-restored at high temperatures. Otherwise, they share the same final path towards the electroweak physical vacuum. In both scenarios, the electroweak symmetry is first broken through the step

$$(0,0)\rightarrow(\tilde{v},0), \tag{3.A.97}$$

where $(\tilde{v},0)$ is an intermediate phase at which the electroweak symmetry is broken while the Z_2 symmetry remains preserved. Since the singlet does not acquire a VEV, it plays no major role in perturbing the potential depth at tree-level. Therefore the phase transition strength in this step is not largely affected by the existence of the extended singlet sector. Solving the finite temperature effective potential under the high temperature approximation, given in Equation (3.17), the strength of such a step is

$$\frac{\tilde{v}(T_c)}{T_c}=\frac{2E^{\rm SM}}{\lambda_h}=\frac{2E^{\rm SM}}{\lambda_h^{\rm SM}}\Big[1-\sin^2\theta\frac{m_S^2-m_H^2}{m_H^2\cos^2\theta+m_S^2\sin^2\theta}\Big]. \tag{3.A.98}$$

The transition is enhanced when $m_S<m_H$. However, the enhancement is bounded from above by constraints from Higgs precision measurements, which roughly set the mixing angle $|\sin\theta|\lesssim 0.4$. Accordingly, the transition strength is bounded as

$$\frac{\tilde{v}(T_c)}{T_c}\leq\frac{2E^{\rm SM}}{\lambda_h^{\rm SM}}\Big[1+\tan^2\theta\Big]\lesssim 1.2\left(\frac{2E^{\rm SM}}{\lambda_h^{\rm SM}}\right)\approx 0.36. \tag{3.A.99}$$

This upper bound on the transition strength is far below the requirement of SFOEWPT. After including the CW potential and the daisy resummation corrections, such a step still yields small values of $\frac{\tilde{v}(T_c)}{T_c}$, provided the couplings still fulfill perturbative unitarity conditions.

From the temperature T_c, at which the $(\tilde{v},0)$ is present, the thermal history proceeds

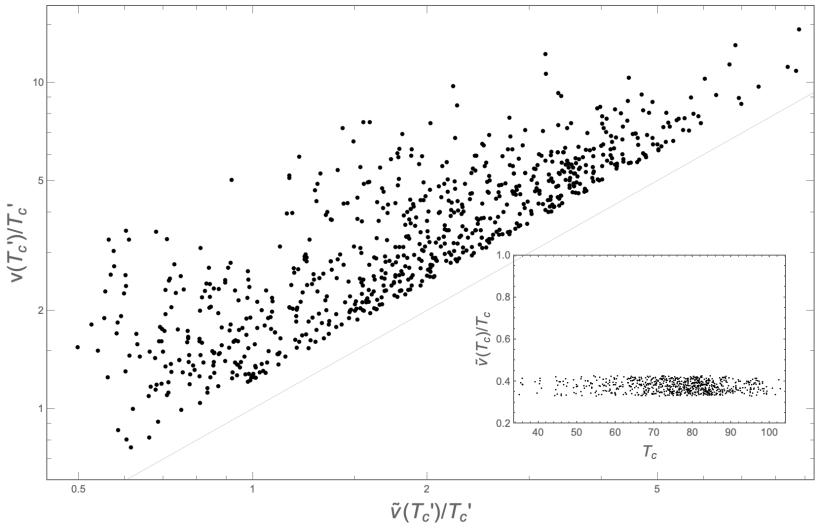

Figure 3.19: Higgs VEV to temperature ratios of the high temperature phase and low temperature phase for the transition step $(\tilde{v}, 0) \to (v, w)$ at a critical temperature T_c'. Results are obtained from numerical scanning with effective potential including tree-level and one-loop thermal potential. The sub figure shows phase transition strength of the previous step $(0, 0) \to (\tilde{v}, 0)$ at a critical temperature T_c, where the electroweak symmetry is first broken and the Higgs obtains its non-zero VEV $\tilde{v}$.

to the next phase transition step, $(\tilde{v}, 0) \to (v, w)$, at a lower temperature T_c', which breaks Z_2 and may further change the value of the electroweak symmetry breaking vacuum. Such a step is either a smooth cross over, or a first-order phase transition. If it is of first-order nature, the singlet field can play a role in rendering the strength of the phase transition strong first order. As shown in Figure 3.19, such is the case for $\frac{v(T_c')}{T_c'} \gtrsim 1$ at T_c', for which the sphaleron rate inside the bubble is suppressed. However, we observe that the sphaleron rate outside the bubble is also suppressed during the bubble nucleation whenever the ratio of the high temperature phase $\frac{\tilde{v}(T_c')}{T_c'} \gtrsim 1$. Therefore although the step $(\tilde{v}, 0) \to (v, w)$ can evolve a strong first order phase transition, no net baryon asymmetry can be created during the bubble nucleation.

In summary, although this type of thermal history occupies a sizable parameter space, it is not of special interests for modeling electroweak baryogenesis. The first electroweak breaking step $(0, 0) \to (\tilde{v}, 0)$ is weakly first-order, and any baryon asymmetry created is to

be erased. For the following step $(\tilde{v},0)\to(v,w)$, although the phase transition can be strong first order, the sphaleron process is suppressed both inside and outside the bubble through the transition, therefore, no baryon asymmetry can be sourced.

3.B Appendices for NMSSM

3.B.1 Field-dependent masses

In this appendix, we present explicit expressions for the field-dependent masses after inclusion of the leading stop corrections, but without corrections from the CW potential. As argued in subsection 3.3.1, it suffices to study the potential as a function of the three neutral CP-even degrees of freedom $\left\{H^{\rm SM},H^{\rm NSM},H^{\rm S}\right\}$.

Let us begin by presenting the expression for the field-dependent (squared) masses in the scalar sector. These can be directly obtained from the scalar potential,

$$\widehat{m}_{\Phi_i,\Phi_j}=\widehat{m}_{i,j}(H^{\rm SM},H^{\rm NSM},H^{\rm S})\equiv\left.\frac{\partial^2 V}{\partial\Phi_i\partial\Phi_j}\right|_{\substack{H^{\rm SM}\neq 0\\ H^{\rm NSM}\neq 0\\ H^{\rm S}\neq 0}}\ . \tag{3.B.1}$$

The entries involving the CP-even interaction states are

$$\begin{aligned}\widehat{m}^2_{H^{\rm SM},H^{\rm SM}}=&\left(m_Z^2c_{2\beta}^2+\lambda^2v^2s_{2\beta}^2+2\Delta\lambda_2v^2s_\beta^4\right)\left\{1+\frac{3\left[(H^{\rm SM})^2-2v^2\right]}{4v^2}\right\}\\&+\frac{\lambda^2}{2}\left(1-\frac{\kappa}{\lambda}s_{2\beta}\right)\left[(H^{\rm S})^2-\frac{2\mu^2}{\lambda^2}\right]-\frac{\lambda}{\sqrt{2}}\left(\frac{M_A^2}{2\mu}s_{2\beta}-\frac{\kappa\mu}{\lambda}\right)s_{2\beta}\left(H^{\rm S}-\frac{\sqrt{2}\mu}{\lambda}\right)\\&+\frac{(H^{\rm NSM})^2}{4v^2}\left[m_Z^2s_{2\beta}^2+\lambda^2v^2c_{2\beta}^2-\left(m_Z^2-\lambda^2v^2\right)c_{4\beta}\right]\\&-\frac{3H^{\rm SM}H^{\rm NSM}}{4v^2}\left(m_Z^2-\lambda^2v^2\right)s_{4\beta}\\&+\frac{3H^{\rm NSM}}{4v}\Delta\lambda_2vs_\beta s_{2\beta}\left(2H^{\rm SM}s_\beta+H^{\rm NSM}c_\beta\right)\ ,\end{aligned} \tag{3.B.2}$$

$$\widehat{m}^2_{H^{\rm SM},H^{\rm NSM}} = -\left(m_Z^2 - \lambda^2 v^2 - \Delta\lambda_2 v^2 \frac{s_\beta^2}{c_{2\beta}}\right) s_{2\beta}c_{2\beta}\left\{1 + \frac{3\left[(H^{\rm SM})^2 - 2v^2\right]}{4v^2}\right\}$$
$$+ \frac{H^{\rm SM}H^{\rm NSM}}{4v^2}\left[m_Z^2\left(1 - 3c_{4\beta}\right) + \lambda^2 v^2\left(1 + 3c_{4\beta}\right) + 3\Delta\lambda_2 v^2 s_{2\beta}^2\right]$$
$$+ \frac{3(H^{\rm NSM})^2}{4v^2}\left(m_Z^2 - \lambda^2 v^2 + \Delta\lambda_2 v^2 \frac{c_\beta^2}{c_{2\beta}}\right) s_{2\beta}c_{2\beta}$$
$$- \frac{\lambda}{2}c_{2\beta}\left(\kappa H^{\rm S} + \frac{M_A^2}{\sqrt{2}\mu}s_{2\beta}\right)\left(H^{\rm S} - \frac{\sqrt{2}\mu}{\lambda}\right)\ , \tag{3.B.3}$$

$$\widehat{m}^2_{H^{\rm SM},H^{\rm S}} = 2\lambda v\mu\left[\frac{H^{\rm SM}}{\sqrt{2}v}\frac{H^{\rm S}}{\sqrt{2}\mu/\lambda} - \frac{M_A^2}{4\mu^2}\frac{H^{\rm SM}}{\sqrt{2}v}s_{2\beta}^2\right.$$
$$\left. - \frac{\kappa}{\lambda}\left(\frac{H^{\rm SM}}{\sqrt{2}v}s_{2\beta} + \frac{H^{\rm NSM}}{\sqrt{2}v}c_{2\beta}\right)\left(\frac{1}{2} + \frac{H^{\rm S} - \sqrt{2}\mu/\lambda}{\sqrt{2}\mu/\lambda}\right)\right]$$
$$- \frac{\sqrt{2}\lambda M_A^2}{8\mu}H^{\rm NSM}s_{4\beta}\ , \tag{3.B.4}$$

$$
\begin{aligned}
\widehat{m}^2_{H^{\rm NSM},H^{\rm NSM}} = & M_A^2 + \left(m_Z^2 - \lambda^2 v^2 + \frac{\Delta\lambda_2 v^2}{2}\right) s_{2\beta}^2 \\
& + \left[m_Z^2\left(1-3c_{4\beta}\right) + \lambda^2 v^2\left(1+3c_{4\beta}\right) + 3\Delta\lambda_2 v^2 s_{2\beta}^2\right]\frac{(H^{\rm SM})^2 - 2v^2}{8v^2} \\
& + \frac{\lambda^2}{2}\left(1+\frac{\kappa}{\lambda}s_{2\beta}\right)\left[(H^{\rm S})^2 - \frac{2\mu^2}{\lambda^2}\right] + \frac{\lambda}{\sqrt{2}}\left(\frac{M_A^2}{2\mu}s_{2\beta} - \frac{\kappa\mu}{\lambda}\right) s_{2\beta}\left(H^{\rm S} - \frac{\sqrt{2}\mu}{\lambda}\right) \\
& + \frac{3H^{\rm SM}H^{\rm NSM}}{4v^2}\left(m_Z^2 s_{4\beta} - \lambda^2 v^2 s_{4\beta} + 2\Delta\lambda_2 v^2 s_{2\beta}c_\beta^2\right) \\
& + \frac{3(H^{\rm NSM})^2}{4v^2}\left(m_Z^2 c_{2\beta}^2 + \lambda^2 v^2 s_{2\beta}^2 + 2\Delta\lambda_2 v^2 c_\beta^4\right) \ , \qquad \text{(3.B.5)}
\end{aligned}
$$

$$
\begin{aligned}
\widehat{m}^2_{H^{\rm NSM},H^{\rm S}} = & -\frac{H^{\rm SM}}{\sqrt{2}}\lambda\mu c_{2\beta}\left\{\frac{\kappa}{\lambda}\left[1 + \frac{2\left(H^{\rm S} - \sqrt{2}\mu/\lambda\right)}{\sqrt{2}\mu/\lambda}\right] + \frac{M_A^2}{2\mu^2}s_{2\beta}\right\} \\
& + \sqrt{2}H^{\rm NSM}\lambda\mu\left\{\frac{M_A^2}{4\mu^2}s_{2\beta}^2 + \frac{\lambda}{\sqrt{2}\mu}H^{\rm S} + \frac{\kappa}{2\lambda}s_{2\beta}\left[1 + \frac{2\left(H^{\rm S} - \sqrt{2}\mu/\lambda\right)}{\sqrt{2}\mu/\lambda}\right]\right\} \ , \qquad \text{(3.B.6)}
\end{aligned}
$$

$$
\begin{aligned}
\widehat{m}^2_{H^{\rm S},H^{\rm S}} = & \frac{\lambda^2 v^2}{2}s_{2\beta}\left\{\frac{M_A^2}{2\mu^2}s_{2\beta} - \frac{\kappa}{\lambda}\left[1 + \frac{(H^{\rm SM})^2 - 2v^2}{v^2}\right]\right\} \\
& + \frac{\kappa\mu}{\lambda}\left\{A_\kappa\left[1 + \frac{2\left(H^{\rm S} - \sqrt{2}\mu/\lambda\right)}{\sqrt{2}\mu/\lambda}\right] + 4\frac{\kappa\mu}{\lambda}\left[1 + \frac{(H^{\rm S})^2 - 2\mu^2/\lambda^2}{4\mu^2/3\lambda^2}\right]\right\} \\
& + \lambda^2 v^2\frac{(H^{\rm SM})^2 - 2v^2}{2v^2} - \frac{\lambda\kappa H^{\rm NSM}}{2}\left[2H^{\rm SM}c_{2\beta} - H^{\rm NSM}\left(\frac{\lambda}{\kappa} + s_{2\beta}\right)\right] \ . \qquad \text{(3.B.7)}
\end{aligned}
$$

The entries involving the CP-odd states are

$$\widehat{m}^2_{A^{\rm NSM},A^{\rm NSM}} = M_A^2 \tag{3.B.8}$$
$$\begin{aligned}
&+\left[\lambda^2 v^2\left(3+c_{4\beta}\right)-2m_Z^2 c_{2\beta}^2+\Delta\lambda_2 v^2 s_{2\beta}^2\right]\frac{(H^{\rm SM})^2-2v^2}{8v^2}\\
&\quad+\frac{\lambda^2}{2}\left(1+\frac{\kappa}{\lambda}s_{2\beta}\right)\left[(H^{\rm S})^2-\frac{2\mu^2}{\lambda^2}\right]+\frac{\lambda}{\sqrt{2}}\left(\frac{M_A^2}{2\mu}s_{2\beta}-\frac{\kappa\mu}{\lambda}\right)s_{2\beta}\left(H^{\rm S}-\frac{\sqrt{2}\mu}{\lambda}\right)\\
&\quad+\left(\lambda^2 v^2 s_{2\beta}^2+m_Z^2 c_{2\beta}^2+2\Delta\lambda_2 v^2 c_\beta^4\right)\frac{(H^{\rm NSM})^2}{4v^2}\\
&\quad-\left(\lambda^2 v^2 s_{4\beta}-m_Z^2 s_{4\beta}-2\Delta\lambda_2 v^2 s_{2\beta}c_\beta^2\right)\frac{H^{\rm SM}H^{\rm NSM}}{4v^2}\,,
\end{aligned} \tag{3.B.9}$$

$$\widehat{m}^2_{A^{\rm NSM},A^{\rm S}} = \lambda v\frac{H^{\rm SM}}{\sqrt{2}v}\left[\frac{M_A^2}{2\mu}s_{2\beta}-3\frac{\kappa\mu}{\lambda}\left(1+\frac{H^{\rm S}-\sqrt{2}\mu/\lambda}{3\mu/\sqrt{2}\lambda}\right)\right]\,, \tag{3.B.10}$$

$$\begin{aligned}
\widehat{m}^2_{A^{\rm NSM},G^0} =& -\left(m_Z^2 c_{2\beta}-\lambda^2 v^2 c_{2\beta}-\Delta\lambda_2 v^2 s_\beta^2\right)s_{2\beta}\frac{(H^{\rm SM})^2-2v^2}{4v^2}\\
&+\left(m_Z^2 c_{2\beta}-\lambda^2 v^2 c_{2\beta}+\Delta\lambda_2 v^2 c_\beta^2\right)s_{2\beta}\frac{(H^{\rm NSM})^2}{4v^2}\\
&+\left(m_Z^2-\lambda^2 v^2+\frac{\Delta\lambda_2 v^2}{2}\right)s_{2\beta}^2\frac{H^{\rm SM}H^{\rm NSM}}{2v^2}\\
&-\frac{\lambda\kappa}{2}c_{2\beta}\left[(H^{\rm S})^2-\frac{2\mu^2}{\lambda^2}\right]-\frac{\lambda}{\sqrt{2}}\left(\frac{M_A^2}{2\mu}s_{2\beta}-\frac{\kappa\mu}{\lambda}\right)c_{2\beta}\left(H^{\rm S}-\frac{\sqrt{2}\mu}{\lambda}\right)\,,
\end{aligned} \tag{3.B.11}$$

$$\begin{aligned}\widehat{m}^2_{A^{\rm S},A^{\rm S}} = &\frac{\lambda^2 v^2}{2} s_{2\beta}\left(\frac{M_A^2}{2\mu^2}s_{2\beta}+\frac{3\kappa}{\lambda}\right)-\frac{3\kappa\mu A_\kappa}{\lambda}\\ &+\kappa^2\left[(H^{\rm S})^2-\frac{2\mu^2}{\lambda^2}\right]-\sqrt{2}\kappa A_\kappa\left(H^{\rm S}-\frac{\sqrt{2}\mu}{\lambda}\right)\\ &+\lambda^2 v^2\left(1+\frac{\kappa}{\lambda}s_{2\beta}\right)\frac{(H^{\rm SM})^2-2v^2}{2v^2}+\lambda^2 v^2\left(1-\frac{\kappa}{\lambda}s_{2\beta}\right)\frac{(H^{\rm NSM})^2}{2v^2}\\ &+\lambda\kappa c_{2\beta}H^{\rm SM}H^{\rm NSM}\,,\end{aligned} \tag{3.B.12}$$

$$\widehat{m}^2_{A^{\rm S},G^0} = \lambda H^{\rm NSM}\left(\kappa H^{\rm S}+\frac{\kappa\mu}{\sqrt{2}\lambda}-\frac{M_A^2}{2\sqrt{2}\mu}s_{2\beta}\right)\,, \tag{3.B.13}$$

$$\begin{aligned}\widehat{m}^2_{G^0,G^0} = &\left(m_Z^2c_{2\beta}^2+\lambda^2v^2s_{2\beta}^2+2\Delta\lambda_2v^2s_\beta^4\right)\frac{(H^{\rm SM})^2-2v^2}{4v^2}\\ &-\left[2m_Z^2c_{2\beta}^2-\lambda^2v^2\left(3+c_{4\beta}\right)-\Delta\lambda_2v^2s_{2\beta}^2\right]\frac{(H^{\rm NSM})^2}{8v^2}\\ &-\left(m_Z^2c_{2\beta}-\lambda^2v^2c_{2\beta}-\Delta\lambda_2v^2s_\beta^2\right)s_{2\beta}\frac{H^{\rm SM}H^{\rm NSM}}{2v^2}\\ &+\frac{\lambda^2}{2}\left(1-\frac{\kappa}{\lambda}s_{2\beta}\right)\left[(H^{\rm S})^2-\frac{2\mu^2}{\lambda^2}\right]-\frac{\lambda}{\sqrt{2}}\left(\frac{M_A^2}{2\mu}s_{2\beta}-\frac{\kappa\mu}{\lambda}\right)s_{2\beta}\left(H^{\rm S}-\frac{\sqrt{2}\mu}{\lambda}\right)\,.\end{aligned} \tag{3.B.14}$$

Note that as required, at the physical minimum, i.e. where $\widehat{m}_{\Phi_i\Phi_j}\left(H^{\rm SM},H^{\rm NSM},H^{\rm S}\right)\to\widehat{m}_{\Phi_i\Phi_j}\left(\sqrt{2}v,0,\sqrt{2}\mu/\lambda\right)\equiv m_{\Phi_i\Phi_j}$,

$$m_{G^0,G^0}=m_{A^{\rm NSM},G^0}=m_{A^{\rm S},G^0}=0\,, \tag{3.B.15}$$

or in words, the neutral Goldstone mode G^0 is massless and decouples from the other CP-odd neutral states $A^{\rm NSM}$ and $A^{\rm S}$.

The elements involving the charged states are

$$\begin{aligned}\widehat{m}^2_{H^+,H^-} &= M_A^2 - \lambda^2 v^2 + m_W^2 \\ &\quad - \left(m_Z^2 c_{2\beta}^2 + \lambda^2 v^2 s_{2\beta}^2 - 2m_W^2 - \frac{\Delta\lambda_2 v^2}{2} s_{2\beta}^2\right) \frac{(H^{\rm SM})^2 - 2v^2}{4v^2} \\ &\quad + \left(m_Z^2 c_{2\beta}^2 + \lambda^2 v^2 s_{2\beta}^2 + 2\Delta\lambda_2 v^2 c_\beta^4\right) \frac{(H^{\rm NSM})^2}{4v^2} \\ &\quad + \left(m_Z^2 c_{2\beta} - \lambda^2 v^2 c_{2\beta} + \Delta\lambda_2 v^2 c_\beta^2\right) s_{2\beta} \frac{H^{\rm SM} H^{\rm NSM}}{2v^2} \\ &\quad + \frac{\lambda^2}{2}\left(1 + \frac{\kappa}{\lambda} s_{2\beta}\right)\left[(H^{\rm S})^2 - \frac{2\mu^2}{\lambda^2}\right] + \frac{\lambda}{\sqrt{2}}\left(\frac{M_A^2}{2\mu} s_{2\beta} - \frac{\kappa\mu}{\lambda}\right) s_{2\beta}\left(H^{\rm S} - \frac{\sqrt{2}\mu}{\lambda}\right) ,\end{aligned} \tag{3.B.16}$$

$$\begin{aligned}\widehat{m}^2_{H^+,G^-} = \widehat{m}^2_{H^-,G^+} &= -\left(m_Z^2 c_{2\beta} - \lambda^2 v^2 c_{2\beta} - \Delta\lambda_2 v^2 s_\beta^2\right) s_{2\beta} \frac{(H^{\rm SM})^2 - 2v^2}{4v^2} \\ &\quad + \left(m_Z^2 c_{2\beta} - \lambda^2 v^2 c_{2\beta} + \Delta\lambda_2 v^2 c_\beta^2\right) s_{2\beta} \frac{(H^{\rm NSM})^2}{4v^2} \\ &\quad + \left(m_Z^2 s_{2\beta}^2 + \lambda^2 v^2 c_{2\beta}^2 - m_W^2 + \frac{\Delta\lambda_2 v^2}{2} s_{2\beta}^2\right) \frac{H^{\rm SM} H^{\rm NSM}}{2v^2} \\ &\quad - \frac{\lambda\kappa}{2} c_{2\beta}\left[(H^{\rm S})^2 - \frac{2\mu^2}{\lambda^2}\right] - \frac{\lambda}{\sqrt{2}}\left(\frac{M_A^2}{2\mu} s_{2\beta} - \frac{\kappa\mu}{\lambda}\right) c_{2\beta}\left(H^{\rm S} - \frac{\sqrt{2}\mu}{\lambda}\right) ,\end{aligned} \tag{3.B.17}$$

$$\begin{aligned}\widehat{m}^2_{G^+,G^-} &= \left(m_Z^2 c_{2\beta}^2 + \lambda^2 v^2 s_{2\beta}^2 + 2\Delta\lambda_2 v^2 s_\beta^4\right) \frac{(H^{\rm SM})^2 - 2v^2}{4v^2} \\ &\quad - \left(m_Z^2 c_{2\beta}^2 + \lambda^2 v^2 s_{2\beta}^2 - 2m_W^2 - \frac{\Delta\lambda_2 v^2}{2} s_{2\beta}^2\right) \frac{(H^{\rm NSM})^2}{4v^2} \\ &\quad - \left(m_Z^2 c_{2\beta} - \lambda^2 v^2 c_{2\beta} - \Delta\lambda_2 v^2 s_\beta^2\right) s_{2\beta} \frac{H^{\rm SM} H^{\rm NSM}}{2v^2} \\ &\quad + \frac{\lambda^2}{2}\left(1 - \frac{\kappa}{\lambda} s_{2\beta}\right)\left[(H^{\rm S})^2 - \frac{2\mu^2}{\lambda^2}\right] - \frac{\lambda}{\sqrt{2}}\left(\frac{M_A^2}{2\mu} s_{2\beta} - \frac{\kappa\mu}{\lambda}\right) s_{2\beta}\left(H^{\rm S} - \frac{\sqrt{2}\mu}{\lambda}\right) .\end{aligned} \tag{3.B.18}$$

At the physical minimum, we again find

$$m_{G^+G^-} = m_{H^+,G^-} = m_{H^-,G^+} = 0 \,, \tag{3.B.19}$$

or in words, the charged Goldstone mode $G^\pm$ is massless and decouples from the charged Higgs $H^\pm$.

The remaining entries of the (symmetric) (10×10) matrix of the $\widehat{m}_{\Phi_i,\Phi_j}$ not listed above vanish due to CP- and charge conservation.

The field-dependent masses for the electroweak gauge bosons are given by

$$\widehat{m}^2_{W^\pm} = \frac{g_2^2}{4}\left[(H^{\rm SM})^2 + (H^{\rm NSM})^2\right] \,, \tag{3.B.20}$$

$$\widehat{m}^2_{Z} = \frac{g_1^2+g_2^2}{4}\left[(H^{\rm SM})^2 + (H^{\rm NSM})^2\right] \,, \tag{3.B.21}$$

with the weak mixing angle $\cos\theta_W = g_2/\sqrt{g_1^2+g_2^2} = m_W/m_Z$. The masses of the vector bosons at the physical minimum are related to the gauge couplings as

$$g_1 = \sqrt{2}\sin\theta_W \frac{m_Z}{v} \,, \quad g_2 = \sqrt{2}\frac{m_W}{v} \,. \tag{3.B.22}$$

For the 5 neutralinos, the (symmetric) matrix of field-dependent masses in the basis

$\left\{\widetilde{B}, \widetilde{W}^3, \widetilde{H}_d^0, \widetilde{H}_u^0, \widetilde{S}\right\}$ can be written as

$$\widehat{\mathcal{M}}_{\chi^0} = \begin{pmatrix} M_1 & 0 & -\frac{g_1}{2}\left(c_\beta H^{\mathrm{SM}} - s_\beta H^{\mathrm{NSM}}\right) & \frac{g_1}{2}\left(s_\beta H^{\mathrm{SM}} + c_\beta H^{\mathrm{NSM}}\right) & 0 \\ & M_2 & \frac{g_2}{2}\left(c_\beta H^{\mathrm{SM}} - s_\beta H^{\mathrm{NSM}}\right) & -\frac{g_2}{2}\left(s_\beta H^{\mathrm{SM}} + c_\beta H^{\mathrm{NSM}}\right) & 0 \\ & & 0 & -\frac{\lambda}{\sqrt{2}} H^{\mathrm{S}} & -\frac{\lambda}{\sqrt{2}}\left(s_\beta H^{\mathrm{SM}} + c_\beta H^{\mathrm{NSM}}\right) \\ & & & 0 & -\frac{\lambda}{\sqrt{2}}\left(c_\beta H^{\mathrm{SM}} - s_\beta H^{\mathrm{NSM}}\right) \\ & & & & \sqrt{2}\kappa H^{\mathrm{S}} \end{pmatrix} . \tag{3.B.23}$$

In the basis $\psi_i^\pm = \left\{\widetilde{W}^+, \widetilde{H}_u^+, \widetilde{W}^-, \widetilde{H}_d^-\right\}$ the field-dependent mass terms for the charginos can be written as

$$\mathcal{L} \supset -\frac{1}{2}(\psi^\pm)^T \begin{pmatrix} 0 & \widehat{X}^T \\ \widehat{X} & 0 \end{pmatrix} \psi^\pm + \text{h.c.} , \tag{3.B.24}$$

where

$$\widehat{X} = \begin{pmatrix} M_2 & \frac{g_2}{\sqrt{2}}\left(s_\beta H^{\mathrm{SM}} + c_\beta H^{\mathrm{NSM}}\right) \\ \frac{g_2}{\sqrt{2}}\left(c_\beta H^{\mathrm{SM}} - s_\beta H^{\mathrm{NSM}}\right) & \frac{\lambda}{\sqrt{2}} H^{\mathrm{S}} \end{pmatrix} . \tag{3.B.25}$$

Finally, the field-dependent mass of the top quark is given by

$$\widehat{m}_t = \frac{1}{\sqrt{2}} h_t \left(s_\beta H^{\mathrm{SM}} + c_\beta H^{\mathrm{NSM}}\right) , \tag{3.B.26}$$

where the Yukawa coupling h_t is related to the (running) top quark mass m_t via $h_t = m_t / s_\beta v$.

We compute the contributions to the CW potential as well as to the thermal potential in the Landau gauge. This is useful since in the Landau gauge the ghosts decouple and we do not have to include them in our calculations. The quantities entering the CW and the thermal potential are the eigenvalues of the respective mass matrices. Recall that the number

of degrees of freedom are $n_i = 1$ for the three neutral CP-even and three neutral CP-odd states, $n_i = 2$ for the two charged Higgs states, $n_i = 6$ for the $W^\pm$ bosons, and $n_i = 3$ for the Z-boson. Out of the fermions, the top quark has $n_i = 12$ and the five neutralinos have $n_i = 2$ each. Since we wrote the chargino mass matrix, Equation (3.B.24), in terms of four Majorana states (which combine to two physical Dirac fermions), the four eigenvalues of Equation (3.B.24) enter with $n_i = 2$ each.

3.B.2 Counterterm coefficients

In order to maintain the location of the physical minimum at $\left\{H^{\rm SM}, H^{\rm NSM}, H^{\rm S}\right\} = \sqrt{2}\left\{v, 0, \mu/\lambda\right\}$, preserve $m_{h_{125}} = 125\,\text{GeV}$, and $\mathcal{M}^2_{S,13} \to 0$ (i.e. alignment of $H^{\rm S}$ and $H^{\rm S}$) after including the CW corrections, we include the counterterms given in Equation (3.68). The solutions for the counterterms to satisfy these conditions are

$$\delta_{m^2_{H_d}} = -\frac{1}{2v}\left(\sqrt{2}\frac{\partial V_1}{\partial H^{\rm SM}} - \sqrt{2}\tan\beta\frac{\partial V_1}{\partial H^{\rm NSM}} - \frac{\mu}{\lambda\cos^2\beta}\frac{\partial^2 V_1}{\partial H^{\rm SM}\,\partial H^{\rm S}}\right)\,, \tag{3.B.27}$$

$$\begin{aligned}\delta_{m^2_{H_u}} = \frac{1}{2v\sin^2\beta}\Bigg[&\frac{\cos(2\beta)-2}{\sqrt{2}}\frac{\partial V_1}{\partial H^{\rm SM}} - \frac{\sin(2\beta)}{\sqrt{2}}\frac{\partial V_1}{\partial H^{\rm NSM}} \\ &+v\left(\frac{\partial^2 V_1}{\partial H^{\rm SM}\,\partial H^{\rm SM}} - m^2_{h_{125}}\right) + \frac{\mu}{\lambda}\frac{\partial^2 V_1}{\partial H^{\rm SM}\,\partial H^{\rm S}}\Bigg]\,,\end{aligned} \tag{3.B.28}$$

$$\delta_{m^2_S} = -\frac{\lambda}{2\mu}\left(\sqrt{2}\frac{\partial V_1}{\partial H^{\rm S}} - v\frac{\partial^2 V_1}{\partial H^{\rm SM}\,\partial H^{\rm S}}\right)\,, \tag{3.B.29}$$

$$\delta_{\lambda A_\lambda} = \frac{1}{v\sin(2\beta)}\frac{\partial^2 V_1}{\partial H^{\rm SM}\,\partial H^{\rm S}}\,, \tag{3.B.30}$$

$$\delta_{\lambda_2} = \frac{1}{2\sqrt{2}v^3\sin^4\beta}\left[\frac{\partial V_1}{\partial H^{\rm SM}} + \sqrt{2}v\left(m^2_{h_{125}} - \frac{\partial^2 V_1}{\partial H^{\rm SM}\,\partial H^{\rm SM}}\right)\right]\,, \tag{3.B.31}$$

where

$$V_1 = V_1(T=0) = V_0^{\rm eff} + V_{1-\rm loop}^{\rm CW}\,, \tag{3.B.32}$$

is the effective potential including the CW corrections $V_{1-\rm loop}^{\rm CW}$ at zero temperature, all derivatives are evaluated at the physical minimum, $\left\{H^{\rm SM}, H^{\rm NSM}, H^{\rm S}\right\} = \sqrt{2}\left\{v, 0, \mu/\lambda\right\}$,

and $m_{h_{125}}$ is an input parameter which sets the mass of the $H^{\rm SM}$ interaction eigenstate of the Higgs basis.

3.B.3 Daisy coefficients

The Daisy coefficients c_i for the thermal masses

$$\widetilde{m}_i^2 = \widehat{m}_i^2 + c_i T^2 \ , \tag{3.B.33}$$

can be obtained from the high-temperature limit of the thermal corrections to the effective potential,

$$c_{ij} = \frac{1}{T^2} \left. \frac{\partial^2 V_{1-\text{loop}}^{T\neq 0}(\widehat{m}^2)}{\partial\phi_i \, \partial\phi_j} \right|_{T\gg\widehat{m}^2} \ . \tag{3.B.34}$$

Note that for the derivation of the Daisy coefficient, $V_{1-\text{loop}}^{T\neq 0} = V_{1-\text{loop}}^{T\neq 0}(\widehat{m}_i^2)$ is computed with the temperature independent field-dependent masses $\widehat{m}_i^2$, while when computing the temperature-dependent effective potential, the Daisy-resummation improved thermal masses $\widetilde{m}_i^2$ are inserted in $V_{1-\text{loop}}^{T\neq 0}$ as well as in the CW potential.

Note also that while we gave explicit expressions for the $\widehat{m}_i^2$ as a function of the three neutral CP-even Higgs boson interaction states, $H^{\rm SM}$, $H^{\rm NSM}$, and $H^{\rm S}$, in appendix 3.B.1, when computing the Daisy coefficients via Equation (3.B.34), the field-dependent masses must be inserted as a function of all bosonic fields, i.e.

$$\widehat{m}_{i,j}^2 = \widehat{m}_{i,j}^2(H^{\rm SM}, H^{\rm NSM}, H^{\rm S}, A^{\rm NSM}, A^{\rm S}, H^{\pm}, G^0, G^{\pm}, Z^0, W^{\pm}) \ . \tag{3.B.35}$$

The non-vanishing coefficients involving the neutral Higgs bosons are

$$c_{H^{\rm SM}H^{\rm SM}} = c_{G^0G^0} = \frac{\lambda^2}{4} + \frac{m_Z^2 + 2m_W^2}{4v^2} + \frac{m_t^2}{4v^2} + \frac{\Delta\lambda_2}{4}s_\beta^2 \,, \tag{3.B.36}$$

$$c_{H^{\rm SM}H^{\rm NSM}} = c_{A^{\rm NSM}G^0} = \frac{m_t^2}{4v^2}\frac{1}{t_\beta} + \frac{\Delta\lambda_2}{8}s_{2\beta} \,, \tag{3.B.37}$$

$$c_{H^{\rm NSM}H^{\rm NSM}} = c_{A^{\rm NSM}A^{\rm NSM}} = \frac{\lambda^2}{4} + \frac{m_Z^2 + 2m_W^2}{4v^2} + \frac{m_t^2}{4v^2}\frac{1}{t_\beta^2} + \frac{\Delta\lambda_2}{4}c_\beta^2 \,, \tag{3.B.38}$$

$$c_{H^{\rm S}H^{\rm S}} = c_{A^{\rm S}A^{\rm S}} = \frac{\lambda^2 + \kappa^2}{2} \,, \tag{3.B.39}$$

and those involving the charged Higgs bosons are

$$c_{H^+H^-} = \frac{\lambda^2}{6} + \frac{m_Z^2 + 2m_W^2}{6v^2} + \frac{m_t^2}{4v^2}\frac{1}{t_\beta^2} + \frac{\Delta\lambda_2}{4}c_\beta^2 \,, \tag{3.B.40}$$

$$c_{H^+G^-} = c_{H^{\rm SM}H^{\rm NSM}} \tag{3.B.41}$$

$$c_{G^+G^-} = \frac{\lambda^2}{6} + \frac{m_Z^2 + 2m_W^2}{6v^2} + \frac{m_t^2}{4v^2} + \frac{\Delta\lambda_2}{4}s_\beta^2 \,. \tag{3.B.42}$$

The Daisy coefficients for the longitudinal modes of the gauge bosons are [269, 270]

$$c_{W_L^+W_L^-} = c_{W_L^3W_L^3} = \frac{5}{2}g_2^2 = 5\frac{m_W^2}{v^2} \,, \quad c_{B_LB_L} = \frac{13}{6}g_1^2 \,. \tag{3.B.43}$$

Note that the photon gets a temperature-dependent mass. In order to properly account for this appearance of the longitudinal degree of freedom of the photon, the Daisy resummation improved thermal masses of the neutral electroweak gauge bosons must thus be included as

the eigenvalues of mass matrix,

$$\widetilde{m}^2_{Z_L,A_L}(H^{\rm SM},H^{\rm NSM},H^{\rm S};T) = \frac{(H^{\rm SM})^2+(H^{\rm NSM})^2}{4}\begin{pmatrix} g_2^2 & -g_1g_2 \\ -g_1g_2 & g_1^2 \end{pmatrix} + T^2\begin{pmatrix} 5g_2^2/2 & 0 \\ 0 & 13g_1^2/6 \end{pmatrix}. \tag{3.B.44}$$

After removing the contribution from the neutralinos and charginos to $V^{T\neq 0}_{1-\rm loop}(\widehat{m}^2)$, these results agree with the results in ref. [189] (where the neutralino and chargino contribution were neglected).

CHAPTER 4

AN ALTERNATIVE THERMAL HISTORY: ELECTROWEAK SYMMETRY NON-RESTORATION

In the SM, the EW symmetry was restored at temperatures above the EW scale. With input from new physics sectors those couple to the SM Higgs, such a restoration behavior could have been changed. It is interesting to explore an alternative thermal history - the EW symmetry remains broken at temperatures well above the EW scale, which has several intriguing implications for (electroweak) baryogenesis, early universe thermal histories and Higgs phenomenology.

In this chapter, an introduction to electroweak symmetry non-restoration will be presented in section 4.1. In section 4.2, we propose a new approach for electroweak symmetry non-restoration via an inert Higgs sector that couples to the SM Higgs as well as an extended scalar singlet sector. We implement renormalization group improvements and thermal resummation, necessary to evaluate the effective potential spanning over a broad range of energy scales and temperatures. We present examples of benchmark scenarios that allow for electroweak symmetry non-restoration all the way up to hundreds of TeV temperatures, and also feature suppressed sphaleron washout factors down to the electroweak scale. Higgs and collider phenomenology, which provides important scrutinization of such a scenario will also be discussed. This work was performed in collaboration with Marcela Carena, Claudius Krause and Zhen Liu. It is under review in Physical Review D [271].

Last but not least, in section 4.3, we provide an outlook for an ultraviolet completion of such a scenario, where EWBG at hundreds of TeV could be realized, evading severe low energy constraints, e.g. from electron dipole moment.

4.1 Introduction

The phenomenon of symmetry broken/non-restoration due to temperature effects has been studied a long time ago. In 1974, Weinberg first discussed spontaneous symmetry breaking driven by finite temperature effects considering an $\mathcal{O}(n) \times \mathcal{O}(n)$-invariant theory with two independent scalar multiplets [26]. With different values of the quartic couplings in the two scalar sectors, such a toy model exhibits rich symmetry breaking patterns from zero temperature up to high temperatures. Later on, various studies appeared applying the idea to symmetries tackling problems such as CP violation, domain wall, monopole, etc [272–278]. For example, in [274], the authors pointed out that GUT symmetry could remain broken at finite temperatures in $SU(5)$ theory. Without a phase transition from the symmetry phase to the broken phase, the overproduction of monopoles can be avoided thus being consistent with cosmological constraints.

Only recently, the idea of symmetry non-restoration has been applied to the electroweak symmetry [90,132,133,279–283], which has interesting implementations on models generating the BAU. With new physics inputs, in contrast to the SM case, the EW symmetry can remain broken, say non-restored, up to temperatures well above the EW scale. Taking a bottom-up approach, we called these scenarios: i) delayed restoration, if the electroweak symmetry is restored at very high temperatures, or ii) non-restoration if the electroweak symmetry remains broken all the way up to some high energy scale Λ of validity of the theory. Electroweak non-restoration (EWNR) or delayed restoration scenarios have advantages in modeling mechanisms for baryogenesis, as it allows for the asymmetry creation to happen at a scale much above the EW scale. For example, in the case of EWBG, one important advantage is that the additional, required sources of CP violation will only be effective at high energies and, therefore, will avoid current electric dipole moment experimental bounds.

In particular, new ideas of electroweak non-restoration or delayed restoration have been discussed [132,133,281,282] by extending the SM Higgs sector with additional singlet scalars

that couple to the SM Higgs and provide it with a negative thermal mass at very high temperatures. Such models typically require several hundreds of new scalar fields. On top of the new scalar sectors, for models with delayed restoration, the ultraviolet (UV) completions typically require additional scalar and/or fermion fields that couple with the EW sector and yield electroweak symmetry restoration, as well as a strong first-order phase transition, at very high temperatures [132, 281, 282].

In the next section, we propose a new mechanism to realize EWNR, where the EW symmetry breaking at high temperatures are driven by an inert Higgs field acquiring non-zero VEV. With such a construction, a minimally coupled scenario, where the only non-zero coupling between the BSM sector and the SM section at tree level is the gauge coupling between the inert Higgs doublet and the SM gauge bosons, can be compatible with the EWNR as well as suppressed sphaleron processes through the thermal history.

4.2 A new approach to electroweak symmetry non-restoration

In this section, we explore the electroweak symmetry non-restoration or delayed restoration with an extended-Inert Two Higgs Doublet Model (I2HDM) [284, 285], where, instead of the SM Higgs, it is the inert Higgs who acquires a non-zero VEV up to very high temperature by coupling to an additional scalar sector. Such a model requires minimal couplings between the new scalar fields and the SM Higgs boson, and opens the window to different realizations for baryogenesis at very high energy scales. Due to the lack of large Yukawa couplings to the inert sector, the number of scalars required to achieve negative thermal masses is somewhat reduced. Specific new physics models for high scale EW baryogenesis in the context of extensions of the I2HDM will be the topic of a forthcoming publication.

The EWNR sets the boundary conditions at high temperatures ($\lesssim T_{\rm UV}$), while the observed EW vacuum defines them at zero temperature; see the top row of Figure 4.1 for a schematic view. For intermediate temperatures, the I2HDM allows different phase histories

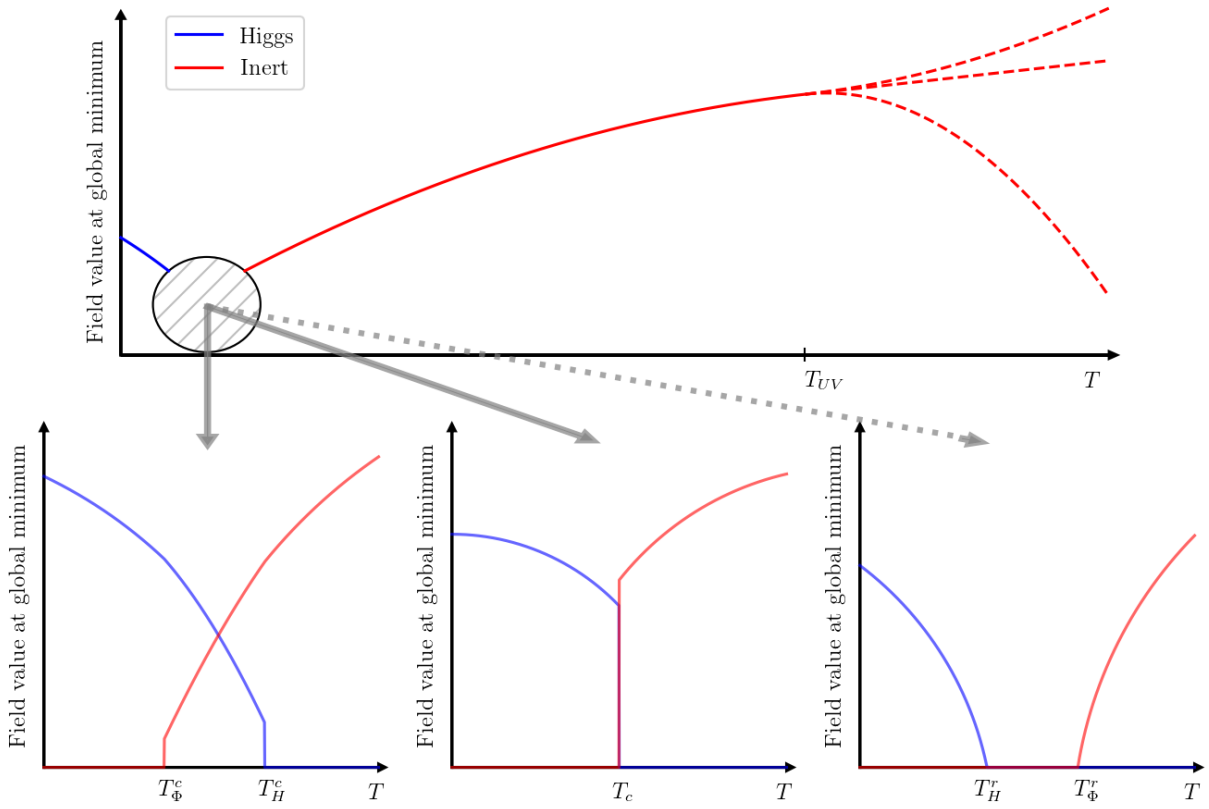

Figure 4.1: Schematic illustration of the phase values of Higgs and Inert scalar at the global minimum for non-restoration and delayed restoration. The top panel shows the global view up to very high temperatures, where the non-retoration can either persist or the symmetry becomes eventually restored (depicted by dashed lines). The lower panel zooms into the gray region and shows three different scenarios of the transition between the two doublets.

that we depict in the bottom row of Figure 4.1. There could either be a temperature range (between T_H^c and T_Φ^c - to be precisely defined below) for which the global minumum is given by non-vanishing VEVs of both the Higgs and the inert fields (left plot), or there could be a discrete jump between the Higgs and the inert phases at a critical Temperature T_c (central plot). A third option is given by a scenario in which the Higgs VEV goes to zero at a restoration temperature T_H^r lower than the temperature T_Φ^r above which the inert VEV starts to grow (right plot). In the temperature range between T_H^r and T_Φ^r the system is in a EW preserving vacuum.

In this work, we utilize the EP method to calculate the finite-temperature phase structure and quantities relevant to the baryon asymmetry. However, unlike for typical EWPT calculation's for which the electroweak symmetry breaking takes place close to the EW scale, here we need to take into account important effects due to the large scale separation between the high temperatures ($\gtrsim \mathcal{O}(1-100)$ TeV)- high field values and the EW scale, which requires careful treatment and improvement of the perturbative calculation. For this purpose, we will implement RG improvement and daisy resummation of the EP to ameliorate the perturbative convergence.

This section is organized as follows: in subsection 4.2.1, we introduce our model and discuss its zero temperature constraints. Based on a mean-field approach, we present an analytical study of the possible thermal histories. In subsection 4.2.2, we set up schemes for an improved perturbative calculation, and present results of the full numerical computation of the finite-temperature phase structure for two benchmark (BM) scenarios. In subsection 4.2.3, we discuss the baryon washout conditions, based on baryogenesis model building considerations, and consider them in light of the thermal history results for the two BM scenarios. In subsection 4.2.4, we discuss phenomenological constraints in this type of model. Various technical aspects will be collected in appendices of this thesis.

4.2.1 The model and a mean field analysis to the thermal history

The effective potential at tree level

We consider an extension of the SM Higgs sector that includes an Inert Higgs Doublet with additional singlet scalars. In such case, the most general $\mathbb{Z}_2$-symmetric potential reads [1],

$$V_{\mathbb{Z}_N+\text{I2HDM}} = -\mu_H^2 H^\dagger H + \lambda_H (H^\dagger H)^2 \tag{4.2.1}$$

$$+ \mu_\Phi^2 (\Phi^\dagger \Phi) + \lambda_\Phi (\Phi^\dagger \Phi)^2 + \lambda_{H\Phi} (H^\dagger H)(\Phi^\dagger \Phi) + \widetilde{\lambda}_{H\Phi} (H^\dagger \Phi)(\Phi^\dagger H) \tag{4.2.2}$$

$$+ \frac{\mu_\chi^2}{2}\chi_i^2 + \frac{\widetilde{\lambda}_\chi}{4}\chi_i^4 + \frac{\lambda_\chi}{4}(\chi_i\chi_i)^2 + \frac{\lambda_{\Phi\chi}}{2}\chi_i^2(\Phi^\dagger\Phi) + \frac{\lambda_{H\chi}}{2}\chi_i^2(H^\dagger H),$$

where the two Higgs doublets are written as

$$H = \begin{pmatrix} G^+ \\ \frac{1}{\sqrt{2}}(h + iG_0) \end{pmatrix} \tag{4.2.3}$$

$$\Phi = \begin{pmatrix} \phi^+ \\ \frac{1}{\sqrt{2}}(\varphi + i\phi_0) \end{pmatrix}, \tag{4.2.4}$$

and the fields χ_i represent N real, singlet scalars. Assuming that extra sources of CP violation will come from a new sector, once we study the complete UV theory, we impose CP invariance in the Higgs sector and define all model parameters to be real. The assumed $\mathbb{Z}_2$-symmetry forbids couplings of the type $\mu_{12}^2(H^\dagger\Phi), \lambda_6(H^\dagger\Phi H^\dagger H)$, and $\lambda_7(H^\dagger\Phi\Phi^\dagger\Phi)$. Portal couplings of the form $(\Phi^\dagger H)(\Phi^\dagger H)$ and $(H^\dagger\Phi)(H^\dagger\Phi)$ are allowed by the $\mathbb{Z}_2$ symmetry and are related to the operator $(H^\dagger\Phi)(\Phi^\dagger H)$ by custodial symmetry [286]. However, assuming

1. Here $\mathbb{Z}_2$ is defined as $H \to H$, $\chi_i \to -\chi_i$, and $\Phi \to -\Phi$. As we shall discuss later, instead of the $\mathbb{Z}_2$, we require a continuous global $U(1)$ symmetry on the doublet Φ to ensure it being inert, which forbids additional terms that we omitted here in the potential.

a $U(1)$-symmetry on (one of the) doublets forbids these additional portal couplings and simplifies the potential. Given the custodial symmetry and the additional $U(1)$-symmetry, we can set the coupling $\widetilde{\lambda}_{H\Phi}$ to 0 as well. However, this is not stable under RG-running, as the hypercharge gauge coupling breaks custodial symmetry. We therefore keep track of the operator with the coefficient $\widetilde{\lambda}_{H\Phi}$ for future RG improvement of the EP. In addition, to better accommodate phenomenological constraints, we set $\lambda_{H\chi} = 0$, although, similarly to $\widetilde{\lambda}_{H\Phi}$ this coupling will also be induced by the renormalization group evolution (RGE), and we will keep track of its effects. Finally, observe that $\widetilde{\lambda}_{\chi} = 0$ is protected by an $SO(N)$ symmetry of the singlet sector, and we shall impose such symmetry. In the case of a potential with generic values of $\widetilde{\lambda}_{\chi}$, the singlet sector exhibits a discrete $\mathbb{Z}_N$ symmetry.

To summarize, parameters in the above potential can be separated as follows:

- fixed parameters: $\{\mu_H^2, \lambda_H\}$,
- free parameters: $\{\mu_\Phi^2, \mu_\chi^2, \lambda_\Phi, \lambda_\chi, \lambda_{\Phi\chi}, \lambda_{H\Phi}, N\}$,
- free parameters set to zero: $\{\widetilde{\lambda}_{H\Phi}, \lambda_{H\chi}, \widetilde{\lambda}_{\chi}\}$,
- RGE induced parameters: $\{\widetilde{\lambda}_{H\Phi}, \lambda_{H\chi}\}$,

where the two fixed parameters are given by the current observation of the EW VEV $v_0 = 246$ GeV and the SM Higgs mass $m_h = 125$ GeV.

In general, there could be charge breaking and CP breaking minima in two Higgs doublet models. However, [287, 288] showed that at tree level, if an EW breaking minimum exists, any possibly existing charge breaking or CP breaking extremum is necessarily a saddle point above the EW breaking minimum. Although the validity of this result may not hold after the inclusion of radiative corrections, and its validation requires a more detailed analysis beyond the scope of this work, we shall only allow for the neutral CP even components to develop non-zero vacuum expectation values at any temperature. Therefore, from now on,

we focus on analyzing the effective potential of the CP-even components of the two Higgs doublets, and the singlet sector. The tree-level CP even potential reads,

$$V_{0,\text{CP even}}^{\mathbb{Z}_N+\text{I2HDM}} = -\frac{\mu_H^2}{2}h^2 + \frac{\lambda_H}{4}h^4 + \frac{\mu_\Phi^2}{2}\varphi^2 + \frac{\lambda_\Phi}{4}\varphi^4 + \frac{\lambda_{H\Phi}+\widetilde{\lambda}_{H\Phi}}{4}h^2\varphi^2 + \frac{\mu_\chi^2}{2}\chi_i^2 + \frac{\widetilde{\lambda}_\chi}{4}\chi_i^4 + \frac{\lambda_\chi}{4}(\chi_i\chi_i)^2 + \frac{\lambda_{\Phi\chi}}{4}\chi_i^2\varphi^2 + \frac{\lambda_{H\chi}}{4}\chi_i^2 h^2. \tag{4.2.5}$$

The particles in the plasma include bosons $\{h, G_0, G^\pm, \varphi, \phi_0, \phi^\pm, \chi, \gamma, W^\pm, Z\}$ with corresponding particle degrees of freedom (d.o.f.) $n_{bos} = \{1, 1, 2, 1, 1, 2, N, 3, 6, 3\}$, and fermions, $\{t\}$ with corresponding particle d.o.f. $n_{ferm} = \{12\}$ that couple (self-couple) to the dynamical fields. Notice that we work in the Landau gauge so there are no ghost d.o.f. We collect the effective, field-dependent masses of these particles in appendix subsection 4.A.1.

Zero temperature constraints

In this section, we present the tree-level, zero temperature constraints on our model, including the bounded from below (BFB) conditions, and the correct vacuum structure of the tree-level potential. This study provides guidance, later on, in defining the viable parameter space for which we shall perform numerical calculations to constrain the model after the inclusion of radiative corrections.

- Bounded From Below Conditions

  The bounded from below (BFB) conditions, which need to be satisfied simultaneously,

for the generic tree level potential given in eq. (4.2.1) are

$$\lambda_H > 0, \qquad \lambda_\Phi > 0, \qquad \Lambda_{\chi,n} > 0,$$

$$\Lambda_{H\Phi} > -\sqrt{4\lambda_H\lambda_\Phi}, \qquad \lambda_{\Phi\chi} > -\sqrt{4\lambda_\Phi\Lambda_{\chi,n}}, \qquad \lambda_{H\chi} > -\sqrt{4\lambda_H\Lambda_{\chi,n}}, \tag{4.2.6}$$

$$\sqrt{4\lambda_H\lambda_\Phi\Lambda_{\chi,n}} + \Lambda_{H\Phi}\sqrt{\Lambda_{\chi,n}} + \lambda_{\Phi\chi}\sqrt{\lambda_H} + \lambda_{H\chi}\sqrt{\lambda_\Phi} \tag{4.2.7}$$

$$+\sqrt{\left(\Lambda_{H\Phi} + \sqrt{4\lambda_H\lambda_\Phi}\right)\left(\lambda_{\Phi\chi} + \sqrt{4\lambda_\Phi\Lambda_{\chi,n}}\right)\left(\lambda_{H\chi} + \sqrt{4\lambda_H\Lambda_{\chi,n}}\right)} > 0,$$

where for simplicity we define the effective couplings

$$\Lambda_{\chi,n} \equiv \frac{1}{n}\widetilde{\lambda}_\chi + \lambda_\chi \quad \text{and} \quad \Lambda_{H\Phi} \equiv \lambda_{H\Phi} + \widetilde{\lambda}_{H\Phi}\rho^2. \tag{4.2.8}$$

There are two variables in these conditions, $n \in \{1, \ldots, N\}$ and $\rho^2 \in [0, 1]$, where the conditions have to hold for all of their values. Notice that they only enter the conditions through $\Lambda_{\chi,n}$ and $\Lambda_{H\Phi}$. If $\widetilde{\lambda}_\chi > 0$, $\Lambda_{\chi,n}$ is the smallest when $n = N$, while if $\widetilde{\lambda}_\chi < 0$, the smallest $\Lambda_{\chi,n}$ is found for $n = 1$. Similar considerations apply to $\Lambda_{H\Phi}$ and ρ. A detailed derivation of these conditions can be found in the appendix B of the original paper.

- Vacuum Structure

  In order to be consistent with the current Higgs and EW precision measurements, as the inert doublet is charged under the EW gauge group, we consider the case that at zero temperature, both the inert Higgs and the singlets have zero VEV, say the physical vacuum is

$$\langle\{h, \varphi, \chi_1, \cdots, \chi_N\}\rangle = \{v_0, 0, 0, \cdots, 0\}, \tag{4.2.9}$$

  where $v_0 = 246$ GeV, and we require such vacuum state to be the global minimum of

the zero temperature potential. Firstly, for the physical vacuum to be a minimum, one needs to avoid tachyonic solutions, which give constraints on the bare mass parameters of the potential (at tree level)

$$\mu_\Phi^2 + \frac{\lambda_{H\Phi}}{2} v_{\rm EW}^2 \geq 0, \quad \mu_\chi^2 \geq 0. \tag{4.2.10}$$

Equation (4.2.10) does not involve the RG-generated parameters, $\widetilde{\lambda}_{H\Phi}$ and $\lambda_{H\chi}$ since it refers to the couplings at the physical minimum.

As stated above, at tree level, any possibly existing CP or charge breaking extrema are saddle points lying above the EW vacuum, which, therefore, do not put any further constraints on the viable parameter space. To secure that the EW vacuum is the global minimum of the tree-level potential in the subfield space of the two CP even components and the singlet degrees of freedom, we find all possible extrema of the polynomial potential (see all possible extrema at tree level in appendix B of our original paper) and we numerically impose the necessary conditions to establish that for each extremum either it cannot exist, or it is above the physical one.

Mean field analysis for the thermal history

This section provides an analytical understanding of the model parameter space compatible with the desired thermal history - the electroweak symmetry stays non-restored in the inert sector up to temperatures much higher than the EW scale, whereas the agent of the electroweak symmetry breaking changes at temperatures around the EW scale from the inert Higgs sector to the SM one. In this work, we do not explicitly discuss the UV scale physics completion that may lead to electroweak symmetry restoration at even higher energies and hence would allow for the possibility of EWBG. However, we will study the conditions necessary for the suppression of the sphaleron rate as a function of the model parameter space

through the whole temperature regime for which the electroweak symmetry is broken. More specifically, we will explore the constraints on the ratio between the electroweak symmetry breaking VEV/s to the temperature that may allow for such a suppressed sphaleron rate. This will provide a framework for future EWBG model building. If, instead, the new physics UV completion would directly provide a source of baryon asymmetry at the high scale, such as, for example, in the case of Leptogenesis, GUT-baryogenesis or Affleck-Dine baryogenesis [289], then the requirement on the sphaleron rate could be ignored. A discussion of possibilities for baryogenesis as well as specific details on the sphaleron rate relevant for our model will be presented in subsection 4.2.3.

We summarize the above desired thermal history with three conditions as follows

- **C1: Non-restoration of the electroweak symmetry**

  This is realized up to very high temperatures by having a non-trivial inert phase: $\langle\varphi\rangle_{\text{highT}} \neq 0$;

- **C2: Phase transitions from the inert Higgs phase to the SM Higgs phase**

  This condition secures that the universe is at the SM vacuum at zero temperature, while being compatible with C1.

- **C3[2]: Sufficiently suppressed sphaleron rate after EWSB**

  This would allow preserving any baryon number density that may be generated through an EWBG mechanism at the ultraviolet.

To gain an analytical understanding of the model parameter space compatible with the above conditions, we use a mean-field approximation of the finite temperature effective potential, where the thermal potential is evaluated up to leading order of the high-temperature

2. As discussed above, this condition is optional.

expansion

$$
\begin{aligned}
V^{\mathrm{MF}}_{\mathbb{Z}_N+\mathrm{I2HDM}} = &-\frac{1}{2}\left(\mu_H^2 - c_h T^2\right) h^2 + \frac{1}{2}\left(\mu_\Phi^2 + c_\varphi T^2\right)\varphi^2 + \frac{1}{2}\left(\mu_\chi^2 + c_\chi T^2\right)\chi_i^2 \\
&+ \frac{\lambda_H}{4}h^4 + \frac{\lambda_\Phi}{4}\varphi^4 + \frac{\widetilde{\lambda}_\chi}{4}\chi_i^4 + \frac{\lambda_\chi}{4}(\chi_i\chi_i)^2 \\
&+ \frac{\Lambda_{H\Phi}}{4}\varphi^2 h^2 + \frac{\lambda_{\Phi\chi}}{4}\varphi^2\chi_i^2 + \frac{\lambda_{H\chi}}{4}h^2\chi_i^2,
\end{aligned}
\tag{4.2.11}
$$

where c_i for $i = h, \varphi, \chi$ are given in eqs. (4.A.12)–Equation (4.A.14). Such a mean-field potential is a reliable approximation before considering RG improvement and daisy resummation, especially at high temperatures. We shall include resummations in the next section for a full numerical study at high field values and temperatures. Here we provide an analytical study based on the mean-field potential to obtain a coarse understanding of how the desired thermal history is achieved within our model.

Let us first study the SM and inert Higgs sector phases of the potential in Equation (4.2.11) . An inert phase P_Φ, where only the inert Higgs field has a non-zero field value, reads

$$
\mathrm{P}_\Phi : \langle (h, \varphi, \chi_1, \cdots, \chi_N) \rangle = (0, w(T), 0, \cdots, 0) \tag{4.2.12}
$$

with

$$
w(T) = \sqrt{-\frac{\mu_\Phi^2 + c_\varphi T^2}{\lambda_\Phi}}. \tag{4.2.13}
$$

At very high temperatures, $T^2 \gg \mu_\Phi^2$, one can approximate

$$
w(T) \approx \sqrt{-\frac{c_\varphi}{\lambda_\Phi}}T. \tag{4.2.14}
$$

Given the BFB condition that $\lambda_\Phi > 0$, a negative thermal mass coefficient c_φ,

$$c_\varphi = \frac{\lambda_\Phi}{2} + \frac{\lambda_{H\Phi} + \widetilde{\lambda}_{H\Phi}/2}{6} + \frac{3g^2 + g'^2}{16} + N\frac{\lambda_{\Phi\chi}}{24}, \tag{4.2.15}$$

generates a non-zero inert phase at very high temperatures, which is the key to achieve EWNR (or delayed restoration) in the inert sector in our model. This provides for condition C1 in the mean field approximation as

$$\mathrm{C1_{MF}} \quad \rightarrow \quad c_\varphi < 0. \tag{4.2.16}$$

The main driver of a negative c_φ is a negative cross quartic between the inert and the singlet sector $\lambda_{\Phi\chi}$, whose negative contribution is magnified by the number of singlets N. If the inert mass parameter $\mu_\Phi^2 \geq 0$, such a phase where only the inert field has a non-zero VEV would disappear at a temperature T_Φ^r (either as a global or local minimum), where

$$T_\Phi^r = \sqrt{\frac{\mu_\Phi^2}{-c_\varphi}}. \tag{4.2.17}$$

A low restoration temperature T_Φ^r facilitates the existence of phase transitions between the inert and SM Higgs phases as well as the associated condition for a suppressed sphaleron rate, which will be discussed in more detail below. Instead, if $\mu_\Phi^2 < 0$, this inert phase exists at zero temperature, which puts a constraint

$$\mu_\Phi^2 > -\sqrt{\frac{\lambda_\Phi}{\lambda_H}}\mu_H^2 \tag{4.2.18}$$

for it to be above the EW vacuum at $T = 0$, i.e. $V_0(0, w(0), 0, \cdots 0) > V_0(v_0, 0, 0, \cdots 0)$, in addition to condition in Equation (4.2.10).

A SM Higgs phase P_H of the potential, where only the SM Higgs has a non-zero field

value, reads

$$\mathrm{P}_H : \langle (h, \varphi, \chi_1, \cdots, \chi_N) \rangle = (v(T), 0, 0, \cdots, 0) \tag{4.2.19}$$

with

$$v(T) = \sqrt{\frac{\mu_H^2 - c_h T^2}{\lambda_H}}, \tag{4.2.20}$$

where at zero temperature it becomes the EW vacuum with $v(0) = v_0$. Such a phase appears at a temperature

$$T_H^r = \sqrt{\frac{\mu_H^2}{c_h}}. \tag{4.2.21}$$

Another phase that possibly exists during the thermal history is when both the SM Higgs and the inert Higgs fields acquire simultaneously non-zero values

$$\mathrm{P}_{H\Phi} : \langle (h, \varphi, \chi_1, \cdots, \chi_N) \rangle = (\widetilde{v}(T), \widetilde{w}(T), 0, \cdots, 0) \tag{4.2.22}$$

where

$$\widetilde{v}(T) = \sqrt{\frac{\widetilde{\mu}_H^2 - \widetilde{c}_h T^2}{\widetilde{\lambda}_H}}, \quad \widetilde{w}(T) = \sqrt{-\frac{\widetilde{\mu}_\Phi^2 + \widetilde{c}_\varphi T^2}{\widetilde{\lambda}_\Phi}} \tag{4.2.23}$$

with

$$\begin{aligned} \widetilde{\mu}_H^2 &\equiv \mu_H^2 + \frac{\Lambda_{H\Phi}}{2\lambda_\Phi}\mu_\Phi^2, \quad \widetilde{\mu}_\Phi^2 \equiv \mu_\Phi^2 + \frac{\Lambda_{H\Phi}}{2\lambda_H}\mu_H^2, \\ \widetilde{c}_h &\equiv c_h - \frac{\Lambda_{H\Phi}}{2\lambda_\Phi}c_\varphi, \quad \widetilde{c}_\varphi \equiv c_\varphi - \frac{\Lambda_{H\Phi}}{2\lambda_H}c_h, \\ \widetilde{\lambda}_H &\equiv \lambda_H - \frac{\Lambda_{H\Phi}^2}{4\lambda_\Phi}, \quad \widetilde{\lambda}_\Phi \equiv \lambda_\Phi - \frac{\Lambda_{H\Phi}^2}{4\lambda_H}, \end{aligned} \tag{4.2.24}$$

implying that this phase is governed by the Higgs-Inert mixing coupling $\Lambda_{H\Phi}$ defined in Equation (4.2.8). An important feature of this phase is that given the potential in Equation (4.2.11), the potential difference reads

$$\begin{aligned} V(\mathrm{P}_{H\Phi};T) - V(\mathrm{P}_{H};T) &\propto -(4\lambda_{\Phi}\lambda_{H} - \lambda_{H\Phi}^{2})^{-1} \\ V(\mathrm{P}_{H\Phi};T) - V(\mathrm{P}_{\Phi};T) &\propto -(4\lambda_{\Phi}\lambda_{H} - \lambda_{H\Phi}^{2})^{-1}, \end{aligned} \tag{4.2.25}$$

where the proportionality coefficients are always positive independent of the temperature. Thus, if $4\lambda_{\Phi}\lambda_{H} - \lambda_{H\Phi}^{2} \leq 0$, the Higgs-inert phase $\mathrm{P}_{H\Phi}$ is irrelevant as it is always shallower than either the SM or inert Higgs phases. On the contrary, if $4\lambda_{\Phi}\lambda_{H} - \lambda_{H\Phi}^{2} \geq 0$, as long as such a Higgs-inert phase exits, it is deeper than both the SM or inert Higgs phases, thus becoming the global minimum.

Concentrating on the case where $\mathrm{P}_{H\Phi}$ is the global minimum at a given temperature, notice that the situation $4\lambda_{\Phi}\lambda_{H} - \lambda_{H\Phi}^{2} \geq 0$ coincides with the BFB condition if $\lambda_{H\Phi} \leq 0$, hence for negative/zero cross quartic, the Higgs-inert phase will be the global minimum at finite temperature. Moreover, at zero temperature, the non-tachyonic condition enforced in Equation (4.2.10) implies $\widetilde{\mu}_{\Phi}^{2} = m_{\phi}^{2} \geq 0$. This yields that whenever $4\lambda_{\Phi}\lambda_{H} - \lambda_{H\Phi}^{2} \geq 0 \rightarrow \widetilde{\lambda}_{\Phi} \geq 0$, there is no real solution for $\widetilde{w}(0)$ in Equation (4.2.23), as expected since the non-tachyonic solution was derived under the assumption that the P_{H} at $T = 0$ being the physical vacuum. In addition, let's recall that at very high temperatures we have restricted our case to the inert phase P_{Φ} being the global minimum (no electroweak symmetry breaking in the SM Higgs sector), hence Equation (4.2.23) implies that we voluntarily enforced

$$\widetilde{c}_{h} \geq 0 \vee \widetilde{c}_{\varphi} \geq 0 \tag{4.2.26}$$

whenever $T^{2} \gg \widetilde{\mu}_{H(\Phi)}^{2}$. Given the above constraints (P_{H} and P_{Φ} are the global minimum at $T = 0$ and high temperatures, respectively), if the phase $\mathrm{P}_{H\Phi}$ ever appears, in a temperature

regime $T^2 \sim \widetilde{\mu}^2_{H(\Phi)}$, it develops at a temperature $\text{Max}\{\widetilde{T}^r_H, \widetilde{T}^r_\Phi\}$ and must disappear at a lower temperature $\text{Min}\{\widetilde{T}^r_H, \widetilde{T}^r_\Phi\}$. These two characteristic restoration temperatures are defined from Equation (4.2.23) demanding that either $\widetilde{v}(\widetilde{T}^r_H) = 0$ or $\widetilde{w}(\widetilde{T}^r_\Phi) = 0$, respectively. Observe that, within the mean field approximation we are considering, from eqs. (4.2.13), Equation (4.2.20) and Equation (4.2.23), it follows $w(T^c_H) = \widetilde{w}(T^c_H)$ and $v(T^c_\Phi) = \widetilde{v}(T^c_\Phi)$. As a consequence, $V(\text{P}_{H\Phi}; \widetilde{T}^r_H) = V(\text{P}_\Phi; \widetilde{T}^r_H)$ and $V(\text{P}_{H\Phi}; \widetilde{T}^r_\Phi) = V(\text{P}_H; \widetilde{T}^r_\Phi)$, which implies that, the critical temperature defining the transition between the $\text{P}_{H\Phi}$ and $\text{P}_\Phi(\text{P}_H)$ phases is given by $T^c_H = \widetilde{T}^r_H$ ($T^c_\Phi = \widetilde{T}^r_\Phi$), indicating that these transitions are second order within the mean field approximation. These equalities imply that,

$$T^c_H = \sqrt{\frac{\widetilde{\mu}^2_H}{\widetilde{c}_h}}, \quad T^c_\Phi = \sqrt{\frac{\widetilde{\mu}^2_\Phi}{-\widetilde{c}_\varphi}}, \tag{4.2.27}$$

and their existence demands

$$\frac{\widetilde{\mu}^2_H}{\widetilde{c}_h} \geq 0 \wedge \frac{\widetilde{\mu}^2_\Phi}{-\widetilde{c}_\varphi} \geq 0. \tag{4.2.28}$$

In the numerical study where we consider the full thermal potential as well as daisy contributions, such phase transitions could be affected and become first order. However, they would hardly be strongly first order in the absence of large thermal or tree level barriers.

Other possible phases associated with the finite temperature potential Equation (4.2.11) include the trivial point, which, as long as any of the above phases exist, yields a shallower value of the potential, as well as phases involving singlets with non-zero field values. The latter will not be further considered in this section as they are unlikely to participate in the thermal history. When evaluating the thermal history in the numerical section, however, all possible phases will be taken into account.

After having considered the existence of all possible phases and some of their properties, let us now concentrate on the specifics of the phase transitions from the inert sector to the

SM Higgs sector.

First, we discuss the simpler case where the phase $\mathrm{P}_{H\Phi}$ either never appears or is irrelevant. In such a case, there should be a phase transition from P_{Φ} to P_{H}, as illustrated on the middle penal of the second row in Figure 4.1. Given the potential in Equation (4.2.11), such a transition happens at a critical temperature

$$T_c = \sqrt{\frac{\mu_H^2 + \sqrt{\lambda_H/\lambda_\Phi}\mu_\Phi^2}{c_h - \sqrt{\lambda_H/\lambda_\Phi}c_\varphi}}, \tag{4.2.29}$$

at which the potential becomes degenerate $V(\mathrm{P}_H; T_c) = V(\mathrm{P}_\Phi; T_c)$. The condition for such a T_c to exist reads (with help from the zero temperature constraint Equation (4.2.10))

$$-\sqrt{\frac{\lambda_\Phi}{\lambda_H}}\mu_H^2 < \mu_\Phi^2 < -\frac{c_\varphi}{c_h}\mu_H^2, \tag{4.2.30}$$

and this will have a relevant impact on the allowed values of the inert Higgs boson mass, as will be discussed later on.

As mentioned in C3, to allow for the possibility of a EWBG after UV completion, we will look at the conditions on the sphaleron rate at finite temperatures. The dilution of the baryon number density after the onset of a UV induced EWPT responsible for the EWBG will be double exponentially suppressed by the ratio of the sphaleron energy to temperature, see discussion in subsection 4.2.3. Hence successful EWBG in the complete model will require (see e.g. [39])

$$\xi(T) = \frac{v_{\mathrm{EW}}(T)}{T} \equiv \frac{\sqrt{\langle\varphi(T)\rangle^2 + \langle h(T)\rangle^2}}{T} \gtrsim 1, \tag{4.2.31}$$

where φ and h are the inert and SM Higgs fields charged under the EW gauge group. This condition should be satisfied at any temperatures throughout the thermal history from the creation of baryon asymmetry up to present times. It can be shown that such a condition

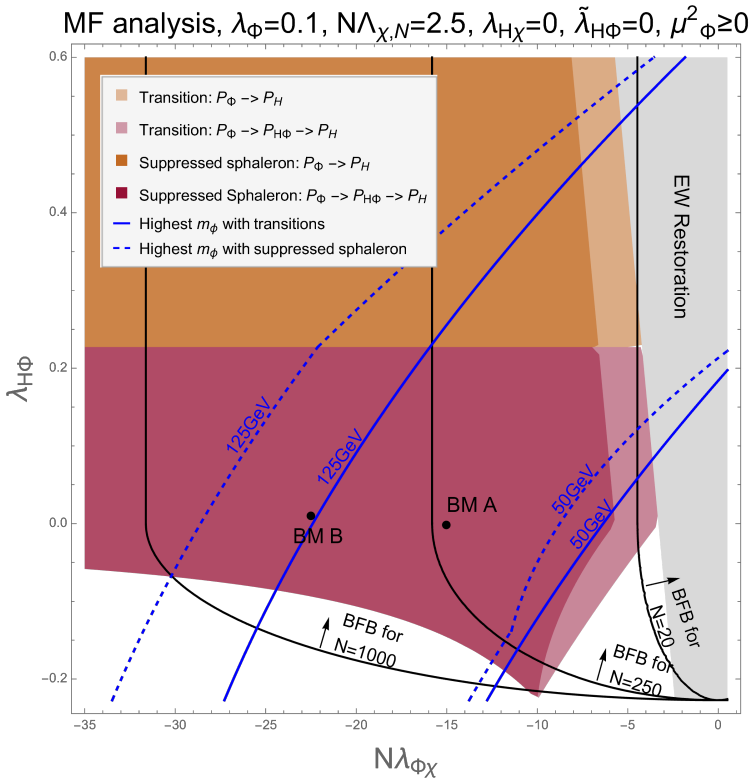

Figure 4.2: Parameter space on the $N\lambda_{\Phi\chi} - \lambda_{H\Phi}$ plane compatible with desired thermal histories based on a mean field analysis. Relevant zero temperature constraints are also shown. Other parameters are fixed: $\lambda_\Phi = 0.1$, $N\Lambda_{\chi,n} = 2.5$, $\lambda_{H\chi} = 0$, $\widetilde{\lambda}_{H\Phi} = 0$, and $\mu_\Phi^2 \geq 0$ is imposed.

can be satisfied if the phase transition P_Φ to P_H fulfills

$$\mathrm{Min}\left\{\frac{w(T_c)}{T_c}, \frac{v(T_c)}{T_c}\right\} \gtrsim 1. \tag{4.2.32}$$

This follows from the fact that as long as $\mu_\Phi^2 \geq 0$, as will be implemented in our BM scenarios,

$$\xi(T) = \frac{w(T)}{T} \geq \frac{w_c}{T_c} \quad \text{for} \quad \mathrm{T} \geq \mathrm{T_c}, \tag{4.2.33}$$

$$\xi(T) = \frac{v(T)}{T} \geq \frac{v_c}{T_c} \quad \text{for} \quad \mathrm{T} \leq \mathrm{T_c}. \tag{4.2.34}$$

Next, we discuss the case where the phase $\mathrm{P}_{H\Phi}$ is relevant and appears as a global min-

imum in the thermal history, as illustrated on the left panel of the second row in Figure 4.1. To have a two step phase transition near the EW scale

$$\mathrm{P}_{\Phi} \xrightarrow{T_H^c} \mathrm{P}_{H\Phi} \xrightarrow{T_\Phi^c} \mathrm{P}_H, \tag{4.2.35}$$

one needs

$$T_H^c \geq T_\Phi^c, \tag{4.2.36}$$

with

$$\widetilde{\mu}_H^2 \geq 0, \quad \widetilde{c}_h \geq 0, \quad \widetilde{\mu}_\Phi^2 \geq 0, \quad \widetilde{c}_\varphi \leq 0, \tag{4.2.37}$$

which corresponds to the condition for these two temperatures to exist given by Equation (4.2.28).

Analogous to the previous case, the condition to avoid baryon asymmetry washout in the context of a EWBG in an UV completed theory, would require

$$\mathrm{Min}\left\{\frac{w(T_H^c)}{T_H^c}, \frac{v(T_\Phi^c)}{T_\Phi^c}\right\} \gtrsim 1. \tag{4.2.38}$$

Another thing to notice in this case is the role played by the mixing quartic $\lambda_{H\Phi}$, which controls the deviation from T_H^c to T_H^r and from T_Φ^c to T_Φ^r. The smaller the mixing quartic, which is the region that we are mainly interested in, the smaller the deviations are. Moreover, in the region of small $\lambda_{H\Phi}$, the phase transition pattern $\mathrm{P}_\Phi \to \mathrm{P}_{H\Phi} \to \mathrm{P}_H$ is most likely to happen due to the decoupled contributions from the inert and SM Higgs minima to render the $\mathrm{P}_{H\Phi}$ minimum in the intermediate temperature range. This is apparent in Figure 4.2 to be discussed below.

It is also possible to have a temporary electroweak symmetry restoration at temperatures

between those supporting the two EW breaking phase structures P_Φ and P_H. This is the case when T^r_Φ is higher than T^r_H, as illustrated on the right penal of the second row in Figure 4.1. Since in the temperature range between T^r_H and T^r_Φ the system is in a EW restoring phase, this scenario would allow for the EW sphaleron to be active in this regime. The sphaleron will wash out any baryon asymmetry that could have been generated by high scale EWBG. At this moment, we will mainly focus on the previous cases that are compatible with an UV EWBG mechanism.

Another possible case is a more fine-tuned four-step phase transition when $T^c_H \leq T^c_\Phi$ and $T^r_H \geq T^r_\Phi$. This case will require large mixing quartic and significant fine-tuning of the parameter space. We do not further concentrate on this case.

In Figure 4.2, we show the parameter space spanned by $N\lambda_{\Phi\chi} - \lambda_{H\Phi}$ considering the zero temperature constraints discussed in subsection 4.2.1 and the different thermal history possibilities discussed above. The region violating condition $\mathrm{C1_{MF}}$ is shaded gray, while the regions satisfying the thermal history patterns and the non-washout conditions are highlighted with light and dark orange (light and dark maroon) for the transition pattern $\mathrm{P}_\Phi \to \mathrm{P}_H$ ($\mathrm{P}_\Phi \to \mathrm{P}_{H\Phi} \to \mathrm{P}_H$), respectively. There is no region that satisfies the rare four-step phase transition. The conditions for the correct zero temperature vacuum structure are satisfied on the whole parameter space if we impose $\mu^2_\Phi, \mu^2_\chi \geq 0$. The region giving a tree-level BFB potential, calculated from conditions Equation (4.2.6), is at the right side of the black solid lines for different number of singlet scalars N. Notice that, within the mean-field approximation, the thermal history patterns, as well as the non-washout requirements, are independent on N as long as the value of $N\lambda_{\Phi\chi}$ is kept a constant. Since both the thermal histories and non-washout conditions are strongly correlated to the inert mass parameter, the mass of the inert Higgs boson is in turn also constrained. In Figure 4.2, we show solid blue lines that determine the maximal value of the inert Higgs boson mass compatible with the corresponding phase transition patterns for a given value of $N\lambda_{\Phi\chi}$ and $\lambda_{H\Phi}$. Higher values

of the inert Higgs boson mass can be achieved to the left of the lines. Similar lines for the suppressed sphaleron rate conditions are shown by the dotted blue lines. Other parameters have been fixed in Figure 4.2 to be $\lambda_\Phi = 0.1$, $N\Lambda_{\chi,n} = 2.5$ and $\lambda_{H\chi} = 0$, $\widetilde{\lambda}_{H\Phi} = 0$. The SM Higgs sector parameters are fixed to satisfy the Higgs VEV and mass at the tree level. We constrain the discussion to the case $\mu_\Phi^2 \geq 0$, which makes conditions Equation (4.2.32) and Equation (4.2.38) sufficient to secure a suppressed sphaleron rate within the mean field approximation as discussed above. In addition, in Figure 4.2, we also show the two benchmark points A and B [3], which will be discussed in the full numerical study in the next section.

From Figure 4.2, one notices that the region where the cross quartic coupling between the inert and the SM Higgs sectors almost vanishes, i.e. $\lambda_{H\Phi} \sim 0$ and hence the SM Higgs sector is minimally perturbed, can be compatible with the desired thermal history. Main constraints on the parameter space come from the tension between the BFB and desired thermal history: the more negative the cross quartic $N\lambda_{\Phi\chi}$, the easier the non-restoration and the lower the critical temperatures which yield larger EW VEV to temperature ratios $\xi(T)$. A more negative cross quartic coupling $N\lambda_{\Phi\chi}$ makes it harder for the potential to be BFB, as shown in Equation (4.2.6). Moreover, a larger number of singlets in turn helps to relax the BFB condition on $N\lambda_{\Phi\chi}$ by relaxing its lower bound while increasing the singlet effective quartic coupling $N\lambda_\chi$. As mentioned above, another constraint is on the mass of the inert Higgs boson. The restriction on the parameter space is alleviated for a lighter inert Higgs boson mass, especially in the region where the cross quartic $\lambda_{H\Phi}$ is small. This can be easily understood, for example in the $\mathrm{P}_\Phi \to \mathrm{P}_H$ phase transition pattern, since a smaller inert mass parameter μ_Φ^2 yields a lower critical temperature T_c, as is shown in Equation (4.2.29). A similar argument, although more involved, applies to the two-step phase transition. The direct correlation between a smaller inert Higgs boson mass and a smaller inert mass parameter μ_Φ^2 especially holds in the region of small $\lambda_{H\Phi}$, as the one

3. BM point B has a slightly different value of $N\Lambda_{\chi,n}$ than the one used in Figure 4.2. However, the error of this point's position in the $N\lambda_{\Phi\chi} - \lambda_{H\Phi}$ plane is within the thickness of the point drawn in the plot.

considered here. Observe however, an inert Higgs boson mass above half of the SM Higgs mass can be achieved, even with $\lambda_{H\Phi} \sim 0$, as far as the number of singlets is sufficient to be in the BFB allowed region.

The analysis in this section is based on the mean-field approach, where we consider the leading order high-temperature expansion of the thermal potential. For temperatures well above the EW scale however, including the RG improvement and the daisy resummation becomes necessary. In the next section, we perform a full numerical study for two benchmark points and present the results for different approximations.

4.2.2 Numerical implementation and results

In this section, we explore the thermal histories of two model benchmark points based on numerical calculation of the finite temperature effective potential, including RG improvement and thermal resummations, which have been introduced in chapter 2. Here we summarize the relevant contributions, and define the effective potential prescriptions used to perform the thermal calculation.

At one-loop order, the zero temperature loop correction can be taken into account through the CW potential under the $\overline{\text{MS}}$-renormalization scheme, where the field dependent masses of all degrees of freedom in the plasma for our model are given in appendix subsection 4.A.1. We work in the Landau gauge [59], which introduces a gauge-dependence of the EP [51, 52, 80, 81, 123–125, 127, 128] [4]. The CW potential changes the shape of the zero temperature potential, introducing deviations from the tree level constraints at zero temperature that we

4. Given that we observe that the high-temperature expansion approximation is in good qualitative agreement with the full treatment of the temperature effects when considering the EWNR analysis, we argue that the main results of this work will not be qualitative changed by effects of gauge dependence. Indeed, the EW non-restoration at high temperatures relies on a negative thermal mass for the inert Higgs that is governed by the leading order term in the high-temperature expansion, which in turn does not exhibit gauge dependence. Indeed Ref [127, 128] shows that the gauge dependence appears only in the sub-leading temperature-dependent terms in the high-temperature expansion. A dedicated study of the gauge dependence considering a numerical analysis of the full temperature-dependent EP would be necessary to fully understand the relevance of gauge-dependent effects in the analysis of EW non-restoration, which is beyond the scope of this work.

discussed in the last section. Specifically, to accommodate the Higgs VEV of 246 GeV and a 125 GeV mass eigenstate the parameters μ_H^2 and λ_H have to be adjusted to recover the two physical conditions at $T = 0$. Other zero temperature constraints, including the BFB and correct vacuum structure, also need to be adjusted numerically, as necessary, so that they remain robust after the inclusion of loop corrections. The leading temperature dependence is given by the thermal one-loop effective potential.

At very high temperatures and very large field values, which are the relevant scales for the electroweak symmetry non-restoration or delayed restoration scenarios, perturbative convergence of the fixed-order calculation becomes compromised, for both the CW and the one-loop thermal potential. To account for higher order thermal loop contributions, we implement the full dressing daisy resummation which involves adding thermal corrections to the tree level effective masses in the effective potential, as has been discussed in section 2.2. We implement the high-T thermal masses in Equation (2.24), the truncated thermal masses in Equation (2.23), and the gap thermal masses in Equation (2.22) in comparison, to effectively resum higher-order daisy diagrams. In Figure 4.3, we show the squared thermal mass of the scalars as a function of the inert field values at a temperature of $T = 5000$ GeV, computed with the different levels of accuracy described above, for the BM scenario B to be defined in Table 4.1. The high-T thermal masses should be independent of the inert field value ϕ, however, Figure 4.3 shows a small variation with respect to the field value due to the RG improvement implementation to be discussed below. The truncated thermal masses have an enhanced dependence of the inert field value, especially for the inert thermal mass itself, but a more sizable variation occurs for the gap thermal masses. The differences among thermal masses for different implementations as shown in Figure 4.3 will end up, however, having a very small impact on the results relevant for the phase structure of the EW non-restoration BMs.

We implement the RG improvement of the effective potential for all numerical calculations

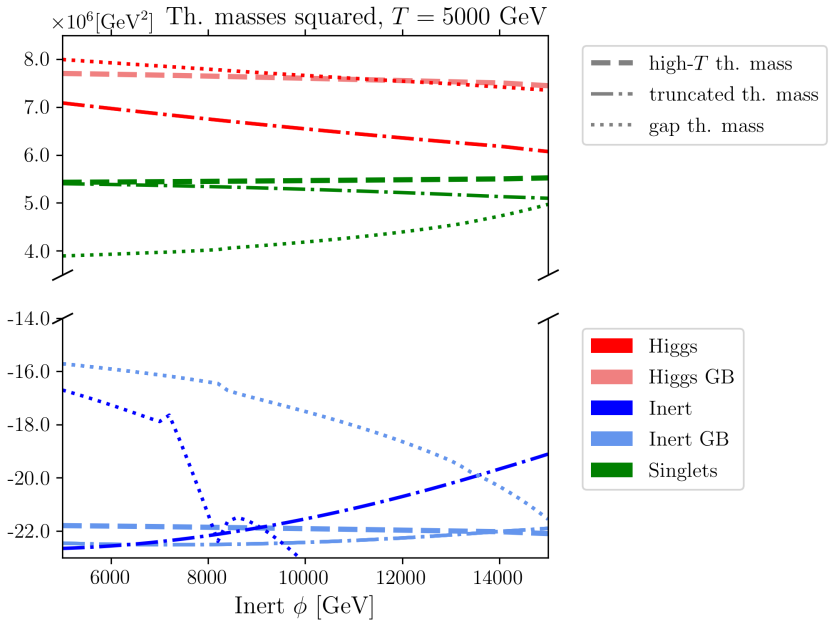

Figure 4.3: Squared thermal mass of the scalars for the BM scenario B as a function of the inert field values at $T = 5000$ GeV for different thermal mass implementations.

to account for higher order logarithmic corrections arising from zero temperature loops, as has been discussed in section 2.3. At finite temperature, the choice of the renormalization scale, should vanish or minimize the un-resummed logarithms such as $\log^{\mathcal{N}}\left(\frac{M_i^2(\hat{\Phi})+\Pi_i^2}{\mu_{\rm R}^2}\right)$ for $\mathcal{N} \geq 2$ [73,75]. Our model at hand involves multiple degrees of freedoms, therefore, there is no single choice of the scale to make all the logarithms negligible. In this work, we choose

$$\mu_R^2 = \text{Max}\left\{M_i^2(\hat{\Phi}) + c_i T^2; (246\text{ GeV})^2\right\}, \tag{4.2.39}$$

where i runs over all degrees of freedom (mass eigenstates) in the plasma and the short-handed notation has been introduced for the dynamical fields $\hat{\Phi} \equiv \{h, \varphi, \chi_1, \chi_2, \cdots, \chi_N\}$. This is a convenient choice as long as there is no large separation between scales of the particles' masses, including the thermal mass contribution, as well as between the particle masses and the temperature, as it is the case in our study. The CW potential further

includes polynomial contributions of the radiative corrections. It also partially accounts for multi-scale particle threshold effects beyond the one single scale threshold taken into account through the RG improvement. We collect the one-loop beta functions and wave function renormalization factors for our model in appendix subsection 4.A.3. [5]

Details of our `python` implementation can be found in Appendix F in our original paper. The main result of the algorithm is the value of the global minimum at a given temperature. The set of all global minima at a given set of temperatures defines the phase history we consider. A phase transition is observed when there is a change of phase pattern (e.g. from an inert-only-phase to an inert-SM Higgs phase) at a certain temperature[6]. In this section, we also explore the value of the EW VEV to temperature ratio $\xi(T)$, which is relevant for obtaining information on the sphaleron rate.

We define two characteristic benchmark points for our model - benchmark A that has inert Higgs eigenstates with masses slightly above half of the Z boson mass, and a benchmark B that has inert Higgs eigenstates with masses slightly above half of the SM Higgs boson mass. Inert mass eigenstates with masses above 100 GeV can be achieved, but they would either lead to restoration of the electroweak symmetry at intermediate temperature scales or would require a number of singlet scalars of order $\mathcal{O}(1000)$ or more. The specific values of the model parameters and masses are given in Table 4.1.

We implement the RG improvement on the BFB conditions of Equation (4.2.6) and find that, at scales of the order of 10^5 GeV, these conditions are violated for both BMs [7]. Such an energy scale is of the order of the scale at which the SM Higgs quartic coupling becomes negative through its SM one loop RGE. This is expected since we consider that the SM

5. Notice that here the RG improvement we perform does not involve temperature flow as has been proposed, for example in [87–89], where they treat temperature as an independent scale that participates in the RG flow and thermal diagrams, like daisy and super-daisy, would have been resumed as a result.

6. We leave a detailed scan of the transition using nucleation temperatures instead of critical temperatures to later work.

7. There is a small dependence on the CW treatment that somewhat perturbs the SM Higgs quartic coupling as is explained above.

Higgs only interacts with the extended scalar sector through a tiny inert-Higgs coupling, and therefore its quartic coupling evolution should be minimally perturbed compared to its SM behavior. The scale above gives a rough estimate of the energy scales up to which our results can be trusted. By minimizing the finite temperature potential numerically, we have checked that the potential remains stable up to high energy scales shown below for both BMs. We also ran the RGE of the model (see eqs.Equation (4.A.18)) for BMs A and B and found that Landau poles appear at energies around $2.5 \cdot 10^{14}$ GeV and 10^{15} GeV, respectively - well above the scale of validity of the theory at the one-loop RGE level.

Table 4.1: Parameter choices for the BMs A and B. The dimensionful quantities are in units of GeV.

	μ_H^2	λ_H	μ_Φ^2	λ_Φ	μ_χ^2	λ_χ	$\lambda_{H\Phi}$	$\widetilde{\lambda}_{H\Phi}$
BM A	8994.45	0.119	2500	0.1	100	0.01	-0.001	0
BM B	8991.84	0.119	5800	0.1	5000	0.004	0.01	0

	$\lambda_{\Phi\chi}$	$\widetilde{\lambda}_\chi$	$\lambda_{H\chi}$	N	m_h	m_ϕ	m_χ	
BM A	-0.06	0	0	250	125	48.47	9.8	
BM B	-0.0375	0	0	600	125	84.58	68.87	

In Figure 4.4 and Figure 4.5, we show the phase structure (upper panel) and EW VEV-temperature ratio (lower panel) for BMs A and B, respectively, and for different implementations of the finite temperature effective potential as introduced in **??**. In the phase structure plot, we are showing as a function of the temperature the field values of the SM Higgs (red), inert Higgs (blue), and singlet (green) [8] at the global minimum. In the VEV-temperature ratio plot, we show the value of $\xi(T)$, as defined in eq. (4.2.31), as a function of the temperature. To showcase the uncertainties associated with different finite temperature implementations, we show results obtained with no daisy resummation (solid lines), daisy resummation with high-T thermal masses, as in eq. (2.24), (dashed lines), and daisy resum-

8. We assume all singlets have the same VEV — it's either all or none. Given that $\widetilde{\lambda}_\chi = 0$, which we chose at tree level and is protected against RGE, we have the $SO(N)$ symmetry that we can use to rotate in that form.

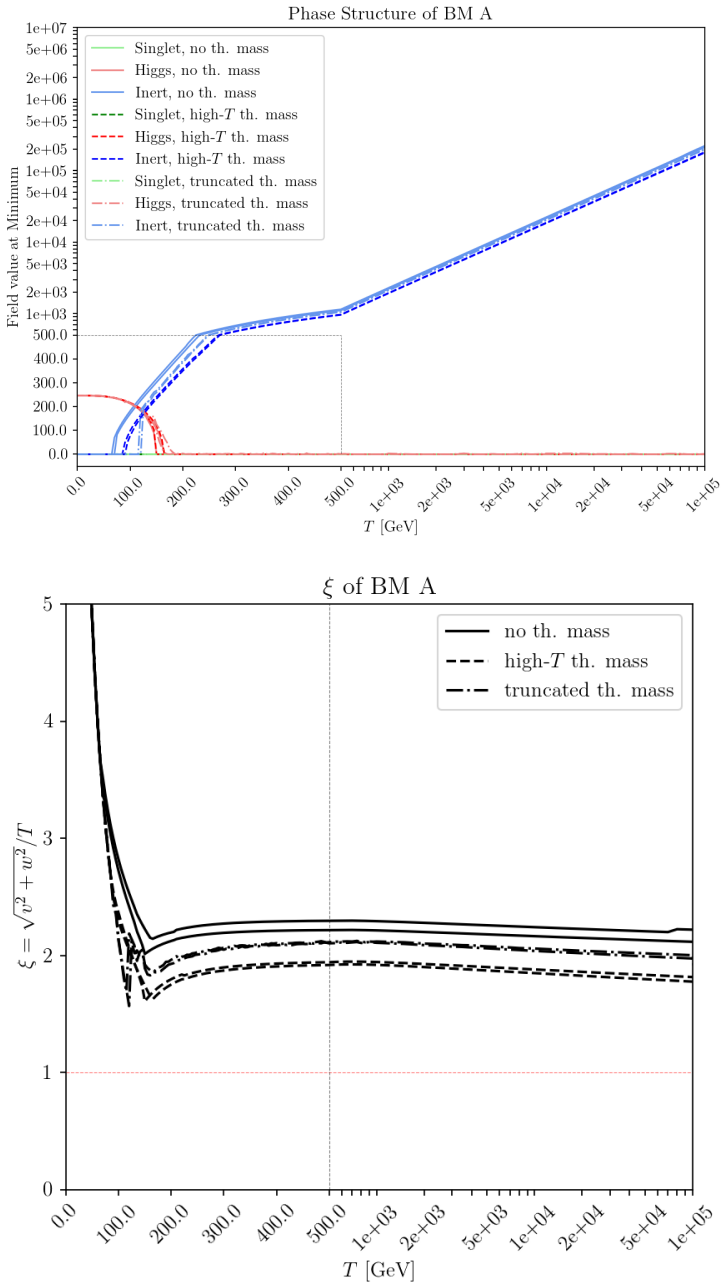

Figure 4.4: Phase structure (upper panel) and EW VEV-temperature ratio (lower panel) as a function of temperature, for different finite temperature implementations, for BM point A as defined in Table 4.1

mation with truncated thermal masses, as in eq. (2.23), (dashed-dotted lines). In addition, we have included the RG improvement for all calculations, and consider the uncertainties

related to the CW potential, which takes care of multi-scale issues beyond the RG improvement. In the figures, we use the same type of lines to represent a given finite temperature approximation with or without the CW contribution. Hence the space in between the lines shows the uncertainty related to the CW effects. It is apparent from the figures that this accounts for a small effect, and we will not discuss it any further.

In Figure 4.4, for BM A, one observes that the major uncertainty is caused by the effects of daisy resummation and the impact of different thermal mass treatments within the daisy resummation. However, the most important feature of these results is that the qualitative behavior of the phase structure, in Figure 4.4 upper panel, and the EW VEV-temperature ratio affecting the sphaleron rate, in Figure 4.4 lower panel, is not significantly modified by the different finite temperature treatments. In fact, BM A exhibits both the feature of EW non-restoration until high energies and $\xi(T) > 1$. The plots of BM A are shown up to the temperature of 10^5 GeV, after which the potential becomes unbounded from below. Observe that there is a kink below/about 200 GeV, which is due to the phase transition pattern from the P_{Φ} phase to the $\mathrm{P}_{H\Phi}$ phase, and it is a physical effect. In addition, there is a spike at $T \sim 110$ GeV for the daisy resummation with truncated thermal masses, which is, however, a defect of this finite temperature implementation. We expect this effect to be smoothed out when implementing an improved treatment of the thermal masses [9].

In Figure 4.5, we show similar results as for Figure 4.4, but for a heavier inert Higgs boson mass of the order of $m_h/2$ that will allow for different phenomenology. Same as BM A, BM B exhibits both the feature of EW non-restoration until high energies and $\xi(T) > 1$. The plots are shown up to the temperature of $T = 4 \cdot 10^4$ GeV, after which the potential becomes unbounded from below. For the BM B, there is a kink above/about 100 GeV, which

9. This spike is a defect associated with the truncated thermal mass calculation, where the second derivative of the thermal potential diverges when its argument, M^2/T^2, is close to 0. Indeed, such an effect does not happen for implementation with high-T thermal masses, as the divergence does not exist for the thermal potential within this approximation. Using the full gap equation, where the IR divergence is cured by including the thermal correction prior to performing the derivative, we expect the spike artifact shown in Figure 4.4 lower panel to disappear.

is due to the phase transition from the $P_{H\Phi}$ phase to the P_H phase. In addition, analogs to BM A, there is a spike at around $300 - 400$ GeV for the daisy resummation with truncated thermal masses, which we understand is the same type of artifact as discussed above and will be cured by implementing an improved treatment of the thermal masses.

As described above, using the gap equation, eq. (2.22), to derive the thermal masses is the most robust procedure. However, solving the gap equation at every step in the minimization of the potential is computationally extremely expensive and is beyond the scope of this work. However, in order to secure that the non-restoration behavior at high temperatures survives the most precise treatment of the thermal masses through the gap equation, we checked for several high-temperature values all the way down close to the EW scale, that the non-restoration behavior and $\xi(T) > 1$ survive for both BM scenarios.

4.2.3 Baryogenesis and sphaleron rate

An important additional issue related to the high energy EWBG mechanism in the framework of delayed electroweak symmetry restoration, is that one needs to secure that a strong first-order phase transition takes place at the time of electroweak symmetry breaking. This is required by the out-of-equilibrium condition of Sakharov. Here, it is possible to exploit the existence of an inert fermion sector that suppresses the strength of the inert self-coupling and thereby enhances the strength of the phase transition.

As it is clear from the above discussion, a successful UV model of high-temperature EWBG will demand detailed model building, which we leave for future publication. In the following, we will concentrate on the EW non-restoration case at hand, where the SM Higgs sector is minimally perturbed, to discuss details of the sphaleron rate.

Once the UV completion allows for the creation of the baryon asymmetry through an EWGB mechanism at high temperatures, one needs to evaluate the sphaleron washout factor to preserve the asymmetry all the way down to zero temperatures. Our model generically

Table 4.2: Dilution factors $f_{w.o.} = 1 - n_B(t_{\rm now})/n_B(t_{\rm high})$ for our benchmark models as defined by the integral in eq. (4.2.42). The upper limit of the integration, $T_{\rm high}$, is taken as the highest temperatures in Figure 4.4 and Figure 4.5 respectively. The three entries per cell correspond to uncertainty choices of κ as 0.01κ / $\boldsymbol{\kappa}$ / 100κ. Top and bottom row per BM refer to using the CW contribution (top) or not (bottom).

	no th. mass	high-T th. mass
BM A	$< 10^{-16}$ / $\mathbf{10^{-16}}$ / 10^{-14}	10^{-11} / $\mathbf{10^{-9}}$ / 10^{-7}
	$< 10^{-16}$ / $\mathbf{4 \cdot 10^{-15}}$ / $4 \cdot 10^{-13}$	$2 \cdot 10^{-11}$ / $\mathbf{2 \cdot 10^{-9}}$ / $2 \cdot 10^{-7}$
BM B	$9 \cdot 10^{-10}$ / $\mathbf{9 \cdot 10^{-8}}$ / $9 \cdot 10^{-6}$	$4 \cdot 10^{-5}$ / $\mathbf{4 \cdot 10^{-3}}$ / 0.296
	$4 \cdot 10^{-12}$ / $\mathbf{4 \cdot 10^{-10}}$ / $4 \cdot 10^{-8}$	$2 \cdot 10^{-8}$ / $\mathbf{2 \cdot 10^{-6}}$ / $2 \cdot 10^{-4}$

	truncated th. mass
BM A	$8 \cdot 10^{-11}$ / $\mathbf{8 \cdot 10^{-9}}$ / $8 \cdot 10^{-7}$
	10^{-12} / $\mathbf{10^{-10}}$ / 10^{-8}
BM B	$7 \cdot 10^{-5}$ / $\mathbf{7 \cdot 10^{-3}}$ / 0.498
	10^{-4} / $\mathbf{0.012}$ / 0.694

predicts a slowly varying $\xi = v_{\rm EW}(T)/T$ up to high temperature, as well as a low scale phase transition between the inert doublet and the SM Higgs doublet phases near the weak scale. Following a high-scale SFOPT triggered by a UV completion of the model, the sphaleron will become inactive quite fast after that transition, but there will be some dependence on its rate on the model parameters. To properly compute the washout (dilution) of the baryon number density, one should integrate the effects of the sphaleron rate over a large range of temperatures (a large period of time), instead of the usual assumption that the washout factor is dominated near the vicinity of the phase transition and is treated as a constant.

Specifically, the amount of sphaleron induced washout is determined by two quantities: the product of prefactors entering in the sphaleron rate and the energy of the sphaleron that appears in one of the exponentials. The latter is straightforward to compute and largely depends on the gauge structure of the theory. We provide the necessary steps to get the sphaleron energy [290, 291] in detail in appendix subsection 4.A.4. The computation of the prefactors of the sphaleron rate are more model dependent. There are two different sources of

deviations from the SM results. First, we have an extended scalar sector and the additional particles might contribute through indirect effects in the prefactors. Second, we focus on the inert doublet, and its quartic coupling is different than the quartic of the SM Higgs. We therefore discuss the specifications of the prefactors from the SM values [38, 292] in detail in appendix subsection 4.A.4.

The sphaleron rate can be written as

$$\frac{\Gamma}{V} = 4\pi\omega_{-}\mathcal{N}_{tr}\mathcal{N}_{rot}T^3\left(\frac{v_{\rm EW}(T)}{T}\right)^6 \kappa \exp\left[-E_{sph}(T)/T\right], \tag{4.2.40}$$

where the evaluation of the prefactors $\omega_{-}, \mathcal{N}_{tr}, \mathcal{N}_{rot}$, and κ are explained in detail in appendix subsection 4.A.4 and in Figure 4.6.

The survival rate of the baryon number density at any given time t, after the onset of the transition at $t = 0$ is [39, 127, 293]

$$\frac{n_B(t_{now})}{n_B(0)} = \exp\left[-\frac{13n_f}{2}\int_0^{t_{now}} dt\,\frac{\Gamma(T(t))}{VT^3(t)}\right], \tag{4.2.41}$$

where we consider present time, $t = t_{now}$, and with n_f the number of fermion families.

In a radiation dominated Universe, changing the integration variable from time to temperature, the above equation reads

$$\frac{n_B(t_{\rm now})}{n_B(t_{\rm high})} = \exp\left[-\frac{13n_f}{2}\int_0^{T_{\rm high}} dT\,\frac{\Gamma(T)}{VT^6}M_{Pl}\sqrt{\frac{90}{8\pi^3 g^*}}\right], \tag{4.2.42}$$

where M_{Pl} is the Planck mass and g^* is the number of relativistic degrees of freedom. In our case, it is $g^* = 106.75 + 4 + N$ for the range of temperatures under consideration.

Based on the calculation presented above, we can define the washout or dilution factor as $f_{w.o.} = 1 - \frac{n_B(t_{\rm now})}{n_B(t_{\rm high})}$. In Table 4.2 we show the values of $f_{w.o.}$ for our two benchmarks.

We see that BM A has a negligible washout factor for all choices of parameters, even for the most aggressive assumption for the fluctuation determinant κ, which is a factor 100 larger than the value suggested in [294]. BM B shows sub-percent or even negligible washout for the majority of approximations. Only for the most aggressive choice of κ, we observe values that can be as high as 70%, which can be compensated by producing an initial asymmetry about three times larger than the asymmetry we observe now. If we consider the central value for κ, we see a washout of at most 1.2%. We also note that the washout factor governed by eq. (4.2.42) is much less sensitive to $T_{\rm high}$ than to effects at temperatures close to the EW scale. This is the case since at higher temperatures the double exponential in eq. (4.2.42) is larger than at EW temperatures. Indeed, at temperatures around the EW scale, there is an enhancement from the inverse of the Hubble expansion rate, as well as from the exponent proportional to $\exp\left[-\xi(T)\right]$, where $\xi(T)$ has its lowest values. That makes the double exponent in eq. (4.2.42) to take its smallest values for temperatures close to the EW scale. Hence at such temperatures is when the main effect of the exponential washout takes place. In other words, the relevant contribution to the washout factor is only at scales between the EW scale and around 500 GeV, while at high temperatures the exponential washout remains negligible. This holds as long as $\xi(T)$ does not fall fast below 1 at high temperatures, which is the case for our BMs. This ensures that high-temperature EWBG could build in through a proper UV completion of our model.

4.2.4 Phenomenology implementations

In this session, we discuss the general particle physics phenomenology considerations for our model framework, including Higgs and Z boson invisible decays, disappearing tracks, Higgs global coupling shifts, as well as Higgs diphoton coupling shifts. We note that our benchmark choices in the previous section are explicitly set to satisfy these constraints. Still, the content in section provide estimation of current physics constraints and future perspectives for this

model.

There are several phenomenological implications for our benchmark scenarios. At the zero temperature EW vacuum, there exists an additional discrete $\mathbb{Z}_2$ symmetry under which the new scalar fields Φ and χ_i are odd and the SM fields are even. This renders the χ_i and the neutral components of the inert doublet scalar Φ stable and invisible once produced.

The possible existence of light scalars, Φ and χ_i will open the possibilities of the SM Higgs decaying into invisible particles, via the generic portal couplings

$$\mathcal{L} \supset \lambda_{H\Phi}(H^\dagger H)(\Phi^\dagger \Phi) + \widetilde{\lambda}_{H\Phi}(H^\dagger \Phi)(\Phi^\dagger H) + \lambda_{H\chi}\chi_i^2(H^\dagger H). \tag{4.2.43}$$

The generic Higgs decay width into new scalars via this portal coupling is (per scalar degree of freedom):

$$\Gamma(h \to ss) = \frac{\lambda_{Hs}^2 v_0^2}{32\pi m_h}\sqrt{1 - \frac{4m_s^2}{m_h^2}}, \tag{4.2.44}$$

where the coupling λ_{Hs} can be one of the above quartics, $\lambda_{H\Phi}$, $\widetilde{\lambda}_{H\Phi}$ or $\lambda_{H\chi}$, and m_s can be the mass of the Φ or χ states, respectively.

The current LHC 95% confidence level (C.L.) limit on Higgs invisible decays is 26% [295, 296] and the HL-LHC projection is 5.6% [137]. When $m_s \ll m_h$, the phase space suppression is negligible and this translates into an upper limit for the SM-new scalars mixing quartics. The current and future limits on the mixing quartics read

$$\sqrt{N\lambda_{H\chi}^2 + 2(\lambda_{H\Phi} + \widetilde{\lambda}_{H\Phi})^2 + 2\lambda_{H\Phi}^2} \leqslant 0.015\ (0.007) \tag{4.2.45}$$

for LHC (HL-LHC). In the above, by including $2\lambda_{H\Phi}^2$, we also include the Higgs decays into a pair of the charged states from the inert doublet.

In the absence of other mass splitting generating interactions, e.g. $\widetilde{\lambda}_{H\Phi}$ being zero, one-loop SM effects generate mass splittings between the charged and neutral eigenstate of the

inert doublet of about 360 MeV [297]. The charged state will decay back to the neutral state via a soft charged pion, or via the three-body decay mediated by an off-shell W boson. The typical lifetime is independent of the inert doublet mass and is a few mm. Hence, this charged state can also be treated as invisible at colliders. In fact, precision Z boson measurements of its invisible decays exclude all inert masses below 45 GeV, and hence we shall only consider inert masses beyond the 45 GeV value [298].

Still, one can attempt to look for signals beyond the missing energy at colliders. At high energy colliders, such as the LHC, although challenging, one can look for the disappearing track signatures from the charged eigenstate of the inert doublet. However, it is well-known that this channel is difficult for Higgsinos, to which our inert doublet model signature resembles most. The current sensitivity from LHC disappearing track searches can exclude pure Higgsinos up to 78 GeV [299]. The inert doublet production rate from the Drell-Yan process is roughly a factor of four lower than that of Higgsino production, due to the inert charged Higgs being a scalar rather than a fermion. Furthermore, for small mixing quartics such as $\widetilde{\lambda}_{H\Phi}$, one can arrange additional contributions to the mass splitting between the neutral and charged inert doublet states. This will make the charged state decay promptly and therefore the disappearing track searches will no longer apply. Given the above, we are entitled to ignore the disappearing track search limits and only comply with the LEP Z invisible bounds for our benchmark scenarios. Future tests on disappearing tracks could still shed light on our model.

Summarizing, considering direct search constraints for our electroweak symmetry non-restoring model, we observe that the mixing quartics $\lambda_{H\Phi}$ and $\lambda_{H\chi}$ are bounded by constraints on invisible SM Higgs decay rates. This can give a strong handle for testing possible benchmarks, but at the same time there are models, like our BMs, in which they happen to have neglibible values. In this sense, the more direct and inevitable probe for our model at colliders are through the invisible Z decays, relying only on the gauge coupling structure.

Disappearing charged track searches open a new window of opportunity, if not undermined by parameter choices of the various mixing quartic couplings.

There are additional U(1) global symmetries in the inert sector Φ as well as $\mathbb{Z}_2$ symmetries under which the singlet fields χ_i are odd, that prevent direct mixings between these states with our SM Higgs doublet. There are, however, loop-induced corrections to the SM that can be probed through precision observables. The leading contribution to the electroweak precision observables (EWPO) is from the custodial symmetry breaking term $\widetilde{\lambda}_{H\Phi}$, inducing an operator contributing to the T-parameter [300]

$$\mathcal{O}_T = \frac{1}{2}(H^\dagger \overleftrightarrow{D}_\mu H)^2,\ c_T = \frac{\widetilde{\lambda}^2_{H\Phi}}{192\pi^2\mu^2_\Phi}. \tag{4.2.46}$$

For an inert doublet mass scale μ_Φ around half the Higgs mass, the EW precision measurement constrains the T-parameter with uncertainty 0.07 [301,302], constraining $|\widetilde{\lambda}_{H\Phi}| < 0.36$ at 95% C.L. Although this estimation is subject to sizable corrections due to the fact that μ_Φ is of the order the Higgs mass, this gives an estimate of the bounds on $\widetilde{\lambda}_{H\Phi}$ not being very stringent coming from one-loop suppressed effects. For our benchmarks, we simply set $\widetilde{\lambda}_{H\Phi}$ to zero at tree level.

The next set of constraints comes from the Higgs boson coupling precision measurements, through the coefficient of the operator,

$$\begin{aligned} \mathcal{O}_H &= \frac{1}{2}(\partial_\mu |H|^2)^2, \\ c_H &= \frac{4\lambda^2_{H\Phi} + 4\lambda_{H\Phi}\widetilde{\lambda}_{H\Phi} + \widetilde{\lambda}^2_{H\Phi} + N\lambda^2_{H\chi}\mu^2_\Phi/\mu^2_\chi}{192\pi^2\mu^2_\Phi}. \end{aligned} \tag{4.2.47}$$

This results in an overall reduction of the Higgs couplings by $1/2c_H v_0^2$. We note here that this EFT matching is subject to large corrections and higher-order terms since the scales μ^2_Φ and μ^2_χ are not far from the Higgs mass squared. On the other hand, our non-restoration mechanism has limited dependence on these parameters. In particular, we have set $\widetilde{\lambda}_{H\Phi}$ and

$\lambda_{H\chi}$ to be zero in our BM scenarios, leaving only a shift of the Higgs couplings of about $-1/2c_H = -\lambda_{H\Phi}^2 v_0^2/(96\pi^2\mu_\Phi^2)$. For an inert doublet with μ_Φ around half the Higgs mass, it yields a global shift in the Higgs couplings of around $-\lambda_{H\Phi}^2/(6\pi^2)$, bounding $|\lambda_{H\Phi}| < 1.1$ (at 95% C.L.) if we were to achieve 1% Higgs coupling precision at the HL-LHC [136]. This constraint is much weaker when we compare it to bounds from direct invisible Higgs decay searches discussed earlier in this section. It could however be relevant for scenarios with heavy inert masses, since the Higgs invisible decay bound no longer applies. However, in such case, as we shall see next, the precision measurements on Higgs to diphoton coupling provide a stronger constraint than the one derived from eq. (4.2.47).

The EW charged inert doublet also radiatively modifies Higgs couplings to EW gauge bosons, through

$$\begin{aligned}
\mathcal{O}_{BB} &= g'^2|H|^2 B_{\mu\nu}B^{\mu\nu}, \qquad c_{BB} = \frac{2\lambda_{H\Phi} + \widetilde{\lambda}_{H\Phi}}{768\pi^2\mu_\Phi^2}, \\
\mathcal{O}_{WW} &= g^2|H|^2 W_{\mu\nu}W^{\mu\nu}, \qquad c_{WW} = \frac{2\lambda_{H\Phi} + \widetilde{\lambda}_{H\Phi}}{768\pi^2\mu_\Phi^2}, \\
\mathcal{O}_{WB} &= 2gg' H^\dagger \tau^a H W^a_{\mu\nu} B^{\mu\nu}, \quad c_{WB} = \frac{\widetilde{\lambda}_{H\Phi}}{384\pi^2\mu_\Phi^2}.
\end{aligned} \tag{4.2.48}$$

Here τ^a are the $SU(2)$ generators. Consequently, the Higgs diphoton coupling is modified by

$$1 - \kappa_{\gamma\gamma} \simeq 10\pi^2 v_0^2 \left(c_{BB} + c_{WW} - c_{WB}\right), \tag{4.2.49}$$

where $\kappa_{\gamma\gamma} \equiv g_{h\gamma\gamma}/g_{h\gamma\gamma}^{\rm SM}$. Due to the fact that the SM Higgs to diphoton coupling is loop-induced, this provides a strong constraint on $|\lambda_{H\Phi}|$ to be smaller than 0.04 (at 95% C.L.) for a 1.9% precision [136] on the Higgs to diphoton coupling at HL-LHC. The current Higgs precision uncertainty of 17% [303] translates to a constraint on $|\lambda_{H\Phi}| < 0.4$ (at 95% C.L.). Again, in deriving this limit, we assume that $\widetilde{\lambda}_{H\Phi} = 0$, μ_Φ being half the Higgs mass, and ignore the deviation of the form factor from unity from the inert doublet running in the loop.

Beyond the above, the model also generate less constraining effects on EWPO (W and Y parameter) and Higgs self-coupling [300, 304], whose current and future perspective sensitivities can be found in Refs. [156, 304, 305]. This may provide, in the future, further complementary information about the model.

4.3 Outlook: electroweak baryogenesis at hundreds of TeVs

In this section, we give an outlook for possibilities of high-scale baryogenesis scenarios based on 1) EW-symmetry non-restoration up to scales as high as the GUT/Planck scale or 2) electroweak symmetry restoration around a UV scale of the order of validity of our model at which a new UV theory is in place. In the latter case, we expect to build a UV theory that allows for EWBG. Hence, in this case, we would like to explore in more detail the sphaleron washout constraints in our BM scenarios to preserve the created asymmetry down to zero temperature.

If the EW symmetry, through a specific UV completion, were to remain broken well above the scale of validity of our current model [10], possibly up to the GUT or Planck scale, this would enable baryogenesis mechanisms with little dependence on how the EWSB is triggered. In such case, the baryon asymmetry can be generated by a mechanism that creates a source of B-L$\neq$ 0, such as, for example, GUT-genesis, leptogenesis, or Afflect-Dine baryogenesis ([306] and references therein). Recall that, sphaleron processes preserve B-L, and hence an asymmetry will subsist once generated. However, they tend to wash out B+L as long as they remain active, thereby enabling conversion of Baryon (anti-Baryon) number into anti-Lepton (Lepton) number. For any specific B-L$\neq$ 0 mechanism, there will be additional model-building considerations for successful baryogenesis, including specifics of the new sources of CP violation and out of equilibrium conditions. It is important to notice

10. Our study is only including one-loop RGEs, but in analogy to the SM, we expect the validity of our model to be extended to higher energies by considering higher-order loop RGEs.

that the two BMs we consider in this work imply that the sphaleron rate is suppressed during the broken-electroweak symmetry epoch, hence a mechanism such as Leptogenesis, that requires active sphalerons to convert Leptons into antiBaryons will not work. Other BMs could be studied that allow for sphalerons to become active at some intermediate energy scale during the temporary restoration of the EW symmetry, as in the lower right panel of Figure 4.1. Exploring these new ideas for baryogenesis will be the subject of future work.

In the case of a UV completion that induces a restoration of the EW symmetry at high energy scales of the order of the validity of our model, one can also require that such UV theory induces a strong first order phase transition and enables EWBG. Although building such UV theory will remain a topic of future work, let us briefly comment on the various ways that we can picture such a scenario.

In our minimal model, the restoration can occur through the RGE of the quartic couplings. Under the high-temperature expansion, one can visualize this possibility through the thermal coefficient c_φ given in eq. (4.2.15). If c_φ, which at lower temperatures has a negative value, were to become positive at a given high scale through the RGEs, this will render EW restoration at high temperatures. For simplicity, let's consider the limit where in the IR the mixing quartics $\lambda_{H\Phi}$, $\widetilde{\lambda}_{H\Phi}$, and $\lambda_{H\chi}$ are zero, and neglect the leading log impact of these mixing quartics. The running of the thermal coefficient is then determined by the running of the linear combination of $\lambda_\Phi/2 + (3g^2 + g'^{\,2})/16 + N\lambda_{\Phi\chi}/24$. In our model the inert doublet self-coupling λ_Φ generically becomes larger at higher scales, while the mixing quartic $\lambda_{\Phi\chi}$, whose initial value is negative, could also increase, depending on the specific region of parameter space. However, we checked that the latter is not fulfilled for our BMs, hence, additional effects will be needed to restore the EW symmetry in these cases. There are indeed different ways to change the running behavior of c_φ, to allow for EW restoration. For instance, one can consider that the inert doublet is charged under some new sponta-

neously broken U(1) gauge group with coupling g''. This will affect c_φ directly by adding a $g''^{\,2}/16$ term after crossing the scale where the new U(1) is restored, rendering its gauge boson massless such that it starts contributing to the thermal mass of the inert doublet. Similarly, one can also introduce some heavy vector-like fermions (under SM gauge groups) that have Yukawa couplings to the inert doublet. When above the heavy fermion mass scale, this will add new positive contributions to the thermal coefficient c_φ by $y_F^2 N_F/12$, where N_F is the color-factor or the specifies of new heavy fermions.

Beyond directly changing the thermal coefficient c_φ above some mass threshold scale, one can also modify the running of the couplings contributing to c_φ, by adding new gauge and/or matter content. The minimal and simplest implementation would be to charge the χ field under some new $SU(N)$ gauge group. It directly contributes positively to the beta function of $\lambda_{\Phi\chi}$, which is the only source of negative quantities in the thermal coefficient c_φ, helping restore the EW symmetry at a higher scale. On the contrary, matter fields interacting with the inert Higgs field seem to contribute negatively to the beta functions of the quartics contributing to c_φ, although, as discussed below, they may be required to secure a strong first-order phase transition. An additional source of symmetry restoration could be to add scalar fields that directly couple to the inert field and acquire masses at high energies at which restoration would take place [132].

4.4 Summary of the chapter

The exploration of EWPT patterns leading to EW symmetry breaking allows us to envision plausible paths for EWBG, as well as details of the cosmological history of our universe. In particular, the possibility of EWNR up to high energy scales, conceivably up to the GUT or Planck scale, or the opportunity for delayed EW symmetry restoration up to scales of the order of 100 TeVs, open new windows for baryogenesis mechanisms.

In this section, we first proposed a novel approach to realize new thermal histories, by

enabling the agent of EWSB to be an inert doublet that yields electroweak symmetry non-restoration up to high temperatures. These possibilities allow for diverse thermal histories with multi phase transition patterns, involving the SM Higgs, the inert Higgs and the SM-inert Higgs mixing phases at finite temperatures. Our new approach for EWNR at high energies has interesting computational requirements. Since the thermal history of our model, as defined in subsection 4.2.1, spans over large scale separations from the EW scale to high temperatures, in our study we carefully implement the effects of RGE and thermal resummation, as detailed in subsection 4.2.2. When considering daisy resummation, we compute thermal masses with different approximations and observe that they lead to similar quantitively results. In subsection 4.2.1 we perform an analytical study at leading order in the high-temperature (mean field) approximation that helps us zoom in into the promising region of parameter space for our numerical study. In subsection 4.2.2, we report our numerical calculations for two benchmark points, and show that our results are robust under various treatments of thermal resummation while including RGE effects. Most importantly, the non-restoration patterns can hold at least up to high scales of the order of 10^5 GeV, within the one loop RG resumed effective potential. An UV completion of our model could take place at higher energy scales. In subsection 4.2.3, we present a detailed study of the sphaleron washout effects over a broad range of temperatures, and show that for our two benchmark scenarios, the washout rates are such that high temperature EWBG could be realized after a proper UV completion. Observe that the crucial ingredient of our BM scenarios is that the EW symmetry is non-restored from high temperatures all the way down to the EW scale.

Most importantly, our mechanism for transmitting broken electroweak symmetry from the SM sector to an inert sector has a specific interesting feature: It can work *even if* one decouples the two Higgs sectors in the tree level scalar potential, implying that the effect of the new doublet enters our zero-temperature particle physics tests at the electroweak-loop level. This enables the existence of large model parameter space compatible with

experimental constraints and at the same time calls for new precision tests of the SM. As discussed in subsection 4.2.4, our model will find scrutiny at the HL-LHC through electroweak and Higgs precision tests, invisible decays and searches for disappearing tracks.

At high temperatures, our model opens up to possible UV completions that would enable various baryogenesis mechanisms, as has been discussed in section 4.3. If we go through EWBG, where a SFOEWPT is necessary, it would give rise to gravitational wave signals. The peak frequency, instead of populating around the LISA band (mHZ), will increase to higher frequencies, at reach of facilities [307,308] such as BBO, DECIGO, and even aLIGO. Moreover, the additional singlets χ in our study can themselves go through phase transitions, further enriching the possible thermal histories of our universe. Beyond all the above, one can also explore such relay of the EW-broken phase between the SM Higgs and scalars under other EW representations.

4.A Appendices for the chapter

4.A.1 Effective field-dependent masses

In this appendix, we list field-dependent masses of all degrees of freedoms in the plasma, those are relevant calculating one-loop effective potentials. The field-dependent scalar mass matrix squared $m^2(\hat{\Phi})$ is defined as

$$m^2_{ab}(\hat{\Phi}) \equiv \left.\frac{\delta^2 V}{(\delta\Phi_a)(\delta\Phi_b)}\right|_{\Phi=\hat{\Phi}}, \tag{4.A.1}$$

where we introduced a short-handed notation $\Phi \equiv \{h, \varphi, \chi_1, \chi_2, \cdots, \chi_N\}$, and a caret is used to indicate background fields. The field-dependent gauge field mass matrix squared is given by [59]

$$M^2(\hat{\Phi})_{ab} = g_a g_b (T_a\hat{\Phi})(T_b\hat{\Phi}), \tag{4.A.2}$$

with g_a the gauge coupling and T_a the generator of the ath gauge field[11]. The field-dependent fermion mass matrix squared is $mm^\dagger(\hat{\Phi})$ where $m(\hat{\Phi})$ is defined in the Lagrangian as

$$\mathcal{L} = \bar{\Psi}^a m_{ab}(\hat{\Phi})\Psi^b + \dots. \tag{4.A.3}$$

All contributions to the CW-potential are formally taken as traces of the squared mass matrices, which in practice can be diagonalized and the potential is then evaluated for the eigenvalues. Next, we list all field-dependent mass matrices squared in our model.

In the space of $\Big(h, \frac{-i}{\sqrt{2}}(G^+ - G^-), \frac{1}{\sqrt{2}}(G^+ + G^-), -G_0,\ \ \varphi, \frac{-i}{\sqrt{2}}(\phi^+ - \phi^-), \frac{1}{\sqrt{2}}(\phi^+ + \phi^-)$ $, -\phi_0, \chi_i)$, the symmetric field dependent mass matrix squared of the scalar sector is given by

$$m^2(\hat{h}, \hat{\varphi}, \hat{\chi}_i) = \begin{pmatrix} M_H^2 & M_{H\Phi}^2 & M_{H\chi}^2 \\ M_{H\Phi}^2 & M_\Phi^2 & M_{\Phi\chi}^2 \\ M_{H\chi}^2 & M_{\Phi\chi}^2 & M_\chi^2 \end{pmatrix} \tag{4.A.4}$$

11. It might has to be symmetrized in a and b

with

$$M_H^2(\hat{h},\hat{\varphi},\hat{\chi}_i) = \begin{pmatrix} -\mu_H^2 + 3\lambda_H\hat{h}^2 & & & & \\ +\frac{\lambda_{H\Phi}}{2}\hat{\varphi}^2 + \frac{\widetilde{\lambda}_{H\Phi}}{2}\hat{\varphi}^2 & & & & \\ +\frac{\lambda_{H\chi}}{2}\sum_i \hat{\chi}_i^2 & & & & \\ & -\mu_H^2 + \lambda_H\hat{h}^2 & & & \\ & +\frac{\lambda_{H\Phi}}{2}\hat{\varphi}^2 & & & \\ & +\frac{\lambda_{H\chi}}{2}\sum_i \hat{\chi}_i^2 & & & \\ & & -\mu_H^2 + \lambda_H\hat{h}^2 & & \\ & & +\frac{\lambda_{H\Phi}}{2}\hat{\varphi}^2 & & \\ & & +\frac{\lambda_{H\chi}}{2}\sum_i \hat{\chi}_i^2 & & \\ & & & -\mu_H^2 + \lambda_H\hat{h}^2 & \\ & & & +\frac{\lambda_{H\Phi}}{2}\hat{\varphi}^2 & \\ & & & +\frac{\widetilde{\lambda}_{H\Phi}}{2}\hat{\varphi}^2 + \frac{\lambda_{H\chi}}{2}\sum_i \hat{\chi}_i^2 \end{pmatrix}, \quad (4.A.5)$$

$$M^2_\Phi(\hat{h},\hat{\varphi},\hat{\chi}_i) =$$

$$\begin{pmatrix}
\mu^2_\Phi + 3\lambda_\Phi\hat{\varphi}^2 & & & & & & \\
+\frac{\lambda_{H\Phi}}{2}\hat{h}^2 + \frac{\widetilde{\lambda}_{H\Phi}}{2}\hat{h}^2 & & & & & & \\
+\frac{\lambda_{\Phi\chi}}{2}\sum_i \hat{\chi}_i^2 & & & & & & \\
& \mu^2_\Phi + \lambda_\Phi\hat{\varphi}^2 & & & & & \\
& +\frac{\lambda_{H\Phi}}{2}\hat{h}^2 + \frac{\lambda_{\Phi\chi}}{2}\sum_i \hat{\chi}_i^2 & & & & & \\
& & \mu^2_\Phi + \lambda_\Phi\hat{\varphi}^2 & & & & \\
& & +\frac{\lambda_{H\Phi}}{2}\hat{h}^2 + \frac{\lambda_{\Phi\chi}}{2}\sum_i \hat{\chi}_i^2 & & & & \\
& & & \mu^2_\Phi + \lambda_\Phi\hat{\varphi}^2 + \frac{\lambda_{H\Phi}}{2}\hat{h}^2 & & & \\
& & & +\frac{\widetilde{\lambda}_{H\Phi}}{2}\hat{h}^2 + \frac{\lambda_{\Phi\chi}}{2}\sum_i \hat{\chi}_i^2 & & &
\end{pmatrix}, \tag{4.A.6}$$

$$M^2_\chi(\hat{h},\hat{\varphi},\hat{\chi}_i)$$

$$= \begin{pmatrix}
3\widetilde{\lambda}_\chi\hat{\chi}_1^2 + \lambda_\chi(\sum_i \hat{\chi}_i^2 + 2\hat{\chi}_1^2) & 2\lambda_\chi\hat{\chi}_1\hat{\chi}_2 & \cdots & 2\lambda_\chi\hat{\chi}_1\hat{\chi}_N \\
+\frac{\lambda_{\Phi\chi}}{2}\hat{\varphi}^2 + \frac{\lambda_{H\chi}}{2}\hat{h}^2 + \mu^2_\chi & & & \\
2\lambda_\chi\hat{\chi}_2\hat{\chi}_1 & \ddots & \ddots & \vdots \\
\vdots & \ddots & \ddots & 2\lambda_\chi\hat{\chi}_{N-1}\hat{\chi}_N \\
2\lambda_\chi\hat{\chi}_N\hat{\chi}_1 & \cdots & 2\lambda_\chi\hat{\chi}_N\hat{\chi}_{N-1} & 3\widetilde{\lambda}_\chi\hat{\chi}_N^2 + \lambda_\chi(\sum_i \hat{\chi}_i^2 + 2\hat{\chi}_N^2) \\
 & & & +\frac{\lambda_{\Phi\chi}}{2}\hat{\varphi}^2 + \frac{\lambda_{H\chi}}{2}\hat{h}^2 + \mu^2_\chi
\end{pmatrix}, \tag{4.A.7}$$

$$M^2_{H\phi}(\hat{h},\hat{\varphi},\hat{\chi}_i) = \begin{pmatrix} (\lambda_{H\Phi}+\widetilde{\lambda}_{H\Phi})\hat{h}\hat{\varphi} & & & \\ & \frac{\widetilde{\lambda}_{H\Phi}}{2}\hat{h}\hat{\varphi} & & \\ & & \frac{\widetilde{\lambda}_{H\Phi}}{2}\hat{h}\hat{\varphi} & \\ & & & 0 \end{pmatrix}, \tag{4.A.8}$$

$$M^2_{H\chi}(\hat{h},\hat{\varphi},\hat{\chi}_i) = \begin{pmatrix} \lambda_{H\chi}\hat{h}\hat{\chi}_1 & \cdots & \lambda_{H\chi}\hat{h}\hat{\chi}_N \\ 0 & \cdots & 0 \\ 0 & \cdots & 0 \\ 0 & \cdots & 0 \end{pmatrix}, \tag{4.A.9}$$

$$M^2_{\phi\chi}(\hat{h},\hat{\varphi},\hat{\chi}_i) = \begin{pmatrix} \lambda_{\Phi\chi}\hat{\varphi}\hat{\chi}_1 & \cdots & \lambda_{\Phi\chi}\hat{\varphi}\hat{\chi}_N \\ 0 & \cdots & 0 \\ 0 & \cdots & 0 \\ 0 & \cdots & 0 \end{pmatrix}, \tag{4.A.10}$$

where cells left blank are zero, while cells represented by dots are following previous cells' pattern. In addition, we have [309, 310]

$$m_W^2 = \frac{g^2}{4}(\hat{h}^2+\hat{\varphi}^2), \quad m_Z^2 = \frac{g^2+g'^2}{4}(\hat{h}^2+\hat{\varphi}^2), \quad m_t^2 = \frac{y_t^2}{2}\hat{h}^2. \tag{4.A.11}$$

4.A.2 Leading order daisy coefficients

As stated in the main text, at high temperatures, there will be sizable higher loop thermal contributions which may break the perturbative validity at some field values. In order to resum such contributions, a naive treatment is to include a thermal mass contribution on top

of the tree level effective mass. Formally, the thermal mass should be calculated using the gap equation. However, if one truncates the thermal potential at leading order in the expansion of the thermal mass, as well as in the leading order in the high-temperature expansion, one would obtain analytical leading order thermal mass contributions to each degree of freedom. Here we quote such leading order contributions of our model.

$$\Pi_{0,h} = \Pi_{0,G} = c_h T^2 = \left(\frac{\lambda_H}{2} + \frac{\lambda_{H\Phi}}{6} + \frac{3g^2 + g'^2}{16} + \frac{y_t^2}{4} + \frac{\widetilde{\lambda}_{H\Phi}}{12} + \frac{N}{24}\lambda_{H\chi} \right) T^2 \quad (4.A.12)$$

$$\Pi_{0,\varphi} = \Pi_{0,\phi} = c_\varphi T^2 = \left(\frac{\lambda_\Phi}{2} + \frac{\lambda_{H\Phi}}{6} + \frac{3g^2 + g'^2}{16} + \frac{\widetilde{\lambda}_{H\Phi}}{12} + \frac{N}{24}\lambda_{\Phi\chi} \right) T^2 \quad (4.A.13)$$

$$\Pi_{0,\chi_i} = c_\chi T^2 = \left(\frac{\lambda_\chi}{12}(N+2) + \frac{\lambda_{\Phi\chi}}{6} + \frac{\lambda_{H\chi}}{6} + \frac{\widetilde{\lambda}_\chi}{4} \right) T^2. \quad (4.A.14)$$

For later convenience, we define constants $c_i = \Pi_i^2/T^2\big|_{\hat{h}=\hat{\varphi}=0}$. The thermal masses of W and Z are as given in [309, 310], they only contribute to the longitudinal components:

$$\Pi_{0,W_L} = 2g^2T^2 \quad (4.A.15)$$

$$\Pi_{0,Z_L,A_L} = -\frac{g^2 + g'^2}{8}(\hat{h}^2 + \hat{\varphi}^2) + (g^2 + g'^2)T^2 \pm \Delta \quad (4.A.16)$$

$$\Delta^2 = \left(\frac{g^2 + g'^2}{8} \right)^2 \left(\hat{h}^2 + \hat{\varphi}^2 + 8T^2 \right)^2 - g^2 g'^2 T^2 \left(\hat{h}^2 + \hat{\varphi}^2 + 4T^2 \right). \quad (4.A.17)$$

4.A.3 RGEs

RG improvement is necessary to resum large log contributions at large field values. To compute the RGEs, we follow the steps discussed in [311], using the real representation of the $SU(2)$-doublets discussed in [312]. This approach utilizes the background-field method and super-heat-kernel expansion. Our results have been checked in the SM limit [313] and the pure inert 2HDM limit presented in [309], as well as two independent computations. Note that the wavefunction renormalizations are gauge dependent (therefore there is a difference

compared to [313]). This is another manifestation of the gauge-dependence of $v_{\rm EW}(T)$ that was discussed in [51, 52, 80, 81, 123–125, 127, 128]. Given the Lagrangian of eq. (4.2.1), we

find the β-functions, defined as $\beta(c) \equiv 16\pi^2 \frac{d}{d\log\mu_R} c$, to be:

$$\beta(g_s) = -7g_s^3 \tag{4.A.18}$$

$$\beta(g) = -3g^3 \tag{4.A.19}$$

$$\beta(g') = 7g'^3 \tag{4.A.20}$$

$$\beta(\mu_H^2) = -4\lambda_{H\Phi}\mu_\Phi^2 - 2\widetilde{\lambda}_{H\Phi}\mu_\Phi^2 - \mu_H^2(-12\lambda_H + \tfrac{3}{2}(3g^2 + g'^2) - 6y_t^2) - N\mu_\chi^2\lambda_{H\chi} \tag{4.A.21}$$

$$\beta(\mu_\Phi^2) = -4\lambda_{H\Phi}\mu_H^2 - 2\widetilde{\lambda}_{H\Phi}\mu_H^2 - \mu_\Phi^2(-12\lambda_\Phi + \tfrac{3}{2}(3g^2 + g'^2)) - N\mu_\chi^2\lambda_{\Phi\chi} \tag{4.A.22}$$

$$\beta(\mu_\chi^2) = 4\mu_\Phi^2\lambda_{\Phi\chi} + 6\widetilde{\lambda}_\chi\mu_\chi^2 - 4\mu_H^2\lambda_{H\chi} + 2(N+2)\mu_\chi^2\lambda_\chi \tag{4.A.23}$$

$$\begin{aligned}\beta(\lambda_H) = {} & 2\lambda_{H\Phi}^2 + 2\lambda_{H\Phi}\widetilde{\lambda}_{H\Phi} + \widetilde{\lambda}_{H\Phi}^2 + 24\lambda_H^2 - 3\lambda_H(3g^2 + g'^2) \\ & + \frac{3}{8}(3g^4 + 2g^2g'^2 + g'^4) + 12\lambda_H y_t^2 - 6y_t^4 + \tfrac{N}{2}\lambda_{H\chi}^2\end{aligned} \tag{4.A.24}$$

$$\begin{aligned}\beta(\lambda_\Phi) = {} & 2\lambda_{H\Phi}^2 + 2\lambda_{H\Phi}\widetilde{\lambda}_{H\Phi} + \widetilde{\lambda}_{H\Phi}^2 + 24\lambda_\Phi^2 - 3\lambda_\Phi(3g^2 + g'^2) \\ & + \frac{3}{8}(3g^4 + 2g^2g'^2 + g'^4) + \tfrac{N}{2}\lambda_{\Phi\chi}^2\end{aligned} \tag{4.A.25}$$

$$\beta(\lambda_\chi) = 2\lambda_{\Phi\chi}^2 + 2\lambda_{H\chi}^2 + 16\lambda_\chi^2 + 12\widetilde{\lambda}_\chi\lambda_\chi + 2N\lambda_\chi^2 \tag{4.A.26}$$

$$\begin{aligned}\beta(\lambda_{H\Phi}) = {} & \frac{3}{4}(3g^4 - 2g^2g'^2 + g'^4) + 4\lambda_{H\Phi}^2 + 2\widetilde{\lambda}_{H\Phi}^2 + 4\widetilde{\lambda}_{H\Phi}(\lambda_H + \lambda_\Phi) \\ & + \lambda_{H\Phi}(12\lambda_\Phi + 12\lambda_H - 3(3g^2 + g'^2)) + 6\lambda_{H\Phi}y_t^2\end{aligned} \tag{4.A.27}$$

$$\beta(\widetilde{\lambda}_\chi) = 18\widetilde{\lambda}_\chi^2 + 24\widetilde{\lambda}_\chi\lambda_\chi \tag{4.A.28}$$

$$\begin{aligned}\beta(\lambda_{\Phi\chi}) = {} & (-\tfrac{3}{2}(3g^2 + g'^2) + 12\lambda_\Phi + 6\widetilde{\lambda}_\chi + 4\lambda_{\Phi\chi} + 2N\lambda_\chi + 4\lambda_\chi)\lambda_{\Phi\chi} \\ & + 4\lambda_{H\Phi}\lambda_{H\chi} + 2\widetilde{\lambda}_{H\Phi}\lambda_{H\chi}\end{aligned} \tag{4.A.29}$$

$$\begin{aligned}\beta(\lambda_{H\chi}) = {} & (-\tfrac{3}{2}(3g^2 + g'^2) + 12\lambda_H + 6\widetilde{\lambda}_\chi + 4\lambda_{H\chi} + 2N\lambda_\chi + 4\lambda_\chi + 6y_t^2)\lambda_{H\chi} \\ & + 4\lambda_{H\Phi}\lambda_{\Phi\chi} + 2\widetilde{\lambda}_{H\Phi}\lambda_{\Phi\chi}\end{aligned} \tag{4.A.30}$$

$$\begin{aligned}\beta(\widetilde{\lambda}_{H\Phi}) = {} & 3g^2g'^2 - 3\widetilde{\lambda}_{H\Phi}(3g^2 + g'^2) + 6\widetilde{\lambda}_{H\Phi}y_t^2 + 4\widetilde{\lambda}_{H\Phi}(\lambda_H + \lambda_\Phi) \\ & + 8\lambda_{H\Phi}\widetilde{\lambda}_{H\Phi} + 4\widetilde{\lambda}_{H\Phi}^2\end{aligned} \tag{4.A.31}$$

$$\beta(y_t) = -8y_t g_s^2 - \tfrac{9}{4}y_t g^2 - \tfrac{17}{12}y_t g'^2 + \tfrac{9}{2}y_t^3. \tag{4.A.32}$$

As mentioned in subsection 4.2.1, the couplings $\widetilde{\lambda}_{H\Phi}$ and $\lambda_{H\chi}$ are not protected by a symmetry (hypercharge breaks the custodial symmetry of $\widetilde{\lambda}_{H\Phi}$) and will run away from their initial, vanishing value. The wave function renormalization of the scalar fields are

$$\gamma_H = -3g^2 - g'^2 + 3y_t^2, \tag{4.A.33}$$

$$\gamma_\Phi = -3g^2 - g'^2, \tag{4.A.34}$$

$$\gamma_\chi = 0. \tag{4.A.35}$$

4.A.4 Details on the sphaleron rate calculation

In this section, we give some details on calculating the sphaleron rate across a large range of temperatures, which would prove essential in evaluating the baryon asymmetry in a model with UV EWBG. The sphaleron rate per unit volume is [38, 292]

$$\frac{\Gamma}{V} = \frac{\omega_-}{2\pi}\mathcal{N}_{tr}(\mathcal{N}V)_{rot}\left(\frac{\alpha_w T}{4\pi}\right)^3 \alpha_3^{-6}\kappa \exp\left[-E_{sph}(T)/T\right]. \tag{4.A.36}$$

This rate depends on the profile functions of the sphaleron solution that can be obtained by solving the equations of motion for the SU(2) and U(1) gauge bosons, and Higgs doublets [290, 291]. In the limit of neglecting the U(1) gauge coupling, $g' = 0$, a spherically symmetric ansatz gives a system of differential equations that can be numerically solved, for example, using the Newton-Kantorovich method as done in [314]. Given the uncertainties of the thermal potential calculation, we use the values of λ/g^2 as shown in Figure 4.6, where $g = g(\mu_{\rm R})$ is the SU(2) gauge coupling, and we consider $\lambda = \lambda_H(\mu_{\rm R})$ when we are in the phase P_H, and $\lambda = \lambda_\Phi(\mu_{\rm R})$ when we are in the phases P_Φ or $\mathrm{P}_{H\Phi}$. This is justified by the fact that the sphaleron solution depends on the $SU(2)$ structure of the theory, and our model mostly has either the SM Higgs or the inert Higgs taking a VEV.

The sphaleron energy is then given by $E_{sph}(T) = E_{sph}(T=0)\frac{v_{\rm EW}(T)}{v_{\rm EW}(T=0)} = \frac{4\pi}{g}B\, v_{\rm EW}(T)$,

where the energy prefactor B can be obtained by performing the volume integral of the stress-energy tensor using the previously obtained profile functions. Our choice of B as a function of λ/g^2 is shown in Figure 4.6, which is consistent with [39].

$\mathcal{N}_{tr}$ and $\mathcal{N}_{rot}$ are the normalization of the zero-frequency translation and rotation modes [292]. They can be computed from small fluctuations around the sphaleron solution. The resulting formula depends again on the profile functions and can therefore be either computed numerically or read off from [292, Fig. 5]. We pursue the latter and show the values we use in Figure 4.6.

ω_- is the frequency of the unstable mode [292, 315]. It can be found as a negative eigenvalue of a system of equations that also depends on the profile functions. We use the values of [292, Fig. 6] directly and show them in Figure 4.6 (Note that this plot shows ω_-^2 in units of $(gv)^2$).

κ is the fluctuation determinant. A first numerical evaluation was given in [38], and later improved in [294, 316–318]. We use the values given in [294] and assume a rather large uncertainty of $[0.01\kappa, 100\kappa]$ to also partially parametrize uncertainties in the other prefactors [314].

Finally, $V_{rot} = 8\pi^2$ is the volume of the rotation group; $\alpha_w = g^2/4\pi^2$ is the weak coupling constant; and $\alpha_3 = \alpha_w/(g\xi(T))$ is the weak coupling in the three-dimensional high-temperature effective theory.

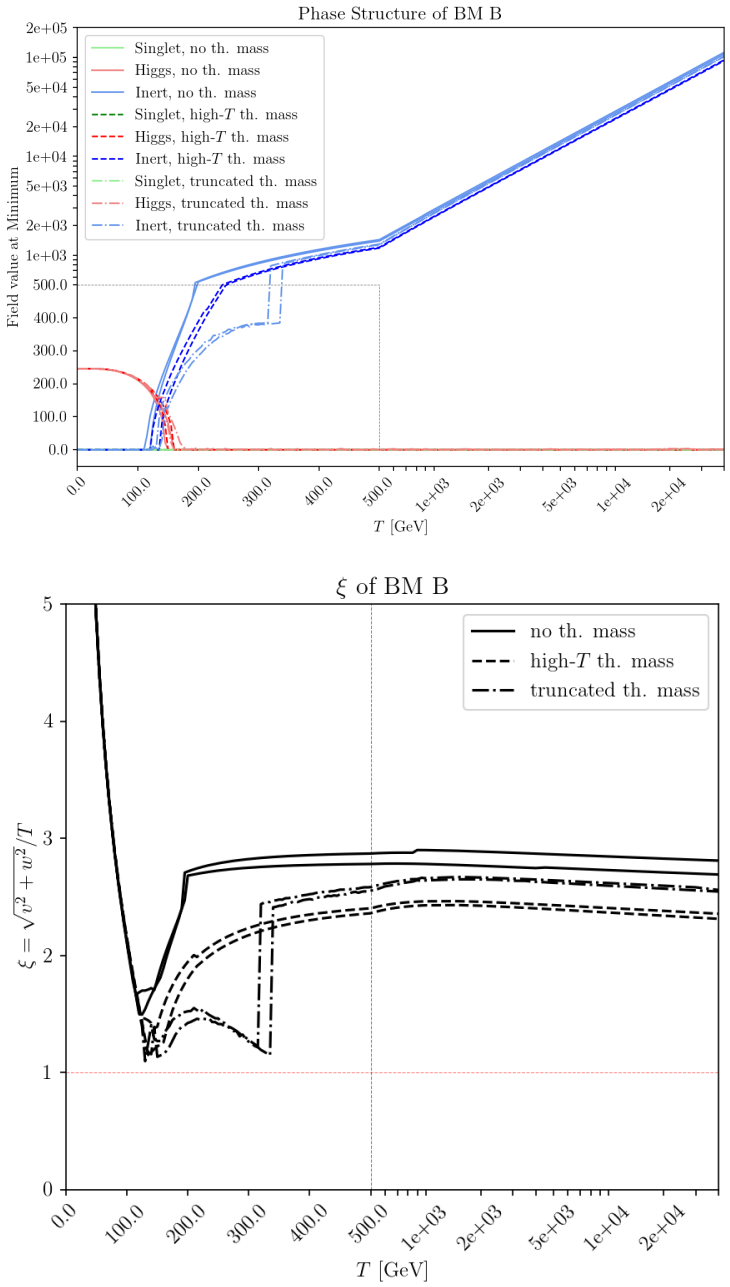

Figure 4.5: Phase structure (upper panel) and EW VEV-temperature ratio (lower panel) of BM B. Model parameters of the BM are given in Table 4.1

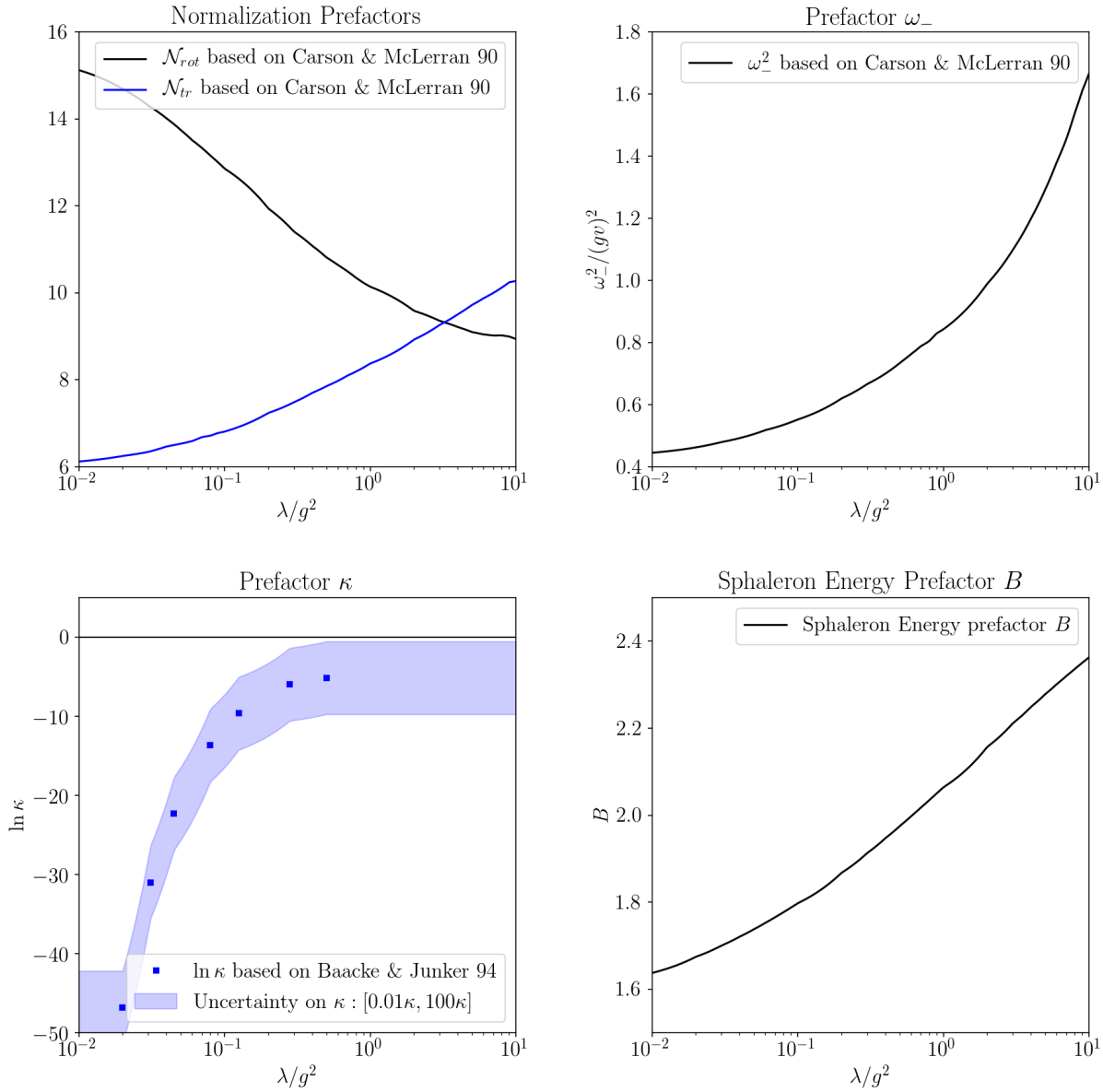

Figure 4.6: Input values for the sphaleron decay rate in eq. (4.2.40). $\mathcal{N}_{tr}$ and $\mathcal{N}_{rot}$ are taken from [292, Fig. 5], ω_- is taken from [292, Fig. 6], and κ is taken from [294], including uncertainties as explained in the text, and the energy prefactor B is computed also as discussed in the text. All quantities are plot against λ/g^2, the ratio of the corresponding quartic to the gauge coupling.

CHAPTER 5

ELECTROWEAK PHASE TRANSITION AND GRAVITATIONAL WAVES SIGNALS

The development of gravitational wave observatories provides a new window to understand the thermal history of the electroweak symmetry. If there was a first order electroweak phase transition in the early universe, the departure from thermal equilibrium during the bubble nucleation process, would provide a suitable environment for production of gravitational wave radiation, that has the potential to be detected by the next generation of gravitational wave experiments [319–322].

In this chapter, we first give a brief introduction to the simulation of gravitational wave signals generated by a first order electroweak phase transition in section 5.1, followed by an example in the singlet extension of the SM with spontaneous Z_2 breaking, where we provide a rough estimate of the gravitational wave signatures of the various underlying thermal histories and evaluate the opportunities to observe them at current and future gravitational wave detection experiments.

Next in section section 5.2, we focus on the bubble wall speed during a first order electroweak phase transition by analyzing the Higgs condensate bubble expansion, which plays a key role in determining the gravitational wave signals in a model independent way. The interaction of particles with the bubble wall can be accompanied by the emission of multiple soft gauge bosons. When computed at fixed-order in perturbation theory, this process exhibits large logarithmic enhancements which must be resummed to all orders when the wall velocity is large. We perform this resummation both analytically and numerically at leading logarithmic accuracy. The numerical simulation is achieved by means of a particle shower in the broken phase of the electroweak theory. The two approaches agree to the 10% level. For fast-moving walls, we find the scaling of the thermal pressure exerted against the wall to be $P \sim \gamma^2 T^4$, independent of the particle masses, implying a significantly slower terminal

velocity than previously suggested. The work was performed in collaboration with Stefan Hoeche, Jonathan Kozaczuk, Andrew J. Long and Jessica Turner. It has been published in Journal of Cosmology and Astroparticle Physics [323].

5.1 Gravitational waves from strong first order cosmological phase transitions

5.1.1 Introduction

Cosmological phase transition processes can induce gravitational wave (GW) radiations through bubble collisions, dubbed as Ω_ϕ, propagation of the sound wave, dubbed Ω_{sw}, and the decay of magnetohydrodynamic (MHD) turbulence, dubbed Ω_{MHD}, respectively [18, 319, 320, 324]. The stochastic GW background power spectrum is the summation of these three sources,

$$h^2\Omega_{GW}(f) \simeq h^2\Omega_\phi(f) + h^2\Omega_{sw}(f) + h^2\Omega_{MHD}(f), \tag{5.1.1}$$

whose specific strengths are determined by specifics of the cosmological phase transition (PT). However, contributions from these sources commonly depend on a few characteristic properties of the PT:

- The inverse duration of the PT, which is characterized by

$$\beta \simeq \dot{\Gamma}/\Gamma \tag{5.1.2}$$

with Γ being the bubble nucleation rate. Conventionally, it is normalized by the Hubble

parameter when simulating the GW signal, which reads

$$\frac{\beta}{H_*} \sim T \left. \frac{d(S_3/T)}{dT} \right|_{T=T_*}, \tag{5.1.3}$$

where S_3/T is the $O(3)$-symmetric bounce Euclidean action, T_* denotes the temperature of the thermal bath when the GW was generated, and H_* is the corresponding Hubble parameter at temperature T_*. For a strong first order phase transition without significant reheating, T_* is approximately the nucleation temperature T_n. As will be shown later, the bubble collision generated power spectrum is suppressed by two powers of the duration of the PT, H_*/β, while the corresponding spectra generated by the sound waves and turbulences last longer and are suppressed by only one power of the duration of the PT.

- Fraction of vacuum energy released during the transition with respect to the radiation bath, which specifically reads

$$\alpha = \frac{\rho_{\rm vac}}{\rho_{\rm rad}|_{T=T_*}}. \tag{5.1.4}$$

  The radiation energy density, ρ_{rad}, is approximately given by $g_*\pi^2 T_*^4/30$, where g_* is the number of relativistic degrees of freedom in the plasma at T_*. Note that as mentioned in Ref. [319,320], α also approximately coincides with the latent heat of the PT in the limit of a strong PT and large supercooling.

- Bubble wall velocity. If the wall velocity is small, then the GW spectrum is suppressed and hence less detectable. Detailed understanding of bubble wall velocity is, however, difficult, although one generically expects the plasma and matter reflection effects to let the bubble reach a relativistic terminal velocity [319]. In the next section, we will study such a quantity explicitly, and showcase the important effect of particles in the plasma slowing down a relativistic bubble wall by emitting soft and collinear radiations passing through the bubble wall.

- Fraction of vacuum energy that gets converted into bulk motion of the fluid and into gradient energy of the Higgs-like field,

$$\kappa_v = \frac{\rho_v}{\rho_{\rm vac}}, \quad \kappa_\phi = \frac{\rho_\phi}{\rho_{\rm vac}}, \tag{5.1.5}$$

  respectively.

With these quantities, following Ref. [320], power spectra of the GW from different sources can be simulated as

- Bubble collision

  The GW contribution from the bubble collision can be treated using the envelope approximation, where

$$h^2\Omega_\phi(f) = h^2\Omega_{\rm env}(f)|_{\kappa=\kappa_\phi}, \tag{5.1.6}$$

  with

$$h^2\Omega_{\rm env}(f) = 1.67\times10^{-5}\ \left(\frac{H_*}{\beta}\right)^2\ \left(\frac{\kappa\alpha}{1+\alpha}\right)^2\ \left(\frac{100}{g_*}\right)^{\frac{1}{3}}\ \left(\frac{0.11v_w^3}{0.42+v_w^2}\right)\ S_{\rm env}(f). \tag{5.1.7}$$

  $S_{\rm env}(f)$ parametrizes the spectral shape, witch based on simulation data reads

$$S_{\rm env}(f) = \frac{3.8\ (f/f_{\rm env})^{2.8}}{1+2.8\ (f/f_{\rm env})^{3.8}}, \tag{5.1.8}$$

  where the peak frequency today $f_{\rm env}$ is red-shifted from the peak frequency at T_* as

$$f_{\rm env} = 16.5\ \times\ 10^{-3}{\rm mHz}\ \left(\frac{f_*}{\beta}\right)\ \left(\frac{\beta}{H_*}\right)\ \left(\frac{T_*}{100{\rm GeV}}\right)\ \left(\frac{g_*}{100}\right)^{\frac{1}{6}}\ , \tag{5.1.9}$$

  and the peak frequency f_* is determined by the time scale of the PT based on simulation

as

$$\frac{f_*}{\beta} = \frac{0.62}{1.8 - 0.1 v_w + v_w^2}; \tag{5.1.10}$$

- Sound waves

  The GW contribution from sound waves, as bulk motion in the fluid produced by percolation, can be fitted as

$$h^2 \Omega_{\rm sw}(f) = 2.65 \times 10^{-6} \left(\frac{H_*}{\beta}\right) \left(\frac{\kappa_v \alpha}{1+\alpha}\right)^2 \left(\frac{100}{g_*}\right)^{\frac{1}{3}} v_w \, S_{\rm sw}(f), \tag{5.1.11}$$

  where the power spectrum shape

$$S_{\rm sw}(f) = (f/f_{\rm sw})^3 \left(\frac{7}{4 + 3\,(f/f_{\rm sw})^2}\right)^{7/2}, \tag{5.1.12}$$

  and a conservative estimate of the peak frequency today $f_{\rm sw}$ reads

$$f_{\rm sw} = 1.9 \;\times\; 10^{-2} {\rm mHz} \, \frac{1}{v_w} \left(\frac{\beta}{H_*}\right) \left(\frac{T_*}{100 {\rm GeV}}\right) \left(\frac{g_*}{100}\right)^{\frac{1}{6}} ; \tag{5.1.13}$$

- MHD turbulence

  The GW contribution from turbulence in the plasma can be modeled as

$$h^2 \Omega_{\rm trub}(f) = 3.35 \times 10^{-4} \left(\frac{H_*}{\beta}\right) \left(\frac{\kappa_{\rm turb} \alpha}{1+\alpha}\right)^{\frac{3}{2}} \left(\frac{100}{g_*}\right)^{\frac{1}{3}} v_w \, S_{\rm turb}(f), \tag{5.1.14}$$

  where $\kappa_{\rm turb}$ is the fraction of latent heat that is transformed into MHD turbulence, and the power spectrum shape

$$S_{\rm turb}(f) = (f/f_{\rm sw})^3 \frac{1}{(1 + \;(f/f_{\rm sw}))^{11/3}\,(1 + 8\pi f/h_*)}, \tag{5.1.15}$$

and a conservative estimate of the peak frequency today $f_{\rm turb}$ reads

$$f_{\rm turb} = 2.7 \times 10^{-2}{\rm mHz}\, \frac{1}{v_w} \left(\frac{\beta}{H_*}\right) \left(\frac{T_*}{100{\rm GeV}}\right) \left(\frac{g_*}{100}\right)^{\frac{1}{6}} . \tag{5.1.16}$$

The behavior of the bubble wall, say either it runs away, and if it runs away, either that is driven by vacuum or plasma effects, play a crucial role in determining the relative importance of different contributions, and in estimating the fraction of latent heat that is transformed into different sources. We will not illustrate details for different situations here. Instead, as an explicit example of the GWs generated by a SFOEWPT, in the next subsection, we show the potential for detectability of GW in the singlet extension of the SM with spontaneous Z_2 breaking, that has been introduced in section 3.2. In this study, we assumed the bubble wall speed to be 0.5 of the speed of light, corresponding to non-runaway bubbles in the plasma. In such a case, the energy from the scalar field is negligible, and the sound wave contribution to the GW signal dominates.

5.1.2 GWs from SFOEWPT with spontaneous Z_2 breaking

In Figure 5.1 we show the GW spectral density associated to the strong first order electroweak phase transition for various scenarios in comparison to the corresponding LISA [325], DECIGO [326], BBO [327] and Einstein Telescope (ET) [328] projected power-law integrated sensitivities [307, 308]. Other GW observatories such as Taiji [329] and TianQin [330] have similar sensitivities to LISA but different frequency bands, and future ones can further extend the GW sensitivities [321, 331, 332]. The green and orange curves correspond to scenarios A and B, respectively, in the tree-level plus one-loop thermal calculation, for a sufficiently strong first order phase transition and allowing for nucleation. The dark red curves represent the calculation including Coleman-Weinberg potential and daisy resummation, containing both scenario A and B points, again requiring nucleation. Given the smallness and indetectability

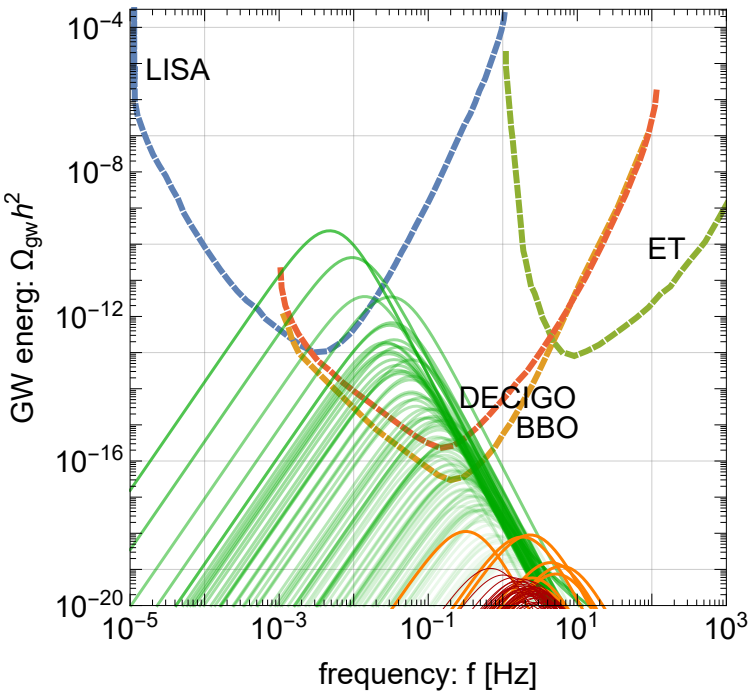

Figure 5.1: The gravitational wave (GW) power spectra generated during SFOEWPT as a function of frequency for model points of the singlet extension of the SM with spontaneous Z_2 breaking. The green and orange curves correspond to scenarios A and B, respectively, including the tree-level and one-loop thermal calculation. The dark red curves correspond to the full 1-loop evaluation plus the daisy resummation. Also shown are the power-law integrated sensitivities of the LISA, BBO, DECIGO and ET projections, obtained from Ref [308]. The transparency of the green curves further indicates the strength of the EWPT for the corresponding GW spectrum; the less transparent, the stronger the EWPT.

of these sets of signals, we do not distinguish among the different scenarios in the figure. Observe that in our study, the temperature of the thermal bath at the time when GWs are produced is close to the nucleation temperature, since the system does not undergo a large supercooling, and hence we use $T_* = T_n$ in the calculations. The GW signal is generated during the final or single step that gives place to the EWPT. In the cases of a two-step phase transition (scenarios A and B-NR), where relevant definitions can be found in section 3.2, the first step always involves a second order phase transition.

Now we comment on the several important aspects and underlying parameters of these GW spectra. We conservatively assume that the contribution from the MHD turbulence represents about 5% of the total sound wave energy. The nucleation temperature mainly spans over the range of 50 to 100 GeV for all the scenarios considered in this study. However, for the thermal-only calculation of scenario A and A-NR, the nucleation temperature can extend to values as low as a few GeV. For the green curves, the GW parameter α spans through the whole range from 5×10^{-4} to 100, [1] which strongly correlates with the strength of EWPT. The larger the α, the stronger the EWPT and as well the lower the nucleation temperature. β/H spans over the range 5×10^2 to 10^5, with higher density of results around 10^3. The β/H anti-correlates with the strength of the EWPT. We use the transparency of the green curves to indicate the corresponding strength of the EWPT and to highlight the connection between the strength of the EWPT and the parameters α and β/H: the less transparent the green curves, the stronger the EWPT. The stronger the phase transition, the lower the nucleation temperature and β/H, and the higher the value of α. These facts lead to the strongest GW spectrum with a peak frequency around 3 mHz. We observe that the nucleation calculation effectively removes many model parameter points in scenario B with strong EWPT, and with our current statistics, scenario B spreads over α between 0.005

1. For strong-transitions, with α of order 1 or larger, the dynamics of the GW becomes more complex and the GW strength computation has a large uncertainty that requires an improved treatment [333]. We note that the strongest four GW spectra shown by the green upper curves in Figure 5.1 correspond to this case.

and 0.02, and β/H between 7×10^4 and 5×10^5. For the full calculation with CW and daisy resummation, which corresponds to the dark red curves, α spans over the range 0.003 to 0.007 and β/H over the range 3×10^3 to 4×10^5. The points are more scattered around due to the enhanced complexity of the model parameter space due to the higher order radiative corrections to the scalar potential, with no obvious correlations. As argued earlier, the CW plus daisy resummation calculation, as well as the nucleation calculation, leaves model points with higher nucleation temperature, above 50 GeV, together with higher value of β/H. This, in turn, corresponds to a higher peak frequency at Hz level but suppressed strength of the GW signals for dark red and orange curves.

Our present results show that future GW experiments such as LISA and BBO would have limited sensitivity to detect GW signals associated to the EWPT in models with spontaneous Z_2 breaking. As explained above, the dark red curves correspond to the full one-loop with daisy resummation study, and this renders a much weaker GW signal. This is related to the loss of points with very strong first order phase transition, that, in the tree level plus one-loop thermal analyses (green and orange curves), are associated with smaller values of $\tilde{\lambda}_h$. In turn, smaller values of $\tilde{\lambda}_h$ will be more likely to become unstable (acquire negative values with RG running at large scales) and will be discarded from the accepted solutions. We already discussed this in detail in section 3.2.2. The reason that in Figure 5.1 we are showing both sets, those with the tree level plus one-loop thermal potential and those including the full one-loop corrections with daisy resummation, is because we anticipate that a further improvement in the computation of the scalar potential, namely the RG-improved CW potential, will affect the running of $\tilde{\lambda}_h$ and stabilize some of the discarded solutions, therefore yielding stronger GW signals. In fact, we expect that an RG improved effective potential treatment will yield results that lie somewhere in between the dark red and the thermal-only contours. This will require an additional comprehensive analysis that we postpone for a future work.

5.2 Bubble wall speed: towards an all-order calculation

It is important to understand the dynamics of Higgs-field bubbles during the PT [334], as they directly affect the production of various cosmological relics including the matter-antimatter asymmetry, topological defects, primordial magnetic fields, and a stochastic background of GW radiation.

A first order electroweak phase transition proceeds through the nucleation, growth, and percolation of bubbles. As the bubbles are expanding, their speed is controlled by a balance of pressures. A vacuum pressure, resulting from the underlying symmetry-breaking Higgs potential, "pushes" the bubble walls outward. Meanwhile a thermal pressure, resulting from the interactions of the wall with the ambient plasma, retards the bubble's expansion, and acts as a source of friction. If the vacuum pressure exceeds the thermal pressure, then the bubble wall will "runaway" with its velocity approaching the speed of light [335]. On the other hand, if the thermal pressure balances the vacuum pressure then the wall reaches a (possibly ultrarelativistic) terminal velocity [336]. Therefore, to understand the dynamics of Higgs-phase bubble walls during a first order electroweak phase transition, a key quantity of interest is the thermal pressure induced by the plasma of Standard Model particles.

Thermal pressure arises, in general, from the scattering of particles whose masses or couplings vary across the bubble wall. The authors of Ref. [336] argued that for fast moving walls, the pressure is dominated by the emission of soft vector bosons when particles cross the wall, a phenomenon known as transition radiation. For example, in the Standard Model an incident top quark can be put off-shell through a momentum transfer with the wall and may radiate soft Z-bosons to return to its mass shell. In Ref. [336] the authors calculated the corresponding thermal pressure assuming a *single emission* of the soft vector boson. They found that this channel dominates the non-radiative process, due to its enhancement in the infrared (IR) region. In this work, we note that the appearance of infrared singularities and the associated large logarithms implies that the fixed-order calculation underestimates the

pressure and resummation of soft radiation is necessary to obtain an accurate result when the wall velocity is large.

In this section, I present the work where we calculate the thermal pressure that results from the scattering of Standard Model particles on an ultrarelativistic Higgs-phase bubble wall while accounting for multiple soft emissions that collectively comprise a particle shower. We begin in subsection 5.2.1 with the definition of thermal pressure and motivate the need for resummation of soft radiation. Further, in subsection 5.2.2 we establish the framework for our calculation and the relation to Ref. [336]. In subsection 5.2.3 we compute the logarithmically enhanced radiative corrections and perform an analytic resummation. In addition to the analytic result, we simulate a particle shower in the broken Higgs phase in subsection 5.2.4. We find that the results agree well with the analytic calculation. The cosmological implications are presented in subsection 5.2.5 and we discuss and conclude in subsection 5.2.6.

5.2.1 Thermal pressure and why Higgs bubbles need a shower

In this section, we provide an intuitive understanding of the (net) thermal pressure exerted against the wall, $P \equiv F/A$ (the retarding force per unit area) and we review several fixed-order calculations of P from the literature. We argue that the fixed-order calculations must break down for sufficiently large wall velocities $\gamma \gg 1$, and thus we motivate an all-orders calculation which is carried out in the following sections using well-known analytic resummation and numerical techniques based on QCD parton showers.

Consider a Higgs-phase bubble in a plasma with weak-scale temperature $T \sim 100$ GeV. On the length scales of interest, the curvature of the bubble can be neglected, and the local bubble wall can be treated as planar. For concreteness let $\vec{v}_{\rm w} = -v\,\vec{e}_z$ with $v > 0$ be the velocity of the wall in the rest frame of the plasma, and let $\gamma = 1/\sqrt{1-v^2}$ be the corresponding Lorentz factor. We are interested in ultrarelativistic walls for which $\gamma \gg 1$,

and typically $\gamma \sim 10 - 1000$. In this regime, all SM particles are assumed to enter the broken phase with negligible reflection probability, the flux of particles passing the wall from inside the bubble is exponentially suppressed, and the distributions of the incoming particles are just the usual Bose-Einstein or Fermi-Dirac equilibrium distributions. Throughout this article we work in a frame where the bubble wall is at rest, and the plasma has an average velocity $\vec{v}_{\rm pl} = v\,\vec{e}_z$. In this frame, particles from the plasma are incident on the wall with boosted energies $E \sim \gamma T$ and fluxes $\mathcal{F} \sim \gamma T^3$. As $\gamma T \gg 100$ GeV, there is no kinematic restriction toward producing a large number of weak-scale particles when a particle interacts with the wall. The thermal pressure P can be written schematically as the product,

$$P \;=\; \mathcal{F} \;\times\; \langle \Delta p \rangle \;, \qquad \text{with} \qquad \langle \Delta p \rangle = \Delta p_z \;\times\; \mathbb{P} \;, \tag{5.2.1}$$

where $\mathcal{F}$ is the thermal flux of incident particles on the wall (number per area per time) and $\langle \Delta p \rangle$ is the average momentum transferred to the wall by each incident particle. For each particle that hits the wall, multiple scattering channels are possible and $\mathbb{P}$ represents the probability for a given scattering while Δp_z is the longitudinal momentum transfer of that scattering. We are particularly interested in how the thermal pressure scales with the Lorentz factor γ, as it will be compared against the vacuum pressure that scales as $P_{\rm vac} \sim \gamma^0$. Since $\mathcal{F} \sim \gamma^1$ in general, we only need to determine how $\langle \Delta p \rangle$ scales with γ.

Generally, $\langle \Delta p \rangle$ is given by a sum over all possible scatterings with each weighted by its associated probability. Ref. [335] considered the pressure that results from a particle entering the bubble and acquiring mass m, without any other emission. Based on simple kinematics, one can show $\Delta p_z \sim m^2/(2E)$, which scales as $E^{-1} \sim \gamma^{-1}$. Additionally taking $\mathbb{P} = 1$, since nearly all particles are transmitted into the bubble, Ref. [335] found that the pressure for such 1-to-1 transitions scales like $P \sim \gamma^0$ since $\mathcal{F} \sim \gamma^1$. The same authors revisited the calculation of thermal pressure in Ref. [336], and allowed the incident particle to emit an additional particle, which they refer to as a 1-to-2 transition. They argue that the pressure

is dominated by a region of phase space in which the emitted particle is soft with transverse momentum close to its mass. This leads to $\Delta p_z \sim m_{\rm soft}$, where $m_{\rm soft}$ is the on-shell mass of the emission, and $\mathbb{P} \sim \alpha\, \gamma^0$, where $\alpha = g^2/4\pi$ is the appropriate three-particle coupling. As such, Ref. [336] found $P \sim \gamma^1$, implying that the thermal pressure grows as the wall speeds up. Since the vacuum pressure does not grow with increasing γ, a balance of pressures is inevitable, and a terminal velocity will be reached.

Such a possibility naturally leads to the question: what is the effect of 1-to-many transitions? To estimate whether these channels could be relevant, we can calculate the probability for a 1-to-2 transition in the soft region of phase space favored by Ref. [336]. Here there is both a soft and a collinear enhancement, each of which contribute a logarithmic factor. The probability is parametrically given by (see for example section 5.2.3, Eq. (5.2.62))

$$\mathbb{P}_{1\to 2} \approx \mathbb{P}_{1\to 1} \times \sum_i C_i \, \frac{\alpha_i}{2\pi} \, \log^2 \frac{p_{\rm UV}^2}{p_{\rm IR}^2}, \tag{5.2.2}$$

where we sum over different emission channels with the appropriate couplings $\alpha_i = g_i^2/4\pi$ and charges C_i (see App. 5.A.1 for notation). Additionally, $p_{\rm UV} \sim \gamma T$ is the energy of the incident particle, $p_{\rm IR} \sim m \sim T$ is the mass of the emitted particle, and $\mathbb{P}_{1\to 1}$ is the probability of the $1 \to 1$ transition. The factorization of $\mathbb{P}_{1\to 2}$ into $\mathbb{P}_{1\to 1}$ and a doubly-logarithmic enhanced contribution from the $1 \to 2$ splitting process is a universal feature of gauge theories in the high-energy limit that is rooted in the soft singular behavior of classical dipole radiation. If $\gamma \gg 1$, then there is a large hierarchy between the UV and IR energy scales, and the probability ratio may become $\mathbb{P}_{1\to 2}/\mathbb{P}_{1\to 1} = \mathcal{O}(1)$ due to the large logarithms. A probability of order 1 would invalidate the fixed-order calculation and imply that 1-to-many channels should be taken into account. Using the approximate formula

above, we find that $\mathbb{P}_{1\to 2} > \mathbb{P}_{1\to 1}$ in the regime

$$\gamma > \exp\left[\sqrt{\frac{\pi}{2\sum_i C_i \alpha_i}}\right]. \tag{5.2.3}$$

For example, if the coupling is $\alpha_i \approx 0.01$, the charge is $C_i \approx 1$, and there are ~ 10 channels in the sum, then we estimate that the fixed-order 1-to-2 calculation should break down when $\gamma \gtrsim \mathcal{O}(10-100)$. As the fixed-order calculation in Ref. [336] implies $\gamma \sim 100 - 1000$ at the terminal velocity, the 1-to-many channels play an important role and this is what we study in the remainder of the article.

5.2.2 Perturbative computation of the thermal pressure

In this section we introduce the framework for the computation, following the methods developed in Ref. [336]. We also establish the notation that will allow us to compute radiative corrections in subsection 5.2.3.

Kinematics and one-particle states

We begin by defining the relevant kinematic variables. We work in the rest frame of the bubble wall, which is assumed to be planar and located at $z = 0$. In the rest frame of the plasma, the wall's velocity is $\vec{v}_{\rm w} = -\vec{v} = -v\,\vec{e}_z$, and in the rest frame of the wall, the plasma's velocity is $\vec{v}_{\rm pl} = \vec{v} = v\,\vec{e}_z$; the associated Lorentz factor is $\gamma = 1/\sqrt{1-v^2}$. We assume that particles of type a have a mass $m_{a,{\rm s}}$ in front of the wall ($z < 0$, symmetric phase) and a mass $m_{a,{\rm h}}$ behind the wall ($z > 0$, Higgs phase). This mass-varying background breaks spatial-translation invariance in the direction normal to the wall. Noether's theorem implies that the z-component of momentum is not conserved, and there is an ambiguity in the construction of a complete Fock space because we cannot label single-particle states by their x-, y-, and z-momentum, since the last one is not a good quantum number. To

address this ambiguity we follow Ref. [336]. One-particle states of flavor a are defined to be momentum eigenstates in the symmetric phase, and are therefore labeled by the momentum $\vec{p}_{a,\mathrm{s}} = (p_{a,x}, p_{a,y}, p_{a,z,\mathrm{s}})$ a particle has in the symmetric phase, based on its energy and transverse momentum. They are normalized according to [337]

$$\langle \vec{p}\,'_{a,\mathrm{s}} | \vec{p}_{a,\mathrm{s}} \rangle = (2\pi)^3 \, 2E_a \, \delta^{(3)}(\vec{p}\,'_{a,\mathrm{s}} - \vec{p}_{a,\mathrm{s}}) \; , \qquad \int \frac{\mathrm{d}^3 \vec{p}_{a,\mathrm{s}}}{(2\pi)^3} \frac{1}{2E_a} \; |\vec{p}_{a,\mathrm{s}}\rangle \langle \vec{p}_{a,\mathrm{s}}| = 1 \; , \tag{5.2.4}$$

where $\vec{p}_{a,\perp} = (p_{a,x}, p_{a,y}, 0)$ and $p^2_{a,z,\mathrm{s}} = E_a^2 - \vec{p}^{\,2}_{a,\perp} - m^2_{a,\mathrm{s}}$. If the particle in question is located in front of the wall ($z < 0$), and $\vec{p}_a$ is the particle's three momentum, then we have the dispersion relation $E_a^2 = \vec{p}_a^{\,2} + m^2_{a,\mathrm{s}}$, and the projection

$$\langle \vec{x} \, | \vec{p}_{a,\mathrm{s}} \rangle = \sqrt{2E_a} \exp\{ i \vec{p}_{a,\perp} \vec{x}_\perp \} \chi(z) \; , \tag{5.2.5}$$

is a plane wave, i.e. $\chi(z) = \exp\{ i p_{a,z,\mathrm{s}} z \}$, because the label momentum, $\vec{p}_{a,\mathrm{s}}$, agrees with the kinematical momentum. If the particle is instead located behind the wall ($z > 0$), we have $E_a^2 = \vec{p}_a^{\,2} + m^2_{a,\mathrm{h}}$, and the free particle states must be found by solving the associated evolution equation in the presence of the bubble wall, because the label momentum does not agree with the kinematical momentum. This can be achieved by using the WKB approximation [336] to determine the mode functions $\chi(z)$, leading to the zeroth order result $\chi(z) = \exp\{ i p_{a,z,\mathrm{h}} z \}$, where $p^2_{a,z,\mathrm{h}} = E_a^2 - \vec{p}^{\,2}_{a,\perp} - m^2_{a,\mathrm{h}}$. In summary, the functional form of $\chi(z)$ agrees with the vacuum case for all z if $\chi(z)$ is evaluated with the *kinematical* z-momentum, $\chi(z) = \exp\{ i p_{a,z} z \}$.[2] Note in particular that the δ functions in Eq. (5.2.4) do not imply z-momentum conservation. Written in terms of conserved kinematical quantities

2. This result can be understood from a different perspective: The relative phase shift between the WKB solution and a plane wave amounts to the relative momentum transfer of a free particle to the bubble wall, which is given by $\Delta p_z/(\gamma T) \approx \Delta m^2/(\gamma T)^2$. In the high-energy limit $\gamma T \gg m_{a,\mathrm{h}}$ the amplitude of the wave function is unaltered, because a small momentum change will not cause the particle to be reflected off the wall. Hence the free-particle momentum eigenstate at $z > 0$ is simply the plane wave solution in Eq. (5.2.5) with the appropriate dispersion relation for $z > 0$.

they read instead

$$\delta^{(3)}(\vec{p}\,'_{a,\mathrm{s}} - \vec{p}_{a,\mathrm{s}}) = \frac{p_{a,z,\mathrm{s}}}{E_a}\,\delta(E'_a - E_a)\,\delta^{(2)}(\vec{p}\,'_{a,\perp} - \vec{p}_{a,\perp})\,. \tag{5.2.6}$$

Definition of thermal pressure

We can now define the thermal pressure, P, and proceed to derive a master formula that allows us to calculate this pressure from scattering amplitudes. First we write

$$P = \sum_{a\in\mathcal{S}} P_a\,, \tag{5.2.7}$$

where P_a is the pressure resulting from incident particles of species a specifically. We sum a over the set of massive Standard Model particle species, $\mathcal{S}$. Next we can write

$$P_a = \int \mathrm{d}\mathcal{F}_a\ \langle \Delta p^\nu \rangle_a N_\nu\,, \tag{5.2.8}$$

where N_μ is a space-like four-vector normal to the wall, $\mathrm{d}\mathcal{F}_a = \mathrm{d}j_a^\mu N_\mu$ is the flux of incident a-particles, $\mathrm{d}j_a^\mu$ is the differential a-particle-number current density, and $\langle \Delta p^\mu \rangle_a$ is the average four-momentum transfer to the wall when a single a-particle is incident. To construct the normal vector, N_μ, suppose that the wall is parametrized by a scalar field $m_a^2(x^\mu)$ that represents the inhomogeneous squared mass of a-particles; then we define $N_\mu = \partial_\mu m_a^2/\sqrt{-(\partial m_a^2)^2}$, which is evaluated at the wall, implying $N_\mu = \{0,0,0,1\}$ in the frame where the wall is at rest and $m^2(x^\mu)$ increases from $m_{a,\mathrm{s}}^2$ at $z \to -\infty$ to $m_{a,\mathrm{h}}^2$ at $z \to +\infty$. The differential current density can be written as

$$\mathrm{d}j_a^\mu = \nu_a \frac{\mathrm{d}^3\vec{p}_a}{(2\pi)^3}\, f_a\, \frac{p_a^\mu}{E_a}\,, \tag{5.2.9}$$

where ν_a counts the redundant internal degrees of freedom (e.g., color and spin), and f_a is the phase space distribution function of a-particles. The plasma in front of the wall is assumed to be in thermal equilibrium at temperature T. If the wall moves ultrarelativistically, as we assume throughout our study, the distribution functions for bosons and fermions are the equilibrium Bose-Einstein and Fermi-Dirac distributions, respectively, boosted from the plasma frame to the wall frame:

$$f_a = \frac{1}{e^{p^\mu u_\mu^{\rm pl}/T} \pm 1} = \frac{1}{e^{(\gamma E_a - \gamma \vec{p}_a \cdot \vec{v}_{\rm pl})/T} \pm 1} \,, \tag{5.2.10}$$

where $u_\mu^{\rm pl}$ is the four-velocity of the plasma that equals $u_\mu^{\rm pl} = \{\gamma, 0, 0, \gamma \vec{v}_{\rm pl}\}$ in the rest frame of the wall. Eq. (5.2.10) generates average momenta of $p_{a,z} \sim \gamma T \gg p_{a,x} \sim p_{a,y} \sim T$. We also assume $\gamma T \gg m_a$ such that $E_a \sim \gamma T$ and parametrically the flux is Lorentz-boosted, $\mathrm{d}\mathcal{F}_a \sim \gamma T^3$.

The average momentum transfer from incident a-particles, $\langle \Delta p^\mu \rangle_a$, can be written as

$$\langle \Delta p^\mu \rangle_a = \sum_{n=1}^{\infty} \sum_{\{b\} \in \mathcal{S}} \int \mathrm{d}\mathbb{P}_{a \to b_1 b_2 \cdots b_n} \, \Delta p^\mu \,, \tag{5.2.11}$$

where $\mathrm{d}\mathbb{P}_{a \to b_1 b_2 \cdots b_n}$ is the differential probability for a single a-particle with momentum $\vec{p}_a$ to create a shower of n particles of species $\{b\}$ and label momenta $\{\vec{p}_{b,\mathrm{s}}\}$. The probability is weighted by the four-momentum transferred to the wall, which we write as

$$\Delta p^\mu = p_a^\mu - \sum_{i=1}^{n} p_{b_i}^\mu \,. \tag{5.2.12}$$

The probability density $\mathrm{d}\mathbb{P}_{a \to b_1 \cdots b_n}$ enforces energy and transverse momentum conservation (see Eq. (5.2.6)), hence we find that $\Delta p^\mu N_\mu = p_{a,z} - \sum_i p_{b_i,z}$. We can write the differential

probability as [337]

$$\mathrm{d}\mathbb{P}_{a\to b_1\cdots b_n} = \left[\prod_{i=1}^{n}\frac{\mathrm{d}^3\vec{p}_{b_i,\mathrm{s}}}{(2\pi)^3 2E_{b_i}}(1\pm f_{b_i})\right]\left|\langle\vec{p}_{b_1,\mathrm{s}}\cdots\vec{p}_{b_n,\mathrm{s}}|i\hat{T}|\psi_a(\vec{p}_a)\rangle\right|^2, \tag{5.2.13}$$

where $\mathrm{d}^3\vec{p}_{b_i,\mathrm{s}}/((2\pi)^3 2E_{b_i})$ is the Lorentz-invariant differential phase space volume element for the final-state particle i, $(1\pm f_{b_i})$ accounts for Bose enhancement (if b_i is a boson) or Pauli blocking (if b_i is a fermion), and $\langle\vec{p}_{b_1,\mathrm{s}}\cdots\vec{p}_{b_n,\mathrm{s}}|i\hat{T}|\psi_a(\vec{p}_a)\rangle$ is the transition matrix element for particle a represented by the state $|\psi_a(\vec{p}_a)\rangle$ to scatter into n particles. We will assume that the occupation numbers are small and thus approximate $1\pm f_{b_i}\approx 1$ in our calculation. The incoming wave packet is defined in terms of the wave function $\psi(\vec{p}\,'_{a,\mathrm{s}};\vec{p}_a)$ of particle a with momentum $\vec{p}_a$ as

$$|\psi_a(\vec{p}_a)\rangle = \int\frac{\mathrm{d}^3\vec{p}\,'_{a,\mathrm{s}}}{(2\pi)^3}\frac{1}{2E'_a}\,\psi(\vec{p}\,'_{a,\mathrm{s}};\vec{p}_a)\,|\vec{p}\,'_{a,\mathrm{s}}\rangle\,, \tag{5.2.14}$$

which leads to the proper normalization $\langle\psi_a(\vec{p}_a)|\psi_a(\vec{p}_a)\rangle = 1$. The transition amplitude can then be written as

$$\langle\vec{p}_{b_1,\mathrm{s}}\cdots\vec{p}_{b_n,\mathrm{s}}|i\hat{T}|\psi_a(\vec{p}_a)\rangle = \int\frac{\mathrm{d}^3\vec{p}\,'_{a,\mathrm{s}}}{(2\pi)^3 2E'_a}\,\psi(\vec{p}\,'_{a,\mathrm{s}};\vec{p}_a)\,\langle\vec{p}_{b_1,\mathrm{s}}\cdots\vec{p}_{b_n,\mathrm{s}}|i\hat{T}|\vec{p}\,'_{a,\mathrm{s}}\rangle\,. \tag{5.2.15}$$

It can be expressed in terms of the corresponding scattering amplitude $\mathcal{M}_{a\to b_1\cdots b_n}$ as follows[3]

$$\langle\vec{p}_{b_1,\mathrm{s}}\cdots\vec{p}_{b_n,\mathrm{s}}|i\hat{T}|\vec{p}_{a,\mathrm{s}}\rangle = (2\pi)^3\,\delta^{(3)}(\vec{p}_{a,\mathrm{s}}-\sum_{i=1}^{n}\vec{p}_{b_i,\mathrm{s}})\;i\mathcal{M}_{a\to b_1\cdots b_n}(\vec{p}_{a,\mathrm{s}},\vec{p}_{b_1,\mathrm{s}},\cdots\vec{p}_{b_n,\mathrm{s}})\,. \tag{5.2.16}$$

Both the transition matrix element and the scattering amplitude depend on the particles' spins, which we have suppressed to avoid unnecessary notation. Spins of final-state particles are summed, and the spin of the initial-state particle is averaged. Note that we only factor

3. Our normalization convention for $\mathcal{M}$ differs from Ref. [336] by a factor $p_{a,z,\mathrm{s}}/E_a$ due to Eq. (5.2.6).

off three Dirac delta functions in Eq. (5.2.16), rather than the usual four [337], because the z-component of momentum is not conserved in a background with inhomogenous particle masses. The combination of Eqs. (5.2.15) and (5.2.16) leads to two initial-state phase-space integrals, one of which can be evaluated trivially using three of the δ functions. We obtain

$$\begin{aligned}&\left|\langle \vec{p}_{b_1,\mathrm{s}} \cdots \vec{p}_{b_n,\mathrm{s}} | i\hat{T} | \psi_a(\vec{p}_a)\rangle\right|^2 \\ &\qquad = \int \frac{\mathrm{d}^3\vec{p}\,'_{a,\mathrm{s}}}{(2\pi)^3} \frac{\left|\psi(\vec{p}\,'_{a,\mathrm{s}};\vec{p}_a)\right|^2}{(2E'_a)^2} (2\pi)^3\, \delta^{(3)}(\vec{p}\,'_{a,\mathrm{s}} - \sum_{i=1}^{n} \vec{p}_{b_i,\mathrm{s}}) \left|\mathcal{M}_{a\to b_1 \ldots b_n}\right|^2 .\end{aligned} \tag{5.2.17}$$

We now use the fact that the wave function $\psi(\vec{p}\,'_{a,\mathrm{s}};\vec{p}_a)$ is tightly peaked around $\vec{p}_a$ because the incident particle has a well defined momentum. Formally, we can write $|\psi(\vec{p}\,'_{a,\mathrm{s}};\vec{p}_a)|^2 = (2\pi)^3\, 2E_a\, \delta^{(3)}(\vec{p}\,'_{a,\mathrm{s}} - \vec{p}_a)$. The integral over $\vec{p}\,'_{a,\mathrm{s}}$ is again trivial, and we obtain the differential probability [336]

$$\mathrm{d}\mathbb{P}_{a\to b_1 \cdots b_n} = \frac{1}{2E_a} \left[\prod_{i=1}^{n} \frac{\mathrm{d}^3\vec{p}_{b_i,\mathrm{s}}}{(2\pi)^3 2E_{b_i}}\right] (2\pi)^3\, \delta^{(3)}(\vec{p}_{a,\mathrm{s}} - \sum_{i=1}^{n} \vec{p}_{b_i,\mathrm{s}})\ |\mathcal{M}_{a\to b_1 \cdots b_n}|^2 . \tag{5.2.18}$$

By combining Eqs. (5.2.7)-(5.2.9), (5.2.11), (5.2.12), and (5.2.18), and further assuming the high-energy limit, such that $p_{a,z,\mathrm{s}}/E_a \approx 1$ in Eq. (5.2.9), one obtains a "master formula" for the thermal pressure,

$$\begin{aligned}P = \sum_{a\in\mathcal{S}} \nu_a \int \frac{\mathrm{d}^3\vec{p}_a}{(2\pi)^3 2E_a}\, f_a(\vec{p}_a) \sum_{n=1}^{\infty} \sum_{\{b\}\in\mathcal{S}} \left[\prod_{i=1}^{n} \int \frac{\mathrm{d}^3\vec{p}_{b_i,\mathrm{s}}}{(2\pi)^3 2E_{b_i}}\right] \\ \times (2\pi)^3\, \delta^{(3)}(\vec{p}_{a,\mathrm{s}} - \sum_{i=1}^{n} \vec{p}_{b_i,\mathrm{s}})\ |\mathcal{M}_{a\to b_1 \cdots b_n}|^2 \big(p_{a,z} - \sum_{i=1}^{n} p_{b_i,z}\big) ,\end{aligned} \tag{5.2.19}$$

that allows it to be calculated by specifying scattering processes and calculating the associated scattering amplitudes.

Transition radiation splitting

As a first example, we will determine the $1 \to 1$ transition matrix element to leading order in the perturbative expansion. This is given quite simply by the normalization condition in Eq. (5.2.4)

$$\langle \vec{p}_{b,\mathrm{s}} | \vec{p}_{a,\mathrm{s}} \rangle^{(0)} = (2\pi)^3 \delta^{(3)}(\vec{p}_{a,\mathrm{s}} - \vec{p}_{b,\mathrm{s}})\, \mathcal{M}^{(0)}_{a\to b} = (2\pi)^3 2E_a \delta^{(3)}(\vec{p}_{a,\mathrm{s}} - \vec{p}_{b,\mathrm{s}}) \,, \tag{5.2.20}$$

leading to $\mathcal{M}^{(0)}_{a\to b} = 2E_a$. The extension to fermion and vector fields is straightforward and yields identical results due to identical normalization of the one-particle eigenstates. Inserting the result into Eq. (5.2.19) leads to the pressure formula for $1 \to 1$ transitions which was derived in Ref. [335].

In what follows, the quantities we compute will be normalized to the leading order matrix element $\mathcal{M}^{(0)}_{a\to b}$ for particle a interacting with the wall and producing particle b. This allows us to formulate the radiative corrections to the leading order $a \to b$ process probabilistically. The fact that $\mathcal{M}^{(0)}_{a\to b} = 2E_a$ implies that all incoming particles which couple to the Standard Model Higgs condensate will interact with the bubble wall with a probability of unity, independent of the size of their Yukawa coupling. This is analogous to the more familiar situation of a charged particle interacting with the material in a detector: as long as the length of the detector along the direction of propagation is substantially longer than the particle's mean free path, the probability for interaction (and the initiation of a shower) is unity. In the case of particles impinging on a bubble of Higgs condensate, determining a mean free path would require a microscopic description of the interactions with Higgs quanta in the wall, which is beyond the scope of our study. Our assumption therefore corresponds to assuming a small mean free path for massive SM particles' interactions with the wall relative to the length scale associated with plasma interactions, which can also dissipate the incoming particle's momentum. Note that this is also implicitly assumed in Refs. [335, 336]. We emphasize,

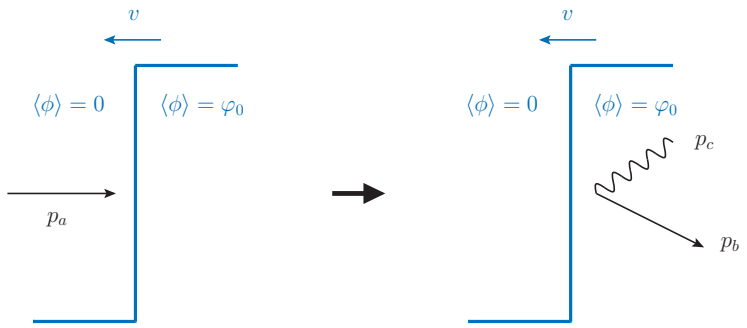

Figure 5.2: Sketch of the real-emission kinematics. The bubble wall is shown in blue and moves in the $-z$-direction with speed v in the rest frame of the plasma in front of the wall. The Higgs vacuum expectation value is denoted as $\langle\phi\rangle$. The incoming particle a has a light-like four momentum p_a in the wall's rest frame. The scattered particle b and the soft emission, c, have four momenta p_b and p_c.

however, that in scenarios beyond the SM, this assumption may no longer apply. For example, a decoupled hidden sector particle will have zero probability of interacting with the wall and should not be counted as contributing to the pressure: even though naively one still has $\mathcal{M}^{(0)}_{a\to b} = 2E_a$, the interpretation of $\mathcal{M}^{(0)}_{a\to b}$ as a matrix element for interacting with the wall no longer holds, since there is no coupling to the Higgs condensate in this case. We do not consider such scenarios further, and instead concentrate on the massive SM degrees of freedom.

To discuss the transition radiation process computed in [336], it is useful to introduce the Sudakov parametrization of the $1 \to 2$ kinematics sketched in Fig. 5.2 [338]. We work in light-cone coordinates, which make the cylindrical symmetry of the problem manifest. We define two light-like auxiliary vectors, $n = (1, 0, 0, 1)$ and $\bar{n} = (1, 0, 0, -1)$, which parametrize the forward $(+)$ and backward $(-)$ directions. All momenta can then be written in terms of their forward, backward, and transverse components,

$$p_+^\mu = \frac{p_+}{2}\, n^\mu \,, \qquad p_-^\mu = \frac{p_-}{2}\, \bar{n}^\mu \,, \qquad p_\perp^\mu = p^\mu - p_+^\mu - p_-^\mu \,, \tag{5.2.21}$$

where the scalar light-cone momenta p_+ and p_- are given by

$$p_+ = \bar{n}p \;, \qquad p_- = np \;. \tag{5.2.22}$$

Scalar products of four momenta can be written in terms of light-cone momenta and transverse momenta as $p^\mu q_\mu = (\,p_+ q_- + p_- q_+)/2 + p_\perp^\mu q_{\perp\mu}$. The final-state momenta p_b and p_c can now be written as

$$p_b^\mu = \;\tilde{z}\, p_a^\mu + \frac{\vec{k}_\perp^{\,2} + m_b^2}{\tilde{z}\, 2p_a\bar{n}}\, \bar{n}^\mu + k_\perp^\mu \;, \qquad p_c^\mu = \;(1-\tilde{z})\, p_a^\mu + \frac{\vec{k}_\perp^{\,2} + m_c^2}{(1-\tilde{z})\, 2p_a\bar{n}}\, \bar{n}^\mu - k_\perp^\mu, \tag{5.2.23}$$

where $\tilde{z} = p_{b,+}/p_{a,+}$ is the forward light-cone momentum fraction carried by particle b, and m_b and m_c are the final-state masses of the particles b and c, respectively. From Eq. (20) of Ref. [336], we obtain the following form of the leading order $1 \to 2$ particle scattering amplitude

$$\mathcal{M}^{(0)}_{a\to bc} = 2iE_a \left(\frac{V_h}{A_h} - \frac{V_s}{A_s}\right) \;, \tag{5.2.24}$$

where $V_h = V_s = V$ are the vertex functions. They are related to the Altarelli-Parisi splitting functions [339–342] as[4]

$$|V|^2 = 2g^2\, t\, P_{ab}(\tilde{z}) \;, \qquad \text{where} \qquad t = \frac{k_\perp^2}{\tilde{z}(1-\tilde{z})} \;. \tag{5.2.25}$$

The kinematical quantities A_h and A_s are defined as

$$A = (p_a - p_b - p_c)_- = m_a^2 - \frac{k_\perp^2 + m_b^2}{\tilde{z}} - \frac{k_\perp^2 + m_c^2}{1-\tilde{z}} \;, \tag{5.2.26}$$

where the appropriate "s" or "h" subscripts on the masses are implied. In the soft limit,

4. We follow the convention in Tab. I of Ref. [336]. We also changed the notation $x \to 1-\tilde{z}$, and swapped the particle labels b and c in order to agree with the notation in subsection 5.2.2.

$k_\perp \to 0$, $\tilde{z} \to 1$, the squared matrix element reduces to

$$|\mathcal{M}^{(0)}_{a\to bc}|^2 = (2E_a)^2\,|V|^2\,\frac{(A_h - A_s)^2}{A_h^2 A_s^2} \approx (2E_a)^2\,|V|^2\,\frac{\tilde{z}^2(1-\tilde{z})^2}{k_\perp^4}\frac{m_c^4}{(k_\perp^2+m_c^2)^2} \approx (2E_a)^2\,\frac{|V|^2}{t^2}\,. \tag{5.2.27}$$

Inserting the soft limit of Eq. (5.2.25) yields the factorized form of the $1 \to 2$ matrix element [339–342] (see also [343])

$$|\mathcal{M}^{(0)}_{a\to bc}|^2 = (2E_a)^2\,\frac{8\pi\alpha}{t}\,P^{(\mathrm{soft})}_{ab}(\tilde{z}) = |\mathcal{M}^{(0)}_{a\to b}|^2\,\frac{8\pi\alpha}{t}\,P^{(\mathrm{soft})}_{ab}(\tilde{z})\,, \tag{5.2.28}$$

where the soft enhanced part of the massive Altarelli-Parisi kernels for vector boson emission is given by [344]

$$P^{(\mathrm{soft})}_{ab}(\tilde{z}) = C_a\left(\frac{2}{1-\tilde{z}} - \frac{m_a^2}{p_a p_c}\right)\,. \tag{5.2.29}$$

The factorized form of the phase space, which corresponds to Eq. (5.2.28) and will allow to recover the result of [336], is given in Eq. (5.A.11). Combining this with Eq. (5.2.28) we obtain, to leading order and in the soft limit,

$$\mathrm{d}\mathbb{P}_{a\to bc} = \mathrm{d}\mathbb{P}_{a\to b}\int\frac{\mathrm{d}t}{t}\int\mathrm{d}\tilde{z}_i\int\frac{\mathrm{d}\phi_i}{2\pi}\,\frac{\alpha}{2\pi}P^{(\mathrm{soft})}_{ab}(\tilde{z})\,. \tag{5.2.30}$$

We will not proceed to derive the pressure here. In the following section, we will instead derive the above formulae based on a much simpler, semi-classical approximation and deduce a consistent treatment of the infrared enhancement that will enable us to resum the radiative corrections to all orders in the leading logarithmic approximation.

5.2.3 Factorization and resummation of radiative corrections

It was highlighted in Ref. [336] that the transition radiation effects discussed in section 5.2.2 significantly alter the pressure transfer in the $1 \to 1$ transition. The changes originate in logarithmically-enhanced radiative corrections to the light-to-heavy current parametrizing

a fast particle that crosses the domain wall. For massless emissions, these logarithms will become infrared poles, which are canceled to all orders by the virtual corrections to the light-to-heavy transition. The appropriate treatment for such effects is Sudakov resummation [338]. Running coupling effects can easily be incorporated in the calculation [345], and certain higher-logarithmic corrections may be resummed for simple observables as well [346]. In this section we will develop the formalism and compute an analytic estimate of the pressure at leading logarithmic accuracy.

Fixed-order perturbative computation

We derive the leading logarithmic approximation of the emission rate using source theory. Due to the universal structure of the matrix elements in the soft gauge boson limit, our eventual result will resemble the treatment of infrared divergences in QED [343]. The formal derivation here is strictly valid only for non-flavor-changing reactions, but it can easily be extended to flavor-changing processes. We will also find that non-flavor-changing reactions of QCD type provide the largest contribution to the overall momentum transfer in the Standard Model, which can be traced back to the relatively large number of degrees of freedom, $\nu_q = 2 \times 3$ for quarks and the large number of quarks (see Tab. 5.1 for details). This may seem somewhat surprising, given the small Yukawa couplings of the light quarks to the Higgs condensate, but follows from taking the probability for all massive SM species to interact with the bubble wall to be unity.

We begin with a classical vector current associated with the moving charge of the incoming particle a. This will allow us to treat the radiative corrections for scalars, fermions and vector bosons in a unified way. The classical current is parametrized as

$$j^\mu(x) = g \int \mathrm{d}s \, \frac{dy^\mu(s)}{ds} \, \delta^{(4)}(x - y(s)) \,. \tag{5.2.31}$$

In this context, g is the coupling, $y^\mu(s)$ is the particle's location, $\mathrm{d}s$ is the differential line element, and we integrate along the particle's trajectory. In momentum space, this current reads

$$j^\mu(k) = \int \mathrm{d}^4x\, e^{ikx}\, j^\mu(x) = g \int \mathrm{d}s\, \frac{dy^\mu(s)}{ds}\, e^{iky(s)}\,. \tag{5.2.32}$$

For simplicity, throughout our analysis we will consider the thin wall limit, $mL_w \ll 1$, with L_w the wall width, for which the bubble profile can be approximated as a step function at $z = 0$. We can then parametrize the line element as $\mathrm{d}s = \mathrm{d}z$, and write $y^\mu(s) = z\, p^\mu(z)/p_0(z)$ where we have $p(z) \to p_a$ if $z < 0$ and $p(z) \to p_b$ if $z > 0$. This parametrization leads to[5]

$$j^\mu(k) = g \int_{-\infty}^{0} \mathrm{d}z\, \frac{p_a^\mu}{p_{a,0}}\, \exp\left\{ i\, \frac{p_a k}{p_{a,0}} z \right\} + g \int_0^{+\infty} \mathrm{d}z\, \frac{p_b^\mu}{p_{b,0}}\, \exp\left\{ i\, \frac{p_b k}{p_{b,0}} z \right\}\,. \tag{5.2.33}$$

Upon inserting a regulator, we obtain the classical current

$$\begin{aligned} j^\mu(k) &= g \int_{-\infty}^{0} \mathrm{d}z\, \frac{p_a^\mu}{p_{a,0}}\, \exp\left\{ i \left(\frac{p_a k}{p_{a,0}} - i\varepsilon \right) z \right\} + g \int_0^{+\infty} \mathrm{d}z\, \frac{p_b^\mu}{p_{b,0}}\, \exp\left\{ i \left(\frac{p_b k}{p_{b,0}} + i\varepsilon \right) z \right\} \\ &= ig \left(\frac{p_b^\mu}{p_b k + i\varepsilon} - \frac{p_a^\mu}{p_a k - i\varepsilon} \right)\,. \end{aligned} \tag{5.2.34}$$

Eq. (5.2.34) could alternatively be obtained by matching the result of the full QFT to the soft limit [347], and by rewriting the factorized form of the matrix element $\mathcal{M}^{(1)}_{a\to b}$ in Sec. 5.2.2 [348]. We now proceed to compute the radiation field $A_\mu(x)$ of this current. Note that only the cross section for radiation of massless vector boson fields exhibits a double logarithmic enhancement in the soft region (a double pole in dimensional regularization). If we work in the soft approximation we therefore do not need to consider the radiation of

5. Note that Eq. (5.2.33) is structurally equivalent to Eq. (20) in Ref. [336] in the soft limit, $\tilde{z} \to 1$.

scalars and fermions. Let us consider the interaction Hamiltonian density

$$\mathcal{H}_{\rm int}(x) = j^\mu(x) A_\mu(x) \,, \tag{5.2.35}$$

which we require to derive the vacuum persistence amplitude,

$$W_{a\to b} = \langle 0|T\left[\exp\left\{i\int \mathrm{d}^4x\, j^\mu(x)A_\mu(x)\right\}\right]|0\rangle \,. \tag{5.2.36}$$

The probability of no emission off the classical current is given by $|W_{a\to b}|^2$. Note that the only dynamical degrees of freedom in this calculation are the vector bosons radiated by the fast, classical particle, hence the above notion of a "vacuum" persistence amplitude is justified. In terms of the matrix elements used in Eq. (5.2.19), we find, in the soft limit

$$|W_{a\to b}|^2 = \frac{|\mathcal{M}_{a\to b}|^2}{|\mathcal{M}^{(0)}_{a\to b}|^2} \,, \tag{5.2.37}$$

where $\mathcal{M}^{(0)}_{a\to b}$ is given by Eq. (5.2.20). The vacuum persistence amplitude can be expanded into a power series in the coupling constant, g, as $W_{a\to b} = \sum W^{(n)}_{a\to b}/n!$, with $W^{(n)}_{a\to b} \propto g^n$. The zeroth order term is trivially $W^{(0)}_{a\to b} = 1$. The first order term vanishes, as $\langle 0|A_\mu(x)|0\rangle = 0$. The second-order term is the first non-trivial result and gives

$$\begin{aligned} W^{(2)}_{a\to b} &= -\int \mathrm{d}^4x \int \mathrm{d}^4y\, j^\mu(x) j^\nu(y) \langle 0|T\left[A_\mu(x)A_\nu(y)\right]|0\rangle \\ &= -\int \mathrm{d}^4x \int \mathrm{d}^4y\, j^\mu(x) i\Delta_{F,\mu\nu}(x,y) j^\nu(y) \,. \end{aligned} \tag{5.2.38}$$

This is a very intuitive result, as it describes the emission and re-absorption of a soft field quantum by the same classical current after propagation from x to y. The propagation is

described by the time-ordered Green's function $i\Delta_F(x,y)$. It can be written as

$$\begin{aligned} i\Delta_F^{\mu\nu}(x,y) &= \Theta(y_0-x_0)\langle 0|A^\nu(y)A^\mu(x)|0\rangle + \Theta(x_0-y_0)\langle 0|A^\mu(x)A^\nu(y)|0\rangle \\ &= \int \frac{\mathrm{d}^3\vec{k}}{(2\pi)^3\,2E_k}\left[\Theta(y_0-x_0)e^{-ik(y-x)} + \Theta(x_0-y_0)e^{ik(y-x)}\right]\sum_{\lambda=\pm}\varepsilon_\lambda^\mu(k,l)\varepsilon_\lambda^{\nu\,*}(k,l)\,, \end{aligned} \tag{5.2.39}$$

where $\vec{k}$ is the soft particle's momentum, and E_k is determined by the dispersion relation $E_k^2 = \vec{k}^2 + m(z)^2$, with $m(z)$ the position dependent mass of the soft emission. We will discuss this position dependence further below. The polarization vectors ε_λ^μ can be constructed for example by using the Weyl-van-der-Waerden spinor formalism [349,350]. For massless vector bosons they obey the relation

$$\sum_{\lambda=\pm}\varepsilon_\lambda^\mu(k,l)\,\varepsilon_\lambda^{\nu\,*}(k,l) \;=\; -g^{\mu\nu} + \frac{k^\mu l^\nu + k^\nu l^\mu}{kl}\,, \tag{5.2.40}$$

where l represents a light-like auxiliary vector, that must not be parallel to k. Eq. (5.2.40) will be sufficient for computing helicity summed amplitudes in the remainder of this section. We note that for massive bosons one instead obtains the polarization sum

$$\sum_{\lambda=\pm,0}\varepsilon_\lambda^\mu(k,l)\,\varepsilon_\lambda^{\nu\,*}(k,l) \;=\; -g^{\mu\nu} + \frac{k^\mu k^\nu}{k^2}\,, \tag{5.2.41}$$

where the individual polarization vectors in depend on l, while their sum does not. Eq. (5.2.41) applies to all massive gauge bosons of the Standard Model in the high-energy limit $E \gg m$ due to the Goldstone boson equivalence theorem [351, 352]. Both polarization sums lead to the same results when squared matrix elements are computed using the soft current defined in Eq. (5.2.34).

The on-shell mass $m(z)$ of the emitted vector boson may change at the domain wall, which affects E_k by means of the dispersion relation. However, this is a dynamical effect,

which must be described by (resummed) higher-order corrections in the VEV insertion approximation [199,353,354]. We neglect these corrections here, because they are suppressed by $\mathcal{O}(1/(\alpha \log^2(\gamma T/m)))$ and therefore irrelevant in the high-energy limit $\gamma \gg 1$. The suppression factor will be justified further below, where we will find that the radiative corrections involving vector boson emission scale like $\alpha \log^2(\gamma T/\mu)$, with μ a mass scale of order m. In contrast, mass insertions scale like the leading-order terms in Sec. 5.2.2, and are therefore γ-independent. Note that our approximation is equivalent to the choice $V_h = V_s$ in Eq. (23) of Ref. [336]. In subsection 5.2.4 we will nevertheless include all kinematic effects for $m_c \neq 0$ (cf. App. 5.A.2), which leads to the exact quantities A_h and A_s in Eq. (20) of Ref. [336] by means of our Eqs. (5.2.34) and (5.2.23).

Using these approximations, we obtain the massless Feynman propagator

$$\Delta_F^{\mu\nu}(x,y) = \int \frac{\mathrm{d}^4k}{(2\pi)^4} \frac{e^{-ik(y-x)}}{k^2+i\varepsilon} \sum_{\lambda=\pm} \varepsilon_\lambda^\mu(k) \varepsilon_\lambda^{\nu\,*}(k) \; . \tag{5.2.42}$$

Inserting Eq. (5.2.42) into Eq. (5.2.38) yields

$$\begin{aligned} W_{a\to b}^{(2)} &= -i \int \mathrm{d}^4x \int \mathrm{d}^4y \int \frac{\mathrm{d}^4k}{(2\pi)^4} \frac{e^{-ik(y-x)}}{k^2+i\varepsilon} \sum_{\lambda=\pm} \big(j(x)\varepsilon_\lambda(k)\big)\big(j(y)\varepsilon_\lambda(k)\big)^* \\ &= -i \int \frac{\mathrm{d}^4k}{(2\pi)^4} \frac{1}{k^2+i\varepsilon} \sum_{\lambda=\pm} \big(j(k)\varepsilon_\lambda(k)\big)\big(j(k)\varepsilon_\lambda(k)\big)^* \; . \end{aligned} \tag{5.2.43}$$

Inserting the soft current of Eq. (5.2.34) and using the completeness relation, Eq. (5.2.40) or (5.2.41) we obtain

$$W_{a\to b}^{(2)} = -i\,|g|^2 \int \frac{\mathrm{d}^4k}{(2\pi)^4} \frac{1}{k^2+i\varepsilon} \left(\frac{2p_a p_b}{(p_a k)(p_b k)} - \frac{m_a^2}{(p_a k)^2} - \frac{m_b^2}{(p_b k)^2} \right) \; . \tag{5.2.44}$$

Note that while Eq. (5.2.40) was derived in a light-like axial gauge, the result is actually gauge independent. The infrared divergent part of Eq. (5.2.44) can be computed using

dimensional regularization in $D = 4 - 2\varepsilon$ dimensions. For one massive particle, b, we obtain, in the $\overline{\text{MS}}$ scheme (cf. App. 5.A.3)

$$W_{a\to b}^{(2)\,\text{IR}} = -\frac{\alpha}{\pi}\, C_{abc} \left(\frac{1}{2\varepsilon^2} - \frac{1}{2\varepsilon} \left(1 + \log \frac{(2p_a p_b)^2}{\mu^2 p_b^2} \right) + \frac{1}{4} \log^2 \frac{(2p_a p_b)^2}{\mu^2 p_b^2} - \frac{1}{2} \log^2 \frac{2p_a p_b}{p_b^2} + \dots \right) . \tag{5.2.45}$$

The quantity $4\pi\alpha = |g|^2$ is the coupling squared for the transition $a \to bc$, and C_{abc} is an associated charge factor in the collinear limit (see App. 5.A.1 for details). We have only listed the poles and leading logarithmic terms, as the subleading logarithmic and finite contributions are irrelevant for the resummation we intend to perform. Note that, as $p_b^2 \to 0$, Eq. (5.2.45) develops an additional infrared singularity. Comparing with Eq. (5.A.18), one finds that the leading pole is then doubled, which agrees with the intuitive notion that two massless charged particles will radiate twice as many gauge bosons as a single particle.

We now proceed to compute the real-emission corrections. The all-orders single emission amplitude squared is

$$\mathrm{d}W_{a\to bc}^2(p_c) = \frac{\mathrm{d}^3\vec{p}_c}{(2\pi)^3\, 2E_c} \left| \langle \vec{p}_c | T \left[\exp\left\{ i \int \mathrm{d}^4x\, j^\mu(x) A_\mu(x) \right\} \right] |0\rangle \right|^2 . \tag{5.2.46}$$

It is related to the matrix elements used in Eq. (5.2.19) in the soft limit as

$$\mathrm{d}W_{a\to bc}^2(p_c) = \frac{\mathrm{d}^3\vec{p}_c}{(2\pi)^3\, 2E_c} \frac{|\mathcal{M}_{a\to bc}|^2}{|\mathcal{M}_{a\to b}^{(0)}|^2} , \tag{5.2.47}$$

where $\mathcal{M}_{a\to b}^{(0)}$ is given by Eq. (5.2.20). Eq. (5.2.46) can be expanded into a power series in the coupling constant, g, as $\mathrm{d}W_{a\to bc}(p_c) = \sum \mathrm{d}W_{a\to bc}^{(n)}(p_c)/n!$, with $\mathrm{d}W_{a\to bc}^{(n)}(p_c) \propto g^n$. The zeroth order term vanishes, as $\langle \vec{p}_c | 0 \rangle = 0$. The first order term is the first non-trivial result

and gives

$$\begin{aligned} \mathrm{d}W^{2\,(1)}_{a\to bc}(p_c) &= \frac{\mathrm{d}^3\vec{p}_c}{(2\pi)^3\,2E_c}\left|\, i\int \mathrm{d}^4x\, j^\mu(x)\langle\vec{p}_c|A_\mu(x)|0\rangle\right|^2 \\ &= -\frac{\mathrm{d}^3\vec{p}_c}{(2\pi)^3\,2E_c}\sum_{\lambda=\pm}\big(j(p_c)\varepsilon_\lambda(p_c)\big)\big(j(p_c)\varepsilon_\lambda(p_c)\big)^*\,, \end{aligned} \tag{5.2.48}$$

which we integrate over the full final-state phase space in order to obtain the correction to the inclusive rate:

$$\int \mathrm{d}W^{2\,(1)}_{a\to bc} = |g|^2\int\frac{\mathrm{d}^3\vec{p}_c}{(2\pi)^3\,2E_c}\left(\frac{2p_ap_b}{(p_ap_c)(p_bp_c)}-\frac{m_a^2}{(p_ap_c)^2}-\frac{m_b^2}{(p_bp_c)^2}\right)\,. \tag{5.2.49}$$

The infrared divergent part of Eq. (5.2.49) can be extracted using dimensional regularization in $D=4-2\varepsilon$ dimensions. We obtain (cf. App. 5.A.4)

$$\begin{aligned} \int \mathrm{d}W^{2\,(1)\,\mathrm{IR}}_{a\to bc} = +\frac{\alpha}{\pi}\,C_{abc}\left(\frac{1}{2\varepsilon^2}-\frac{1}{2\varepsilon}\left(1+\log\frac{(2p_ap_b)^2}{\mu^2p_b^2}\right)+\frac{1}{4}\log^2\frac{(2p_ap_b)^2}{\mu^2p_b^2}\right. \\ \left.-\frac{1}{2}\log^2\frac{2p_ap_b}{p_b^2}+\dots\right)\,. \end{aligned} \tag{5.2.50}$$

Using the first order expansion of $W_{a\to b}$ and $\int \mathrm{d}W^2_{a\to bc}$, we find the no-emission and integrated one-emission probability are

$$\begin{aligned} \mathbb{P}^{\mathrm{IR}\,(1)}_{a\to b} &= \left|\,1+\frac{W^{(2)\,\mathrm{IR}}_{a\to b}}{2!}+\mathcal{O}(\alpha^2)\,\right|^2 = 1+W^{(2)\,\mathrm{IR}}_{a\to b}+\mathcal{O}(\alpha^2)\,, \\ \int \mathrm{d}\mathbb{P}^{\mathrm{IR}\,(1)}_{a\to bc} &= \int \mathrm{d}W^{2\,(1)\,\mathrm{IR}}_{a\to bc}+\mathcal{O}(\alpha^2) = -W^{(2)\,\mathrm{IR}}_{a\to b}+\mathcal{O}(\alpha^2)\,. \end{aligned} \tag{5.2.51}$$

The singular terms in the amplitudes cancel at first order in perturbation theory[6]. Similar

6. Note that the cancellation of singularities can be derived more elegantly. The loop integrand can be rewritten using

$$\frac{1}{k^2+i\varepsilon} = \mathrm{PV}\,\frac{1}{k^2}-i\pi\delta(k^2)\,, \tag{5.2.52}$$

where PV stands for the principal value. This implies that Eq. (5.2.50) can be obtained from Eq. (5.2.45)

results will be obtained at all higher orders, but we will not proceed to compute these terms. Instead, we will use Eq. (5.2.38) to construct the analytic resummation formalism in section 5.2.3 and a numerical simulation in subsection 5.2.4.

We conclude this section by noting that it is not sufficient to compute only the real-emission corrections to the $1 \to 1$ transition. This is apparent in the case where a massless particle becomes massive, as outlined above. The situation is more subtle when both the incoming and the outgoing particle is massive. However, we will show in section 5.2.3 that in the limit $\gamma T \gg \min(m_a, m_b)$ the differential real-emission amplitude squared $\mathrm{d}W^2_{a\to bc}$ vanishes as the gauge boson transverse momentum tends to zero. This result is qualitatively different from the behavior in [336], where the amplitude tends to infinity instead. The difference is due to the fact that we consider the transition radiation process to be a quantum correction to the zeroth order light-to-heavy form factor, $|\mathcal{M}^{(0)}_{a\to b}|^2$, while in [336] it is considered to be a leading-order reaction by itself.

All-orders result

To derive the all-orders result, we start from Eq. (5.2.36). Terms of order $2n+1$ in the expansion vanish, since $\langle 0|A(x_1)\dots A(x_{2n+1})|0\rangle = 0$. The $2n$-th order term is given by

$$W^{(2n)}_{a\to b} = \Big[\prod_{i=1}^{2n} i\int \mathrm{d}^4x_i j^{\mu_i}(x_i)\Big]\,\langle 0|T\Big[\prod_{i=1}^{2n} A_{\mu_i}(x_i)\Big]|0\rangle\ . \tag{5.2.53}$$

and vice versa [343, 355, 356].

One can use the decomposition of the time-ordered product into Feynman propagators and the symmetry of the integrand in the currents to show that

$$\begin{aligned}\frac{W_{a\to b}^{(2n)}}{(2n)!} &= \frac{(2n-1)(2n-3)\dots 3\cdot 1}{(2n)!}\Big[\prod_{i=1}^{2n} i\int \mathrm{d}^4x_i j^{\mu_i}(x_i)\Big]\prod_{i=1}^{n}\langle 0|T\left[A_{\mu_{2i}}(x_{2i})A_{\mu_{2i+1}}(x_{2i+1})\right]|0\rangle \\ &= \frac{1}{2^n n!}\left(-\int \mathrm{d}^4x\int \mathrm{d}^4y\, j^\mu(x) i\Delta_{\mu\nu}(x,y) j^\nu(y)\right)^n = \frac{1}{n!}\left(\frac{W_{a\to b}^{(2)}}{2}\right)^n .\end{aligned} \tag{5.2.54}$$

Summing all orders in α, we obtain the vacuum persistence amplitude squared

$$\mathbb{P}_{a\to b} = |W_{a\to b}|^2 = \left|\sum_{n=0}^{\infty}\frac{1}{n!}\left(\frac{W_{a\to b}^{(2)}}{2}\right)^n\right|^2 = \exp\left\{W_{a\to b}^{(2)}\right\} . \tag{5.2.55}$$

Using Eqs. (5.2.45) and (5.2.50), we obtain to leading logarithmic accuracy

$$\mathbb{P}_{a\to b}^{\mathrm{IR}} = \exp\left\{W_{a\to b}^{(2)\,\mathrm{IR}}\right\} = \exp\left\{-\int \mathrm{d}W_{a\to bc}^{2\,(1)\,\mathrm{IR}}\right\} . \tag{5.2.56}$$

A similar calculation leads to

$$\mathrm{d}\mathbb{P}_{a\to bc}^{\mathrm{IR}} = \mathrm{d}W_{a\to bc}^{2\,\mathrm{IR}}(k) = \mathrm{d}W_{a\to bc}^{2\,(1)\,\mathrm{IR}}(k)\,\exp\left\{-\int \mathrm{d}W_{a\to bc}^{2\,(1)\,\mathrm{IR}}\right\} . \tag{5.2.57}$$

Note that these results still exhibit unphysical IR divergences, which are canceled in the matching to the fragmentation function of the incoming and outgoing particle. The matching can be interpreted as an experimental resolution, which requires a photon to be of sufficient energy and sufficiently separated in angle from the classical particle in order to be resolved as transition radiation. In dimensional regularization, the fragmentation functions are pure IR divergences, hence for the light-to-massive transition we obtain the renormalized emission

amplitude in the $\overline{\text{MS}}$ scheme

$$\int \mathrm{d}W^{2\,(1)}_{a\to b,\,r} = \frac{\alpha}{2\pi}\, C_{abc} \left(\frac{1}{2} \log^2 \frac{(2p_a p_b)^2}{\mu^2 p_b^2} - \log^2 \frac{2p_a p_b}{p_b^2} + \dots \right) , \tag{5.2.58}$$

where the dots stand for higher-logarithmic and finite contributions. In this context, μ plays the role of the experimental resolution scale which regularizes the above expression. In our case of interest, this implies the bubble wall is not sensitive to emissions which are arbitrarily soft. Eqs. (5.2.55) and (5.2.57) are then related to the zero and one-event probabilities according to a Poisson distribution with mean value $\int \mathrm{d}W^{2\,(1)}_{a\to b,\,r}$. Using this result, the all-orders computation can be performed by means of QCD-based resummation techniques or parton showers.

Momentum transfer at leading logarithmic accuracy

In this section we estimate the average momentum transfer to the wall per incident particle. The structure of the perturbative result in section 5.2.3 allows us to derive a resummation formalism similar to the techniques employed for the computation of collider observables [357]. We work in the leading logarithmic approximation, hence the collinear anomalous dimensions can be set to zero. We also assume that particle masses are small compared to the particle's energies, and can therefore be neglected. Numerical studies will be carried out in subsection 5.2.4 using the full kinematical mass dependence. Here we focus instead on the qualitative predictions at $\gamma T \gg \max(m_a, m_b)$ and for fixed coupling.

We begin by computing the so-called radiator function [357], which corresponds to the sum of the integrated S-matrix elements $\int \mathrm{d}W^{2\,(1)\,\mathrm{IR}}_{a\to bc}$ and $W^{(2)\,\mathrm{IR}}_{a\to b}$. However, instead of being an inclusive quantity, the radiator function implements the physical constraint that the momentum transfer in any branching $a \to bc$ cannot be larger than the eventually observed value of the momentum transfer for all emissions in the resummed theory. This

restriction is most easily implemented by working in the leading logarithmic approximation and using the fact that the $1/\varepsilon^2$ and $1/\varepsilon$ poles cancel between $\int \mathrm{d}W^{2\,(1)\,\mathrm{IR}}_{a\to bc}$ and $W^{(2)\,\mathrm{IR}}_{a\to b}$. This implies that instead of computing the finite difference between two individually IR divergent quantities, we may compute the finite remainder directly by making use of the unitarity constraint. In practice, it is achieved by placing a lower bound on the relative momentum transfer per splitting

$$V(p_a, p_b, p_c) = \frac{q_z}{\gamma T} \approx \frac{p_{c,\perp}^2/(p_a\bar{n})^2}{1-\tilde{z}} \,, \tag{5.2.59}$$

where the last equality holds in the soft limit. In terms of $V(p_a, p_b, p_c)$, the radiator function $R(V)$ for any given value of V is given by

$$R_{abc}(V) = |g|^2 \int \frac{\mathrm{d}^3\vec{p}_c}{(2\pi)^3\, 2E_c} \frac{2p_a p_b}{(p_a p_c)(p_b p_c)} \Theta(\eta_c)\Theta(V(p_a, p_b, p_c) - V) \,, \tag{5.2.60}$$

where $\eta_c = \log[p_{c,\perp}/(\gamma T)/(1-\tilde{z})]$ is the rapidity of the emitted soft particle c of momentum p_c with respect to the emitting antenna spanned by particles a and b. The constraint $\Theta(\eta_c)$ arises from the requirement that the emitted particles must enter the Higgs condensate. Using the Sudakov parametrization in section 5.2.2, we can rewrite Eq. (5.2.60) as

$$R_{abc}(V) = \int_V^1 \frac{\mathrm{d}V'}{V'} \int_0^1 \mathrm{d}\tilde{z}\, \frac{\alpha}{2\pi} \frac{2\,C_{abc}}{1-\tilde{z}}\, \Theta\!\left(\log\frac{1-z}{V'}\right) \,, \tag{5.2.61}$$

Performing the integrals we obtain

$$R_{abc}(V) = \frac{\alpha}{2\pi}\, C_{abc}\, L^2 \,, \qquad \text{where} \qquad L = \log\frac{1}{V} \,. \tag{5.2.62}$$

Up to running coupling effects, this corresponds to the well-known radiator function for the thrust in e^+e^- annihilation [358,359]. To leading logarithmic accuracy, the resummed cumulative cross section at V is given by the vacuum persistence amplitude squared, Eq. (5.2.55), with $W^{(2)}_{a\to b}$ replaced by $R(V)$ [357]. This can be understood in the following intuitive way:

The radiator function $R_{abc}(V)$ corresponds to a probability for the decay of particle a into the two final states b and c. However, in order for particle a to produce a relative momentum transfer of V, it must not have produced a relative momentum transfer $V(p_a, p_b, k) > V$, as otherwise it would not exist anymore in its present state. This is analogous to a nuclear decay process, where the nucleus can decay at any given time only if it has not decayed at earlier times. This "survival probability" is encapsulated in an exponential suppression factor conventionally called the Sudakov factor, which can be read off Eq. (5.2.56)

$$\Delta_a(V) = \exp\Big\{-\sum_b R_{ab}(V)\Big\}\,, \qquad \text{where} \qquad R_{ab}(V) = \sum_c R_{abc}(V)\,. \tag{5.2.63}$$

The rate at which particle a branches into any particles b and c is eventually given by

$$\frac{1}{N_a}\frac{\mathrm{d}N_a(V)}{\mathrm{d}V} = \sum_b \frac{\mathrm{d}R_{ab}(V)}{\mathrm{d}V}\,\Delta_a(V) = -\frac{\mathrm{d}\Delta_a(V)}{\mathrm{d}V}\,, \tag{5.2.64}$$

which, at leading logarithmic accuracy, leads to the normalized cumulative cross section [357]

$$\frac{1}{\sigma}\int_V^1 \mathrm{d}V'\,\frac{\mathrm{d}\sigma(V')}{\mathrm{d}V'} = \Delta_a(V)\,. \tag{5.2.65}$$

The average relative momentum transfer from all branchings is obtained by weighted summation over particle species, where the weight is given by the incident flux, times the cross section for interaction with the Higgs condensate. The leading-order cross section in the high-energy limit is identical for all massive Standard Model particles, which we denote as the set $\mathcal{S}$ (cf. Eq. (5.2.8)). We can thus write

$$\Big\langle\frac{\Delta p_z}{\gamma T}\Big\rangle = \int \mathrm{d}V\,V\frac{\mathrm{d}}{\mathrm{d}V}\prod_{a\in\mathcal{S}}\Delta_a(V)\,. \tag{5.2.66}$$

Phase-space restrictions play a significant role for the agreement between analytic and nu-

meric resummation of event shape observables [360]. This problem is amplified here, because we compute the average value of V, which is impacted significantly by modest changes of the differential cross section at large V. If no fixed-order matching is performed, the proper definition of V is therefore of vital importance. The simplest solution is to replace $V \to V/2$ in the weighting factor of Eq. (5.2.66), which introduces an overall factor of $1/2$. This redefinition corresponds to a single-logarithmic correction which is beyond the formal accuracy of our approach. At fixed coupling, the modified Eq. (5.2.66) is then given by

$$2\Big\langle \frac{\Delta p_z}{\gamma T} \Big\rangle_{\text{FC}} = \int \mathrm{d}L\, e^{-L}\, \frac{(\alpha C)_\Sigma}{\pi}\, L \exp\left\{ -\frac{(\alpha C)_\Sigma}{2\pi}\, L^2 \right\}, \quad \text{where} \quad (\alpha C)_\Sigma = \sum_{a,b\in\mathcal{S}} \alpha_{abc} C_{abc}\,, \tag{5.2.67}$$

where α_{abc} is the coupling associated to the splitting $a \to bc$. The relevant couplings are listed in App. 5.A.1. Equation (5.2.67) has the solution

$$2\Big\langle \frac{\Delta p_z}{\gamma T} \Big\rangle_{\text{FC}} = 1 - e^{\frac{1}{2\zeta}} \sqrt{\frac{\pi}{2\zeta}}\, \text{Erfc}\left(\frac{1}{\sqrt{2\zeta}}\right) \approx \zeta\,, \qquad \text{where} \qquad \zeta = \frac{(\alpha C)_\Sigma}{\pi}\,. \tag{5.2.68}$$

The linear approximation is very simple and works up to relative pressures of $\langle V \rangle_{\text{FC}} \approx 1\%$. It can alternatively be obtained from the fixed-order expansion of Eq. (5.2.67)

$$2\Big\langle \frac{\Delta p_z}{\gamma T} \Big\rangle_{\text{FC,FO}} = \int \mathrm{d}L\, e^{-L}\, \frac{(\alpha C)_\Sigma}{\pi}\, L = \zeta\,. \tag{5.2.69}$$

Running coupling effects should be included to obtain a more reliable resummed result. They induce a mild change in the scaling behavior of the radiator function. The corresponding expressions can be found in App. A of [357]. For the qualitative discussion in this section, it is sufficient, however, to consider Eq. (5.2.68).

Note in particular that $\langle \Delta p_z \rangle \propto \gamma T$, independent of the particle masses, as long as $\gamma T \gg m$. This is in contrast to [336], where a γ-independent value was obtained for the average pressure transfer, which implies $P \sim \gamma^1$ once the flux factor is taken into account,

cf. subsection 5.2.2. This result was derived based on the assumption that the dominant contribution to the integral is obtained from the region $k_T \approx m$, and by cutting off the divergent k_T-integral at this value. A similar procedure would turn Eq. (5.2.69) into

$$2\left\langle \frac{\Delta p_z}{\gamma T} \right\rangle_{\text{FC,FO}}^{(\text{cut})} = \zeta \, \frac{m}{\gamma T} \left(1 + \log \frac{\gamma T}{m} \right) \, . \tag{5.2.70}$$

The logarithmic contribution has been neglected in [336], which indeed results in $\langle \Delta p_z \rangle \propto m$. The origin of the discrepancy is the fundamentally different treatment of the divergence in the real radiative matrix element at $k_T = 0$. We emphasize that regularizing the singularity by such an unphysical cutoff will lead to unitarity violations for large γ when higher-order radiative corrections are not included, as is evident from Eq. (5.2.50).

5.2.4 Numerical simulation

In the following we establish the connection of the above formalism to parton showers, which can be used at leading logarithmic accuracy to simulate the physics encapsulated in Eqs. (5.2.55), (5.2.57), and the corresponding equations for higher particle multiplicity. Again, it is important to note that the renormalized counterparts of these equations describe the distribution of emissions according to a Poissonian with average value $\int \mathrm{d}W^{2\,(1)\,\mathrm{IR}}_{a\to bc,r}$. The regularization of $\mathrm{d}W^{2\,(1)\,\mathrm{IR}}_{a\to bc,r}$ in the parton shower follows the procedure outlined in section 5.2.3 and may be performed in any way that allows for an infrared and collinear safe simulation, such as using a transverse momentum cutoff at scales $k_{\perp,0} \ll \gamma T$. We can define the transverse momentum-dependent radiator function for the parton shower as

$$R^{\mathrm{PS}}_{abc}\left(\frac{2k_{\perp,0}}{\gamma T} \right) = |g|^2 \int \frac{\mathrm{d}^3 \vec{p}_c}{(2\pi)^3 \, 2\omega_c} \frac{2p_a p_b}{(p_a p_c)(p_b p_c)} \, \Theta(p_{c,\perp} - k_{\perp,0}) \, . \tag{5.2.71}$$

As long as the cutoff is small compared to the average transverse momentum generated by Eq. (5.2.57), the results of infrared and collinear safe observables such as the relative

z-momentum transfer will be independent of $k_{\perp,0}$. We can rewrite Eq. (5.2.71) as

$$R^{\mathrm{PS}}_{abc}(t, Q^2) = \int_t^{Q^2/4} \frac{\mathrm{d}\bar{t}}{\bar{t}} \int_{\tilde{z}_-}^{\tilde{z}_+} \mathrm{d}\tilde{z} \sum_{a,b} \frac{\alpha}{2\pi} \frac{2C_{abc}}{1-\tilde{z}} \,, \tag{5.2.72}$$

where $t \propto k_\perp^2$ is called the parton-shower evolution variable, and $Q/2 = \gamma T$ is the kinematical boundary. The quantity $4\pi\alpha = |g|^2$ is the coupling squared for the transition $a \to bc$, and C_{abc} is an associated charge factor in the collinear limit (see App. 5.A.1 for details). The integration boundaries $\tilde{z}_\pm$ are determined by the constraint $k_\perp > k_{\perp,0}$. They are given by

$$\tilde{z}_\pm = \frac{1}{2}\left(1 \pm \sqrt{1 - \frac{4k^2_{\perp,0}}{Q^2}}\right) . \tag{5.2.73}$$

We can then generate emissions by setting the Sudakov factor $\Delta_a(t, Q^2)$ equal to a random number and solving for the evolution variable t where

$$\Delta_a(t, Q^2) = \exp\left\{ -\sum_{b,c} R^{\mathrm{PS}}_{abc}(t, Q^2) \right\} . \tag{5.2.74}$$

In addition, we select the light-cone momentum fraction $\tilde{z}$ according to $2/(1-\tilde{z})$ and sample the azimuthal angle from a uniform distribution. For QCD partons, we also choose a color configuration. The kinematics mapping is described in App. 5.A.2, and more details of the algorithm are given in [361–363]. Our numerical implementation is based on the QCD parton shower published in [364]. The evolution variable t is chosen to be the relative transverse momentum in the collinear limit (cf. App 5.A.2), and we solve the soft double-counting problem [365] by means of phase-space partitioning in the dipole rest frame [357]. We have checked that this gives similar results as angular ordered evolution, using the formalism of [366].

We have implemented the above described algorithm in a numerical program based on the

Particle	n_f	ν_a	$\langle \Delta p_z/(\gamma T)\rangle_{\text{FC}}$ analytic	numeric
$l^\pm$	2×3	2	0.44%	0.36%
u	2×3	2×3	1.18%	0.96%
d	2×3	2×3	1.17%	0.95%
$W^\pm$	2	2	1.32%	1.10%
Z	1	2	1.04%	0.88%
h	1	1	0.57%	0.46%
$G_{W^\pm}$	2	1	0.57%	0.46%
G_Z	1	1	0.57%	0.46%

Table 5.1: Average relative momentum transfer per degree of freedom, $\langle \Delta p_z/(\gamma T)\rangle_{\text{FC}}$, assuming that a particle of the given species is incident on the wall, and allowed to shower into the full SM. We compare analytic results from Eq. (5.2.66) and the numerical simulation described in subsection 5.2.4. We have chosen $\gamma = 10^6$, $\alpha_s = 0.04$ and $\alpha = 0.01$, and we have fixed the couplings in order to satisfy the assumptions leading to Eq. (5.2.66). Differences are due to flavor-changing effects, which are not taken into account in Eq. (5.2.66), and due to the definition of the momentum transfer in terms of the initial- and final-state momenta. This is computed in the soft approximation in 5.2.3 and treated exactly in the numerical simulation [360]. We also list the number of flavors of this type, n_f, and the number of the corresponding degrees of freedom, ν_a, per flavor in Eq. (5.2.19).

QCD simulation published in [364], which was validated against the public event generator Sherpa [367]. We employ a 2-loop running strong coupling with threshold matching up to $n_f = 6$ and $\alpha_s(M_Z) = 0.118$. The electroweak input parameters are $\alpha(0) = 1/137$, $m_W = 80.385\,\text{GeV}$, $m_Z = 91.1876\,\text{GeV}$ and $m_H = 125\,\text{GeV}$, leading to $\sin^2\theta_W = 1-(m_W/m_Z)^2 = 0.223$. The relative flux factors for incident particles are given simply by the number of degrees of freedom of the particle. This can be understood by computing the (trivial) leading-order transition amplitudes in section 5.2.2 in a VEV-insertion approximation [199, 353, 354].

Due to the exact kinematics in the numerical simulation, the results display significant threshold effects at small momentum transfer ($\Delta p_z \approx T$), which become irrelevant as $\gamma \to \infty$ due to the parametric behavior derived in Eq. (5.2.68). This leads to a slight distortion of the scaling behavior, which goes beyond running coupling effects. In addition, the computation of the observable with exact kinematics induces a shift in the average pressure, but does not change the qualitative behavior. Table 5.1 shows a comparison between the analytic results

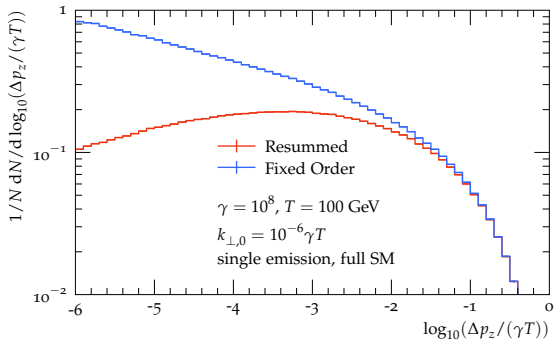

Figure 5.3: Comparison between fixed-order and resummed result for the relative momentum transfer distribution in the full Standard Model using the parton-shower approximation. The number of emissions is limited to one. Note that the fixed-order result is not normalized to the total rate, as the rate tends to infinity in this case.

from Eq. (5.2.66) and the numerical simulation for the most relevant particle species. Given the simplicity of the analytical estimate, the two results agree very well.

Fig. 5.3 exemplifies the structural difference between the fixed-order and all-orders resummed predictions for the relative momentum transfer distribution in the parton-shower approximation. While the fixed-order result diverges as $\Delta p_z/(\gamma T) \to 0$ (cf. Eqs. (5.2.50) and (5.2.62)), the resummed result remains finite and approaches zero (see section 5.2.3). This leads to a cutoff-dependence in the average relative momentum transfer at fixed-order in the method of Ref. [336] which changes the scaling behavior with γ (cf. Eq. (5.2.70)). In resummed perturbation theory the average relative momentum transfer is cutoff-independent, and is primarily determined by the coupling strength, cf. Eq. (5.2.68). This is tested in detail in Fig. 5.4, which shows the cutoff dependence of the relative momentum transfer spectrum in the parton-shower approximation at $\gamma = 10^8$. Note that the cutoff is varied over three orders of magnitude with no significant effect on the spectrum on a linear scale (Fig. 5.4 left). The corresponding values for the average relative momentum transfer are given by $\langle \Delta p_z/(\gamma T)\rangle = 0.832\% - 0.835\%$. Similar results are obtained for all values of γ.

Fig. 5.5 shows the change in the relative momentum transfer with changing γ, which is relatively mild. Note in particular the features in the spectrum at $\gamma = 10$, which originate

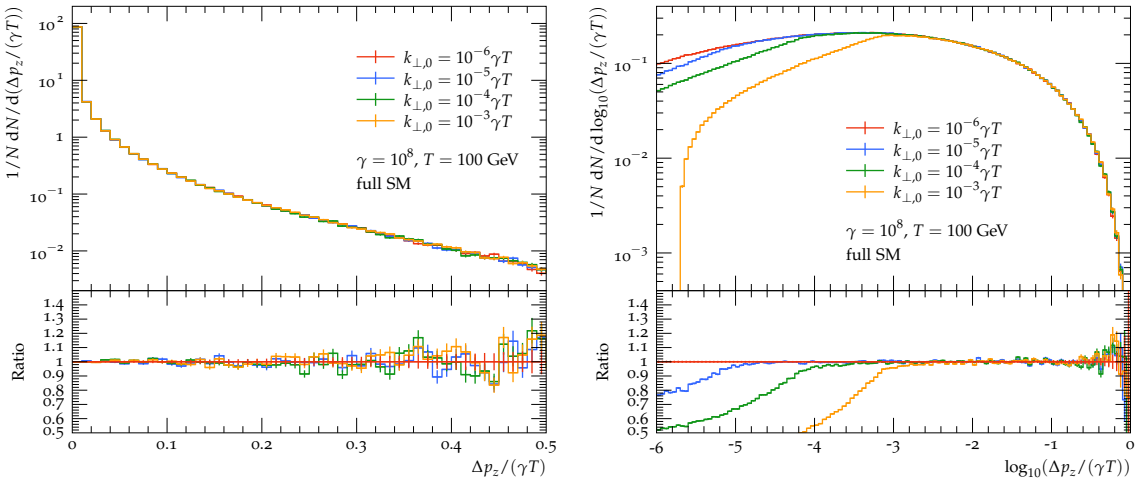

Figure 5.4: Cutoff-dependence of the relative momentum transfer in the parton-shower approximation.

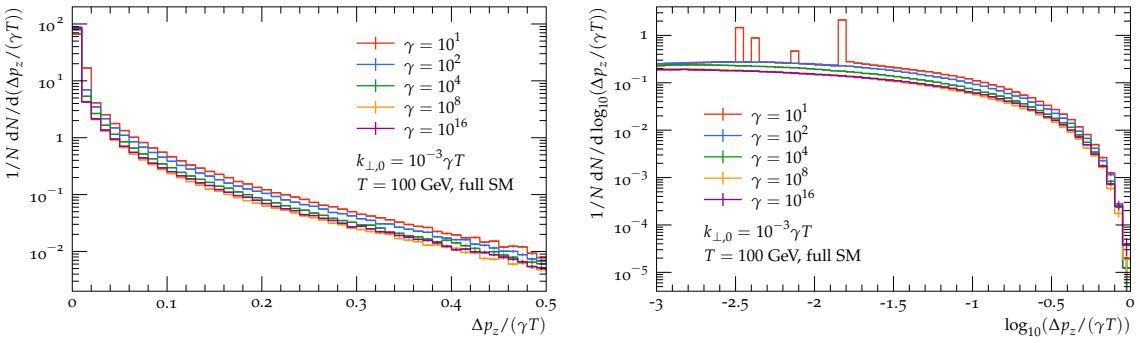

Figure 5.5: Boost factor dependence of the relative momentum transfer in the parton-shower approximation.

in kinematic effects when top-quarks, Higgs bosons, Z bosons and $W^{\pm}$ bosons are put on-shell or produced in $1 \to 2$ splittings at threshold. The net result are monochromatic lines and discontinuities in the momentum transfer spectrum which account for a larger average momentum transfer at small γ. However, in this region the soft approximation breaks down, and a more precise calculation should be performed. Such a calculation is not needed in order to determine the scaling behavior of the relative momentum transfer with γ. In the ultrarelativistic scenario, for $10^2 \lesssim \gamma \lesssim 10^{16}$, we can fit the numerical results for the average

momentum transfer in the full Standard Model at $T = 100$ GeV to the following form

$$\begin{aligned}\left\langle \frac{\Delta p_z}{\gamma T} \right\rangle =& 1.70(3)\% - 0.24(1)\% \, \log_{10}\gamma + 0.024(1)\% \, \log_{10}^2\gamma \\ &+ 0.0012(1)\% \log_{10}^3\gamma + 0.000023(1)\% \log_{10}^4\gamma \, ,\end{aligned} \tag{5.2.75}$$

where the numbers in parentheses are uncertainties on the last digit, determined from cutoff- and ordering parameter variations. Even for smaller γ, the above fit is accurate to within a factor of 2 down to $\gamma \sim 10$, where several of our other approximations begin to break down. Our numerical simulations confirm the analytic result of section 5.2.3. The mild modifications that are due to running coupling effects are captured by Eq. (5.2.75), and the threshold effects only increase the average relative momentum transfer.

Note that our numerical simulations assumed particles in the broken phase to have masses set by their $T = 0$ values. In a realistic phase transition, $\langle\phi\rangle \neq 246$ GeV, and so the broken phase masses depend non-trivially on the details of the Higgs finite-temperature effective potential. However, for sufficiently large velocities such that $\gamma T \gg m$ (required by several of the approximations we have made), the precise values of the broken phase masses are not important and the relative momentum transfer is still expected to be $\sim 1\% \times \gamma T$, with the scaling determined by Eq. (5.2.68).

5.2.5 The bubble wall velocity and its implications for cosmology

Using the above results, we can obtain an estimate for the terminal wall velocity as a function of the phase transition strength. The bubble wall reaches a terminal velocity when the pressure difference between the interior and exterior vanishes. The total pressure difference, $\Delta P_{\rm tot}$ is given by

$$\Delta P_{\rm tot} = -\Delta V + P \, , \tag{5.2.76}$$

where P is the thermal pressure exerted against the wall arising from particles impinging on it and showering as computed in Secs. 5.2.3-5.2.4, and ΔV is the difference in vacuum energy between the two phases. From Eqs. (5.2.11), (5.2.18), and (5.2.19), we can relate the thermal pressure to the average momentum transfer obtained from either the analytic or numerical treatments above. We find:

$$P = \sum_{a\in\mathcal{S}} \nu_a \int \frac{\mathrm{d}^3\vec{p}_a}{(2\pi)^3 E_a} f_a(\vec{p}_a)\, p_{a,z}^2 \left\langle \frac{\Delta p_z}{\gamma T} \right\rangle , \tag{5.2.77}$$

which, up to $\log\gamma$ effects stemming from thresholds and the running of the couplings, is simply a constant times the total z-direction wall-frame plasma pressure in the symmetric phase from particles coupled to the Higgs. In other words, we have found that in the limit of large wall velocities, *the net thermal pressure experienced by the bubble wall in its rest frame is simply a constant fraction ($\sim 1\%$) of the total pressure of the gas of symmetric-phase particles that couple directly to the wall.* We can approximate

$$P \simeq P_{1\to 1} + \gamma^2 \times \lim_{\gamma\to\infty} \left(\frac{P_{\rm FC}}{\gamma^2} \right) , \tag{5.2.78}$$

where

$$P_{1\to 1} \equiv \sum_{a\in\mathcal{S}} \int \frac{\mathrm{d}^3\vec{p}_a}{(2\pi)^3 2E_a} f_a(\vec{p}_a) \Delta m_a^2 , \tag{5.2.79}$$

is the $1 \to 1$ pressure and the 'FC' subscript denotes the fixed-coupling approximation of the relative momentum transfer, $\langle \Delta p_z/(\gamma T)\rangle \approx \langle \Delta p_z/(\gamma T)\rangle_{\rm FC}$ in Eq. (5.2.77) (the results will not be very sensitive to the precise scale chosen).

To obtain a parametric estimate of the terminal wall velocity, Eq. (5.2.76) indicates that P should be compared against the quantity ΔV, which is model-dependent. However, in many cases of interest, it is set roughly by the energy density of the radiation bath during

the transition. We can define the following parameters

$$\alpha_\theta \equiv \frac{\Delta V}{\rho_{\rm rad}}, \qquad \alpha_\infty \equiv \frac{P_{1\to 1}}{\rho_{\rm rad}} \approx 5\times 10^{-3}\,\frac{\langle\phi\rangle^2}{T^2}, \qquad \alpha_{\rm eq} \equiv \lim_{\gamma\to\infty}\left(\frac{P_{\rm FC}}{\gamma^2}\right)\frac{1}{\rho_{\rm rad}} \approx 1\times 10^{-2}\,, \tag{5.2.80}$$

where $\rho_{\rm rad} = \pi^2/30 g_*(T) T^4$ with $g_*(T) \approx 100$, and the numerical values in Eq. (5.2.80) assume SM-like plasma content with $\langle \Delta p_z/(\gamma T)\rangle \approx \langle \Delta p_z/(\gamma T)\rangle_{\rm FC} \approx 1\%$ evaluated from Table. 5.1. The quantity α_θ parametrizes the strength of the phase transition, and appears often in the GW literature (see e.g. Ref. [319] for an in-depth discussion). Models for which $\alpha_\theta > \alpha_\infty$ would satisfy the original runaway wall condition of Ref. [335] if transition radiation was not taken into account. Inserting Eqs. (5.2.77), (5.2.80) into Eq. (5.2.76) and requiring $\Delta P_{\rm tot} = 0$, we find the terminal velocity, expressed in terms of the equilibrium value of γ is

$$\gamma_{\rm eq} = \left(\frac{\alpha_\theta - \alpha_\infty}{\alpha_{\rm eq}}\right)^{1/2} \approx 10\,\sqrt{\alpha_\theta}\,, \tag{5.2.81}$$

where the final approximation applies for $\alpha_\theta \gg \alpha_\infty$ as is the case when $\gamma T \gg m$ (i.e. where our analysis remains self-consistent). Note that, for strong phase transitions, the terminal velocity depends on the strength of the phase transition and the gauge boson couplings, but not the particle masses. This is a strikingly different result than that implied by the fixed-order calculation of Ref. [336].

Throughout our analysis we have assumed $\gamma T \gg m$ for all massive SM particles in the plasma[7]. This allowed us to neglect the reflection of particles back into the symmetric phase, the transmission of particles from the broken into the symmetric phase, and the plasma interactions which drive the distributions back to equilibrium, which substantially complicate the calculation (see Refs. [368–374] for calculations in this slow-wall regime). For an electroweak-scale transition with $T \gtrsim \mathcal{O}(10)$ GeV and a SM-like plasma where the

7. We also worked in the thin-wall limit, $mL_w \ll 1$, which can be violated by the heaviest SM degrees of freedom if L_w is sufficiently thick. However, L_w depends on the underlying effective potential and implicitly on the terminal velocity itself, and so this criterion should be checked on a model-by-model basis.

largest masses are $\mathcal{O}(100)$ GeV, the approximations we have made break down for $\gamma \lesssim \mathcal{O}(10)$. Meanwhile, for many models with SM-like plasma content, one finds $\alpha_\theta \lesssim 1$ (see e.g. [319] and the corresponding benchmark points compiled at ptplot.org), implying that $\gamma_{\rm eq} \lesssim 10$ in these conventional cases. Although our approximations break down for these relatively small values of γ, we can still interpret our result as an upper bound on $\gamma_{\rm eq}$: if $\gamma_{\rm eq}$ were in fact larger than $\mathcal{O}(10)$, then our approximations would be justified and we would find no self-consistent solution for the terminal velocity, implying that the true value of $\gamma_{\rm eq}$ must fall within the regime where our analysis breaks down. For BSM scenarios with large values of α_θ, our predicted value of $\gamma_{\rm eq}$ will become increasingly accurate.

It is illuminating to compare our results for the terminal velocity to those obtained from the earlier fixed-order results of Ref. [336]. To do so, we follow the approach of Ref. [375], which amounts to using $\langle \Delta p_z/(\gamma T)\rangle^{(\rm cut)}_{\rm FC,FO}$ in place of $\langle \Delta p_z/(\gamma T)\rangle$ and neglecting the logarithmic term. Eq. (5.2.76) then becomes

$$P_{\rm tot} \simeq -\Delta V + P_{1\to 1} + P_{1\to 2}^{\rm FO,\,NL}\,, \tag{5.2.82}$$

where

$$P_{1\to 2}^{\rm FO,\,NL} \equiv \sum_{a\in\mathcal{S}} \int \frac{{\rm d}^3\vec{p}_a}{(2\pi)^3} f_a(\vec{p}_a)\,\gamma T \left\langle \frac{\Delta p_z}{\gamma T}\right\rangle^{(\rm cut)}_{\rm FC,FO}\,, \tag{5.2.83}$$

with the logarithmic term dropped in $\langle \Delta p_z/(\gamma T)\rangle^{(\rm cut)}_{\rm FC,FO}$. In analogy with Eq. (5.2.80), we can define

$$\alpha_{\rm eq}^{\rm FO,\,NL} \equiv \frac{P_{1\to 2}^{\rm FO,\,NL}}{\gamma\,\rho_{\rm rad}} \approx 7\times 10^{-5}\,\frac{\langle\phi\rangle}{T}\,, \tag{5.2.84}$$

where the numerical value again assumes SM-like plasma content and only accounts for the electroweak gauge boson contributions, as in Ref. [375]. The analog of Eq. (5.2.81) is

$$\gamma_{\rm eq} = \frac{\alpha_\theta - \alpha_\infty}{\alpha_{\rm eq}^{\rm FO,\,NL}} \approx 1\times 10^4 \left(\frac{\langle\phi\rangle}{T}\right)^{-1} \times \alpha_\theta, \qquad (\text{fixed order, no logarithm})\,, \tag{5.2.85}$$

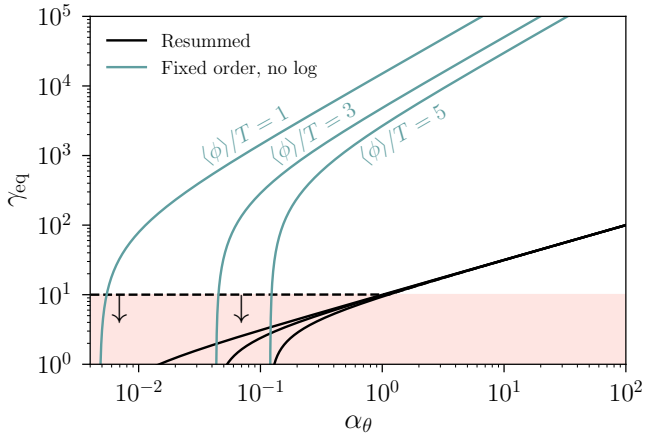

Figure 5.6: Comparison of the terminal Lorentz factor from our analysis (black) compared to those inferred from a fixed-order calculation (blue). We show predictions for different values of the order parameter $\langle\phi\rangle/T$, with $\langle\phi\rangle/T = 1,\ 3,\ 5$ for the set of black curves from top to bottom, and similarly for the blue curves. For large α_θ (strong transitions), our results predict significantly slower walls than implied by previous analyses, with the terminal velocity independent of the particle masses. For an electroweak-scale phase transition in a SM-like plasma, several of the approximations made break down for $\gamma_{\rm eq} \lesssim 10$, rendering the predictions in the shaded pink region unreliable. There, our result should be interpreted as an upper bound on the terminal Lorentz factor, indicated by the dashed black line and the arrows.

with the last approximation again holding for $\alpha_\theta \gg \alpha_\infty$. In this approximation, the terminal velocity in the large-α_θ limit scales as α_θ instead of $\sqrt{\alpha_\theta}$, and further depends on the order parameter of the phase transition due to the mass cutoff in the integration.

We compare our result for the terminal Lorentz factor to the fixed-order prediction in Fig. 5.6. We show the corresponding results for $\langle\phi\rangle/T = 1,\ 3,\ 5$. For strong transitions, our resummed result implies significantly slower walls than suggested by the fixed-order calculation. One should bear in mind, however, that for $\gamma_{\rm eq} \lesssim 10$ or so (for a SM-like plasma) several of the approximations we have made break down - this is indicated by the shaded pink region of Fig. 5.6. In this regime, we instead interpret our results as an upper bound on the wall velocity, indicated by the black dashed line and the arrows: applying our analysis for larger γ would be self-consistent and predict a thermal pressure overwhelming the vacuum energy difference, indicating that such velocities are never reached. We discuss

the implications of these results for cosmology in the remainder of this section.

Cosmological implications

If the cosmological electroweak phase transition was first order in nature, the dynamics of the Higgs-phase bubble walls affect the production of various cosmological relics. In this subsection we briefly discuss the implications of our work for several possible relics.

- Gravitational wave radiation

  The departure from thermal equilibrium during a first order electroweak phase transition provides a suitable environment for production of GW radiation. GWs arise predominantly from three sources [18, 319, 320, 324]: the collisions of bubble walls, sound waves that are produced when bubble walls push through the plasma, and the decay of magnetohydrodynamic turbulence that is produced when bubbles collide. If the bubble walls were able to runaway, such that $\gamma \to \infty$ as $v \to 1$ without bound before colliding with other bubbles, then the latent heat of the phase transition would be transferred predominantly to the kinetic energy of the bubble walls and their collisions would provide the dominant source of GW energy. However, when the bubble walls reach a terminal velocity before they collide with each other, then the kinetic energy of the bubble walls saturates and most of the energy of the phase transition is transferred into the kinetic motion of the plasma [376]. In this case, the sound waves and turbulence are the dominant sources of GW radiation. The scalar field, sound wave, and turbulence contributions to the GW background differ in terms of their spectral shapes and dependence on the phase transition parameters. This implies that the detection prospects of the corresponding signal can depend quite strongly on which source(s) dominates.

  To assess the impact of our results on GW predictions, note that at early stages of expansion when the friction is negligible, the bubble expands as in vacuum, for which

the radius grows as

$$R \sim \gamma R_0 \,, \tag{5.2.86}$$

where R_0 is the initial radius, which itself is usually close to the critical radius R_c. The average size reached by the bubbles at collision, R_*, is set by the typical separation between bubble centers [319],

$$R_* \simeq (8\pi)^{1/3} \beta^{-1} \,, \tag{5.2.87}$$

for fast walls, where β parametrizes the duration of the PT and is typically $\sim \mathcal{O}(10 - 1000) H_*$ for models predicting a sizable GW signal with SM-like field content, with H_* the Hubble parameter at the transition (see Ref. [319] for a detailed discussion and examples). Eqs. (5.2.86) and (5.2.87) can be combined to define a characteristic Lorentz factor at collision in the absence of significant friction [375]:

$$\gamma_* \equiv \frac{(8\pi)^{1/3}}{R_c \beta} \gtrsim \frac{10^{-3}}{R_c H_*} \,, \tag{5.2.88}$$

for models with $\beta/H_* \lesssim 10^3$ as typically required for detection at LISA [319]. This Lorentz factor should be compared with our prediction for $\gamma_{\rm eq}$: if $\gamma_* \lesssim \gamma_{\rm eq}$, the bubbles effectively run away and the GW signal is dominated by the scalar field contributions. If $\gamma_* \gtrsim \gamma_{\rm eq}$, then the fluid sources (sound waves and turbulence) dominate. For thermal transitions, one typically expects $R_c \sim 1/T$, $H_* \sim T^2/M_{\rm Pl}$ with $M_{\rm Pl}$ the reduced Planck mass. Then

$$\gamma_* \gtrsim 10^{-3} \frac{M_{\rm Pl}}{T} \sim 10^{13} \,, \tag{5.2.89}$$

where the last approximate equality holds for EW-scale transitions with $T \sim 100$ GeV. From these considerations, we find that the GW signal will be completely dominated by contributions from the fluid for transitions with $\gamma_{\rm eq} \ll 10^{13}$ in models of interest.

From Fig. 5.6, we observe that for electroweak phase transition scenarios with SM-like potentials and $\alpha \sim \mathcal{O}(1)$ or so, both our result and the earlier $1 \to 2$ estimates predict $\gamma_{\rm eq} \ll \gamma_*$, so the qualitative picture does not change once higher-order effects are accounted for. However, there exist models with phase transitions arising from non-polynomial potentials, which can feature extremely large values of α (see [319,375,377–392] for examples). In these cases, our results will likely yield substantially different predictions for the GW signal. It could be the case that due to the $P \propto \gamma^2$ scaling, models which were previously thought to exhibit $\gamma_{\rm eq} > \gamma_*$, and hence a large scalar field contribution to the GW signal, do not once higher order effects are accounted for. We intend to apply our methods to such BSM scenarios in future work.

- Matter-antimatter asymmetry

  The cosmological excess of matter over antimatter may have arisen at the electroweak phase transition through the physics of electroweak baryogenesis [36,393] (see Ref. [34] for a review). There are various implementations of electroweak baryogenesis.

  Theories of *non-local* electroweak baryogenesis [15] rely on the transport of charge (particle number asymmetries) from the Higgs-phase bubble wall, where CP is violated, to the symmetric phase in front of the wall, where B is violated. These theories require the non-relativistic wall velocities, as the CP-violating source becomes suppressed for walls moving significantly faster than the speed of sound in the plasma[8], $c_s \approx 1/\sqrt{3} \simeq 0.577$. Otherwise, charge simply enters the bubble without diffusing into the symmetric phase, and there is insufficient time for B-violation to act. Our results imply that the friction from Standard Model particles in the plasma will lead to a relativistic wall with $\gamma = \mathcal{O}(10)$ for SM-like electroweak transitions with $\alpha_\theta \sim 1$, which does not provide the necessary environment for non-local electroweak baryogenesis [395,396]. However,

8. Ref. [394] recently showed that the resulting baryon asymmetry does not necessarily vanish for velocities exceeding c_s, however it is still generally suppressed relative to the subsonic case and vanishes as $v \to 1$.

a viable scenario can be obtained for smaller values of α_θ or by lowering the wall's terminal velocity by introducing new species of particles in the plasma to raise the thermal pressure beyond the Standard Model prediction.

Alternatively, theories of *local* electroweak baryogenesis [397] implement both CP and B violation at the Higgs-phase bubble wall. For instance, the passage of bubble walls through regions of plasma with nonzero gauge-Higgs field winding will trigger these configurations to unwind and generate an anomalous B number. A related idea was proposed recently in Ref. [398] where the collisions of ultrarelativistic bubble walls creates heavy particles that decay out of equilibrium to generate the baryon asymmetry. In these theories, there is no upper limit on the wall's speed, and baryogenesis may be viable even for ultrarelativistic walls. However, our results preclude the possibility of runaway bubbles at SM-like electroweak transitions, which could impact the viability of mechanisms like that proposed in Ref. [398], depending on the details of the plasma content and potential assumed.

- Primordial magnetic fields

  The collisions of Higgs-phase bubble walls at the electroweak phase transition are expected to generate a primordial magnetic field [399]. For instance, bubble collisions stir up the charged constituents of the plasma [400], and the associated magnetohydrodynamic turbulence leads to a magnetic field with coherence on the scale of the bubble radius.

  The subsequent evolution of this primordial magnetic field from the electroweak phase transition until today can be studied with the theory of magnetohydrodynamics, for instance using numerical lattice simulations [401,402]. This cosmological magnetic field is expected to survive in the Universe today where it may play an important role in the generation of galactic magnetic fields and may be probed by various cosmological and astrophysical observations; see Ref. [403] for a general review, and see Ref. [404]

for a discussion of the electroweak phase transition, in particular. We are not aware of any studies that specifically address how the primordial magnetic field's strength depends on the bubble wall's speed in the regime where $\gamma \gg 1$, and this would be interesting to investigate further. Nevertheless, it is reasonable to expect some level of magnetic field creation for any γ, since electromagnetic radiation can arise even for a vacuum electroweak phase transition [405], which corresponds to the regime $\gamma \to \infty$ with a runaway bubble wall.

5.2.6 Summary and discussion of the section

We have presented an all-orders calculation of the pressure exerted by Standard Model particles on fast-moving bubble walls produced during a first order electroweak phase transition in the early Universe. We built on and extended the pioneering works of Refs. [335] and [336] which calculated the pressure induced from $1 \to 1$ and $1 \to 2$ processes respectively. These fixed-order calculations receive large corrections in the limit of large wall velocities, motivating an all-orders calculation in the leading-logarithmic approximation, which we have performed for the first time.

We carried out a fixed-order calculation where we parametrized the radiating particle in terms of a classical current. From this, the vacuum persistence amplitude was calculated, at leading logarithmic accuracy, for both the real emissions and virtual corrections. This is necessary as infrared divergences cancel once the virtual corrections and real emissions are combined at the same order in perturbation theory. The vacuum persistence amplitude squared is exponentiated to calculate the resummed average momentum transfer, $\langle \Delta p_z \rangle$, to the wall. This calculation closely follows the resummation of the thrust observable at colliders. As seen in Eq. (5.2.68), we found $\langle \Delta p_z \rangle \sim \gamma T$, where the coefficient depends on the coupling of the incident particle species to the radiated particle. The corresponding pressure is given by Eqs. (5.2.7) and (5.2.8). In addition to the analytic resummation we numerically

simulated a particle shower inside the bubble and extracted the average momentum transfer to the wall. We found the numerical and analytical resummation results to be consistent with each other at the 10% level and exhibit the same parametric dependence on the the boost factor; see Table. 5.1.

For a wall with Lorentz factor $\gamma \gg 1$, both approaches indicate an average momentum transfer of $\sim 1\% \times \gamma T$. The results in Table. 5.1 show that the pressure is dominated by both incoming vector bosons and quarks. Interestingly, gluon emission from light quarks presents a non-negligible contribution to the pressure due to the number of degrees of freedom for quarks and the magnitude of the strong coupling. This is in contrast with previous work, which found that the pressure is always dominated by the showered particles receiving the largest mass at the transition. As the pressure is a product of the incident particle flux and the average momentum transfer, our results indicate that the net thermal pressure experienced by the wall is parametrically $P \sim \gamma^2 T^4$ in its rest frame, and is simply a constant fraction ($\sim 1\%$) of the total pressure of the ideal gas of symmetric-phase particles that couple directly to the wall. This result in fact matches the scaling of the pressure in a different class of scenarios for which local thermal equilibrium is maintained across the wall, as shown recently in [374]. However, $P \sim \gamma^2 T^4$ is in contrast with Ref. [336], which instead found $P \sim \gamma \Delta m T^3$ with Δm the change in mass of the emitted gauge bosons. We trace this difference back to an ad-hoc cutoff of the momentum integrals and the neglect of large logarithms in Ref. [336], which must be resummed. As such, we conclude that Higgs-phase bubble walls at strong electroweak phase transitions reach significantly slower terminal velocities than previously thought.

Our results have implications for various cosmological observables. Of particular interest is their impact on the scaling of the terminal bubble wall velocity with γ and the strength of the phase transition, as this affects the associated gravitational wave (GW) spectrum. In Fig. 5.5, we show the terminal Lorentz boost factor ($\gamma_{\rm eq}$) of the bubble wall as a function of

the vacuum energy difference normalized to the thermal energy of the bath (α_θ). The scaling we calculated is shown in black while the scaling of [336] is shown in blue. This figure demonstrates that for a given value of α_θ, incorporation of off-shell effects significantly reduces the bubble wall velocity and results in $\gamma_{\rm eq} \propto \sqrt{\alpha_\theta}$ as opposed to $\propto \alpha_\theta$. This is important as slower moving bubble walls imply the predominant source of GWs stems from the fluid. As a result, the GW spectrum in models with large α_θ can have a markedly difference shape than in the case where the contribution from collisions is assumed to dominate.

Our work has focused on first order electroweak phase transitions where the plasma content is dominated by SM particles. This led to gluon and electroweak gauge boson emission being the dominant source of momentum transfer at the wall. This is not necessarily the case in other models of interest from the standpoint of GW production. It would be interesting to extend our analysis to these scenarios in the future.

5.A Appendices for the bubble wall speed

5.A.1 Vertex functions

In this appendix we compute the charge factors needed to evaluate Eq. (5.2.68) and to perform the numerical simulations in subsection 5.2.4. For strong interactions, we extract the strong coupling $g_3^2 = 4\pi\alpha_s$. Ignoring subleading N_c contributions, the charge factors are then given by the color Casimir operators

$$C_{qqg} = C_F = \frac{N_c^2 - 1}{2N_c} , \qquad C_{ggg} = C_A = N_c . \tag{5.A.1}$$

The relevant electroweak couplings can be obtained from existing approaches to electroweak showers [351, 406–408]. We give the helicity averaged results, which are sufficient for the target accuracy in our calculation. We denote $\cos\theta_W = m_W/m_Z$ as c_W and $\sin\theta_W$ as s_W. We extract the electromagnetic coupling as $g_1^2 = 4\pi\alpha$. This leaves the following charge

factors for bosonic interactions [351]

$$
\begin{aligned}
&C_{W^\pm W^\mp \gamma} = C_{G_{W^\pm} G_{W^\mp} \gamma} = 1 \,, \quad C_{W^\pm W^\mp Z} = \frac{c_W^2}{s_W^2} \,, \quad C_{G_{W^\pm} G_{W^\mp} Z} = \left(\frac{c_W^2 - s_W^2}{2 c_W s_W} \right)^2 \,, \\
&C_{h G_{W^\pm} W^\mp} = C_{G_Z G_{W^\pm} W^\mp} = \frac{1}{4 s_W^2} \,, \quad C_{h G_Z Z} = \frac{1}{4 c_W^2 s_W^2} \,.
\end{aligned}
\tag{5.A.2}
$$

For radiation off of fermions we obtain

$$
\begin{aligned}
&C_{f_i f_j \gamma} = Q_f^2 \, \delta_{ij} \,, \quad C_{f_i f_j Z} = \left(Q_f \frac{s_W}{c_W} \right)^2 \delta_{ij} + \left(Q_f \frac{s_W}{c_W} - \frac{I_f^3}{c_W s_W} \right)^2 \delta_{ij} \,, \\
&C_{\bar{u}_i d_j W^+} = \frac{1}{4 s_W^2} \, |V_{ij}|^2 \,, \quad C_{\bar{\nu}_i l_j W^+} = \frac{1}{4 s_W^2} \, \delta_{ij} \,,
\end{aligned}
\tag{5.A.3}
$$

where Q_f and I_f^3 are the electric charge and third component of weak isospin for the fermion f, and where V is the CKM matrix.

5.A.2 Kinematics mapping and phase-space factorization

The algorithm for constructing the splitting kinematics in the numerical simulation is modeled on Ref. [409]. We use the following variables for a dipole splitting $\{\widetilde{ij}, \tilde{k}\} \to \{i, j, k\}$ with momentum configuration $\tilde{p}_{ij} + \tilde{p}_k \to p_i + p_j + p_k$:

$$
\tilde{z}_i = \frac{p_i p_k}{p_i p_k + p_j p_k} \,, \qquad s_{ij} = (p_i + p_j)^2 \,, \qquad \text{and} \qquad Q = p_i + p_j + p_k \,. \tag{5.A.4}
$$

The variable $\tilde{z}_i$ corresponds to the splitting variable of the parton shower, while the invariant mass s_{ij} is computed from the evolution and splitting variable as (cf. Sec. 5.2.4)

$$
s_{ij} = t \times \begin{cases} \big(\tilde{z}_i (1 - \tilde{z}_i)\big)^{-1} & \text{if } t = k_T^2 \text{cf. [410]} \\ \tilde{z}_i (1 - \tilde{z}_i) & \text{if } t = \tilde{q}_T^2 \text{cf. [366]} \end{cases} \,. \tag{5.A.5}
$$

The spectator particle k serves as a source of anti-collinear momentum, but is otherwise unaffected by the splitting of the mother particle $\widetilde{ij}$ into the daughter particles i and j. For primary branchings, i.e. those where the particle $\widetilde{ij}$ radiates coherently with the incoming particle p_a, we choose $p_k^\mu = (M, \vec{0})$, where $M \gg \gamma T$. This corresponds to the reaction with the wall being modeled as a fixed-target collision, with an energy transfer that is suppressed by $(\Delta p)^2/2M^2$ compared to the momentum transfer Δp, such that it can be neglected. For secondary branchings we use the standard parton shower assignment of p_k [364]. The kinematics mapping proceeds as follows

1. Determine the new momentum of the spectator parton as

$$p_k^\mu = \left(\tilde{p}_k^\mu - \frac{Q\cdot\tilde{p}_k}{Q^2}\,Q^\mu\right)\sqrt{\frac{\lambda(Q^2,s_{ij},m_k^2)}{\lambda(Q^2,m_{ij}^2,m_k^2)}} + \frac{Q^2+m_k^2-s_{ij}}{2\,Q^2}\,Q^\mu\,, \tag{5.A.6}$$

   with λ denoting the Källen function $\lambda(a,b,c) = (a-b-c)^2 - 4\,bc$
   and $s_{ij} = y_{ij,k}\,(q^2 - m_k^2) + (1-y_{ij,k})\,(m_i^2+m_j^2)$.

2. Construct the new momentum of the emitter parton, p_i, as

$$p_i^\mu = \bar{z}_i\,\frac{\gamma(Q^2,s_{ij},m_k^2)\,p_{ij}^\mu - s_{ij}\,p_k^\mu}{\beta(Q^2,s_{ij},m_k^2)} + \frac{m_i^2+\mathrm{k}_\perp^2}{\bar{z}_i}\,\frac{p_k^\mu - m_k^2/\gamma(Q^2,s_{ij},m_k^2)\,p_{ij}^\mu}{\beta(Q^2,s_{ij},m_k^2)} + k_\perp^\mu\,, \tag{5.A.7}$$

   where $\beta(a,b,c) = \mathrm{sgn}(a-b-c)\sqrt{\lambda(a,b,c)}$, $2\,\gamma(a,b,c) = (a-b-c) + \beta(a,b,c)$ and $p_{ij}^\mu = Q^\mu - p_k^\mu$.
   The parameters $\bar{z}_i$ and $\mathrm{k}_\perp^2 = -k_\perp^2$ of this decomposition are given by

$$\begin{aligned}\bar{z}_i &= \frac{Q^2-s_{ij}-m_k^2}{\beta(Q^2,s_{ij},m_k^2)}\left[\tilde{z}_i - \frac{m_k^2}{\gamma(Q^2,s_{ij},m_k^2)}\frac{s_{ij}+m_i^2-m_j^2}{Q^2-s_{ij}-m_k^2}\right]\,,\\ \mathrm{k}_\perp^2 &= \bar{z}_i\,(1-\bar{z}_i)\,s_{ij} - (1-\bar{z}_i)\,m_i^2 - \bar{z}_i\,m_j^2\,,\end{aligned} \tag{5.A.8}$$

3. The transverse momentum is constructed using an azimuthal angle, ϕ_{ai}

$$k_\perp^\mu = \mathrm{k}_\perp \left(\cos\phi_{ai} \frac{n_\perp^\mu}{|n_\perp|} + \sin\phi_{ai} \frac{l_\perp^\mu}{|l_\perp|} \right) , \qquad \text{where} \quad n_\perp^\mu = \varepsilon^{0\mu}{}_{\nu\rho}\, \tilde{p}_{ij}^\nu\, \tilde{p}_k^\rho , \qquad l_\perp^\mu = \varepsilon^\mu{}_{\nu\rho\sigma}\, \tilde{p}_{ij}^\nu\, \tilde{p}_k^\rho\, n_\perp^\sigma . \tag{5.A.9}$$

In kinematical configurations where $\vec{\tilde{p}}_{aij} = \pm\vec{\tilde{p}}_k$, $n_\perp$ in the definition of Eq. (5.A.9) vanishes. It can then be computed as $n_\perp^\mu = \varepsilon^{0\,i\mu}{}_\nu\, \tilde{p}_{aij}^\nu$, where i may be any Lorentz index that yields a nonzero result.

The phase-space factorization was derived in [411], App. B. Standard s-channel factorization over p_{ij} gives [412, 413]

$$\begin{aligned} \int \mathrm{d}\Phi(p_i, p_j, p_k |\, Q) &= \int \frac{\mathrm{d}s_{ij}}{2\pi} \int \mathrm{d}\Phi(p_{ij}, p_k |\, Q) \int \mathrm{d}\Phi(p_i, p_j |\, p_{ij}) \\ &= \int \frac{\mathrm{d}s_{ij}}{2\pi} \sqrt{\frac{\lambda(Q^2, s_{ij}, m_k^2)}{\lambda(Q^2, m_{ij}^2, m_k^2)}} \int \mathrm{d}\Phi(\tilde{p}_{ij}, \tilde{p}_k |\, Q) \int \mathrm{d}\Phi(p_i, p_j |\, p_{aij}) \\ &= \int \mathrm{d}\Phi(\tilde{p}_{ij}, \tilde{p}_k |\, Q) \int \Big[\mathrm{d}\Phi(p_i, p_j |\, \tilde{p}_{ij}, \tilde{p}_k) \Big] \end{aligned} \tag{5.A.10}$$

where $\mathrm{d}\Phi(p_{i_1}, \ldots, p_{i_n}|Q)$ is given by the n-particle final-state phase space integral in Eq. (5.2.13), times a 4-momentum conservation constraint in the form $(2\pi)^4\delta^{(4)}(Q - p_{i_1} - \ldots - p_{i_n})$. We can rewrite Eq. (5.A.10) as

$$\begin{aligned} \int \Big[\mathrm{d}\Phi(p_i, p_j |\, \tilde{p}_{ij}, \tilde{p}_k) \Big] &= \int \frac{\mathrm{d}s_{ij}}{2\pi} \sqrt{\frac{\lambda(Q^2, s_{ij}, m_k^2)}{\lambda(Q^2, m_{ij}^2, m_k^2)}} \int \mathrm{d}\Phi(p_i, p_j | p_{ij}) \\ &= \int \frac{\mathrm{d}s_{ij}}{2\pi} \frac{1}{\sqrt{\lambda(q^2, m_{ij}^2, m_k^2)}} \int \frac{\mathrm{d}s_{ik}\, \mathrm{d}\phi_i}{4(2\pi)^2} = \frac{J_{\mathrm{FF}}}{16\pi^2} \int \mathrm{d}s_{ij} \int \mathrm{d}\tilde{z}_i \int \frac{\mathrm{d}\phi_i}{2\pi} , \end{aligned} \tag{5.A.11}$$

where $s_{ik} = (p_i + p_k)^2$, and where we have defined the Jacobian factor

$$J_{\rm FF} = \frac{Q^2 - s_{ij} - m_k^2}{\sqrt{\lambda(Q^2, m_{ij}^2, m_k^2)}} \,. \tag{5.A.12}$$

Note that for massless partons, $J_{\rm FF}$ takes the simple form $J_{\rm FF} = 1 - s_{ij}/Q^2$ [414]. In the soft limit, we have $J_{\rm FF} = 1$.

5.A.3 Soft virtual integrals

In $D = 4 - 2\varepsilon$ dimensions, Eq. (5.2.44) reads

$$W^{(2)}_{a\to b} = \, -4i\,|g|^2\mu^{2\varepsilon}\Big(I_1(p_a, p_b) - I_2(p_a) - I_2(p_b)\Big) \,, \tag{5.A.13}$$

where we have defined the basic integrals

$$I_1(p,q) = \int \frac{{\rm d}^D k}{(2\pi)^D}\frac{1}{k^2}\frac{2pq}{(2pk)(2qk)} \,, \qquad I_2(p) = \, \Theta(p^2)\int \frac{{\rm d}^D k}{(2\pi)^D}\frac{1}{k^2}\frac{p^2}{(2pk)^2} \,. \tag{5.A.14}$$

Note that these integrals are both IR and UV divergent. Naive evaluation using dimensional regularization would yield an ill-defined result. However, we are interested only in the cancellation of the IR singularities, which can be separated out at the integrand level. Using the decomposition $I_{1/2}(p,q) = I_{1/2,{\rm UV}}(p,q) + I_{1/2,{\rm IR}}(p,q)$, we define

$$I_{1,{\rm IR}}(p,q) = \int \frac{{\rm d}^D k}{(2\pi)^D}\frac{1}{k^2}\frac{2pq}{(2pk+k^2)(2qk+k^2)} \,, \qquad I_{2,{\rm IR}}(p) = \int \frac{{\rm d}^D k}{(2\pi)^D}\frac{1}{k^2}\frac{p^2}{(2pk+k^2)^2} \tag{5.A.15}$$

We use Feynman parameters to write the integrand of $I_{1,\mathrm{IR}}$ as

$$\frac{1}{k^2(2pk+k^2)(2qk+k^2)} = \int_0^1 \mathrm{d}x \int_0^1 \mathrm{d}y \, \frac{2x}{[K^2-C^2]^3} \,, \qquad \text{where} \qquad \begin{aligned} K &= k + C \\ C &= x(yp+(1-y)q) \end{aligned} \tag{5.A.16}$$

with the obvious change $C \to xp$ in the case of $I_{2,\mathrm{IR}}$. Using the basic integral

$$\int \frac{\mathrm{d}^D K}{(2\pi)^D} \frac{1}{[K^2-C^2]^M} = \frac{i(-1)^M}{(16\pi^2)^{D/4}} \frac{\mathrm{B}(D/2, M-D/2)}{\Gamma(D/2)(C^2)^{M-D/2}} \tag{5.A.17}$$

we obtain, in the massless case

$$I_{1,\mathrm{IR}}(p,q) = -\frac{i}{16\pi^2} \frac{(4\pi)^\varepsilon}{\Gamma(1-\varepsilon)} \frac{(2pq)^{-\varepsilon}}{\varepsilon^2} \frac{\Gamma(1-\varepsilon)^3\Gamma(1+\varepsilon)}{\Gamma(1-2\varepsilon)} \tag{5.A.18}$$

For one massive leg, p, we obtain

$$\begin{aligned} I_{1,\mathrm{IR}}(p,q) &= -\frac{i}{16\pi^2} \frac{(4\pi)^\varepsilon}{\Gamma(1-\varepsilon)} (2pq)^{-\varepsilon} \left(\frac{1}{2\varepsilon^2} + \frac{\log \mu_p^2}{2\varepsilon} - \frac{\log^2 \mu_p^2}{4} - \mathrm{Li}_2(1-\mu_p^2) + \frac{\pi^2}{12} + \mathcal{O}(\varepsilon) \right) \\ I_{2,\mathrm{IR}}(p) &= \frac{i}{16\pi^2} \frac{(4\pi)^\varepsilon}{\Gamma(1-\varepsilon)} \frac{(p^2)^{-\varepsilon}}{2\varepsilon} \Gamma(1-\varepsilon)\Gamma(1+\varepsilon) \end{aligned} \tag{5.A.19}$$

where we have defined $\mu_p^2 = p^2/(2pq)$.

5.A.4 Soft real-emission integrals

In $D = 4-2\varepsilon$ dimensions, Eq. (5.2.49) reads

$$\int \mathrm{d}W^{2\,(1)}_{a\to bc} = -4|g|^2\mu^{2\varepsilon}\Big(\tilde{I}_1(p_a,p_b) - \tilde{I}_2(p_a,p_b) - \tilde{I}_2(p_b,p_a)\Big) \,, \tag{5.A.20}$$

where we have defined the basic integrals

$$\tilde{I}_1(p,q) = \int \frac{\mathrm{d}^D k}{(2\pi)^{D-1}} \frac{2pq}{(2pk)(2qk)}\, \delta^+(k^2)\,, \qquad \tilde{I}_2(p,q) = \Theta(p^2) \int \frac{\mathrm{d}^D k}{(2\pi)^{D-1}} \frac{p^2}{(2pk)^2}\, \delta^+(k^2)\,. \tag{5.A.21}$$

We use the Sudakov parametrization of Eq. (5.2.21). At leading power, we may neglect recoil effects and obtain

$$\mathrm{d}^D k = n\bar{n}\, \mathrm{d}\alpha\, \mathrm{d}\beta\, \mathrm{d}^{D-2} k_T\,, \qquad \text{where} \qquad \alpha = \frac{\bar{n}k}{n\bar{n}}\,, \qquad \beta = \frac{nk}{n\bar{n}}\,. \tag{5.A.22}$$

We redefine the light-like momenta n and $\bar{n}$ as the solutions of

$$p = n + \frac{p^2}{2n\bar{n}}\,\bar{n}\,, \qquad q = \bar{n} + \frac{q^2}{2n\bar{n}}\,n\,, \qquad \text{where} \qquad 2n\bar{n} = pq\left(1 + v_{p,q}\right)\,, \qquad v_{p,q} = \sqrt{1 - \frac{p^2 q^2}{(pq)^2}}\,. \tag{5.A.23}$$

The transverse momentum integral can be solved with the help of the on-shell condition

$$\int \mathrm{d}^{D-2} k_T\, \delta^+(k^2) = \frac{2\pi^{1-\varepsilon}}{\Gamma(1-\varepsilon)}\, \frac{1}{2}\, (2n\bar{n})^{-\varepsilon} \big(\alpha\beta\big)^{-\varepsilon}\,. \tag{5.A.24}$$

This leads to the following result for the massless case

$$\tilde{I}_1(p,q) = -\frac{1}{16\pi^2} \frac{(4\pi)^\varepsilon}{\Gamma(1-\varepsilon)}\, \frac{(2pq)^{-\varepsilon}}{\varepsilon^2}\,. \tag{5.A.25}$$

In the case of one massive leg, $p^2 > 0$, we obtain instead

$$\begin{aligned}
\tilde{I}_1(p,q) =& -\frac{1}{16\pi^2}\frac{(4\pi)^\varepsilon}{\Gamma(1-\varepsilon)}(2pq)^{-\varepsilon}\left(\frac{1}{2\varepsilon^2}+\frac{\log\mu_p^2}{2\varepsilon}-\frac{\log^2\mu_p^2}{4}-\mathrm{Li}_2(-\mu_p^2)-\frac{\pi^2}{12}+\mathcal{O}(\varepsilon)\right)\\
\tilde{I}_2(p,q) =& \frac{1}{16\pi^2}\frac{(4\pi)^\varepsilon}{\Gamma(1-\varepsilon)}(2pq)^{-\varepsilon}\left(\frac{1}{2\varepsilon}-\frac{\log\mu_p^2}{2}+\log(1+\mu_p^2)+\mathcal{O}(\varepsilon)\right).
\end{aligned} \tag{5.A.26}$$

REFERENCES

[1] G. Aad et al. Observation of a new particle in the search for the Standard Model Higgs boson with the ATLAS detector at the LHC. *Phys. Lett. B*, 716:1–29, 2012. arXiv:1207.7214, doi:10.1016/j.physletb.2012.08.020.

[2] S. Chatrchyan et al. Observation of a New Boson at a Mass of 125 GeV with the CMS Experiment at the LHC. *Phys. Lett. B*, 716:30–61, 2012. arXiv:1207.7235, doi:10.1016/j.physletb.2012.08.021.

[3] C.-N. Yang and R. L. Mills. Conservation of Isotopic Spin and Isotopic Gauge Invariance. *Phys. Rev.*, 96:191–195, 1954. doi:10.1103/PhysRev.96.191.

[4] D. J. Gross and F. Wilczek. Ultraviolet Behavior of Nonabelian Gauge Theories. *Phys. Rev. Lett.*, 30:1343–1346, 1973. doi:10.1103/PhysRevLett.30.1343.

[5] H. D. Politzer. Reliable Perturbative Results for Strong Interactions? *Phys. Rev. Lett.*, 30:1346–1349, 1973. doi:10.1103/PhysRevLett.30.1346.

[6] S. L. Glashow. Partial Symmetries of Weak Interactions. *Nucl. Phys.*, 22:579–588, 1961. doi:10.1016/0029-5582(61)90469-2.

[7] S. Weinberg. A Model of Leptons. *Phys. Rev. Lett.*, 19:1264–1266, 1967. doi:10.1103/PhysRevLett.19.1264.

[8] A. Salam. Weak and Electromagnetic Interactions. *Conf. Proc. C*, 680519:367–377, 1968. doi:10.1142/9789812795915_0034.

[9] S. L. Glashow, J. Iliopoulos, and L. Maiani. Weak Interactions with Lepton-Hadron Symmetry. *Phys. Rev. D*, 2:1285–1292, 1970. doi:10.1103/PhysRevD.2.1285.

[10] D. Hanneke, S. Fogwell, and G. Gabrielse. New Measurement of the Electron Magnetic Moment and the Fine Structure Constant. *Phys. Rev. Lett.*, 100:120801, 2008. arXiv:0801.1134, doi:10.1103/PhysRevLett.100.120801.

[11] E. Fermi. An attempt of a theory of beta radiation. 1. *Z. Phys.*, 88:161–177, 1934. doi:10.1007/BF01351864.

[12] F. L. Wilson. Fermi's Theory of Beta Decay. *Am. J. Phys.*, 36(12):1150–1160, 1968. doi:10.1119/1.1974382.

[13] T. D. Lee and C.-N. Yang. Question of Parity Conservation in Weak Interactions. *Phys. Rev.*, 104:254–258, 1956. doi:10.1103/PhysRev.104.254.

[14] R. P. Feynman and M. Gell-Mann. Theory of Fermi interaction. *Phys. Rev.*, 109:193–198, 1958. doi:10.1103/PhysRev.109.193.

[15] A. G. Cohen, D. B. Kaplan, and A. E. Nelson. Baryogenesis at the weak phase transition. *Nucl. Phys. B*, 349:727–742, 1991. doi:10.1016/0550-3213(91)90395-E.

[16] A. Achucarro and T. Vachaspati. Semilocal and electroweak strings. *Phys.Rept.*, 327:347–426, 2000. arXiv:hep-ph/9904229, doi:10.1016/S0370-1573(99)00103-9.

[17] T. Vachaspati. Magnetic fields from cosmological phase transitions. *Phys.Lett.*, B265:258–261, 1991. doi:10.1016/0370-2693(91)90051-Q.

[18] M. Kamionkowski, A. Kosowsky, and M. S. Turner. Gravitational radiation from first order phase transitions. *Phys. Rev.*, D49:2837–2851, 1994. arXiv:astro-ph/9310044, doi:10.1103/PhysRevD.49.2837.

[19] K. Nakamura et al. Review of particle physics. *J. Phys. G*, 37:075021, 2010. doi:10.1088/0954-3899/37/7A/075021.

[20] F. Englert and R. Brout. Broken Symmetry and the Mass of Gauge Vector Mesons. *Phys. Rev. Lett.*, 13:321–323, 1964. doi:10.1103/PhysRevLett.13.321.

[21] P. W. Higgs. Broken symmetries, massless particles and gauge fields. *Phys. Lett.*, 12:132–133, 1964. doi:10.1016/0031-9163(64)91136-9.

[22] P. W. Higgs. Broken Symmetries and the Masses of Gauge Bosons. *Phys. Rev. Lett.*, 13:508–509, 1964. doi:10.1103/PhysRevLett.13.508.

[23] G. S. Guralnik, C. R. Hagen, and T. W. B. Kibble. Global Conservation Laws and Massless Particles. *Phys. Rev. Lett.*, 13:585–587, 1964. doi:10.1103/PhysRevLett.13.585.

[24] D. A. Kirzhnits. Weinberg model in the hot universe. *JETP Lett.*, 15:529–531, 1972.

[25] D. A. Kirzhnits and A. D. Linde. Macroscopic Consequences of the Weinberg Model. *Phys. Lett. B*, 42:471–474, 1972. doi:10.1016/0370-2693(72)90109-8.

[26] S. Weinberg. Gauge and Global Symmetries at High Temperature. *Phys. Rev. D*, 9:3357–3378, 1974. doi:10.1103/PhysRevD.9.3357.

[27] L. Dolan and R. Jackiw. Symmetry Behavior at Finite Temperature. *Phys. Rev. D*, 9:3320–3341, 1974. doi:10.1103/PhysRevD.9.3320.

[28] W.-M. Y. et al. Review of particle physics. *Journal of Physics G: Nuclear and Particle Physics*, 33(1):1–1232, jul 2006. URL: https://doi.org/10.1088/0954-3899/33/1/001, doi:10.1088/0954-3899/33/1/001.

[29] J. M. Cline. Baryogenesis. In *Les Houches Summer School - Session 86: Particle Physics and Cosmology: The Fabric of Spacetime*, 9 2006. arXiv:hep-ph/0609145.

[30] W. Hu and S. Dodelson. Cosmic Microwave Background Anisotropies. *Ann. Rev. Astron. Astrophys.*, 40:171–216, 2002. arXiv:astro-ph/0110414, doi:10.1146/annurev.astro.40.060401.093926.

[31] E. Komatsu et al. Seven-Year Wilkinson Microwave Anisotropy Probe (WMAP) Observations: Cosmological Interpretation. *Astrophys. J. Suppl.*, 192:18, 2011. arXiv:1001.4538, doi:10.1088/0067-0049/192/2/18.

[32] E. W. Kolb and M. S. Turner. *The Early Universe*, volume 69. 1990.

[33] A. D. Sakharov. Violation of CP Invariance, C asymmetry, and baryon asymmetry of the universe. *Pisma Zh. Eksp. Teor. Fiz.*, 5:32–35, 1967. doi:10.1070/PU1991v034n05ABEH002497.

[34] D. E. Morrissey and M. J. Ramsey-Musolf. Electroweak baryogenesis. *New J. Phys.*, 14:125003, 2012. arXiv:1206.2942, doi:10.1088/1367-2630/14/12/125003.

[35] A. Riotto. Theories of baryogenesis. In *ICTP Summer School in High-Energy Physics and Cosmology*, 7 1998. arXiv:hep-ph/9807454.

[36] V. A. Kuzmin, V. A. Rubakov, and M. E. Shaposhnikov. On the Anomalous Electroweak Baryon Number Nonconservation in the Early Universe. *Phys. Lett. B*, 155:36, 1985. doi:10.1016/0370-2693(85)91028-7.

[37] A. G. Cohen, D. B. Kaplan, and A. E. Nelson. WEAK SCALE BARYOGENESIS. *Phys. Lett. B*, 245:561–564, 1990. doi:10.1016/0370-2693(90)90690-8.

[38] L. Carson, X. Li, L. D. McLerran, and R.-T. Wang. Exact Computation of the Small Fluctuation Determinant Around a Sphaleron. *Phys. Rev. D*, 42:2127–2143, 1990. doi:10.1103/PhysRevD.42.2127.

[39] M. Quiros. Finite temperature field theory and phase transitions. pages 187–259, 1999. arXiv:hep-ph/9901312.

[40] M. Laine. Electroweak phase transition beyond the standard model. In *4th International Conference on Strong and Electroweak Matter*, 6 2000. arXiv:hep-ph/0010275, doi:10.1142/9789812799913_0005.

[41] K. Kajantie, M. Laine, K. Rummukainen, and M. E. Shaposhnikov. A Nonperturbative analysis of the finite T phase transition in SU(2) x U(1) electroweak theory. *Nucl. Phys. B*, 493:413–438, 1997. arXiv:hep-lat/9612006, doi:10.1016/S0550-3213(97)00164-8.

[42] K. Rummukainen, M. Tsypin, K. Kajantie, M. Laine, and M. E. Shaposhnikov. The Universality class of the electroweak theory. *Nucl. Phys. B*, 532:283–314, 1998. arXiv:hep-lat/9805013, doi:10.1016/S0550-3213(98)00494-5.

[43] M. Laine and K. Rummukainen. What's new with the electroweak phase transition? *Nucl. Phys. B Proc. Suppl.*, 73:180–185, 1999. arXiv:hep-lat/9809045, doi:10.1016/S0920-5632(99)85017-8.

[44] M. E. Shaposhnikov. Standard model solution of the baryogenesis problem. *Phys. Lett. B*, 277:324–330, 1992. [Erratum: Phys.Lett.B 282, 483 (1992)]. doi:10.1016/0370-2693(92)90753-Q.

[45] W. Heisenberg and H. Euler. Consequences of Dirac's theory of positrons. *Z. Phys.*, 98(11-12):714–732, 1936. arXiv:physics/0605038, doi:10.1007/BF01343663.

[46] J. S. Schwinger. On the Green's functions of quantized fields. 1. *Proc. Nat. Acad. Sci.*, 37:452–455, 1951. doi:10.1073/pnas.37.7.452.

[47] J. S. Schwinger. On the Green's functions of quantized fields. 2. *Proc. Nat. Acad. Sci.*, 37:455–459, 1951. doi:10.1073/pnas.37.7.455.

[48] G. Jona-Lasinio. Relativistic field theories with symmetry breaking solutions. *Nuovo Cim.*, 34:1790–1795, 1964. doi:10.1007/BF02750573.

[49] S. R. Coleman and E. J. Weinberg. Radiative Corrections as the Origin of Spontaneous Symmetry Breaking. *Phys. Rev. D*, 7:1888–1910, 1973. doi:10.1103/PhysRevD.7.1888.

[50] S. Weinberg. Perturbative Calculations of Symmetry Breaking. *Phys. Rev. D*, 7:2887–2910, 1973. doi:10.1103/PhysRevD.7.2887.

[51] R. Jackiw. Functional evaluation of the effective potential. *Phys. Rev. D*, 9:1686, 1974. doi:10.1103/PhysRevD.9.1686.

[52] L. Dolan and R. Jackiw. Gauge Invariant Signal for Gauge Symmetry Breaking. *Phys. Rev. D*, 9:2904, 1974. doi:10.1103/PhysRevD.9.2904.

[53] T. Matsubara. A New approach to quantum statistical mechanics. *Prog. Theor. Phys.*, 14:351–378, 1955. doi:10.1143/PTP.14.351.

[54] R. Kubo. Statistical mechanical theory of irreversible processes. 1. General theory and simple applications in magnetic and conduction problems. *J. Phys. Soc. Jap.*, 12:570–586, 1957. doi:10.1143/JPSJ.12.570.

[55] P. C. Martin and J. S. Schwinger. Theory of many particle systems. 1. *Phys. Rev.*, 115:1342–1373, 1959. doi:10.1103/PhysRev.115.1342.

[56] J. S. Schwinger. Brownian motion of a quantum oscillator. *J. Math. Phys.*, 2:407–432, 1961. doi:10.1063/1.1703727.

[57] L. V. Keldysh. Diagram technique for nonequilibrium processes. *Zh. Eksp. Teor. Fiz.*, 47:1515–1527, 1964.

[58] C. W. Bernard. Feynman Rules for Gauge Theories at Finite Temperature. *Phys. Rev. D*, 9:3312, 1974. doi:10.1103/PhysRevD.9.3312.

[59] S. Coleman. *Aspects of Symmetry*. Cambridge University Press, Cambridge, U.K., 1985. doi:10.1017/CBO9780511565045.

[60] J. S. Schwinger. On gauge invariance and vacuum polarization. *Phys. Rev.*, 82:664–679, 1951. doi:10.1103/PhysRev.82.664.

[61] J. Goldstone, A. Salam, and S. Weinberg. Broken Symmetries. *Phys. Rev.*, 127:965–970, 1962. doi:10.1103/PhysRev.127.965.

[62] J. Iliopoulos, C. Itzykson, and A. Martin. Functional Methods and Perturbation Theory. *Rev. Mod. Phys.*, 47:165, 1975. doi:10.1103/RevModPhys.47.165.

[63] S. P. Martin. Taming the Goldstone contributions to the effective potential. *Phys. Rev. D*, 90(1):016013, 2014. arXiv:1406.2355, doi:10.1103/PhysRevD.90.016013.

[64] J. Elias-Miro, J. R. Espinosa, and T. Konstandin. Taming Infrared Divergences in the Effective Potential. *JHEP*, 08:034, 2014. arXiv:1406.2652, doi:10.1007/JHEP08(2014)034.

[65] C. Delaunay, C. Grojean, and J. D. Wells. Dynamics of Non-renormalizable Electroweak Symmetry Breaking. *JHEP*, 04:029, 2008. arXiv:0711.2511, doi:10.1088/1126-6708/2008/04/029.

[66] C. L. Wainwright. CosmoTransitions: Computing Cosmological Phase Transition Temperatures and Bubble Profiles with Multiple Fields. *Comput. Phys. Commun.*, 183:2006–2013, 2012. arXiv:1109.4189, doi:10.1016/j.cpc.2012.04.004.

[67] P. Athron, C. Balázs, M. Bardsley, A. Fowlie, D. Harries, and G. White. BubbleProfiler: finding the field profile and action for cosmological phase transitions. *Comput. Phys. Commun.*, 244:448–468, 2019. arXiv:1901.03714, doi:10.1016/j.cpc.2019.05.017.

[68] P. Fendley. The effective potential and the coupling constant at high temperature. *Physics Letters B*, 196(2):175 – 180, 1987. URL: http://www.sciencedirect.com/science/article/pii/0370269387905995, doi:https://doi.org/10.1016/0370-2693(87)90599-5.

[69] L. Dolan and R. Jackiw. Symmetry behavior at finite temperature. *Phys. Rev. D*, 9:3320–3341, Jun 1974. URL: https://link.aps.org/doi/10.1103/PhysRevD.9.3320, doi:10.1103/PhysRevD.9.3320.

[70] D. Kirzhnits and A. D. Linde. A Relativistic phase transition. *Sov. Phys. JETP*, 40:628, 1975.

[71] R. R. Parwani. Resummation in a hot scalar field theory. *Phys. Rev. D*, 45:4695–4705, Jun 1992. URL: https://link.aps.org/doi/10.1103/PhysRevD.45.4695, doi:10.1103/PhysRevD.45.4695.

[72] H. Nakkagawa and H. Yokota. Phase structure of the massive scalar phi**4 model at finite temperature: Resummation procedure a la RG improvement. In *Summer School on Introduction to Thermal Field Theory (TFT 98)*, 9 1998. arXiv:hep-ph/9809317.

[73] P. B. Arnold and O. Espinosa. The Effective potential and first order phase transitions: Beyond leading-order. *Phys. Rev.*, D47:3546, 1993. [Erratum: Phys. Rev.D50,6662(1994)]. arXiv:hep-ph/9212235, doi:10.1103/physrevd.50.6662.2, 10.1103/PhysRevD.47.3546.

[74] D. Curtin, P. Meade, and H. Ramani. Thermal Resummation and Phase Transitions. *Eur. Phys. J.*, C78(9):787, 2018. arXiv:1612.00466, doi:10.1140/epjc/s10052-018-6268-0.

[75] M. Laine, M. Meyer, and G. Nardini. Thermal phase transition with full 2-loop effective potential. *Nucl. Phys. B*, 920:565–600, 2017. arXiv:1702.07479, doi:10.1016/j.nuclphysb.2017.04.023.

[76] M. Bando, T. Kugo, N. Maekawa, and H. Nakano. Improving the effective potential. *Phys. Lett.*, B301:83–89, 1993. arXiv:hep-ph/9210228, doi:10.1016/0370-2693(93)90725-W.

[77] M. Bando, T. Kugo, N. Maekawa, and H. Nakano. Improving the effective potential: Multimass scale case. *Prog. Theor. Phys.*, 90:405–418, 1993. arXiv:hep-ph/9210229, doi:10.1143/PTP.90.405.

[78] J. A. Casas, V. Di Clemente, and M. Quiros. The Effective potential in the presence of several mass scales. *Nucl. Phys. B*, 553:511–530, 1999. arXiv:hep-ph/9809275, doi:10.1016/S0550-3213(99)00262-X.

[79] C. Tamarit. Higgs vacua with potential barriers. *Phys. Rev. D*, 90(5):055024, 2014. arXiv:1404.7673, doi:10.1103/PhysRevD.90.055024.

[80] A. Andreassen, W. Frost, and M. D. Schwartz. Consistent Use of Effective Potentials. *Phys. Rev. D*, 91(1):016009, 2015. arXiv:1408.0287, doi:10.1103/PhysRevD.91.016009.

[81] A. Andreassen, W. Frost, and M. D. Schwartz. Consistent Use of the Standard Model Effective Potential. *Phys. Rev. Lett.*, 113(24):241801, 2014. arXiv:1408.0292, doi:10.1103/PhysRevLett.113.241801.

[82] M. B. Einhorn and D. R. T. Jones. A NEW RENORMALIZATION GROUP APPROACH TO MULTISCALE PROBLEMS. *Nucl. Phys. B*, 230:261–272, 1984. doi:10.1016/0550-3213(84)90127-5.

[83] C. Ford and C. Wiesendanger. A Multiscale subtraction scheme and partial renormalization group equations in the O(N) symmetric phi**4 theory. *Phys. Rev. D*, 55:2202–2217, 1997. arXiv:hep-ph/9604392, doi:10.1103/PhysRevD.55.2202.

[84] C. Ford and C. Wiesendanger. Multiscale renormalization. *Phys. Lett. B*, 398:342–346, 1997. arXiv:hep-th/9612193, doi:10.1016/S0370-2693(97)00237-2.

[85] H. Nakano and Y. Yoshida. Improving the effective potential, multimass problem and modified mass dependent scheme. *Phys. Rev. D*, 49:5393–5407, 1994. arXiv:hep-ph/9309215, doi:10.1103/PhysRevD.49.5393.

[86] H. Georgi. Effective field theory. *Ann. Rev. Nucl. Part. Sci.*, 43:209–252, 1993. doi:10.1146/annurev.ns.43.120193.001233.

[87] S.-B. Liao and M. Strickland. Renormalization group approach to field theory at finite temperature. *Phys. Rev. D*, 52:3653–3671, 1995. arXiv:hep-th/9501137, doi:10.1103/PhysRevD.52.3653.

[88] H. Nakkagawa and H. Yokota. RG improvement of the effective potential at finite temperature. *Mod. Phys. Lett. A*, 11:2259–2269, 1996. doi:10.1142/S0217732396002253.

[89] H. Nakkagawa and H. Yokota. Effective potential at finite temperature: RG improvement versus high temperature expansion. *Prog. Theor. Phys. Suppl.*, 129:209–214, 1997. arXiv:hep-ph/9709323, doi:10.1143/PTPS.129.209.

[90] M. Carena, Z. Liu, and Y. Wang. Electroweak phase transition with spontaneous Z_2-breaking. *JHEP*, 08:107, 2020. arXiv:1911.10206, doi:10.1007/JHEP08(2020)107.

[91] S. Baum, M. Carena, N. R. Shah, C. E. M. Wagner, and Y. Wang. Nucleation is More than Critical – A Case Study of the Electroweak Phase Transition in the NMSSM. 9 2020. arXiv:2009.10743, doi:10.1007/JHEP03(2021)055.

[92] D. J. H. Chung, A. J. Long, and L.-T. Wang. 125 GeV Higgs boson and electroweak phase transition model classes. *Phys. Rev. D*, 87(2):023509, 2013. arXiv:1209.1819, doi:10.1103/PhysRevD.87.023509.

[93] X.-m. Zhang. Operators analysis for Higgs potential and cosmological bound on Higgs mass. *Phys. Rev. D*, 47:3065–3067, 1993. arXiv:hep-ph/9301277, doi:10.1103/PhysRevD.47.3065.

[94] C. Grojean, G. Servant, and J. D. Wells. First-order electroweak phase transition in the standard model with a low cutoff. *Phys. Rev.*, D71:036001, 2005. arXiv:hep-ph/0407019, doi:10.1103/PhysRevD.71.036001.

[95] D. Bodeker, L. Fromme, S. J. Huber, and M. Seniuch. The Baryon asymmetry in the standard model with a low cut-off. *JHEP*, 02:026, 2005. arXiv:hep-ph/0412366, doi:10.1088/1126-6708/2005/02/026.

[96] B. Grinstein and M. Trott. Electroweak Baryogenesis with a Pseudo-Goldstone Higgs. *Phys. Rev. D*, 78:075022, 2008. arXiv:0806.1971, doi:10.1103/PhysRevD.78.075022.

[97] P. H. Damgaard, A. Haarr, D. O'Connell, and A. Tranberg. Effective Field Theory and Electroweak Baryogenesis in the Singlet-Extended Standard Model. *JHEP*, 02:107, 2016. arXiv:1512.01963, doi:10.1007/JHEP02(2016)107.

[98] J. de Vries, M. Postma, J. van de Vis, and G. White. Electroweak Baryogenesis and the Standard Model Effective Field Theory. *JHEP*, 01:089, 2018. arXiv:1710.04061, doi:10.1007/JHEP01(2018)089.

[99] M. Chala, C. Krause, and G. Nardini. Signals of the electroweak phase transition at colliders and gravitational wave observatories. *JHEP*, 07:062, 2018. arXiv:1802.02168, doi:10.1007/JHEP07(2018)062.

[100] J. R. Espinosa and M. Quiros. The Electroweak phase transition with a singlet. *Phys. Lett.*, B305:98–105, 1993. arXiv:hep-ph/9301285, doi:10.1016/0370-2693(93)91111-Y.

[101] J. R. Espinosa and M. Quiros. Novel Effects in Electroweak Breaking from a Hidden Sector. *Phys. Rev.*, D76:076004, 2007. arXiv:hep-ph/0701145, doi:10.1103/PhysRevD.76.076004.

[102] S. Profumo, M. J. Ramsey-Musolf, and G. Shaughnessy. Singlet Higgs phenomenology and the electroweak phase transition. *JHEP*, 08:010, 2007. arXiv:0705.2425, doi:10.1088/1126-6708/2007/08/010.

[103] J. R. Espinosa, T. Konstandin, and F. Riva. Strong Electroweak Phase Transitions in the Standard Model with a Singlet. *Nucl. Phys.*, B854:592–630, 2012. arXiv:1107.5441, doi:10.1016/j.nuclphysb.2011.09.010.

[104] V. Barger, D. J. H. Chung, A. J. Long, and L.-T. Wang. Strongly First Order Phase Transitions Near an Enhanced Discrete Symmetry Point. *Phys. Lett.*, B710:1–7, 2012. arXiv:1112.5460, doi:10.1016/j.physletb.2012.02.040.

[105] D. Curtin, P. Meade, and C.-T. Yu. Testing Electroweak Baryogenesis with Future Colliders. *JHEP*, 11:127, 2014. arXiv:1409.0005, doi:10.1007/JHEP11(2014)127.

[106] G. Kurup and M. Perelstein. Dynamics of Electroweak Phase Transition In Singlet-Scalar Extension of the Standard Model. *Phys. Rev.*, D96(1):015036, 2017. arXiv:1704.03381, doi:10.1103/PhysRevD.96.015036.

[107] J. Choi and R. R. Volkas. Real Higgs singlet and the electroweak phase transition in the standard model, (UM-P-93/80, OZ-93/20). *Phys. Lett.*, B317:385–391, 1993. arXiv:hep-ph/9308234, doi:10.1016/0370-2693(93)91013-D.

[108] S. W. Ham, Y. S. Jeong, and S. K. Oh. Electroweak phase transition in an extension of the standard model with a real Higgs singlet. *J. Phys.*, G31(8):857–871, 2005. arXiv:hep-ph/0411352, doi:10.1088/0954-3899/31/8/017.

[109] A. Noble and M. Perelstein. Higgs self-coupling as a probe of electroweak phase transition. *Phys. Rev.*, D78:063518, 2008. arXiv:0711.3018, doi:10.1103/PhysRevD.78.063518.

[110] A. Ashoorioon and T. Konstandin. Strong electroweak phase transitions without collider traces. *JHEP*, 07:086, 2009. arXiv:0904.0353, doi:10.1088/1126-6708/2009/07/086.

[111] S. Das, P. J. Fox, A. Kumar, and N. Weiner. The Dark Side of the Electroweak Phase Transition. *JHEP*, 11:108, 2010. arXiv:0910.1262, doi:10.1007/JHEP11(2010)108.

[112] S. Profumo, M. J. Ramsey-Musolf, C. L. Wainwright, and P. Winslow. Singlet-catalyzed electroweak phase transitions and precision Higgs boson studies. *Phys. Rev.*, D91(3):035018, 2015. arXiv:1407.5342, doi:10.1103/PhysRevD.91.035018.

[113] A. V. Kotwal, M. J. Ramsey-Musolf, J. M. No, and P. Winslow. Singlet-catalyzed electroweak phase transitions in the 100 TeV frontier. *Phys. Rev.*, D94(3):035022, 2016. arXiv:1605.06123, doi:10.1103/PhysRevD.94.035022.

[114] K. E. C. Benson. Avoiding baryon washout in the extended Standard Model. *Phys. Rev.*, D48:2456–2461, 1993. doi:10.1103/PhysRevD.48.2456.

[115] J. McDonald. Electroweak baryogenesis and dark matter via a gauge singlet scalar. *Phys. Lett.*, B323:339–346, 1994. doi:10.1016/0370-2693(94)91229-7.

[116] A. Ahriche. What is the criterion for a strong first order electroweak phase transition in singlet models? *Phys. Rev.*, D75:083522, 2007. arXiv:hep-ph/0701192, doi:10.1103/PhysRevD.75.083522.

[117] J. R. Espinosa, T. Konstandin, J. M. No, and M. Quiros. Some Cosmological Implications of Hidden Sectors. *Phys. Rev.*, D78:123528, 2008. arXiv:0809.3215, doi:10.1103/PhysRevD.78.123528.

[118] C.-Y. Chen, J. Kozaczuk, and I. M. Lewis. Non-resonant Collider Signatures of a Singlet-Driven Electroweak Phase Transition. *JHEP*, 08:096, 2017. arXiv:1704.05844, doi:10.1007/JHEP08(2017)096.

[119] V. Barger, P. Langacker, M. McCaskey, M. Ramsey-Musolf, and G. Shaughnessy. Complex Singlet Extension of the Standard Model. *Phys. Rev.*, D79:015018, 2009. arXiv:0811.0393, doi:10.1103/PhysRevD.79.015018.

[120] T. Tenkanen, K. Tuominen, and V. Vaskonen. A Strong Electroweak Phase Transition from the Inflaton Field. *JCAP*, 1609(09):037, 2016. arXiv:1606.06063, doi:10.1088/1475-7516/2016/09/037.

[121] K. Ghorbani and P. H. Ghorbani. Strongly First-Order Phase Transition in Real Singlet Scalar Dark Matter Model. 2018. arXiv:1804.05798.

[122] M. Carena, Z. Liu, and M. Riembau. Probing the electroweak phase transition via enhanced di-Higgs boson production. *Phys. Rev.*, D97(9):095032, 2018. arXiv:1801.00794, doi:10.1103/PhysRevD.97.095032.

[123] J. S. Kang. Gauge Invariance of the Scalar-Vector Mass Ratio in the Coleman-Weinberg Model. *Phys. Rev.*, D10:3455, 1974. doi:10.1103/PhysRevD.10.3455.

[124] R. Fukuda and T. Kugo. Gauge Invariance in the Effective Action and Potential. *Phys. Rev.*, D13:3469, 1976. doi:10.1103/PhysRevD.13.3469.

[125] I. J. R. Aitchison and C. M. Fraser. Gauge Invariance and the Effective Potential. *Annals Phys.*, 156:1, 1984. doi:10.1016/0003-4916(84)90209-4.

[126] W. Loinaz and R. S. Willey. Gauge dependence of lower bounds on the Higgs mass derived from electroweak vacuum stability constraints. *Phys. Rev.*, D56:7416–7426, 1997. arXiv:hep-ph/9702321, doi:10.1103/PhysRevD.56.7416.

[127] H. H. Patel and M. J. Ramsey-Musolf. Baryon Washout, Electroweak Phase Transition, and Perturbation Theory. *JHEP*, 07:029, 2011. arXiv:1101.4665, doi:10.1007/JHEP07(2011)029.

[128] M. Garny and T. Konstandin. On the gauge dependence of vacuum transitions at finite temperature. *JHEP*, 07:189, 2012. arXiv:1205.3392, doi:10.1007/JHEP07(2012)189.

[129] C. P. D. Harman and S. J. Huber. Does zero temperature decide on the nature of the electroweak phase transition? *JHEP*, 06:005, 2016. arXiv:1512.05611, doi:10.1007/JHEP06(2016)005.

[130] W. Huang, Z. Kang, J. Shu, P. Wu, and J. M. Yang. New insights in the electroweak phase transition in the NMSSM. *Phys. Rev.*, D91(2):025006, 2015. arXiv:1405.1152, doi:10.1103/PhysRevD.91.025006.

[131] G. C. Dorsch, S. J. Huber, K. Mimasu, and J. M. No. The Higgs Vacuum Uplifted: Revisiting the Electroweak Phase Transition with a Second Higgs Doublet. *JHEP*, 12:086, 2017. arXiv:1705.09186, doi:10.1007/JHEP12(2017)086.

[132] I. Baldes and G. Servant. High scale electroweak phase transition: baryogenesis & symmetry non-restoration. *JHEP*, 10:053, 2018. arXiv:1807.08770, doi:10.1007/JHEP10(2018)053.

[133] P. Meade and H. Ramani. Unrestored Electroweak Symmetry. *Phys. Rev. Lett.*, 122(4):041802, 2019. arXiv:1807.07578, doi:10.1103/PhysRevLett.122.041802.

[134] C. Ford, D. R. T. Jones, P. W. Stephenson, and M. B. Einhorn. The Effective potential and the renormalization group. *Nucl. Phys.*, B395:17–34, 1993. arXiv:hep-lat/9210033, doi:10.1016/0550-3213(93)90206-5.

[135] M. Carena, M. Quiros, and C. E. M. Wagner. Effective potential methods and the Higgs mass spectrum in the MSSM. *Nucl. Phys.*, B461:407–436, 1996. arXiv:hep-ph/9508343, doi:10.1016/0550-3213(95)00665-6.

[136] M. Cepeda et al. Higgs Physics at the HL-LHC and HE-LHC. 2019. arXiv:1902.00134.

[137] X. Cid Vidal et al. Beyond the Standard Model Physics at the HL-LHC and HE-LHC. 2018. arXiv:1812.07831.

[138] J. de Blas et al. The CLIC Potential for New Physics. 2018. arXiv:1812.02093, doi:10.23731/CYRM-2018-003.

[139] K. Fujii et al. Physics Case for the 250 GeV Stage of the International Linear Collider. 2017. arXiv:1710.07621.

[140] M. Dong et al. CEPC Conceptual Design Report: Volume 2 - Physics & Detector. 2018. arXiv:1811.10545.

[141] F. An et al. Precision Higgs Physics at CEPC. 2018. arXiv:1810.09037.

[142] A. Abada et al. FCC-ee: The Lepton Collider. *Eur. Phys. J. ST*, 228(2):261–623, 2019. doi:10.1140/epjst/e2019-900045-4.

[143] A. Abada et al. HE-LHC: The High-Energy Large Hadron Collider. *Eur. Phys. J. ST*, 228(5):1109–1382, 2019. doi:10.1140/epjst/e2019-900088-6.

[144] A. Abada et al. FCC-hh: The Hadron Collider. *Eur. Phys. J. ST*, 228(4):755–1107, 2019. doi:10.1140/epjst/e2019-900087-0.

[145] J. De Blas et al. Higgs Boson Studies at Future Particle Colliders. 2019. arXiv:1905.03764.

[146] Z. Liu, L.-T. Wang, and H. Zhang. Exotic decays of the 125 GeV Higgs boson at future e^+e^- lepton colliders. *Chin. Phys.*, C41(6):063102, 2017. arXiv:1612.09284, doi:10.1088/1674-1137/41/6/063102.

[147] D. Curtin et al. Exotic decays of the 125 GeV Higgs boson. *Phys. Rev.*, D90(7):075004, 2014. arXiv:1312.4992, doi:10.1103/PhysRevD.90.075004.

[148] G. Aad et al. Measurements of the Higgs boson production and decay rates and constraints on its couplings from a combined ATLAS and CMS analysis of the LHC pp collision data at $\sqrt{s} = 7$ and 8 TeV. *JHEP*, 08:045, 2016. arXiv:1606.02266, doi:10.1007/JHEP08(2016)045.

[149] D. de Florian et al. Handbook of LHC Higgs Cross Sections: 4. Deciphering the Nature of the Higgs Sector. 2016. arXiv:1610.07922.

[150] A. M. Sirunyan et al. Combined measurements of Higgs boson couplings in proton–proton collisions at $\sqrt{s} = 13\,\text{TeV}$. *Eur. Phys. J. C*, 79(5):421, 2019. arXiv:1809.10733, doi:10.1140/epjc/s10052-019-6909-y.

[151] T. A. collaboration. Combined measurements of Higgs boson production and decay using up to 80 fb^{-1} of proton–proton collision data at $\sqrt{s} = 13$ TeV collected with the ATLAS experiment. 2018.

[152] A. M. Sirunyan et al. Search for an exotic decay of the Higgs boson to a pair of light pseudoscalars in the final state with two b quarks and two τ leptons in proton-proton collisions at $\sqrt{s} = 13$ TeV. *Phys. Lett.*, B785:462, 2018. arXiv:1805.10191, doi:10.1016/j.physletb.2018.08.057.

[153] M. Aaboud et al. Search for the Higgs boson produced in association with a vector boson and decaying into two spin-zero particles in the $H \to aa \to 4b$ channel in pp collisions at $\sqrt{s} = 13$ TeV with the ATLAS detector. *JHEP*, 10:031, 2018. arXiv:1806.07355, doi:10.1007/JHEP10(2018)031.

[154] C.-Y. Chen, S. Dawson, and I. M. Lewis. Exploring resonant di-Higgs boson production in the Higgs singlet model. *Phys. Rev.*, D91(3):035015, 2015. arXiv:1410.5488, doi:10.1103/PhysRevD.91.035015.

[155] S. Dawson and I. M. Lewis. NLO corrections to double Higgs boson production in the Higgs singlet model. *Phys. Rev.*, D92(9):094023, 2015. arXiv:1508.05397, doi:10.1103/PhysRevD.92.094023.

[156] S. Di Vita, G. Durieux, C. Grojean, J. Gu, Z. Liu, G. Panico, M. Riembau, and T. Vantalon. A global view on the Higgs self-coupling at lepton colliders. *JHEP*, 02:178, 2018. arXiv:1711.03978, doi:10.1007/JHEP02(2018)178.

[157] A. Mazumdar and G. White. Review of cosmic phase transitions: their significance and experimental signatures. *Rept. Prog. Phys.*, 82(7):076901, 2019. arXiv:1811.01948, doi:10.1088/1361-6633/ab1f55.

[158] M. Maniatis. The Next-to-Minimal Supersymmetric extension of the Standard Model reviewed. *Int. J. Mod. Phys.*, A25:3505–3602, 2010. arXiv:0906.0777, doi:10.1142/S0217751X10049827.

[159] U. Ellwanger, C. Hugonie, and A. M. Teixeira. The Next-to-Minimal Supersymmetric Standard Model. *Phys. Rept.*, 496:1–77, 2010. arXiv:0910.1785, doi:10.1016/j.physrep.2010.07.001.

[160] E. Witten. Dynamical Breaking of Supersymmetry. *Nucl. Phys. B*, 188:513, 1981. doi:10.1016/0550-3213(81)90006-7.

[161] S. Dimopoulos and H. Georgi. Softly Broken Supersymmetry and SU(5). *Nucl. Phys. B*, 193:150–162, 1981. doi:10.1016/0550-3213(81)90522-8.

[162] E. Witten. Mass Hierarchies in Supersymmetric Theories. *Phys. Lett. B*, 105:267, 1981. doi:10.1016/0370-2693(81)90885-6.

[163] R. K. Kaul and P. Majumdar. Cancellation of Quadratically Divergent Mass Corrections in Globally Supersymmetric Spontaneously Broken Gauge Theories. *Nucl. Phys. B*, 199:36, 1982. doi:10.1016/0550-3213(82)90565-X.

[164] N. Sakai. Naturalness in Supersymmetric Guts. *Z. Phys. C*, 11:153, 1981. doi:10.1007/BF01573998.

[165] C. Cheung, M. Papucci, D. Sanford, N. R. Shah, and K. M. Zurek. NMSSM Interpretation of the Galactic Center Excess. *Phys.Rev.*, D90(7):075011, 2014. arXiv:1406.6372, doi:10.1103/PhysRevD.90.075011.

[166] J. Cao, L. Shang, P. Wu, J. M. Yang, and Y. Zhang. Interpreting the galactic center gamma-ray excess in the NMSSM. *JHEP*, 10:030, 2015. arXiv:1506.06471, doi:10.1007/JHEP10(2015)030.

[167] M. Badziak, M. Olechowski, and P. Szczerbiak. Blind spots for neutralino dark matter in the NMSSM. *JHEP*, 03:179, 2016. arXiv:1512.02472, doi:10.1007/JHEP03(2016)179.

[168] U. Ellwanger. Present Status and Future Tests of the Higgsino-Singlino Sector in the NMSSM. *JHEP*, 02:051, 2017. arXiv:1612.06574, doi:10.1007/JHEP02(2017)051.

[169] J. Cao, Y. He, L. Shang, W. Su, and Y. Zhang. Natural NMSSM after LHC Run I and the Higgsino dominated dark matter scenario. *JHEP*, 08:037, 2016. arXiv:1606.04416, doi:10.1007/JHEP08(2016)037.

[170] J. Cao, Y. He, L. Shang, W. Su, P. Wu, and Y. Zhang. Strong constraints of LUX-2016 results on the natural NMSSM. *JHEP*, 10:136, 2016. arXiv:1609.00204, doi:10.1007/JHEP10(2016)136.

[171] C. Beskidt, W. de Boer, D. I. Kazakov, and S. Wayand. Perspectives of direct Detection of supersymmetric Dark Matter in the NMSSM. *Phys. Lett.*, B771:611–618, 2017. arXiv:1703.01255, doi:10.1016/j.physletb.2017.06.016.

[172] M. Badziak, M. Olechowski, and P. Szczerbiak. Spin-dependent constraints on blind spots for thermal singlino-higgsino dark matter with(out) light singlets. *JHEP*, 07:050, 2017. arXiv:1705.00227, doi:10.1007/JHEP07(2017)050.

[173] S. Baum, M. Carena, N. R. Shah, and C. E. Wagner. Higgs portals for thermal Dark Matter. EFT perspectives and the NMSSM. *JHEP*, 04:069, 2018. arXiv:1712.09873, doi:10.1007/JHEP04(2018)069.

[174] U. Ellwanger and C. Hugonie. The higgsino–singlino sector of the NMSSM: combined constraints from dark matter and the LHC. *Eur. Phys. J. C*, 78(9):735, 2018. arXiv:1806.09478, doi:10.1140/epjc/s10052-018-6204-3.

[175] W. Abdallah, A. Chatterjee, and A. Datta. Revisiting singlino dark matter of the natural Z_3-symmetric NMSSM in the light of LHC. *JHEP*, 09:095, 2019. arXiv:1907.06270, doi:10.1007/JHEP09(2019)095.

[176] M. Pietroni. The Electroweak phase transition in a nonminimal supersymmetric model. *Nucl. Phys.*, B402:27–45, 1993. arXiv:hep-ph/9207227, doi:10.1016/0550-3213(93)90635-3.

[177] A. T. Davies, C. D. Froggatt, and R. G. Moorhouse. Electroweak baryogenesis in the next-to-minimal supersymmetric model. *Phys. Lett.*, B372:88–94, 1996. arXiv:hep-ph/9603388, doi:10.1016/0370-2693(96)00076-7.

[178] S. Huber and M. Schmidt. Electroweak baryogenesis: Concrete in a SUSY model with a gauge singlet. *Nucl. Phys. B*, 606:183–230, 2001. arXiv:hep-ph/0003122, doi:10.1016/S0550-3213(01)00250-4.

[179] A. Menon, D. Morrissey, and C. Wagner. Electroweak baryogenesis and dark matter in the nMSSM. *Phys. Rev. D*, 70:035005, 2004. arXiv:hep-ph/0404184, doi:10.1103/PhysRevD.70.035005.

[180] K. Funakubo, S. Tao, and F. Toyoda. Phase transitions in the NMSSM. *Prog. Theor. Phys.*, 114:369–389, 2005. arXiv:hep-ph/0501052, doi:10.1143/PTP.114.369.

[181] M. Carena, N. R. Shah, and C. E. M. Wagner. Light Dark Matter and the Electroweak Phase Transition in the NMSSM. *Phys. Rev.*, D85:036003, 2012. arXiv:1110.4378, doi:10.1103/PhysRevD.85.036003.

[182] K. Cheung, T.-J. Hou, J. S. Lee, and E. Senaha. Singlino-driven Electroweak Baryogenesis in the Next-to-MSSM. *Phys. Lett. B*, 710:188–191, 2012. arXiv:1201.3781, doi:10.1016/j.physletb.2012.02.070.

[183] C. Balzs, A. Mazumdar, E. Pukartas, and G. White. Baryogenesis, dark matter and inflation in the Next-to-Minimal Supersymmetric Standard Model. *JHEP*, 01:073, 2014. arXiv:1309.5091, doi:10.1007/JHEP01(2014)073.

[184] J. Kozaczuk, S. Profumo, L. S. Haskins, and C. L. Wainwright. Cosmological Phase Transitions and their Properties in the NMSSM. *JHEP*, 01:144, 2015. arXiv:1407.4134, doi:10.1007/JHEP01(2015)144.

[185] X.-J. Bi, L. Bian, W. Huang, J. Shu, and P.-F. Yin. Interpretation of the Galactic Center excess and electroweak phase transition in the NMSSM. *Phys. Rev.*, D92:023507, 2015. arXiv:1503.03749, doi:10.1103/PhysRevD.92.023507.

[186] S. J. Huber, T. Konstandin, G. Nardini, and I. Rues. Detectable Gravitational Waves from Very Strong Phase Transitions in the General NMSSM. *JCAP*, 03:036, 2016. arXiv:1512.06357, doi:10.1088/1475-7516/2016/03/036.

[187] L. Bian, H.-K. Guo, and J. Shu. Gravitational Waves, baryon asymmetry of the universe and electric dipole moment in the CP-violating NMSSM. *Chin. Phys.*, C42(9):093106, 2018. arXiv:1704.02488, doi:10.1088/1674-1137/42/9/093106.

[188] S. Akula, C. Balzs, L. Dunn, and G. White. Electroweak baryogenesis in the $\mathbb{Z}_3$ -invariant NMSSM. *JHEP*, 11:051, 2017. arXiv:1706.09898, doi:10.1007/JHEP11(2017)051.

[189] P. Athron, C. Balazs, A. Fowlie, G. Pozzo, G. White, and Y. Zhang. Strong first-order phase transitions in the NMSSM — a comprehensive survey. *JHEP*, 11:151, 2019. arXiv:1908.11847, doi:10.1007/JHEP11(2019)151.

[190] J. Kang, P. Langacker, T.-j. Li, and T. Liu. Electroweak baryogenesis in a supersymmetric U(1)-prime model. *Phys. Rev. Lett.*, 94:061801, 2005. arXiv:hep-ph/0402086, doi:10.1103/PhysRevLett.94.061801.

[191] P. Kumar and E. Ponton. Electroweak Baryogenesis and Dark Matter with an approximate R-symmetry. *JHEP*, 11:037, 2011. arXiv:1107.1719, doi:10.1007/JHEP11(2011)037.

[192] M. Carena, H. E. Haber, I. Low, N. R. Shah, and C. E. M. Wagner. Alignment limit of the NMSSM Higgs sector. *Phys. Rev.*, D93(3):035013, 2016. arXiv:1510.09137, doi:10.1103/PhysRevD.93.035013.

[193] S. J. Huber, T. Konstandin, T. Prokopec, and M. G. Schmidt. Baryogenesis in the MSSM, nMSSM and NMSSM. *Nucl. Phys. A*, 785:206–209, 2007. arXiv:hep-ph/0608017, doi:10.1016/j.nuclphysa.2006.11.154.

[194] M. Carena, M. Quiros, and C. E. M. Wagner. Opening the window for electroweak baryogenesis. *Phys. Lett.*, B380:81–91, 1996. arXiv:hep-ph/9603420, doi:10.1016/0370-2693(96)00475-3.

[195] D. Delepine, J. M. Gerard, R. Gonzalez Felipe, and J. Weyers. A Light stop and electroweak baryogenesis. *Phys. Lett.*, B386:183–188, 1996. arXiv:hep-ph/9604440, doi:10.1016/0370-2693(96)00921-5.

[196] M. Laine and K. Rummukainen. The MSSM electroweak phase transition on the lattice. *Nucl. Phys. B*, 535:423–457, 1998. arXiv:hep-lat/9804019, doi:10.1016/S0550-3213(98)00530-6.

[197] J. M. Cline and G. D. Moore. Supersymmetric electroweak phase transition: Baryogenesis versus experimental constraints. *Phys. Rev. Lett.*, 81:3315–3318, 1998. arXiv:hep-ph/9806354, doi:10.1103/PhysRevLett.81.3315.

[198] C. Balazs, M. Carena, A. Menon, D. E. Morrissey, and C. E. M. Wagner. The Supersymmetric origin of matter. *Phys. Rev.*, D71:075002, 2005. arXiv:hep-ph/0412264, doi:10.1103/PhysRevD.71.075002.

[199] C. Lee, V. Cirigliano, and M. J. Ramsey-Musolf. Resonant relaxation in electroweak baryogenesis. *Phys. Rev. D*, 71:075010, 2005. arXiv:hep-ph/0412354, doi:10.1103/PhysRevD.71.075010.

[200] M. Carena, G. Nardini, M. Quiros, and C. Wagner. The Baryogenesis Window in the MSSM. *Nucl. Phys. B*, 812:243–263, 2009. arXiv:0809.3760, doi:10.1016/j.nuclphysb.2008.12.014.

[201] D. Curtin, P. Jaiswal, and P. Meade. Excluding Electroweak Baryogenesis in the MSSM. *JHEP*, 08:005, 2012. arXiv:1203.2932, doi:10.1007/JHEP08(2012)005.

[202] T. Cohen, D. E. Morrissey, and A. Pierce. Electroweak Baryogenesis and Higgs Signatures. *Phys. Rev.*, D86:013009, 2012. arXiv:1203.2924, doi:10.1103/PhysRevD.86.013009.

[203] M. Carena, G. Nardini, M. Quiros, and C. E. M. Wagner. MSSM Electroweak Baryogenesis and LHC Data. *JHEP*, 02:001, 2013. arXiv:1207.6330, doi:10.1007/JHEP02(2013)001.

[204] A. Katz and M. Perelstein. Higgs Couplings and Electroweak Phase Transition. *JHEP*, 07:108, 2014. arXiv:1401.1827, doi:10.1007/JHEP07(2014)108.

[205] A. Katz, M. Perelstein, M. J. Ramsey-Musolf, and P. Winslow. Stop-Catalyzed Baryogenesis Beyond the MSSM. *Phys. Rev.*, D92(9):095019, 2015. arXiv:1509.02934, doi:10.1103/PhysRevD.92.095019.

[206] A. Kobakhidze, N. Liu, L. Wu, J. M. Yang, and M. Zhang. Closing up a light stop window in natural SUSY at LHC. *Phys. Lett.*, B755:76–81, 2016. arXiv:1511.02371, doi:10.1016/j.physletb.2016.02.003.

[207] S. Liebler, S. Profumo, and T. Stefaniak. Light Stop Mass Limits from Higgs Rate Measurements in the MSSM: Is MSSM Electroweak Baryogenesis Still Alive After All? *JHEP*, 04:143, 2016. arXiv:1512.09172, doi:10.1007/JHEP04(2016)143.

[208] S. P. Martin. A Supersymmetry Primer. 1997. URL: http://inspirehep.net/search?p=hep-ph/9709356, arXiv:hep-ph/9709356.

[209] I. J. R. Aitchison. Supersymmetry and the MSSM: An Elementary introduction. 2005. arXiv:hep-ph/0505105.

[210] M. E. Krauss, T. Opferkuch, and F. Staub. Spontaneous Charge Breaking in the NMSSM - Dangerous or not? *Eur. Phys. J.*, C77(5):331, 2017. arXiv:1703.05329, doi:10.1140/epjc/s10052-017-4908-4.

[211] J. C. Romao. Spontaneous CP Violation in SUSY Models: A No Go Theorem. *Phys. Lett.*, B173:309–312, 1986. doi:10.1016/0370-2693(86)90522-8.

[212] H. Georgi and D. V. Nanopoulos. Suppression of Flavor Changing Effects From Neutral Spinless Meson Exchange in Gauge Theories. *Phys. Lett.*, B82:95–96, 1979. doi:10.1016/0370-2693(79)90433-7.

[213] J. F. Donoghue and L. F. Li. Properties of Charged Higgs Bosons. *Phys. Rev.*, D19:945, 1979. doi:10.1103/PhysRevD.19.945.

[214] J. Gunion, H. Haber, G. Kane, and S. Dawson. *The Higgs Hunter's Guide*. Frontiers in Physics. Westview Press, 2008. URL: https://books.google.com/books?id=M5moXN_SA-MC.

[215] L. Lavoura and J. P. Silva. Fundamental CP violating quantities in a SU(2) x U(1) model with many Higgs doublets. *Phys. Rev.*, D50:4619–4624, 1994. arXiv:hep-ph/9404276, doi:10.1103/PhysRevD.50.4619.

[216] F. J. Botella and J. P. Silva. Jarlskog - like invariants for theories with scalars and fermions. *Phys. Rev.*, D51:3870–3875, 1995. arXiv:hep-ph/9411288, doi:10.1103/PhysRevD.51.3870.

[217] G. C. Branco, L. Lavoura, and S. J.P. *CP violation*. Oxford University Press, Oxford, UK, 1999.

[218] J. F. Gunion and H. E. Haber. The CP conserving two Higgs doublet model: The Approach to the decoupling limit. *Phys. Rev.*, D67:075019, 2003. arXiv:hep-ph/0207010, doi:10.1103/PhysRevD.67.075019.

[219] S. Baum, K. Freese, N. R. Shah, and B. Shakya. NMSSM Higgs boson search strategies at the LHC and the mono-Higgs signature in particular. *Phys. Rev.*, D95(11):115036, 2017. arXiv:1703.07800, doi:10.1103/PhysRevD.95.115036.

[220] S. Baum, N. R. Shah, and K. Freese. The NMSSM is within Reach of the LHC: Mass Correlations & Decay Signatures. *JHEP*, 04:011, 2019. arXiv:1901.02332, doi:10.1007/JHEP04(2019)011.

[221] G. Aad et al. Combined measurements of Higgs boson production and decay using up to 80 fb^{-1} of proton-proton collision data at $\sqrt{s} = 13$ TeV collected with the ATLAS experiment. *Phys. Rev. D*, 101(1):012002, 2020. arXiv:1909.02845, doi:10.1103/PhysRevD.101.012002.

[222] R. Barbieri, L. J. Hall, Y. Nomura, and V. S. Rychkov. Supersymmetry without a Light Higgs Boson. *Phys. Rev.*, D75:035007, 2007. arXiv:hep-ph/0607332, doi:10.1103/PhysRevD.75.035007.

[223] J. Cao and J. M. Yang. Current experimental constraints on NMSSM with large lambda. *Phys. Rev.*, D78:115001, 2008. arXiv:0810.0989, doi:10.1103/PhysRevD.78.115001.

[224] M. Farina, M. Perelstein, and B. Shakya. Higgs Couplings and Naturalness in λ-SUSY. *JHEP*, 04:108, 2014. arXiv:1310.0459, doi:10.1007/JHEP04(2014)108.

[225] J. P. Derendinger and C. A. Savoy. Quantum Effects and SU(2) x U(1) Breaking in Supergravity Gauge Theories. *Nucl. Phys.*, B237:307–328, 1984. doi:10.1016/0550-3213(84)90162-7.

[226] S. F. King and P. L. White. Resolving the constrained minimal and next-to-minimal supersymmetric standard models. *Phys. Rev.*, D52:4183–4216, 1995. arXiv:hep-ph/9505326, doi:10.1103/PhysRevD.52.4183.

[227] M. Masip, R. Munoz-Tapia, and A. Pomarol. Limits on the mass of the lightest Higgs in supersymmetric models. *Phys. Rev.*, D57:R5340, 1998. arXiv:hep-ph/9801437, doi:10.1103/PhysRevD.57.R5340.

[228] J. R. Ellis, G. Ridolfi, and F. Zwirner. On radiative corrections to supersymmetric Higgs boson masses and their implications for LEP searches. *Phys. Lett. B*, 262:477–484, 1991. doi:10.1016/0370-2693(91)90626-2.

[229] H. E. Haber and R. Hempfling. The Renormalization group improved Higgs sector of the minimal supersymmetric model. *Phys. Rev.*, D48:4280–4309, 1993. arXiv:hep-ph/9307201, doi:10.1103/PhysRevD.48.4280.

[230] J. A. Casas, J. R. Espinosa, M. Quiros, and A. Riotto. The Lightest Higgs boson mass in the minimal supersymmetric standard model. *Nucl. Phys.*, B436:3–29, 1995. [Erratum: Nucl. Phys.B439,466(1995)]. arXiv:hep-ph/9407389, doi:10.1016/0550-3213(94)00508-C,10.1016/0550-3213(95)00057-Y.

[231] M. Carena, J. R. Espinosa, M. Quiros, and C. E. M. Wagner. Analytical expressions for radiatively corrected Higgs masses and couplings in the MSSM. *Phys. Lett.*, B355:209–221, 1995. arXiv:hep-ph/9504316, doi:10.1016/0370-2693(95)00694-G.

[232] G. Lee and C. E. Wagner. Higgs bosons in heavy supersymmetry with an intermediate m_A. *Phys. Rev. D*, 92(7):075032, 2015. arXiv:1508.00576, doi:10.1103/PhysRevD.92.075032.

[233] T. L. Lee, T. Y. Li, and C. H. Tsai. HOM4PS-2.0: a software package for solving polynomial systems by the polyhedral homotopy continuation method. *Computing*, 83(2):109, 2008. doi:10.1007/s00607-008-0015-6.

[234] N. Blinov, J. Kozaczuk, D. E. Morrissey, and C. Tamarit. Electroweak Baryogenesis from Exotic Electroweak Symmetry Breaking. *Phys. Rev. D*, 92(3):035012, 2015. arXiv:1504.05195, doi:10.1103/PhysRevD.92.035012.

[235] LEPSUSYWG, ALEPH, DELPHI, L3 and OPAL experiments, note LEPSUSYWG 01-03.1, (http://lepsusy.web.cern.ch/lepsusy/Welcome.html).

[236] LEPSUSYWG, ALEPH, DELPHI, L3 and OPAL experiments, note LEPSUSYWG 02-04.1, (http://lepsusy.web.cern.ch/lepsusy/Welcome.html).

[237] J. Liu, N. McGinnis, C. E. M. Wagner, and X.-P. Wang. Searching for the Higgsino-Bino Sector at the LHC. *JHEP*, 09:073, 2020. arXiv:2006.07389, doi:10.1007/JHEP09(2020)073.

[238] D. Dicus, A. Stange, and S. Willenbrock. Higgs decay to top quarks at hadron colliders. *Phys. Lett. B*, 333:126–131, 1994. arXiv:hep-ph/9404359, doi:10.1016/0370-2693(94)91017-0.

[239] R. Barcelo and M. Masip. Extra Higgs bosons in $t\bar{t}$ production at the LHC. *Phys. Rev. D*, 81:075019, 2010. arXiv:1001.5456, doi:10.1103/PhysRevD.81.075019.

[240] V. Barger, W.-Y. Keung, and B. Yencho. Azimuthal Correlations in Top Pair Decays and The Effects of New Heavy Scalars. *Phys. Rev. D*, 85:034016, 2012. arXiv:1112.5173, doi:10.1103/PhysRevD.85.034016.

[241] Y. Bai and W.-Y. Keung. Can vanishing mass-on-shell interactions generate a dip at colliders? *Int. J. Mod. Phys. A*, 30(20):1550120, 2015. arXiv:1407.6355, doi:10.1142/S0217751X15501201.

[242] S. Jung, J. Song, and Y. W. Yoon. Dip or nothingness of a Higgs resonance from the interference with a complex phase. *Phys. Rev. D*, 92(5):055009, 2015. arXiv:1505.00291, doi:10.1103/PhysRevD.92.055009.

[243] N. Craig, F. D'Eramo, P. Draper, S. Thomas, and H. Zhang. The Hunt for the Rest of the Higgs Bosons. *JHEP*, 06:137, 2015. arXiv:1504.04630, doi:10.1007/JHEP06(2015)137.

[244] S. Gori, I.-W. Kim, N. R. Shah, and K. M. Zurek. Closing the Wedge: Search Strategies for Extended Higgs Sectors with Heavy Flavor Final States. *Phys. Rev.*, D93(7):075038, 2016. arXiv:1602.02782, doi:10.1103/PhysRevD.93.075038.

[245] M. Carena and Z. Liu. Challenges and opportunities for heavy scalar searches in the $t\bar{t}$ channel at the LHC. *JHEP*, 11:159, 2016. arXiv:1608.07282, doi:10.1007/JHEP11(2016)159.

[246] F. Moortgat, S. Abdullin, and D. Denegri. Observability of MSSM Higgs bosons via sparticle decay modes in CMS. Technical Report hep-ph/0112046. CMS-NOTE-2001-042, CERN, Geneva, Dec 2001. 14 pages, 20 figures Report-no: CMS Note 2001/042. URL: http://cds.cern.ch/record/529361.

[247] D. Denegri, V. Drollinger, R. Kinnunen, K. Lassila-Perini, S. Lehti, F. Moortgat, A. Nikitenko, S. Slabospitsky, and N. Stepanov. Summary of the CMS discovery potential for the MSSM SUSY Higgses. 11 2001. arXiv:hep-ph/0112045.

[248] T. Han, Z. Liu, and A. Natarajan. Dark matter and Higgs bosons in the MSSM. *JHEP*, 1311:008, 2013. arXiv:1303.3040, doi:10.1007/JHEP11(2013)008.

[249] S. Gori, Z. Liu, and B. Shakya. Heavy Higgs as a Portal to the Supersymmetric Electroweak Sector. *JHEP*, 04:049, 2019. arXiv:1811.11918, doi:10.1007/JHEP04(2019)049.

[250] S. Baum and N. R. Shah. Two Higgs Doublets and a Complex Singlet: Disentangling the Decay Topologies and Associated Phenomenology. *JHEP*, 12:044, 2018. arXiv:1808.02667, doi:10.1007/JHEP12(2018)044.

[251] Z. Kang, J. Li, T. Li, D. Liu, and J. Shu. Probing the CP-even Higgs sector via $H_3 \to H_2 H_1$ in the natural next-to-minimal supersymmetric standard model. *Phys. Rev.*, D88(1):015006, 2013. arXiv:1301.0453, doi:10.1103/PhysRevD.88.015006.

[252] S. F. King, M. Mühlleitner, R. Nevzorov, and K. Walz. Discovery Prospects for NMSSM Higgs Bosons at the High-Energy Large Hadron Collider. *Phys. Rev.*, D90(9):095014, 2014. arXiv:1408.1120, doi:10.1103/PhysRevD.90.095014.

[253] U. Ellwanger and M. Rodriguez-Vazquez. Discovery Prospects of a Light Scalar in the NMSSM. *JHEP*, 02:096, 2016. arXiv:1512.04281, doi:10.1007/JHEP02(2016)096.

[254] R. Costa, M. Mühlleitner, M. O. P. Sampaio, and R. Santos. Singlet Extensions of the Standard Model at LHC Run 2: Benchmarks and Comparison with the NMSSM. *JHEP*, 06:034, 2016. arXiv:1512.05355, doi:10.1007/JHEP06(2016)034.

[255] S. von Buddenbrock, N. Chakrabarty, A. S. Cornell, D. Kar, M. Kumar, T. Mandal, B. Mellado, B. Mukhopadhyaya, R. G. Reed, and X. Ruan. Phenomenological signatures of additional scalar bosons at the LHC. *Eur. Phys. J. C*, 76(10):580, 2016. arXiv:1606.01674, doi:10.1140/epjc/s10052-016-4435-8.

[256] U. Ellwanger and M. Rodriguez-Vazquez. Simultaneous search for extra light and heavy Higgs bosons via cascade decays. *JHEP*, P072:817, 2017. arXiv:1707.08522, doi:10.1007/JHEP11(2017)008.

[257] Z. Heng, X. Gong, and H. Zhou. Pair production of Higgs boson in NMSSM at the LHC with the next-to-lightest CP-even Higgs boson being SM-like. *Chin. Phys. C*, 42(7):073103, 2018. arXiv:1805.01598, doi:10.1088/1674-1137/42/7/073103.

[258] P. Huang and C. E. M. Wagner. Blind Spots for neutralino Dark Matter in the MSSM with an intermediate m_A. *Phys. Rev.*, D90(1):015018, 2014. arXiv:1404.0392, doi:10.1103/PhysRevD.90.015018.

[259] H. Baer, A. D. Box, and H. Summy. Neutralino versus axion/axino cold dark matter in the 19 parameter SUGRA model. *JHEP*, 10:023, 2010. arXiv:1005.2215, doi:10.1007/JHEP10(2010)023.

[260] A. D. Linde. Infrared Problem in Thermodynamics of the Yang-Mills Gas. *Phys. Lett. B*, 96:289–292, 1980. doi:10.1016/0370-2693(80)90769-8.

[261] P. H. Ginsparg. First Order and Second Order Phase Transitions in Gauge Theories at Finite Temperature. *Nucl. Phys. B*, 170:388–408, 1980. doi:10.1016/0550-3213(80)90418-6.

[262] T. Appelquist and R. D. Pisarski. High-Temperature Yang-Mills Theories and Three-Dimensional Quantum Chromodynamics. *Phys. Rev. D*, 23:2305, 1981. doi:10.1103/PhysRevD.23.2305.

[263] K. Kajantie, M. Laine, K. Rummukainen, and M. E. Shaposhnikov. Generic rules for high temperature dimensional reduction and their application to the standard model. *Nucl. Phys. B*, 458:90–136, 1996. arXiv:hep-ph/9508379, doi:10.1016/0550-3213(95)00549-8.

[264] K. Kajantie, M. Laine, K. Rummukainen, and M. E. Shaposhnikov. The Electroweak phase transition: A Nonperturbative analysis. *Nucl. Phys. B*, 466:189–258, 1996. arXiv:hep-lat/9510020, doi:10.1016/0550-3213(96)00052-1.

[265] K. Kainulainen, V. Keus, L. Niemi, K. Rummukainen, T. V. Tenkanen, and V. Vaskonen. On the validity of perturbative studies of the electroweak phase transition in the Two Higgs Doublet model. *JHEP*, 06:075, 2019. arXiv:1904.01329, doi:10.1007/JHEP06(2019)075.

[266] L. Niemi, M. Ramsey-Musolf, T. V. Tenkanen, and D. J. Weir. Thermodynamics of a two-step electroweak phase transition. 5 2020. arXiv:2005.11332.

[267] A. Ekstedt and J. Löfgren. A Critical Look at the Electroweak Phase Transition. *JHEP*, 12:136, 2020. arXiv:2006.12614, doi:10.1007/JHEP12(2020)136.

[268] D. Croon, O. Gould, P. Schicho, T. V. Tenkanen, and G. White. Theoretical uncertainties for cosmological first-order phase transitions. 9 2020. arXiv:2009.10080.

[269] M. Carrington. The Effective potential at finite temperature in the Standard Model. *Phys. Rev. D*, 45:2933–2944, 1992. doi:10.1103/PhysRevD.45.2933.

[270] D. Comelli and J. Espinosa. Bosonic thermal masses in supersymmetry. *Phys. Rev. D*, 55:6253–6263, 1997. arXiv:hep-ph/9606438, doi:10.1103/PhysRevD.55.6253.

[271] M. Carena, C. Krause, Z. Liu, and Y. Wang. A New Approach to Electroweak Symmetry Non-Restoration. 4 2021. arXiv:2104.00638.

[272] R. N. Mohapatra and G. Senjanovic. Soft CP Violation at High Temperature. *Phys. Rev. Lett.*, 42:1651, 1979. doi:10.1103/PhysRevLett.42.1651.

[273] R. N. Mohapatra and G. Senjanovic. Broken Symmetries at High Temperature. *Phys. Rev. D*, 20:3390–3398, 1979. doi:10.1103/PhysRevD.20.3390.

[274] R. N. Mohapatra and G. Senjanovic. Broken symmetries at high temperatures and the problem of baryon excess of the universe. In *1979 EPS High-Energy Physics Conference*, Geneva, Switzerland, 6 1979. CERN.

[275] G. R. Dvali and G. Senjanovic. Is there a domain wall problem? *Phys. Rev. Lett.*, 74:5178–5181, 1995. arXiv:hep-ph/9501387, doi:10.1103/PhysRevLett.74.5178.

[276] G. R. Dvali, A. Melfo, and G. Senjanovic. Is There a monopole problem? *Phys. Rev. Lett.*, 75:4559–4562, 1995. arXiv:hep-ph/9507230, doi:10.1103/PhysRevLett.75.4559.

[277] B. Bajc. High temperature symmetry nonrestoration. In *3rd International Conference on Particle Physics and the Early Universe*, pages 247–253, 2000. arXiv:hep-ph/0002187, doi:10.1142/9789812792129_0039.

[278] H. H. Patel, M. J. Ramsey-Musolf, and M. B. Wise. Color Breaking in the Early Universe. *Phys. Rev. D*, 88(1):015003, 2013. arXiv:1303.1140, doi:10.1103/PhysRevD.88.015003.

[279] C. Kilic and S. Swaminathan. Can A Pseudo-Nambu-Goldstone Higgs Lead To Symmetry Non-Restoration? *JHEP*, 01:002, 2016. arXiv:1508.05121, doi:10.1007/JHEP01(2016)002.

[280] M. J. Ramsey-Musolf, P. Winslow, and G. White. Color Breaking Baryogenesis. *Phys. Rev. D*, 97(12):123509, 2018. arXiv:1708.07511, doi:10.1103/PhysRevD.97.123509.

[281] A. Glioti, R. Rattazzi, and L. Vecchi. Electroweak Baryogenesis above the Electroweak Scale. *JHEP*, 04:027, 2019. arXiv:1811.11740, doi:10.1007/JHEP04(2019)027.

[282] O. Matsedonskyi and G. Servant. High-Temperature Electroweak Symmetry Non-Restoration from New Fermions and Implications for Baryogenesis. 2020. arXiv:2002.05174.

[283] Y. Bai, S. J. Lee, M. Son, and F. Ye. Global Electroweak Symmetric Vacuum. 3 2021. arXiv:2103.09819.

[284] G. C. Branco, P. M. Ferreira, L. Lavoura, M. N. Rebelo, M. Sher, and J. P. Silva. Theory and phenomenology of two-Higgs-doublet models. *Phys. Rept.*, 516:1–102, 2012. arXiv:1106.0034, doi:10.1016/j.physrep.2012.02.002.

[285] M. Gustafsson. The Inert Doublet Model and Its Phenomenology. *PoS*, CHARGED2010:030, 2010. arXiv:1106.1719, doi:10.22323/1.114.0030.

[286] A. Pomarol and R. Vega. Constraints on CP violation in the Higgs sector from the rho parameter. *Nucl. Phys.*, B413:3–15, 1994. arXiv:hep-ph/9305272, doi:10.1016/0550-3213(94)90611-4.

[287] P. Ferreira, R. Santos, and A. Barroso. Stability of the tree-level vacuum in two Higgs doublet models against charge or CP spontaneous violation. *Phys. Lett. B*, 603:219–229, 2004. [Erratum: Phys.Lett.B 629, 114–114 (2005)]. arXiv:hep-ph/0406231, doi:10.1016/j.physletb.2004.10.022.

[288] A. Barroso, P. M. Ferreira, and R. Santos. Charge and CP symmetry breaking in two Higgs doublet models. *Phys. Lett.*, B632:684–687, 2006. arXiv:hep-ph/0507224, doi:10.1016/j.physletb.2005.11.031.

[289] I. Affleck and M. Dine. A New Mechanism for Baryogenesis. *Nucl. Phys. B*, 249:361–380, 1985. doi:10.1016/0550-3213(85)90021-5.

[290] J. M. Moreno, D. H. Oaknin, and M. Quiros. Sphalerons in the MSSM. *Nucl. Phys.*, B483:267–290, 1997. arXiv:hep-ph/9605387, doi:10.1016/S0550-3213(96)00562-7.

[291] J. Grant and M. Hindmarsh. Sphalerons in two Higgs doublet theories. *Phys. Rev.*, D64:016002, 2001. arXiv:hep-ph/0101120, doi:10.1103/PhysRevD.64.016002.

[292] L. Carson and L. D. McLerran. Approximate Computation of the Small Fluctuation Determinant Around a Sphaleron. *Phys. Rev.*, D41:647, 1990. doi:10.1103/PhysRevD.41.647.

[293] E. Mottola and S. Raby. Baryon number dissipation at finite temperature in the standard model. *Phys. Rev.*, D42:4202–4208, 1990. doi:10.1103/PhysRevD.42.4202.

[294] J. Baacke and S. Junker. Quantum fluctuations of the electroweak sphaleron: Erratum and addendum. *Phys. Rev.*, D50:4227–4228, 1994. arXiv:hep-th/9402078, doi:10.1103/PhysRevD.50.4227.

[295] A. M. Sirunyan et al. Search for invisible decays of a Higgs boson produced through vector boson fusion in proton-proton collisions at $\sqrt{s} = 13$ TeV. *Phys. Lett. B*, 793:520–551, 2019. arXiv:1809.05937, doi:10.1016/j.physletb.2019.04.025.

[296] M. Aaboud et al. Combination of searches for invisible Higgs boson decays with the ATLAS experiment. *Phys. Rev. Lett.*, 122(23):231801, 2019. arXiv:1904.05105, doi:10.1103/PhysRevLett.122.231801.

[297] M. Cirelli, N. Fornengo, and A. Strumia. Minimal dark matter. *Nucl. Phys. B*, 753:178–194, 2006. arXiv:hep-ph/0512090, doi:10.1016/j.nuclphysb.2006.07.012.

[298] E. Lundstrom, M. Gustafsson, and J. Edsjo. The Inert Doublet Model and LEP II Limits. *Phys. Rev. D*, 79:035013, 2009. arXiv:0810.3924, doi:10.1103/PhysRevD.79.035013.

[299] D. Egana-Ugrinovic, M. Low, and J. T. Ruderman. Charged Fermions Below 100 GeV. *JHEP*, 05:012, 2018. arXiv:1801.05432, doi:10.1007/JHEP05(2018)012.

[300] B. Henning, X. Lu, and H. Murayama. How to use the Standard Model effective field theory. *JHEP*, 01:023, 2016. arXiv:1412.1837, doi:10.1007/JHEP01(2016)023.

[301] M. Baak, M. Goebel, J. Haller, A. Hoecker, D. Kennedy, R. Kogler, K. Moenig, M. Schott, and J. Stelzer. The Electroweak Fit of the Standard Model after the Discovery of a New Boson at the LHC. *Eur. Phys. J. C*, 72:2205, 2012. arXiv:1209.2716, doi:10.1140/epjc/s10052-012-2205-9.

[302] M. Baak, J. Cúth, J. Haller, A. Hoecker, R. Kogler, K. Mönig, M. Schott, and J. Stelzer. The global electroweak fit at NNLO and prospects for the LHC and ILC. *Eur. Phys. J. C*, 74:3046, 2014. arXiv:1407.3792, doi:10.1140/epjc/s10052-014-3046-5.

[303] A. M. Sirunyan et al. Measurements of Higgs boson properties in the diphoton decay channel in proton-proton collisions at $\sqrt{s} = 13$ TeV. *JHEP*, 11:185, 2018. arXiv:1804.02716, doi:10.1007/JHEP11(2018)185.

[304] J. Gu, H. Li, Z. Liu, S. Su, and W. Su. Learning from Higgs Physics at Future Higgs Factories. *JHEP*, 12:153, 2017. arXiv:1709.06103, doi:10.1007/JHEP12(2017)153.

[305] J. De Blas, G. Durieux, C. Grojean, J. Gu, and A. Paul. On the future of Higgs, electroweak and diboson measurements at lepton colliders. *JHEP*, 12:117, 2019. arXiv:1907.04311, doi:10.1007/JHEP12(2019)117.

[306] M. Dine and A. Kusenko. The Origin of the matter - antimatter asymmetry. *Rev. Mod. Phys.*, 76:1, 2003. arXiv:hep-ph/0303065, doi:10.1103/RevModPhys.76.1.

[307] C. J. Moore, R. H. Cole, and C. P. L. Berry. Gravitational-wave sensitivity curves. *Class. Quant. Grav.*, 32(1):015014, 2015. arXiv:1408.0740, doi:10.1088/0264-9381/32/1/015014.

[308] M. Breitbach, J. Kopp, E. Madge, T. Opferkuch, and P. Schwaller. Dark, Cold, and Noisy: Constraining Secluded Hidden Sectors with Gravitational Waves. *JCAP*, 1907(07):007, 2019. arXiv:1811.11175, doi:10.1088/1475-7516/2019/07/007.

[309] N. Blinov, S. Profumo, and T. Stefaniak. The Electroweak Phase Transition in the Inert Doublet Model. *JCAP*, 1507(07):028, 2015. arXiv:1504.05949, doi:10.1088/1475-7516/2015/07/028.

[310] L. Niemi, H. H. Patel, M. J. Ramsey-Musolf, T. V. Tenkanen, and D. J. Weir. Electroweak phase transition in the real triplet extension of the SM: Dimensional reduction. *Phys. Rev. D*, 100(3):035002, 2019. arXiv:1802.10500, doi:10.1103/PhysRevD.100.035002.

[311] G. Buchalla, O. Cata, A. Celis, M. Knecht, and C. Krause. Complete One-Loop Renormalization of the Higgs-Electroweak Chiral Lagrangian. *Nucl. Phys.*, B928:93–106, 2018. arXiv:1710.06412, doi:10.1016/j.nuclphysb.2018.01.009.

[312] G. Buchalla, A. Celis, C. Krause, and J.-N. Toelstede. Master Formula for One-Loop Renormalization of Bosonic SMEFT Operators. 2019. arXiv:1904.07840.

[313] M. B. Einhorn and D. R. T. Jones. The Effective potential, the renormalisation group and vacuum stability. *JHEP*, 04:051, 2007. arXiv:hep-ph/0702295, doi:10.1088/1126-6708/2007/04/051.

[314] X. Gan, A. J. Long, and L.-T. Wang. Electroweak sphaleron with dimension-six operators. *Phys. Rev.*, D96(11):115018, 2017. arXiv:1708.03061, doi:10.1103/PhysRevD.96.115018.

[315] T. Akiba, H. Kikuchi, and T. Yanagida. The Free Energy of the Sphaleron in the Weinberg-Salam Model. *Phys. Rev.*, D40:588, 1989. doi:10.1103/PhysRevD.40.588.

[316] M. Dine, P. Huet, and R. L. Singleton, Jr. Baryogenesis at the electroweak scale. *Nucl. Phys.*, B375:625–648, 1992. doi:10.1016/0550-3213(92)90113-P.

[317] J. Baacke and S. Junker. Quantum corrections to the electroweak sphaleron transition. *Mod. Phys. Lett.*, A8:2869–2874, 1993. arXiv:hep-ph/9306307, doi:10.1142/S0217732393003251.

[318] J. Baacke and S. Junker. Quantum fluctuations around the electroweak sphaleron. *Phys. Rev.*, D49:2055–2073, 1994. arXiv:hep-ph/9308310, doi:10.1103/PhysRevD.49.2055.

[319] C. Caprini et al. Detecting gravitational waves from cosmological phase transitions with LISA: an update. *JCAP*, 03:024, 2020. arXiv:1910.13125, doi:10.1088/1475-7516/2020/03/024.

[320] C. Caprini et al. Science with the space-based interferometer eLISA. II: Gravitational waves from cosmological phase transitions. *JCAP*, 04:001, 2016. arXiv:1512.06239, doi:10.1088/1475-7516/2016/04/001.

[321] S. Kawamura et al. The Japanese space gravitational wave antenna: DECIGO. *Class. Quant. Grav.*, 28:094011, 2011. doi:10.1088/0264-9381/28/9/094011.

[322] G. M. Harry, P. Fritschel, D. A. Shaddock, W. Folkner, and E. S. Phinney. Laser interferometry for the big bang observer. *Class. Quant. Grav.*, 23:4887–4894, 2006. [Erratum-ibid.23:7361,2006]. doi:10.1088/0264-9381/23/15/008.

[323] S. Höche, J. Kozaczuk, A. J. Long, J. Turner, and Y. Wang. Towards an all-orders calculation of the electroweak bubble wall velocity. *JCAP*, 03:009, 2021. arXiv:2007.10343, doi:10.1088/1475-7516/2021/03/009.

[324] C. J. Hogan. Magnetohydrodynamic Effects of a First-Order Cosmological Phase Transition. *Phys. Rev. Lett.*, 51:1488–1491, 1983. doi:10.1103/PhysRevLett.51.1488.

[325] H. Audley et al. Laser Interferometer Space Antenna. 2017. arXiv:1702.00786.

[326] N. Seto, S. Kawamura, and T. Nakamura. Possibility of direct measurement of the acceleration of the universe using 0.1-Hz band laser interferometer gravitational wave antenna in space. *Phys. Rev. Lett.*, 87:221103, 2001. arXiv:astro-ph/0108011, doi:10.1103/PhysRevLett.87.221103.

[327] V. Corbin and N. J. Cornish. Detecting the cosmic gravitational wave background with the big bang observer. *Class. Quant. Grav.*, 23:2435–2446, 2006. arXiv:gr-qc/0512039, doi:10.1088/0264-9381/23/7/014.

[328] B. Sathyaprakash et al. Scientific Objectives of Einstein Telescope. *Class. Quant. Grav.*, 29:124013, 2012. [Erratum: Class.Quant.Grav. 30, 079501 (2013)]. arXiv:1206.0331, doi:10.1088/0264-9381/29/12/124013.

[329] W.-H. Ruan, Z.-K. Guo, R.-G. Cai, and Y.-Z. Zhang. Taiji Program: Gravitational-Wave Sources. 2018. arXiv:1807.09495.

[330] J. Luo et al. TianQin: a space-borne gravitational wave detector. *Class. Quant. Grav.*, 33(3):035010, 2016. arXiv:1512.02076, doi:10.1088/0264-9381/33/3/035010.

[331] J. Crowder and N. J. Cornish. Beyond LISA: Exploring future gravitational wave missions. *Phys. Rev.*, D72:083005, 2005. arXiv:gr-qc/0506015, doi:10.1103/PhysRevD.72.083005.

[332] J. Baker et al. Space Based Gravitational Wave Astronomy Beyond LISA. 2019. arXiv:1907.11305.

[333] D. Cutting, M. Hindmarsh, and D. J. Weir. Vorticity, kinetic energy, and suppressed gravitational wave production in strong first order phase transitions. 6 2019. arXiv:1906.00480.

[334] M. E. Carrington and J. I. Kapusta. Dynamics of the electroweak phase transition. *Phys. Rev.*, D47:5304–5315, 1993. doi:10.1103/PhysRevD.47.5304.

[335] D. Bodeker and G. D. Moore. Can electroweak bubble walls run away? *JCAP*, 05:009, 2009. arXiv:0903.4099, doi:10.1088/1475-7516/2009/05/009.

[336] D. Bodeker and G. D. Moore. Electroweak Bubble Wall Speed Limit. *JCAP*, 1705(05):025, 2017. arXiv:1703.08215, doi:10.1088/1475-7516/2017/05/025.

[337] M. E. Peskin and D. V. Schroeder. *An Introduction to Quantum Field Theory, Sec. 4.5.* Westview Press, Boulder, Colorado, 1995.

[338] V. V. Sudakov. Vertex parts at very high-energies in quantum electrodynamics. *Sov. Phys. JETP*, 3:65–71, 1956. URL: http://inspirehep.net/search?j=SPHJA,3,65.

[339] V. N. Gribov and L. N. Lipatov. Deep inelastic *e-p* scattering in perturbation theory. *Sov. J. Nucl. Phys.*, 15:438–450, 1972. URL: http://inspirehep.net/search?j=SJNCA,15,438.

[340] L. N. Lipatov. The parton model and perturbation theory. *Sov. J. Nucl. Phys.*, 20:94–102, 1975. URL: http://inspirehep.net/search?j=SJNCA,20,94.

[341] Y. L. Dokshitzer. Calculation of the structure functions for deep inelastic scattering and e^+e^- annihilation by perturbation theory in quantum chromodynamics. *Sov. Phys. JETP*, 46:641–653, 1977. URL: http://inspirehep.net/search?j=SPHJA,46,641.

[342] G. Altarelli and G. Parisi. Asymptotic freedom in parton language. *Nucl. Phys.*, B126:298–318, 1977. URL: http://inspirehep.net/search?j=NUPHA,B126,298.

[343] D. R. Yennie, S. C. Frautschi, and H. Suura. The Infrared Divergence Phenomena and High-Energy Processes. *Ann. Phys.*, 13:379–452, 1961. URL: http://inspirehep.net/search?j=APNYA,13,379.

[344] S. Catani, S. Dittmaier, and Z. Trocsanyi. One-loop singular behaviour of QCD and SUSY QCD amplitudes with massive partons. *Phys. Lett.*, B500:149–160, 2001. URL: http://inspirehep.net/search?p=hep-ph/0011222, arXiv:hep-ph/0011222.

[345] D. Amati, A. Bassetto, M. Ciafaloni, G. Marchesini, and G. Veneziano. A treatment of hard processes sensitive to the infrared structure of QCD. *Nucl. Phys.*, B173:429, 1980. URL: http://inspirehep.net/search?j=NUPHA,B173,429, doi:10.1016/0550-3213(80)90012-7.

[346] S. Catani, B. R. Webber, and G. Marchesini. QCD coherent branching and semiinclusive processes at large x. *Nucl. Phys.*, B349:635–654, 1991. URL: http://inspirehep.net/search?j=NUPHA,B349,635, doi:10.1016/0550-3213(91)90390-J.

[347] T. Becher, A. Broggio, and A. Ferroglia. *Introduction to Soft-Collinear Effective Theory*, volume 896. Springer, 2015. arXiv:1410.1892, doi:10.1007/978-3-319-14848-9.

[348] A. Bassetto, M. Ciafaloni, and G. Marchesini. Jet structure and infrared sensitive quantities in perturbative QCD. *Phys. Rept.*, 100:201–272, 1983. URL: http://inspirehep.net/search?j=PRPLC,100,201.

[349] L. J. Dixon. Calculating scattering amplitudes efficiently. 1996. URL: http://inspirehep.net/search?p=hep-ph/9601359, arXiv:hep-ph/9601359.

[350] S. Dittmaier. Weyl-van der Waerden formalism for helicity amplitudes of massive particles. *Phys. Rev.*, D59:016007, 1999. URL: http://inspirehep.net/search?p=hep-ph/9805445, arXiv:hep-ph/9805445.

[351] A. Denner and S. Dittmaier. Electroweak Radiative Corrections for Collider Physics. *Phys. Rept.*, 864:1–163, 2020. arXiv:1912.06823, doi:10.1016/j.physrep.2020.04.001.

[352] A. Denner. private communication.

[353] M. Carena, J. Moreno, M. Quiros, M. Seco, and C. Wagner. Supersymmetric CP violating currents and electroweak baryogenesis. *Nucl. Phys. B*, 599:158–184, 2001. arXiv:hep-ph/0011055, doi:10.1016/S0550-3213(01)00032-3.

[354] M. Carena, M. Quiros, M. Seco, and C. Wagner. Improved Results in Supersymmetric Electroweak Baryogenesis. *Nucl. Phys. B*, 650:24–42, 2003. arXiv:hep-ph/0208043, doi:10.1016/S0550-3213(02)01065-9.

[355] R. J. Eden, P. V. Landshoff, D. I. Olive, and J. C. Polkinghorne. *The analytic S-matrix*. Cambridge Univ. Press, Cambridge, 1966.

[356] Z. Bern, L. J. Dixon, D. C. Dunbar, and D. A. Kosower. Fusing gauge theory tree amplitudes into loop amplitudes. *Nucl. Phys.*, B435:59–101, 1995. URL: http://inspirebeta.net/record/376524, arXiv:hep-ph/9409265, doi:10.1016/0550-3213(94)00488-Z.

[357] A. Banfi, G. P. Salam, and G. Zanderighi. Principles of general final-state resummation and automated implementation. *JHEP*, 03:073, 2005. URL: http://inspirehep.net/record/655163, arXiv:hep-ph/0407286, doi:10.1088/1126-6708/2005/03/073.

[358] E. Farhi. A QCD Test for Jets. *Phys. Rev. Lett.*, 39:1587–1588, 1977. doi:10.1103/PhysRevLett.39.1587.

[359] S. Catani, G. Turnock, B. Webber, and L. Trentadue. Thrust distribution in e+ e- annihilation. *Phys.Lett.*, B263:491–497, 1991. URL: http://inspirehep.net/record/314988, doi:10.1016/0370-2693(91)90494-B.

[360] S. Höche, D. Reichelt, and F. Siegert. Momentum conservation and unitarity in parton showers and NLL resummation. *JHEP*, 01:118, 2018. arXiv:1711.03497, doi:10.1007/JHEP01(2018)118.

[361] B. Webber. Monte Carlo Simulation of Hard Hadronic Processes. *Ann. Rev. Nucl. Part. Sci.*, 36:253–286, 1986. URL: http://inspirebeta.net/record/18125.

[362] T. Sjöstrand. Pythia5.7 and Jetset7.4 Physics and Manual. 1995. URL: http://inspirehep.net/search?p=hep-ph/9508391, arXiv:hep-ph/9508391.

[363] A. Buckley et al. General-purpose event generators for LHC physics. *Phys. Rept.*, 504:145–233, 2011. URL: http://inspirebeta.net/record/884202, arXiv:1101.2599, doi:http://dx.doi.org/10.1016/j.physrep.2011.03.005.

[364] S. Höche. Introduction to parton-shower event generators. In *Proceedings of TASI 2014*, pages 235–295, 2015. URL: http://inspirehep.net/record/1328513/files/arXiv:1411.4085.pdf, arXiv:1411.4085, doi:10.1142/9789814678766_0005.

[365] G. Marchesini and B. R. Webber. Monte Carlo Simulation of General Hard Processes with Coherent QCD Radiation. *Nucl. Phys.*, B310:461,

1988. URL: http://inspirehep.net/search?j=NUPHA,B310,461, doi:10.1016/0550-3213(88)90089-2.

[366] S. Plätzer and S. Gieseke. Coherent Parton Showers with Local Recoils. *JHEP*, 01:024, 2011. URL: http://inspirebeta.net/record/832635, arXiv:0909.5593, doi:10.1007/JHEP01(2011)024.

[367] E. Bothmann et al. Event Generation with Sherpa 2.2. *SciPost Phys.*, 7(3):034, 2019. arXiv:1905.09127, doi:10.21468/SciPostPhys.7.3.034.

[368] G. D. Moore and T. Prokopec. Bubble wall velocity in a first order electroweak phase transition. *Phys. Rev. Lett.*, 75:777–780, 1995. arXiv:hep-ph/9503296, doi:10.1103/PhysRevLett.75.777.

[369] G. D. Moore and T. Prokopec. How fast can the wall move? A Study of the electroweak phase transition dynamics. *Phys. Rev. D*, 52:7182–7204, 1995. arXiv:hep-ph/9506475, doi:10.1103/PhysRevD.52.7182.

[370] P. John and M. Schmidt. Do stops slow down electroweak bubble walls? *Nucl. Phys. B*, 598:291–305, 2001. [Erratum: Nucl.Phys.B 648, 449–452 (2003)]. arXiv:hep-ph/0002050, doi:10.1016/S0550-3213(00)00768-9.

[371] T. Konstandin, G. Nardini, and I. Rues. From Boltzmann equations to steady wall velocities. *JCAP*, 09:028, 2014. arXiv:1407.3132, doi:10.1088/1475-7516/2014/09/028.

[372] J. Kozaczuk. Bubble Expansion and the Viability of Singlet-Driven Electroweak Baryogenesis. *JHEP*, 10:135, 2015. arXiv:1506.04741, doi:10.1007/JHEP10(2015)135.

[373] G. C. Dorsch, S. J. Huber, and T. Konstandin. Bubble wall velocities in the Standard Model and beyond. *JCAP*, 12:034, 2018. arXiv:1809.04907, doi:10.1088/1475-7516/2018/12/034.

[374] M. Barroso Mancha, T. Prokopec, and B. Swiezewska. Field theoretic derivation of bubble wall force. 2020. arXiv:2005.10875.

[375] J. Ellis, M. Lewicki, J. M. No, and V. Vaskonen. Gravitational wave energy budget in strongly supercooled phase transitions. *JCAP*, 06:024, 2019. arXiv:1903.09642, doi:10.1088/1475-7516/2019/06/024.

[376] M. Hindmarsh, S. J. Huber, K. Rummukainen, and D. J. Weir. Gravitational waves from the sound of a first order phase transition. *Phys. Rev. Lett.*, 112:041301, 2014. URL: https://arxiv.org/pdf/1304.2433.pdf, arXiv:1304.2433, doi:10.1103/PhysRevLett.112.041301.

[377] L. Randall and G. Servant. Gravitational waves from warped spacetime. *JHEP*, 05:054, 2007. arXiv:hep-ph/0607158, doi:10.1088/1126-6708/2007/05/054.

[378] T. Konstandin and G. Servant. Cosmological Consequences of Nearly Conformal Dynamics at the TeV scale. *JCAP*, 12:009, 2011. arXiv:1104.4791, doi:10.1088/1475-7516/2011/12/009.

[379] T. Konstandin and G. Servant. Natural Cold Baryogenesis from Strongly Interacting Electroweak Symmetry Breaking. *JCAP*, 07:024, 2011. arXiv:1104.4793, doi:10.1088/1475-7516/2011/07/024.

[380] R. Jinno and M. Takimoto. Probing a classically conformal B-L model with gravitational waves. *Phys. Rev. D*, 95(1):015020, 2017. arXiv:1604.05035, doi:10.1103/PhysRevD.95.015020.

[381] S. Iso, P. D. Serpico, and K. Shimada. QCD-Electroweak First-Order Phase Transition in a Supercooled Universe. *Phys. Rev. Lett.*, 119(14):141301, 2017. arXiv:1704.04955, doi:10.1103/PhysRevLett.119.141301.

[382] B. von Harling and G. Servant. QCD-induced Electroweak Phase Transition. *JHEP*, 01:159, 2018. arXiv:1711.11554, doi:10.1007/JHEP01(2018)159.

[383] A. Kobakhidze, C. Lagger, A. Manning, and J. Yue. Gravitational waves from a supercooled electroweak phase transition and their detection with pulsar timing arrays. *Eur. Phys. J. C*, 77(8):570, 2017. arXiv:1703.06552, doi:10.1140/epjc/s10052-017-5132-y.

[384] L. Marzola, A. Racioppi, and V. Vaskonen. Phase transition and gravitational wave phenomenology of scalar conformal extensions of the Standard Model. *Eur. Phys. J. C*, 77(7):484, 2017. arXiv:1704.01034, doi:10.1140/epjc/s10052-017-4996-1.

[385] T. Prokopec, J. Rezacek, and B. a. Świeżewska. Gravitational waves from conformal symmetry breaking. *JCAP*, 02:009, 2019. arXiv:1809.11129, doi:10.1088/1475-7516/2019/02/009.

[386] T. Hambye, A. Strumia, and D. Teresi. Super-cool Dark Matter. *JHEP*, 08:188, 2018. arXiv:1805.01473, doi:10.1007/JHEP08(2018)188.

[387] C. Marzo, L. Marzola, and V. Vaskonen. Phase transition and vacuum stability in the classically conformal B–L model. *Eur. Phys. J. C*, 79(7):601, 2019. arXiv:1811.11169, doi:10.1140/epjc/s10052-019-7076-x.

[388] P. Baratella, A. Pomarol, and F. Rompineve. The Supercooled Universe. *JHEP*, 03:100, 2019. arXiv:1812.06996, doi:10.1007/JHEP03(2019)100.

[389] S. Bruggisser, B. Von Harling, O. Matsedonskyi, and G. Servant. Electroweak Phase Transition and Baryogenesis in Composite Higgs Models. *JHEP*, 12:099, 2018. arXiv:1804.07314, doi:10.1007/JHEP12(2018)099.

[390] M. Aoki and J. Kubo. Gravitational waves from chiral phase transition in a conformally extended standard model. *JCAP*, 04:001, 2020. arXiv:1910.05025, doi:10.1088/1475-7516/2020/04/001.

[391] L. Delle Rose, G. Panico, M. Redi, and A. Tesi. Gravitational Waves from Supercool Axions. *JHEP*, 04:025, 2020. arXiv:1912.06139, doi:10.1007/JHEP04(2020)025.

[392] K. Fujikura, Y. Nakai, and M. Yamada. A more attractive scheme for radion stabilization and supercooled phase transition. *JHEP*, 02:111, 2020. arXiv:1910.07546, doi:10.1007/JHEP02(2020)111.

[393] M. Shaposhnikov. Possible Appearance of the Baryon Asymmetry of the Universe in an Electroweak Theory. *JETP Lett.*, 44:465–468, 1986.

[394] J. M. Cline and K. Kainulainen. Electroweak baryogenesis at high bubble wall velocities. *Phys. Rev. D*, 101(6):063525, 2020. arXiv:2001.00568, doi:10.1103/PhysRevD.101.063525.

[395] M. Joyce, T. Prokopec, and N. Turok. Nonlocal electroweak baryogenesis. Part 1: Thin wall regime. *Phys. Rev.*, D53:2930–2957, 1996. arXiv:hep-ph/9410281, doi:10.1103/PhysRevD.53.2930.

[396] M. Joyce, T. Prokopec, and N. Turok. Nonlocal electroweak baryogenesis. Part 2: The Classical regime. *Phys. Rev.*, D53:2958–2980, 1996. arXiv:hep-ph/9410282, doi:10.1103/PhysRevD.53.2958.

[397] M. Trodden. Electroweak baryogenesis. *Rev.Mod.Phys.*, 71:1463–1500, 1999. arXiv:hep-ph/9803479, doi:10.1103/RevModPhys.71.1463.

[398] A. Katz and A. Riotto. Baryogenesis and Gravitational Waves from Runaway Bubble Collisions. *JCAP*, 11:011, 2016. arXiv:1608.00583, doi:10.1088/1475-7516/2016/11/011.

[399] D. Grasso and H. R. Rubinstein. Magnetic fields in the early universe. *Phys. Rept.*, 348:163–266, 2001. arXiv:astro-ph/0009061, doi:10.1016/S0370-1573(00)00110-1.

[400] M. Hindmarsh, S. J. Huber, K. Rummukainen, and D. J. Weir. Shape of the acoustic gravitational wave power spectrum from a first order phase transition. *Phys. Rev. D*, 96(10):103520, 2017. [Erratum: Phys.Rev.D 101, 089902 (2020)]. arXiv:1704.05871, doi:10.1103/PhysRevD.96.103520.

[401] T. Kahniashvili, A. G. Tevzadze, A. Brandenburg, and A. Neronov. Evolution of Primordial Magnetic Fields from Phase Transitions. *Phys. Rev. D*, 87(8):083007, 2013. arXiv:1212.0596, doi:10.1103/PhysRevD.87.083007.

[402] A. Brandenburg, T. Kahniashvili, S. Mandal, A. Roper Pol, A. G. Tevzadze, and T. Vachaspati. Evolution of hydromagnetic turbulence from the electroweak phase transition. *Phys. Rev. D*, 96(12):123528, 2017. arXiv:1711.03804, doi:10.1103/PhysRevD.96.123528.

[403] R. Durrer and A. Neronov. Cosmological Magnetic Fields: Their Generation, Evolution and Observation. *Astron. Astrophys. Rev.*, 21:62, 2013. arXiv:1303.7121, doi:10.1007/s00159-013-0062-7.

[404] J. Ellis, M. Fairbairn, M. Lewicki, V. Vaskonen, and A. Wickens. Intergalactic Magnetic Fields from First-Order Phase Transitions. *JCAP*, 09:019, 2019. arXiv:1907.04315, doi:10.1088/1475-7516/2019/09/019.

[405] Y. Zhang, T. Vachaspati, and F. Ferrer. Magnetic field production at a first-order electroweak phase transition. *Phys. Rev. D*, 100(8):083006, 2019. arXiv:1902.02751, doi:10.1103/PhysRevD.100.083006.

[406] J. Chen, T. Han, and B. Tweedie. Electroweak Splitting Functions and High Energy Showering. *JHEP*, 11:093, 2017. arXiv:1611.00788, doi:10.1007/JHEP11(2017)093.

[407] C. W. Bauer, N. Ferland, and B. R. Webber. Combining initial-state resummation with fixed-order calculations of electroweak corrections. *JHEP*, 04:125, 2018. arXiv:1712.07147, doi:10.1007/JHEP04(2018)125.

[408] R. Kleiss and R. Verheyen. Electroweak Radiation in Antenna Parton Showers. 2 2020. arXiv:2002.09248.

[409] S. Catani, S. Dittmaier, M. H. Seymour, and Z. Trocsanyi. The dipole formalism for next-to-leading order QCD calculations with massive partons. *Nucl. Phys.*, B627:189–265, 2002. URL: http://inspirehep.net/search?p=hep-ph/0201036, arXiv:hep-ph/0201036.

[410] S. Schumann and F. Krauss. A parton shower algorithm based on Catani-Seymour dipole factorisation. *JHEP*, 03:038, 2008. URL: http://inspirehep.net/search?p=arXiv:0709.1027, arXiv:0709.1027.

[411] S. Dittmaier. A general approach to photon radiation off fermions. *Nucl. Phys.*, B565:69–122, 2000. URL: http://inspirehep.net/search?p=hep-ph/9904440, arXiv:hep-ph/9904440, doi:10.1016/S0550-3213(99)00563-5.

[412] E. Byckling and K. Kajantie. N-particle phase space in terms of invariant momentum transfers. *Nucl. Phys.*, B9:568–576, 1969. URL: http://inspirehep.net/search?j=NUPHA,B9,568.

[413] E. Byckling and K. Kajantie. *Particle Kinematics*. University of Jyvaskyla, Jyvaskyla, Finland, 1971.

[414] S. Catani and M. H. Seymour. A general algorithm for calculating jet cross sections in NLO QCD. *Nucl. Phys.*, B485:291–419, 1997. URL: http://inspirehep.net/search?p=hep-ph/9605323, arXiv:hep-ph/9605323.